Ferroelectric properties of Barium Calcium Zirconate Titanate $(Ba_{1-x}Ca_x)(Zr_{1-y}Ti_y)O_3$, near morphotropic phase boundary

Thesis Submitted By

Don Biswas

Doctor of Philosophy (Engineering)

Dept. of Instrumentation and Electronics Engineering

Faculty Council of Engineering and Technology

Jadavpur University

Kolkata- 700032, India

2023

JADAVPUR UNIVERSITY

KOLKATA – 700032, INDIA

Index no: 208/19/E

Title of the thesis: **Ferroelectric properties of Barium Calcium Zirconate Titanate ($Ba_{1-x}Ca_x$)($Zr_{1-y}Ti_y$)O_3, near morphotropic phase boundary**

Name & Dept. of the Supervisor/s:

i) Dr. Prolay Sharma

Associate Professor
Department of Instrumentation and Electronics Engineering
Jadavpur University, Salt Lake Campus
Kolkata-700106, India.

List of Publications

Paper Published in International journals:

[1] D. Biswas, N. S. Panwar, P. Sharma, Converse piezoelectric properties of lead free $Ba_{1-x}Ca_xZr_{0.1}Ti_{0.9}O_3$ (x = 0.055) ceramics using double sintered method, Ferroelectrics. 568 (2020) 95. https://doi.org/10.1080/00150193.2020.1811032

[2] D. Biswas, P. Sharma, N. S. Panwar, Dielectric properties of $Na_{1-x}K_xNbO_3$ (NKN) ($0.160 \leq x \leq 0.200$) ceramics synthesized by double sintered method, Ferroelectrics. 571 (2021) 214. https://doi.org/10.1080/00150193.2020.1853757

[3] D. Biswas, P. Sharma, N. S. Panwar, Structural and electrical properties of lead free $Na_{1-x}K_xNbO_3$ ($0.160 \leq x \leq 0.200$) ceramics, Ceramics International. 47 (2021) 13814. https://doi.org/10.1016/j.ceramint.2021.01.246

[4] D. Biswas, P. Sharma, N. S. Panwar, Composition dependent electrical properties of $(Ba_{1-x}Ca_xZr_{0.1}Ti_{0.9})O_3$ ceramics, near morphotropic phase boundary ($0.140 \leq x \leq 0.160$), ECS Journal of Solid State Science and Technology. 10 (2021) 033002. https://doi.org/10.1149/2162-8777/abea61

[5] D. Biswas, S. Singh, P. Thapliyal, V. Rohilla, G. S. Kathait, N. S. Panwar, P. Sharma, Investigation on dielectric and optical properties of $Ba_{1-x}Ca_xZr_{0.1}Ti_{0.9}O_3$ (x = 0.150) ferroelectric ceramics, J. Mountain Res.. 16 (2021) 279. https://doi.org/10.51220/jmr.v16i2.34

[6] D. Biswas, P. Sharma, N. S. Panwar, Structural and piezoelectric properties of $(Ba_{1-x}Ca_xZr_{0.1}Ti_{0.9})O_3$ ceramics, near morphotropic phase boundary ($0.140 \leq x \leq 0.160$), Indian Journal of Pure and Applied Physics. 60 (2022) 111. https://doi.org/10.56042/ijpap.v60i2.57525

[7] D. Biswas, P. Sharma, N. S. Panwar, Temperature dependent dielectric and structural properties of $(Ba_{1-x}Ca_x)(Zr_{0.1}Ti_{0.9})O_3$, ($0.140 \leq x \leq 0.160$) ceramics, ECS Journal of Solid State Science and Technology, 11 (2022) 043007. https://doi.org/10.1149/2162-8777/ac62f3

[8] D. Biswas, P. Sharma, N. S. Panwar, Annealing temperature-dependent structural, optical and electrical properties of $[(Ba_{1-z}Ca_z)(Zr_{0.1}Ti_{0.9})O_3]$, (z = 0.155), films, ECS Journal of

Solid State Science and Technology, 12 (2023) 023011. https://doi.org/10.1149/2162-8777/acbbea

Publication as Book Proceeding: NIL

Publication as Book Chapter: NIL

List of Patents: NIL

Papers published in International Conference Proceedings:

[1] D. Biswas, P. Sharma, N. S. Panwar, Piezoelectric properties of lead free $Ba_{1-x}Ca_xZr_{0.1}Ti_{0.9}O_3$ (x = 0.150) ceramics with different sintering temperature, International conference on Material Science and Applications, Srinagar (Garhwal), Uttarakhand, 2019.

[2] D. Biswas, P. Sharma, N. S. Panwar, Electrical and optical properties of lead free $Ba_{1-x}Ca_xZr_{0.1}Ti_{0.9}O_3$ (x = 0.150) ceramics, International conference on innovative research in applied science engineering, Roorkee, Uttarakhand, 2021.

Statement of Originality

I, ***Don Biswas****, registered on the 5th of July, 2019, do hereby declare that this thesis entitled* ***"Ferroelectric properties of Barium Calcium Zirconate Titanate*** $(Ba_{1-x}Ca_x)(Zr_{1-y}Ti_y)O_3$***, near morphotropic phase boundary"*** *contains a literature survey and original research work done by the undersigned candidate as part of doctoral studies. All information in this thesis has been obtained and presented following existing academic rules and ethical conduct. I declare that, as required by these rules and conduct, I have fully cited and referred all materials and results that are not original to this work. I also declare that I have checked this thesis per the* ***"Policy on Anti Plagiarism, Jadavpur University, 2019"****, and the level of similarity as checked by iThenticate software is 6* ***%.***

Don Biswas
09.06.23

Don Biswas
Index No. 208/19/E
Date:

Prolay Sharma 09/06/2023

Dr. Prolay Sharma

Associate Professor
Department of Instrumentation and Electronics Engg.
Jadavpur University, Salt Lake Campus
Kolkata-700106, India

Dr. Prolay Sharma
Associate Professor
Dept. of Instrumentation and Electronics Engg.
Jadavpur University, Salt Lake Campus,
Sector-III, Block-LB, Plot No - 8, Kolkata-700 106

Certificate from the supervisor

Date: **09.06.23**

This is to certify that the thesis entitled **"*Ferroelectric properties of Barium Calcium Zirconate Titanate ($Ba_{1-x}Ca_x$)($Zr_{1-y}Ti_y$)O_3, near morphotropic phase boundary*"** submitted by **Mr. Don Biswas**, who got his name registered on 5th July 2019 for the award of Ph. D. (Engineering) degree of Jadavpur University, is based upon his work under the supervision of the undersigned; and neither that his thesis nor any part of it has been submitted for any degree/diploma or any other academic award anywhere before.

.

Prolay Sharma 09/06/2023

Dr. Prolay Sharma

Associate Professor
Department of Instrumentation and Electronics Engg.
Jadavpur University, Salt Lake Campus
Kolkata-700106, India.

Dr. Prolay Sharma
Associate Professor
Dept. of Instrumentation and Electronics Engg.
Jadavpur University, Salt Lake Campus,
Sector-III, Block-LB, Plot No - 8, Kolkata-700 106

Dedicated to
my beloved parents and wife,
and to all my teachers

Acknowledgments

First and foremost, I am incredibly grateful to my supervisor, **Dr. Prolay Sharma**, Associate Professor, Department of Instrumentation and Electronics Engineering, Jadavpur University, Kolkata, for his invaluable advice, continuous support, and patience during my Ph. D. study. I am also grateful to **Prof. N. S. Panwar**, Department of Instrumentation Engineering-USIC, H.N.B. Garhwal University, Srinagar (Garhwal), Uttarakhand, for his constant support, enthusiasm and involvement, advice and highly informative discussions that have provided me the new insights in my research domain. I am really grateful to him for his enormous amount of patience while correcting this thesis.

I express my gratitude to **Prof. Rajib Bandyopadhyay** and **Prof. Bipan Tudu**, Professor, Department of Instrumentation and Electronics Engineering, Jadavpur University, Kolkata, for the suggestions and encouragement throughout the research work.

I am thankful to the Department of Instrumentation Engineering-USIC, H.N.B. Garhwal University, Srinagar (Garhwal), Uttarakhand, for allowing me to carry out my research works with all the necessary support and assistance. I want to express my sincere thanks to all of the faculties in our department for their consistent aid and insightful advice on many occasions. Additionally, I want to thank the entire Instrumentation & Electronics Engineering Department staff at Jadavpur University for their cooperation and support in completing this task.

I am sincerely thankful to **Dr. Alok Singh Kandari**, lab senior in the Department of Instrumentation Engineering-USIC, H.N.B. Garhwal University, Srinagar (Garhwal), who helped me a lot in establishing the experimental set up to make the measurements easier. He guided me a lot in the experimentation and different measurements, during my Ph. D. tenure. I am also thankful to my lab senior **Dr. Aradhana Bhandari** for her valuable discussion on the materials and methods.

I am fortunate to associate with my colleagues and lab mates in the Department of Instrumentation Engineering-USIC, H.N.B. Garhwal University, **Dr. Prashant**, **Mr. Gambheer**, **Mr. Vishal**, **Dr. Surendra**, and **Dr. Jyotsana** for their emotional and technical support at various stages of my Ph. D. tenure.

I express my sincere thanks to the technical and other staff of USIC, H.N.B. Garhwal University, for their technical assistance and support.

I am extremely grateful to officials and competent authorities of H.N.B. Garhwal University, Srinagar (Garhwal), for processing my application and permitting me to register the Ph. D. program in IEE department, Jadavpur University.

I would like to convey my deepest gratitude to my parents and family for their love, prayers, caring, sacrifices, continuous support and encouragements for educating and preparing me for my future. I am grateful to my wife and my son for their understanding, love, prayers and continuing support to complete this research work.

Finally, my thanks go to all the well-wishers, who have supported me to complete the research work directly or indirectly.

.

Date: 09.06.2023

Place: Kolkata

Don Biswas
09.06.23

(Don Biswas)

Abstract

The search for the development of new materials of desired properties, both for sophistication and miniaturization, from the technological point of view, has been the motivating source and force of the present study. Ferroelectric materials are employed for the fabrication of many engineering components and thus play a considerable role in our life. Among the lead-free, environmentally friendly ferroelectric ceramics, solid solutions of barium calcium zirconate titanate $(Ba_{1-x}Ca_x)(Zr_{0.1}Ti_{0.9})O_3$ are promising. This widely investigated system exhibits interesting dielectric, piezoelectric and structural properties. The perovskite $(Ba_{1-x}Ca_x)(Zr_{1-y}Ti_y)O_3$ is of particular interest not only because it has structural phase transition but also because of morphotropic phase boundary (MPB) that occurs at a discrete composition (x) range. The MPB is an interesting area in the composition-property diagram, where physical properties are extremal. The composition-dependent dielectric anomaly makes MPB a very interesting region of study. The present thesis entitled '**Ferroelectric properties of Barium Calcium Zirconate Titanate $(Ba_{1-x}Ca_x)(Zr_{1-y}Ti_y)O_3$, near morphotropic phase boundary**' deals with the study of $(Ba_{1-x}Ca_x)(Zr_{1-y}Ti_y)O_3$, (x = 0.140- 0.160, y = 0.9), compositions. The study has been carried out in two parts; the bulk part, which explores the composition(s) near the morphotropic phase boundary in $(Ba_{1-x}Ca_x)(Zr_{1-y}Ti_y)O_3$ at x = 0.150 and y = 0.9; and the thin film part, which deals with the investigations on the optical and electrical measurements of the thin films of a single composition, with x = 0.155, near the MPB.

The first chapter of the thesis broadly introduces the subject, surveys the literature in the field and makes the foundation for the investigations presented in this report. The pellet samples of $(Ba_{1-x}Ca_x)(Zr_{0.1}Ti_{0.9})O_3$, $(0.140 \leq x \leq 0.160)$ were prepared using a solid-state reaction technique followed by double sintering. The preparation method, characterization (using XRD, SEM, EDX,

etc.) and dielectric measurement results have been described in **Chapter- 2**. Among the prepared samples, a break was noticed in the XRD peak shifting tendency indicating anomalous structural behaviour for the compositions with x = 0.150. Anomalous structural and dielectric behaviour indicated morphotropic phase boundary (MPB) in $(Ba_{1-x}Ca_x)(Zr_{1-y}Ti_y)O_3$, (x = 0.140- 0.160, y = 0.9), near the compositions with x = 0.150. The composition-dependent dielectric and structural response has been described in this chapter. The observed variation of the dielectric and structural properties, in a wide temperature range, from room temperature (RT) to 500 °C, has been measured on the compositions near MPB (near x = 0.150), which are described in **Chapter-3**. The structural and dielectric anomaly was observed at the respective transition temperatures in all the prepared compositions. The observed dielectric anomaly, near transition temperature, has been associated with softening of the small-lying optical mode- the soft mode. At the transition temperature, the soft mode ceases, and the lattice observes a structural change, resulting in anomalous dielectric behaviour in the ABO_3-type ferroelectrics. Based on the soft mode theory, the observed results have been analyzed. Experimental observations were observed in fair agreement with the theoretical findings. Measurements of the piezoelectric properties of the compositions near the MPB, with x = 0.150, were carried out. The observed results have been presented in **Chapter- 4**.

In this age of miniaturization, thin film materials play a significant role in high-tech industries. Thin films have primarily been used in communication, optics, microelectronics, energy generation and conservation, and coatings of all types. Deviation from the corresponding bulk properties arises in the thin film material due to its thinness, distinct physical structure and high surface-to-volume ratio, which is a direct result of the growth process. The properties of oxide films are dramatically influenced by annealing, which makes them promising materials for

industrial applications. Thin films were deposited on quartz for optical and silicon for electrical measurements by radio frequency (RF) magnetron sputtering of $(Ba_{0.845}Ca_{0.155})(Zr_{0.1}Ti_{0.9})O_3$ pellet target. The as-deposited $BCZT_{0.9}$ films were annealed at different temperatures in the ambient atmosphere. Prepared films were characterized by XRD- and optical-method. The film deposition and characterization method, observed optical properties and the underlying mechanisms have been discussed in **Chapter- 5**. The electrical measurements were carried out in the MIS (metal-insulator-semiconductor) arrangement. In **Chapter- 6**, the current-voltage (I-V); and **Chapter- 7**, capacitance-voltage (C-V) properties of the $(Ba_{0.845}Ca_{0.155})(Zr_{0.1}Ti_{0.9})O_3$ assisted MIS structures and the mechanisms responsible for the observed behaviour have been discussed. The composition-dependent dielectric and structural properties indicate the existence of a technologically important MPB region in $(Ba_{0.845}Ca_{0.155})(Zr_{0.1}Ti_{0.9})O_3$ system at $x = 0.150$. The measured temperature-dependent structural and dielectric properties have been associated with the soft mode, which softens at the transition temperature (T_c), and the lattice observes a structural change and leads to dielectric and structural anomaly at T_c. The enhanced piezoelectric properties near MPB show the remarkable potential of this system to replace lead-based systems. The measured electrical and optical characteristics of $BCZT_{0.9}$ thin films indicate the potential of the material and electronics applications. All the observed results and underlying mechanisms have been concluded in **Chapter- 8**. The observed properties indicate the exciting potentiality of the $(Ba_{0.845}Ca_{0.155})(Zr_{0.1}Ti_{0.9})O_3$ system for the development of tailor-made materials for industrial and technological applications.

Contents

List of Figures

List of Tables

List of abbreviations

AC	Alternating current
BCZT	Barium calcium zirconate titanate
$BaCO_3$	Barium carbonate
$BaTiO_3$	Barium titanate
BST	Barium strontium titanate
$CaCO_3$	Calcium carbonate
C-V	Capacitance-voltage
C-T	Cubic-tetragonal
DC	Direct current
DRAM	Dynamic random access memory
EDS	Energy dispersive spectroscopy
EDX	Energy Dispersive X-Ray Analysis
EMR	Electron paramagnetic resonance
FN	Fowler-Nordheim
FRAM	Ferroelectric random access memory
HT-XRD	High temperature X-ray diffraction
ICSD	Inorganic Crystal Structure Database
I-V	Current-voltage
IC	Ionic conduction
MEMS	Micro-electro-mechanical systems
MPB	Morphotropic phase boundary
MPT	Morphotropic phase transition
MIM	Metal- insulator- metal
MPM	Metal- piezo material- metal
MIS	Metal- insulator- semiconductor
MOS	Metal oxide semiconductor
NMR	Nuclear magnetic resonance
NKN	Sodium potassium niobate
O-R	Orthorhombic-rhombohedral
PF	Poole-Frenkel
PZT	Lead zirconate titanate
PPT	Polymorphic phase transition
PPB	Polymorphic phase boundary
P-E	Polarization-Electric field
RF	Radio-frequency
RT	Room temperature
SC	Schottky
SCL	Space-charge-limited
SEM	Scanning electron microscopy
SiN_xO_y	Silicon oxynitride
T-O	Tetragonal-orthorhombic
TiO_2	Titanium oxide
Ta_2O_5	Tantalum pentoxide
UHV	Ultra-high vacuum
XRD	X-ray diffraction
ZrO_2	zirconium oxide

CHAPTER-1

Introduction

The study of materials and their properties forms a central research area supporting innovation and technology. Using modern scientific methods, materials scientists can investigate and manipulate materials and produce new materials with remarkable properties. Materials play an important role in our day to day life. New materials are being developed, and new applications are being found. With the same vitality, the demands placed on contemporary materials are growing. Ceramic materials are essential in many of their applications and other invention processes. Researchers are interested in ceramic and glass materials because of their excellent physical and electrical properties. Ceramic materials may have high hardness and meager thermal expansion [1,2]. Also, they behave like an insulator both electrically [3] and thermally [4]. Due to the lack of plastic deformation potential, the shape of the ceramics is likewise relatively stable. Compared with metals, ceramics are especially well suited for high-temperature applications [5], since the uniqueness of ceramic materials is altered at extremely high temperatures, which is far less than that of metals. Ceramics have similar high benefits in view of corrosion and abrasion resistance [6,7].

The three most general forms of solids are amorphous, polycrystalline, and single crystals. The range of an ordered volume inside the solids characterizes each kind. An ordered phase within the solid or material is a spatial volume in which the atoms or molecules are configured periodically or in a regular geometry. Amorphous materials exhibit this order only within a few atomic or molecular dimension. In contrast, polycrystalline materials comprise several angstrom periodic growths, the small crystals, orientated randomly and separated by well-defined boundaries. These ordered volumes, also known as single-crystal regions, are of different sizes and orientations from one another. Crystallites are single-crystallized volumes. Grain can be formed by a single crystallite or a group of crystallites with varied orientations that grow from a common plane. Grain boundaries separate grains from one another. A single-crystal material would exhibit high degree of order, or regular geometric periodicity, over its whole volume. Since grain boundaries impair a material's electrical properties in non-single-crystalline forms, single-crystalline forms typically have better electrical qualities than non-singular ones.

The molecules of a crystalline solid of a particular chemical composition are arranged in a well-defined geometrical pattern- the lattice. The atoms of a molecule in a crystalline solid are pushed to occupy locations in a precise, repeating pattern of the lattice to form the crystal structure. A crystal's lattice structure determines its structural symmetry. The unit cell is the smallest repeating unit of the lattice, and if the number of lattice points per unit cell equals unity, it is referred to as a primitive unit cell. Additionally, according to Neumann's principle, a crystal's external properties reflect the symmetry of its internal arrangement [8]. Crystallographers use (i) a centre of symmetry, (ii) axes of rotation, (iii) mirror planes, and (iv) combinations of these components of symmetry to define symmetry around a point in space, such as the central point of a unit cell. These symmetry elements may split all possible crystal lattices into 32 separate point groups or classes. These 32-point groups are subgroups of seven fundamental crystal structures: triclinic, monoclinic, rhombohedral (trigonal), hexagonal, orthorhombic, tetragonal, and cubic, in order of rising symmetry. Twenty-one out of the 32 point groups are noncentrosymmetric; and when sufficient pressures are applied to the crystal surfaces, positive and negative charges on the opposite faces are formed in 20 of these classes, which are known as piezoelectrics, Fig. 1.1. Piezoelectric materials are a class of materials, which can be polarized by the application of mechanical stress. One class, the point group (432), although it has no centre of symmetry, but still it's not piezoelectric because of other combined symmetry elements [9]. Non-centrosymmetry is a prerequisite for the existence of piezoelectricity. Without an external electric field, some piezoelectric materials still show remnant polarization. Spontaneous polarization refers to the polarization these materials exhibit without an external field. The spontaneous polarization is temperature dependent in the pyroelectric materials. Ten of the 20 piezoelectric classes have pyroelectric properties. Pyroelectricity is a characteristic whereby, owing to the temperature dependency of spontaneous polarization, when the crystal's temperature alters, the electric charges on the account of the change in spontaneous polarization emerge on the crystal's surface, i.e., the electric charge on the surfaces of the crystal changes with change in temperature of the crystal. Ferroelectric materials are the pyroelectrics that can have spontaneous polarization, which may be reversed or reoriented by the introduction of an applied electric field, i.e., the polarity of the spontaneous polarization may be reversed by reversing the polarity of the applied electric field, within the crystal's breakdown limit [9]. One

characteristic distinguishing ferroelectric materials is spontaneous polarization reversal (or switching) by an electric field.

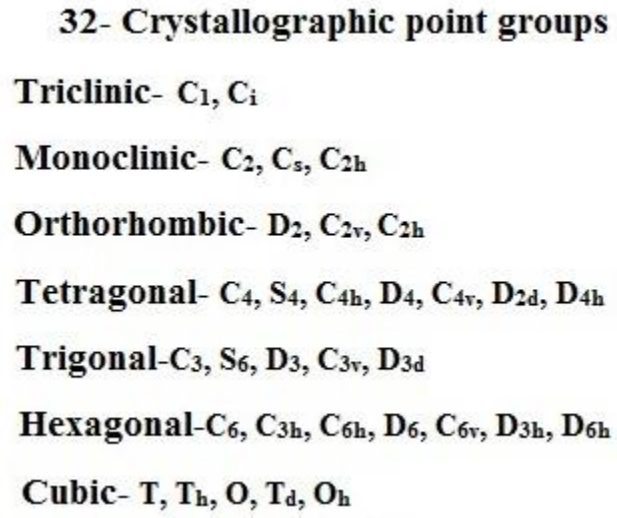

Fig. 1.1 32-Crystallographic point groups in order of increasing symmetry [9].

From a crystallographic point of view, a ferroelectric material must have one of the ten polar point groups, namely C_1, C_s, C_2, C_{2v}, C_3, C_{3v}, C_4, C_{4v}, C_6 and C_{6v} [9]. The belonging relationship categorizes the dielectric materials by taking into consideration the symmetry of all point groups, specifically, ferroelectrics $\subseteq$ pyroelectrics $\subset$ piezoelectrics $\subset$ dielectrics $\subset$ all materials (Fig. 1.1). Owing to the integration of pyroelectric, dielectric, and piezoelectric characteristics, ferroelectrics occupy a central role in the investigation of dielectrics [9]. Ferroelectric compounds have been extensively used in various applications, including capacitors, piezoelectric microsensors and micromotors, nonlinear optical devices, microwave phase filters, memories, and transducers and transistors [9], owing to their robust reactions to mechanical, electrical, optical, and thermal fields. In recent years, there has been a significant advancement in materials design and growth, structural properties, and other electrical characteristics.

A ferroelectric domain is a volume in which all the polarization vectors are parallel and point in the same direction. A ferroelectric material's normal state is a multi-domain state [10-12], with a domain wall separating two neighboring domains. Several domains may have different directions of polarization, and the net polarization of the specimen is the resulting polarization of these domains. When an electric field is applied, the domain walls are decreased (in ceramics) or totally removed (in crystals). The ferroelectric hysteresis loop in the polarization-electric field (P-E) plot is one of the effects of domain-wall switching in ferroelectric materials [13,14]. Fig.

1.2 indicates a typical P-E hysteresis loop of ferroelectric materials. In some circumstances, the orientation of anti-parallel dipoles reduces the energy of the dipole-dipole interaction. Anti-polar crystals are the name given to such crystals. Introducing an external electric field or mechanical stress to an anti-polar crystal, where the anti-polar state's free energy is not significantly different from a polar state's [15-17], may trigger a realignment of antiparallel dipoles. Antiferroelectrics are the name for these crystals [11,18]. The polarization originates from the field induced phase transition in an antiferroelectric phase. The crystal undergoes an electric field-induced phase transition, or ferroelectric phase transition, when the electric field reaches a specific threshold or critical field [11]. Concerning the electric field, the polarization exhibits hysteresis. The crystal recovers to its anti-polar state once the electric field is removed. Therefore, no spontaneous polarization can be seen as a whole, and the crystal exhibits a double hysteresis curve [11]. Beyond a particular temperature, known as the transition temperature or Curie temperature (T_c), ferroelectricity usually vanishes. Beyond T_c, ferroelectric dielectrics are classified as either a non-polar (paraelectric) state or a polar (ferroelectric) phase. Fig. 1.3 exhibits paraelectric-to-ferroelectric phase transition. The P-E plot is linear in a paraelectric phase.

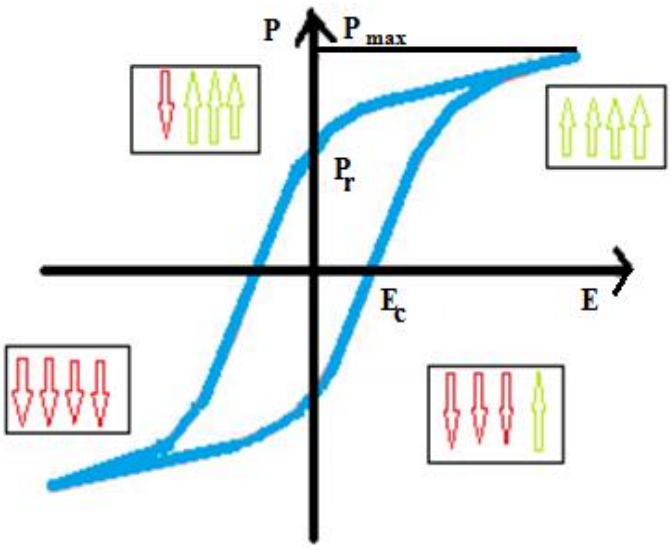

Fig. 1.2 Ferroelectric P-E loop with domain wall switching [9].

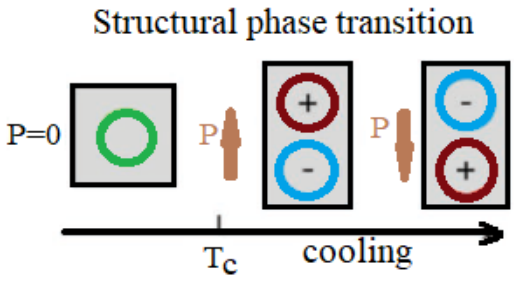

Fig. 1.3 Structural phase transition via Curie temperature T_C [9].

Atomic oscillations in a solid are responsible for various properties, including "specific heat", dielectric, electrical, and optical characteristics. The occurrence of thermal expansion is caused by anharmonicity in the materials followed by temperature fluctuation of elastic constants, the divergence of specific heat from the Dulong-Petit rule at high temperatures, and other phenomena. Theoretically and empirically, several efforts have been made to explain these events in terms of anharmonicity. Numerous researches and studies explore the contribution of anharmonicity on various crystal characteristics [19-22].

The materials observe phase change at certain temperatures, from crystalline to amorphous solid, from solid to liquid, and from liquid to vapor or gaseous form, or vice-versa. Solids, at a certain temperature, observe structural changes. When a solid reaches its structural transition temperature, its structure can change in two ways. First, those transitions in which the atoms of a solid build up a fresh lattice like an amorphous solid transforms into a crystalline form. The second category includes ones in which an ordered lattice is slightly deformed. It might happen due to minor shifts in the lattice locations of individual "atoms or molecules", or due to the arrangement of "atoms or molecules" in different equivalent places. Reconstructive transitions frequently take a long time because of the matter transfer involvement (re-crystallization). They must be of first order since they are transitions that in no way relate to symmetry. The structures of the two phases can be used to describe the symmetry characteristics of crystal phase transitions. The prototype phase is the name given to the high symmetry phase. The symmetry of the crystal alters at the transition temperature. The ordered parameter provides a quantitative description of the transition's low symmetry phase, A(T) [23]. If the transition keeps happening (i.e., A(T) $\rightarrow$ 0, smoothly), the transition is said to be second order. Since it is always possible for a tiny change in A(T) or other attributes to go undetected, one may only experimentally compute a phase transition to be 'almost second order'. It is agreed whenever the term 'second-order' is used. As the second-order transition approaches, the crystal becomes 'soft' with respect

to the order parameter. More specifically, the concerning susceptibility deviates, and the variations of A(T) becomes high and are associated with space-time volume. An important factor in the analysis of phase transitions is the order parameter A(T). Usually, below the transition temperature, it is nonzero and rises with cooling.

The structural phase transition temperature is the temperature at which a solid's structure can change while changing its temperature. The ferroelectric property of a material is temperature dependent. Curie temperature (T_c) refers to the temperature at which a ferroelectric phase changes to a paraelectric phase [19]. The structural phase transition and the ferroelectric phase transition may coexist in ferroelectric materials. Depending on the kind of phase change that takes place at the Curie point, ferroelectric materials can be classified into two types, (i) order-disorder type, such as KH_2PO_4, $NaNO_2$, Triglycine sulphate, and some alums [24], and (ii) displacive type, such as $SrTiO_3$, $NaNbO_3$, $KNbO_3$, $BaTiO_3$, and most of the double oxide ferroelectrics, Fig. 1.4. The statistical disorder of active atoms among many (in the simplest case, two) equilibrium locations set for each cell by the remaining atoms causes the order-disorder type transition [25]. The displacive phase transition is caused due to the displacement of an entire sub-lattice of ions of one type relative to other sub-lattices [26].

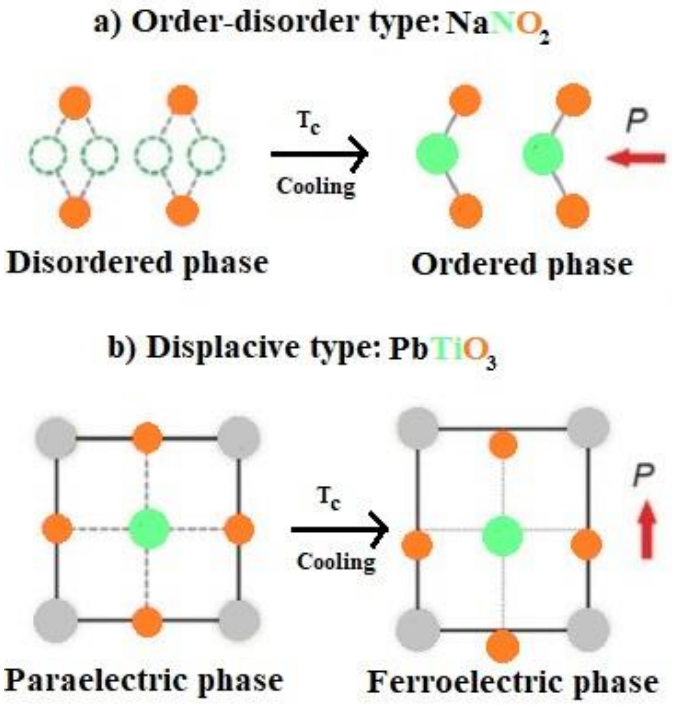

Fig. 1.4 Order-disorder and displacive type phase transitions, respectively [9].

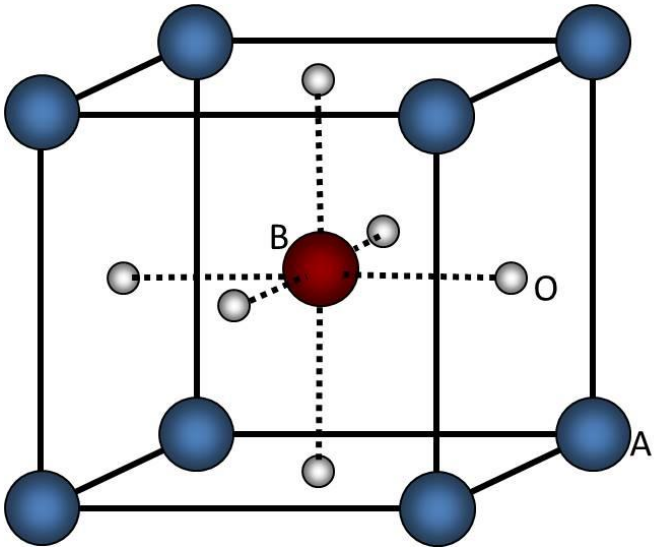

Fig. 1.5 A typical perovskite ABO_3 type structure (cubic) [9,27,32,33].

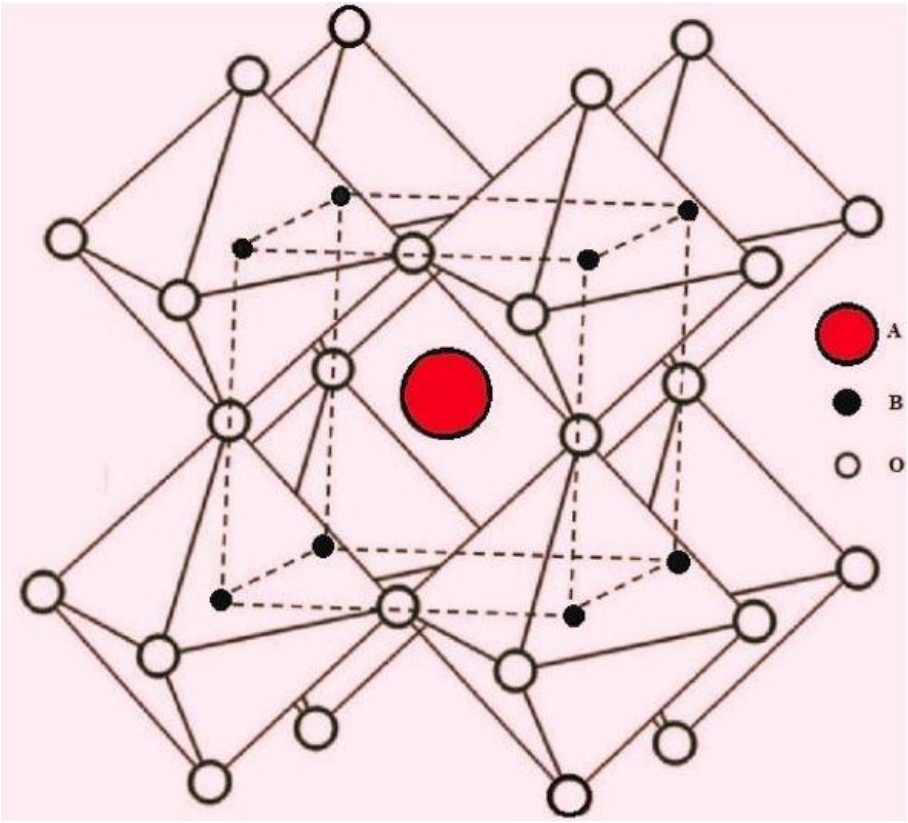

Fig. 1.6 Ideal perovskite cubic structure with BO_6 octahedra [9,27,32,33].

Displacive type ferroelectric materials show polarization owing to the lattice's ionic displacement of particular atoms. Most displacive class type crystals include oxygen octahedra, which is why they're called octahedral ferroelectrics. Perovskite type displacive ferroelectrics (with $CaTiO_3$ structure), such as $PbTiO_3$, $KNbO_3$, $PbZrO_3$, $KTiO_3$, $BaTiO_3$, etc., are the most common ABO_3 type displacive ferroelectrics [27]. Cations occupy the A- or B- site in an ABO_3 type structure depending on their valence states and coordination numbers. Usually, lower valency cations (1 to 3) fill "A- sites", and high valency (3 to 6) cations fill "B- sites". The perovskite structure is a common crystalline structure in oxides, named after the Russian mineralogist L. A. Perovski ($CaTiO_3$ e.g.) [28]. ABO_3 type ferroelectric compounds are technologically important and exhibit significant electrical and optical properties [29]. Perovskite-like structures are not found in all compounds having the formula ABO_3. The ideal perovskite structure comprises one cation, A, using twelve nearest neighbours (12 coordination numbers), and the other, B, with 6 coordination numbers, Fig. 1.5 and 1.6. When A has just 6 closest neighbours, as does B, a completely new structure emerges, as in $FeTiO_3$. In the perovskites, the framework of connected BO_6 octahedra calculates the dimensions of the structure, and hence the size of the A cation to fit exactly into the space surrounded by the encapsulating octahedra. The ideal relation to form a perovskite structure, among the radius of cation A (R_A), B (R_B); and anion (O (R_X), is [30]

$$R_A + R_X = \sqrt{2}(R_B+R_X), \tag{1.1}$$

Ionic radii, on the other hand, are not perfectly constant, varying by a few percent (even after accounting for the fact that radii are consistently more enormous with greater coordination); hence Eq. (1.1) was amended by incorporating a 'tolerance factor' (t) as follows [30].

$$R_A + R_X = t\sqrt{2}\,(R_B + R_X), \tag{1.2}$$

The 'tolerance factor' (t) is close to unity but not quite. Goldschmidt [31] found that the perovskite structure is formed when Eq. (1.2) is fulfilled. If t is much less than 1, a different structure, such as the ilmenite structure, generally appears. Unlike the perovskite structure, Eq. (1.2) is fulfilled by arbitrary parameters, for $t << 1$, so it can adapt quickly to a range of different radii.

The ABO_3 type perovskites can be further classified into four categories, namely (i) Cubic perovskites, (ii) Distorted small-cell perovskites, (iii) Distorted multiple-cell perovskites, and

(iv) Other types (including ilmenite type) [10,32-34]. Many compounds in cubic perovskites have the ideal cubic structure, with only one formula unit, yet many of them are not ferroelectric, at ambient temperature. Examples of cubic perovskite are $SrTiO_3$, $SrZrO_3$, $BaZrO_3$, $BaSnO_3$, $LaMnO_3$, etc. [32,33]. In the distorted small-cell perovskites, the *t* factor is approximately unity but has one or more low-temperature forms with a distorted small cell. This family includes $BaTiO_3$, $KNbO_3$, $PbTiO_3$, etc. [30]. All the structures of this family are ferroelectric at room temperature and may have transition to a perfect cubic structure at higher temperatures, where the ferroelectricity of the material vanishes. Many chemicals in distorted multiple-cell perovskites have a distorted structure in which neighbouring [33] edges are not precisely similar, though nearly so. The true cell is made up of a number of these sub-cells. At ambient temperature, none of these structures is ferroelectric, while some are antiferroelectric. A multiple-cell system cannot have polar symmetry (though it may be physically less probable). Examples of multiple-cell structures are $PbZrO_3$, $NaNbO_3$ and $CaTiO_3$, etc. The other kinds, including the ilmenite type, appear when the factor *t* is about 0.75 [32] for compounds where A has valency 1, which increases with A's valency. Some of the most common forms are based on a closed-packing of oxygen atoms, with the 6- coordinated cation fitting into the crevices and deviating from the perfect packing. $LiNbO_3$, a ferroelectric with the cation sequence Li, Nb, Li, Nb, etc., is a suitable example of incorrect attribution. ABO_3 compounds with low *t* values can also adopt other structural types, such as La_2O_3 and $YCrO_3$, which resembles highly deformed perovskite [32].

In ABO_3 perovskites (from the mineral perovskite $CaTiO_3$) [35], three fundamental structural properties can be recognized; first, the corner-linked O-octahedra are usually only twisted to an infinitesimal level, so that, to a first approximation, they can be treated as rigid units. Second, inside the octahedron, off-centring of B cations can occur, which is attributed to ferroelectricity or antiferroelectricity. Finally, the octahedra can tilt in a variety of ways, which has a significant impact on the lattice characteristics. Structures with tilted octahedra exhibit abnormal elasticity whether or not dipole moments exist and have higher mean linear expansions than structures in which the orientation of the octahedra is fixed by symmetry. The tilting can be explained by three component tilts around the octahedral's three tetrad axis [36].

The theoretical struggle to describe the phase transition phenomenon is often termed the thermodynamic or mean field theory (MFT). Devonshire [37] was the first to propose this

phenomenological hypothesis. A power series in polarization and strain is used to interact with the free energy. The coefficients are, in general, random functions of temperature, which are calculated experimentally. Although this hypothesis was helpful in correlating experimental data, no clear temperature dependence of coefficients has been determined. The associated fluctuations are neglected in MFT, and it's conveyed that the crystal can only be represented by employing its macroscopic (thermodynamic) characteristics. Standard thermodynamic approaches are then used to connect fluctuations in these thermodynamic variables. This estimation is accurate as long as there aren't significant fluctuations in the crystal on a scale more prominent than the interaction range. However, short-range interactions are seen in many systems, and experimental access to the fluctuation-dominated domain is simple. MFT, which is quite effective in summarizing experimental data on structural transitions, should not be applied to all of them. Indeed, a growing portion of the experimental work on structural transitions has been devoted to examining deviations from MFT [37].

The microscopic breakthrough arrived in 1960 with the recognition of the necessary connection between lattice dynamics and ferroelectricity, and the lattice dynamical theory started from very common anharmonic lattice models. A theoretical study was done by Cochran [38] and Anderson [39] in terms of a temperature-dependent low-frequency optical transverse phonon mode-soft mode to characterize the temperature-dependence of relative permittivity (ε) at paraelectric phase transformation. The soft mode unifies the static and dynamic characteristics of structural phase transitions. It was acknowledged as the field's most substantial stimulus and, most importantly, of a soft mode instability at a ferroelectric transition [40]. This quickly led to a thorough investigation of soft modes, in general, using infrared optics, X-ray, and neutron-scattering methods, as well as a classification of the ferroelectric instability as one of several possible classes of lattice instability (i.e., structural transition), each defined in terms of a diffuse or propagating soft mode. From the ferroelectric perspective, the importance of the soft-mode concept is that it allows us to construct a reasonably uniform microscopic figure of ferroelectricity (and antiferroelectricity), the basic simplicity of which is not influenced by the potentially immense difficulty of any particular crystal structure. It then becomes possible to concentrate on the microscopic properties common to all ferroelectrics and to understand the correlation of ferroelectricity to the more general subject of structural transitions and even to critical phenomena.

Several investigations have been conducted in the last century to understand the nature of phase transitions. For the phase transitions from cubic to tetragonal (C-T) and from tetragonal to orthorhombic (T-O), order-disorder type character may be described by a central peak [41-43], and the softening of a transverse optical mode for the orthorhombic-rhombohedral (O-R) transition is used to explain the displacive type character [44-48]. The most direct method for examining a lattice's modes, or their quantization equivalents, the phonons, is through the inelastic scattering of neutrons or photons. An overview of the use of optical methods in the investigation of structural phase transitions was given by Fleury and Lyons [49].

The wave vector scattering breadth of phonons must necessarily be constrained to the Brillouin zone's centre due to the minimum wavelength of light, which is a few thousand angstroms (Å). Thermal neutrons have a wavelength of the order of angstroms and have the same energy as phonons. It enables neutron probing of the Brillouin zone as a whole [50]. The soft mode in the lattice may couple with other modes. Further, the soft mode can couple with acoustic modes if it is an optical soft mode. From the latter part, Brillouin scattering can track variables like soft mode temperature- dependence, damping and other variables. Ultrasonic dispersion and absorption measurements may probe the acoustic mode directly [49]. The occurrence of the local deformations of the atoms in the lattice may be employed to observe a structural phase change. Standard techniques (X-ray and elastic neutron scattering) for this investigation have long been included. Various new and sophisticated methods for investigating the symmetry presence and magnitudes of local deflections in a solid are presently available. The use of optical fluorescence is one method. The Mössbauèr Effect, and nuclear and electron magnetic resonances (NMR and EPR) are additional examples [40,49].

The transitions in displacive dielectrics are attributed to the deformation of an entire sublattice of ions of one kind concerning another sublattice. At the transition point, the atomic displacements are the smallest compared to a unit cell's size. Phonon coordinate is the order parameter in displacive type compounds. The crucial displacements of the ordering magnitude in displacive type are possessed by the soft phonons-the phonon modes that are substantially temperature-dependent and end at the transition temperature. The tunneling of a proton across a barrier between two sites of small potential energy in the double well potential in the hydrogen bond is related to the order-disorder kind of transitions, such as KH_2PO_4, at the transition temperature [51]. The perovskite materials, in which the transition occurs owing to the rotation of BO_6

octahedra, have ABO_3 structure in which A is a first, second, fourth or even fifth group of ions of relevant valency, and B is a transition metal ion, such as Ti, Nb, Ta, Zr, etc. The displacive-type crystal with ABO_3 structure includes $NaNbO_3$, $KNbO_3$, $NaTaO_3$, $KTaO_3$, $SrTiO_3$, $KMnF_3$, $LaAlO_3$, $BaTiO_3$, $PbTiO_3$ etc. These transitions are attributed to the phonon instability [38,39], clearly, the condensation of several classes of modes at the Brillouin zone centre (at q = 0) in ferroelectrics such as $NaTaO_3$, $KNbO_3$, $KTaO_3$, $BaTiO_3$, and others; or at the zone boundary (at q = (½, ½, ½)) in antiferroelectrics such as $NaNbO_3$, $SrTiO_3$, and others. The three fundamental modes that correspond to the octahedron's tilt near the three cube axes can be used. For example, in $SrTiO_3$, one of the triply degenerate mechanisms condenses [52], and in $LaAlO_3$, a linear correlation of all three mechanisms [53]. The tilting of octahedrons about dissimilar cube axes contributes to distinct configurations in the distorted phase; such as, in $LaAlO_3$, and it experiences a trigonal distortion, shown by the tilting of oxygen octahedra [53].

It is commonly accepted that the minimum in the soft mode frequency $\hat{\Omega}(T)$, as the transition temperature is reached, is triggered by the competition between positive short-range and negative coulomb forces [38-40]. Cowley [54], Spitzer et al. [55], Shirane et al. [56-58], utilizing the inelastic scattering of slow neutrons; and Barker and Tinkham [59], from infrared reflectivity measurements, have demonstrated such temperature variation of low lying mode of vibration in non- polar perovskites. Cowley [25] proposed a microscopic theory for ferroelectricity in which the temperature dependence of the soft- mode comes from anharmonic interaction between normal modes. The consideration of anharmonic interactions leads to the stabilization of these modes.

The temperature dependence of permittivity and other physical characteristics of ferroelectrics is illustrated by transition or Curie points, at which the magnitude of permittivity is maximum, and the substance receives or risks the ferroelectric properties as soon as the temperature reaches the Curie point. The structural transition temperature in the materials showing second-order transition (as KDP, TGS) overlaps with the ferroelectric Curie temperature. In the crystals with a first-order transition, the structural transition temperature is slightly larger than the ferroelectric Curie temperature (e.g., about 10 ^oC in $BaTiO_3$). The Curie point considerably relies on impurities and anharmonicity, and is liable for the temperature dependence of relative permittivity, etc. Since the Curie temperature is positive, the anharmonic interactions stabilize the system at a marginally higher transition temperature.

Dielectrics may heat up in an alternating electric field. Dielectric loss (tan δ) refers to the energy loss to heat the dielectric. The dielectric loss includes conduction losses corresponding to a fixed voltage, and loss owing to absorption currents accompanying the processes associated with the sluggish creation of polarization. In the higher field region, the dielectric losses of the ferroelectrics are caused by hysteresis. Microwave losses of the perovskite compounds have been considered by many members [60-64]. In these materials, the temperature dependence of the microwave loss tangent is empirically described by $(T-T_c)\tan\delta = \alpha + \beta T + \gamma T^2$. The temperature- dependence may be understood by evaluating the loss due to the damping of fundamental lattice absorption, which is attributed to the soft optical mode of the material. The power dissipated in a dielectric due to conduction processes is called dielectric loss- the power loss results from the thermal dissipation of the electrical energy the field extends. The high dielectric constant material is preferred for applications requiring a high capacitance in the smallest physical space. It is also essential for these applications to have a small magnitude for the dissipation factor, tan δ.

Pytte [65] studied a lattice dynamical model Hamiltonian to explain the structural phase transition in perovskite ferroelectrics. This model explains a series of transitions in perovskites with the correct parameters. The temperature- dependence of the soft- mode, which is observed to be responsible for the phase transition, was calculated, but Pytte could not explain dielectric properties, because the correlations were decoupled at the very start, and thus all interactions were ignored. Panwar et al. [66] and Semwal et al. [67] modified Pytte's Hamiltonian [57] by taking into account all possible interactions between different vibrational modes. Responses for phonon frequencies and widths, and hence for the relative permittivity and loss tangent, in dissimilar structures, were calculated in those studies. The considerably temperature-dependent modes were found accountable for the measured dielectric properties of the ABO_3 type crystals. Near the transition temperature, the frequency of the temperature-dependent mode ceases, i.e., the mode softens at T_c. Perovskite crystals have been found to depend significantly on the soft mode, both experimentally and theoretically, because the relative permittivity, Curie temperature, loss tangent, acoustic attenuation, and other parameters are significantly dependent on the soft mode [66,67].

Megaw [68] described the transitions in ABO_3 type materials. Premkumar et al. [69] explained the transitions in $(Ba_{1-x}Ca_x)(Zr_{1-y}Ti_y)O_3$ ceramics based on the tilt of the octahedron and the off-

centring of Ca and Ti in its octahedron. In the BCZT system, the polarization may be improved owing to the off-centring of A- and B- site cations leading to the oxygen octahedral distortion. The off- centring occurs by displacing Ti at B- site [69]. The O_6 group surrounds the Ti ions. There is a possibility that the Ti ions are displaced from the centre of the oxygen octahedral. Also, Ca ion can create octahedral distortions and is responsible for causing the local dipole moments. In the BCZT lattice, the net dipole moments are enhanced due to the oxygen octahedral distortion and local displacements at the A- and B- sites [69].

Tilts in ABO_3 type materials can arise around the identical three axes (cubic edge, cube face diagonal, or cubic body diagonal). They can be divided into 1, 2 or 3 equivalent modules around the cube edge [10]. Megaw's theory [68] may be compared with the lattice-dynamical method [70,71]. A soft lattice mode replaces each disappearing tilt module, resulting in the same structure at its extremity. The mechanism may be considered a melting of tilt into lattice modes with rising temperature. The order parameter of Pytte [65] may be physically observed to be the tilt angle of the BO_6 octahedra around its tetrad axis, which is given by the 'soft parameter'. However, for simplicity, the oxygen displacement, which is proportional to the tilt, is used instead of 'soft parameter'.

Perovskite oxides (ABO_3) are the most examined family of ferroelectric oxides. The physical characteristics of these compounds depend considerably on the sample and cationic ordering. The samples may be insulating or metallic and show dissimilar structural and polarization order. Among the ferroelectric applications [73,74], several synthetic perovskites are of great technological significance in piezoelectric [75,76], pyroelectric [75,77], superconductor [78], thermoelectric [79,80], dielectric [81-84], magnetic [85,86], linear and nonlinear electro-optic devices [87], etc.

1.1 Literature survey

1.1.1 Structural and electrical properties of $(Ba_{1-x}Ca_x)(Zr_{1-y}Ti_y)O_3$, (x, y = 0 to 1), near MPB

Perovskite ABO_3 type ferroelectric materials are interesting because of its large dielectric and piezoelectric constant [88,89]. Their high dielectric constant and piezo-coefficient make them potential candidates to be used in the field of capacitors and transducers. The ABO_3 based

materials are also promising candidates for energy storage applications [88,89]. Considering environmental hazards, many lead-free compounds have been found as suitable alternatives in place of lead-based compounds. These substances have been the subject of extensive research [90]. The PZT (lead zirconate titanate) ceramics show large dielectric and piezoelectric constant due to the presence of structurally rhombohedral and tetragonal bridging phases [91-93], a morphotropic phase boundary (MPB), near certain composition (x). The presence of structurally bridging phases may result in several possible polarization directions, near MPB. Extremal electro-physical properties have been observed due to the occurrence of different crystal phases, near MPB [94-99]. The MPB distinguishes two ferroelectric phases with different crystallographic parameters distinguishes two ferroelectric phases with different crystallographic parameters and may significantly improve dielectric and piezoelectric properties. Further, a change in the ferroelectric domain may occur near MPB, which may be the potential reason for the anomalous rise in the dielectric constant. The obtained anomalous nature may be associated with the lattice change at the MPB.

Considering the structure-property correlation of the lead-based compounds, near MPB, many lead-free compounds enable themselves as a suitable alternative to various lead-based compounds. Consequently, researchers have been trying to develop new ferroelectric materials, with extremal electro-physical properties, for the applications of sensors, actuators, and transducers. Many lead-free compounds, like NKN (sodium potassium niobate), BST (barium strontium titanate), BCZT (barium calcium zirconate titanate), etc., have been tried to replace the lead-based piezo-materials [100-105]. Still, piezoelectricity in the NKN and BST compounds was found lower than that of the lead-based compounds [103]. The perovskite lead-free, non-toxic BCZT system shows compatibly high piezo- properties, like PZT, with piezo-constant (d_{33} ~ 620 pC/N) [104,105]. The perovskite ABO_3 structure is maintained, when Ca replaces Ba, and/or Ti by Zr, in the $BaTiO_3$, to prepare $(Ba_{1-x}Ca_x)(Zr_{1-y}Ti_y)O_3$ (BCZT), (x, y = 0 to 1), system [106]. The physical properties of this system can be significantly altered with this replacement at A- and/or B- site, with x ~ 0.150, and y ~ 0.9, near the morphotropic phase boundary.

$BaZr_xTi_{1-x}O_3$ (BZT) is one of the possible alternatives in place of Pb- based materials. $(Ba_{1-x}Ca_x)(Zr_{1-y}Ti_y)O_3$ (BCZT) ceramic systems have received the most attention recently due to the development of a possible MPB region, for the samples with x = 0.150, among the prepared samples. The BCZT (barium calcium zirconate titanate) system exhibits a comparably higher

piezoelectric constant than the lead-based family, such as $PbTiO_3$, $PbZrO_3$, etc. [107]. Li et al. [108,109] found large dielectric and piezoelectric properties in the BCZT system, at MPB. The MPB distinguishes several phases with different crystallographic structures and may greatly improve dielectric and piezoelectric properties [108,109]. Further, a change in the ferroelectric domain may occur near MPB, which may be the potential reason for this kind of rise in the dielectric constant. Zhang et al. [110] found a large piezoelectric constant (338 pC/N) due to the co-existence of orthorhombic and pseudo-cubic phases in BCZT ceramics. The improved electrical properties of $(Ba_{1-x}Ca_x)(Ti_{0.9}Zr_{0.1})O_3$, x = 0.150, ceramics with d_{33} = 350 pC/N, were achieved owing to the presence of MPB [111]. Therefore, the compound $(Ba_{1-x}Ca_x)(Ti_{0.9}Zr_{0.1})O_3$, x = 0.150, is widely investigated to optimize its preparation, dielectric and piezoelectric characteristics [112-116]. According to the earlier reports, the dielectric and piezoelectric characteristics of Ca and Zr-doped $BaTiO_3$ make this compound a suitable substitute for lead-based materials [112-116].

$(Ba_{1-x}Ca_x)(Zr_{1-y}Ti_y)O_3$ (BCZT) is treated as one of the most promising candidates for lead- free piezoelectric ceramics because of its large electrical properties. The solid solutions of $(Ba_{1-x}Ca_x)(Zr_{0.1}Ti_{0.9})O_3$ or BCZT, with a Ba/Ca molar ratio of 85/15, have been the subject of the most research for piezoelectric applications. The Curie temperature of BCZT system is around 100 ^oC (orthorhombic to cubic phase transition). Sen et al. [117] reported that the room temperature (RT) structure of the $(Ba_{1-x}Ca_x)(Zr_{1-y}Ti_y)O_3$ is orthorhombic. It is orthorhombic (C) between ≈ RT and ≈ 100 ^oC (Curie temperature; T_C), and cubic (Pm3m) at higher temperatures [118]. In contrast, a tetragonal structure (P4mm) has been observed due to the change in the ratio of "Ba/Ca" and "Ti/Zr", at RT [119]. The orthorhombic structure is a lower symmetry unit cell (a ≈ 9.80 Å, b ≈ 5.65 Å, c ≈ 6.89 Å), and the cubic indicates a higher symmetry perovskite unit cell (a ≈ b ≈ c ≈ 4 Å, β ≈ 90) [120]. Fu et al. [119] explained the improvement of the dielectric and piezoelectric response because of the occurrence of a MPB between the orthorhombic (O) and tetragonal (T) phases in $(Ba_{1-x}Ca_x)(Zr_{0.1}Ti_{0.9})O_3$, (x = 0.150), ceramics. A polymorphic phase transition (PPT) was observed from tetragonal to orthorhombic, orthorhombic to rhombohedral regions in $(Ba_{1-x}Ca_x)(Zr_{0.1}Ti_{0.9})O_3$, at x = 0.130, which can be owing to the togetherness of these phases at a single concentration and can significantly enhance the suggesting piezoelectric property [119]. Ferroelectric ceramics exhibit piezoelectric response, which has two parts. The piezoelectric phenomena in every ferroelectric domain cause the lattice contribution, which is the

first part. Owing to the displacement of non-180° domain walls, the second part, commonly called the extrinsic contribution, is significant [121]. A ferroelectric material's multi-domain position is natural [10-12]. The piezoelectric response is primarily dominated by domain-wall contributions in several ferroelectric ceramics, including lead zirconate titanate ($Pb(Zr,Ti)O_3$) and barium titanate ($BaTiO_3$) [122]. The ferroelectric hysteresis loop [polarization-electric field (P-E) curve] is one crucial effect of the domain-wall switching in ferroelectric materials [13,14]. The piezoelectric response of a ferroelectric material can also be caused by other processes, which are not always related to domain wall motion [123]. Typically, it was thought that the final piezoelectric properties were positively influenced by the higher polarization vectors, which come from the coexisting ferroelectric phases. An MPB can consist of several possible phases. A combination of these phases may initiate different polarization directions, which might have also contributed to the observed dielectric behaviour, for the compositions near MPB. The polarization extension and rotation, presence of intermediate phases, and elastic softening of lattice contribute to large piezoelectricity in BCZT ceramics, at the morphotropic phase boundary [124,125]. Physical properties such as the dielectric and piezoelectric constant, electromechanical coupling factor and the remanent polarization are improved near the morphotropic phase boundary [126].

The high-temperature phases of tilt systems of the ferroelectric perovskite materials have been studied [127]. The contribution of the domain wall to the elastic, dielectric, and piezoelectric characteristics of ferroelectric compounds was the focus of numerous investigations [128-136]. At the same time, potential piezoelectric coefficients were found near the co-existence of different phases. Instead of the traditional MPB, polymorphic phase boundary (PPB) was the name given to this kind of phase boundary [137].

1.1.2 Thin film deposition by sputtering

A solid material is considered to be in thin film form when it is formed as a thin layer on a solid support, known as substrate, *ab- initio* by prohibited condensation of the individual molecular, atomic, or ionic species; either straightly by a physical reaction, or via a chemical reaction. Thin films have distinct and unique characteristics that aren't just a result of their modest thickness but also part of the microstructure that outcomes from the specific process by which these fundamental building pieces are slowly introduced one by one. No matter how thick they are,

thick films are those formed by directly applying a paste or dispersion of the substance to a substrate and allowing it to cure. These films have distinct characteristics that set them apart from thin films. Owing to their high surface-to-volume ratio, thinness, and different physical structure, thin films frequently differ from the characteristics of similar bulk materials, which indicates a direct result of the growth process. The various methods for depositing thin films are classified as physical and chemical. The specific deposition method chosen depends on the desired film qualities, the production or cost rate offered by the mechanism, the substrate's temperature limit, the uniformity and reliability of the process, and its suitability with earlier and later processing stages. Sometimes thin films deposited in one form are transformed into another form or material.

Sputtering is a physical deposition method in which almost any substance is transported from a source, referred to as the target, to a substrate made of just about any substance. The material is ejected from the target by blasting the surface with inert gas ions accelerated by high voltage. Atomic-sized particles are ejected from the target owing to the momentum transfer between the atoms of the target material and the incident ions. These particles pass through the vacuum unit before forming a thin coating on a substrate. The deposited film has the identical composition and structure as the source material and may be sputtered from an extensive range of materials.

Until the first half of the twentieth century, attention to thin film was primarily focused on its optical properties. The role played by films was principally unitarian, necessitating the measurements of film optical and thickness characteristics. The science and technology of thin films now play a significant role in high-tech sectors. Although thin films have primarily been used in microelectronics, there are many other, steadily expanding uses in communication, optical electronics, coatings of many types, and methods for generating and conserving energy. The use of thin films in microelectronics has increased dramatically, which has sparked significant theoretical interest. Significantly new applications for thin film electrical insulators, conductors, and electronics have been made available by the solid-state revolution. Tiny integrated circuit chips made of thin films may now more efficiently and safely accomplish what involved massive discrete electrical components and systems earlier.

In many instances, the electrodes for the particular film subsequently deposited on the substrate may work as a conducting electrode. Insulating films cannot generally be thought of independently from the electrodes that come into contact with them. The individual metal or

semiconductor electrode materials utilized in a thin film significantly impact the electrical response. The structures include insulator films between semiconductors (SIS), mixed electrodes (MOS, MIS), and metals (MIM). Some factors that may change the nature of charge transfer at an interface involve interfacial adhesions, tension, inter-diffusion, and integrated or adsorbed contaminants. The parameters that have a much more significant impact on the characteristics of thin films than those of their bulk counterparts include film thickness, degree of film continuity, the existence of high electric field conduction phenomena, high chemical reactivity, etc. For example, while the difference between the electrical characteristics of thin films and their bulk counterparts in metals is relatively small, it can be enormous in insulators.

Ferroelectrics play an essential role in a variety of applications. Due to the rising need for suitability with microelectronics, there has been a lot of interest in the processing and study of ferroelectric thin films over the past three decades. Thin-film ferroelectric ceramics provide a number of significant benefits over their bulk counterparts when used as active components in electromechanical devices. Ferroelectric thin films are promising for high-frequency transducer applications due to their tiny inertia mass, which permits greater cut-off frequencies and larger working bandwidths for electromechanical devices. Another essential benefit of ferroelectric thin films is the substantial energy density that may achieve because of high dielectric strength. According to reports [138], breakdown strengths in 10^8 V/m have been observed. They are so preferred for micro-positioning and actuation applications. The third benefit is the low driving voltage and reasonably quick polarization switching speed of ferroelectric thin films for nonvolatile random-access memory. New varieties of ferroelectric thin films that can attain switching strains close to one percent are also being developed. Till now, ferroelectric thin films have been employed in a variety of devices, including micro-actuators [139], electromechanical transducers, microsensors [140], ultrasonic motors [141], nonvolatile computer memories [142], superconductors [78], thermoelectric [79,80], dielectric [81-84], magnetic [85,86], linear and nonlinear electro-optic devices [87], and switching capacitors for integrated circuitry [143]. They can potentially be employed as pressure sensors in pacemakers because of their biocompatibility and excellent piezoelectric characteristics [144].

Ferroelectric films have extended the options for the electromechanical transducers to use them at much higher frequencies and nonvolatile memories too much higher densities [82-84]. The processing of complex ferroelectric oxides has improved, and they may now be integrated with

high-temperature superconductive oxides, reviving interest in ferroelectric memories. Micro-sensors and microelectronics are increasingly combined to create micro-electro-mechanical systems (MEMS). Ferroelectric sheets give MEMS additional functionality, such as sensing capabilities. Portable phones entered the mass market in the late 1990s, and the introduction of polar thin films contributed to their further miniaturization and enhanced performance. Ferroelectric films are currently employed in various commercial things, including memory, micro-devices, and microwave electronic components with piezoelectric and pyroelectric micro-sensors/actuators. Over the last 30 years, an intensive investigation has been conducted to understand better the physics and material concerns that control the working of films in devices. The advancements in the topic are presented in several books [145-147], journal papers [148], and recent reviews [149,150], etc.

1.2 Objectives and outline of the thesis

The present study aims to identify the $(Ba_{1-x}Ca_x)(Zr_{1-y}Ti_y)O_3$ system's optimal electrical properties near the morphotropic phase boundary (MPB). At certain compositions, the MPB, extremal dielectric and piezoelectric properties may be observed owing to the presence of structural bridging phases, which may lead to several possible polarization directions contributing to the dielectric and piezoelectric constant. A large electromechanical response is attributed to the MPB owing to its symmetry-allowed polarization extension. The large electromechanical response of such compositions may be useful for the applications of sensors and transducers. Further, a negligible dielectric loss is required for these applications. With this intention, the lead-free high dielectric and piezoelectric $(Ba_{1-x}Ca_x)(Zr_{0.1}Ti_{0.9})O_3$ ceramics with x = 0.140-0.160 compositions were prepared, and the structural and electrical characteristics of the prepared compositions were measured. A study of the thin film structures of these compositions, near MPB, leads to their further miniaturization and enhanced performance applications. The as-deposited amorphous oxide thin film crystallizes and becomes stable, on annealing at higher temperatures. The large relative permittivity and minimum leakage current density are required for memory device applications. Among the studied ceramic compositions, thin films of the highest dielectric constant $(Ba_{0.845}Ca_{0.155})(Zr_{0.1}Ti_{0.9})O_3$ composition were sputter deposited. To achieve a large relative permittivity and minimum leakage current density, measurements were carried out on the films with different annealing treatments. Also, the optical characteristics of

the prepared films were investigated for optical applications. The measured current conduction mechanisms in the prepared film-assisted MIS (metal-insulator-semiconductor) structures were also examined to comprehend the current conduction process. The structural and electrical properties of the prepared bulk $(Ba_{1-x}Ca_x)(Zr_{0.1}Ti_{0.9})O_3$, $(0.140 \leq x \leq 0.160)$; and $(Ba_{1-x}Ca_x)(Zr_{1-y}Ti_y)O_3$, $(x = 0.155$ and $y = 0.9)$ thin films were studied, near MPB.

In the current study, firstly, bulk compositions of $(Ba_{1-x}Ca_x)(Zr_{0.1}Ti_{0.9})O_3$, $(0.140 \leq x \leq 0.160)$, were prepared by conventional solid-state reaction method followed by double sintering. XRD patterns, dielectric and piezoelectric investigations on the prepared sample exhibit a morphotropic phase boundary close to compositions with $x = 0.150$. The obtained composition-dependent XRD and dielectric measurement results have been discussed in **Chapter- 2**. Composition-dependent piezoelectric properties of BCZT ceramics have been discussed in **Chapter- 3**. In **Chapter- 4,** the observed temperature-dependent dielectric characteristics of the bulk samples were studied and discussed. To continue the study further, a thin film form of the material with one composition, $(Ba_{0.845}Ca_{0.155})(Zr_{0.1}Ti_{0.9})O_3$, with $x = 0.155$, was studied. Thin films were deposited on the quartz and silicon (p- type, <100>) substrates, by radio frequency (RF) magnetron sputtering of $(Ba_{0.845}Ca_{0.155})(Zr_{0.1}Ti_{0.9})O_3$ pellet target, using argon as the bombarding gas. All the films were deposited at ambient temperature and then annealed in ambient air, each at 500, 600, 650, 700, 750 and 800 ^oC, for one hour. **Chapter- 5** includes the preparation technique, measured optical characteristics, and different optical parameters of the prepared thin films. **Chapter- 6** discusses the dominant conduction mechanisms in the prepared metal-insulator-semiconductor (M-I-S) structures and the observed current-voltage (I-V) properties of the prepared films. To see the feasibility of the prepared thin films for memory devices and other applications, capacitance-voltage (C-V) properties of the prepared M-I-S structures were investigated. The observed C-V characteristics of the prepared structures have been described in **Chapter- 7**. All the observations of the present study have been concluded in **Chapter- 8**.

References

[1] F.J. Parker, Al_2TiO_5-$ZrTiO_4$-ZrO_2 Composites: a new family of low-thermal-expansion ceramics, Journal of the American Ceramic Society. 73 (1990) 929-932. https://doi.org/10.1111/j.1151-2916.1990.tb05138.x

[2] Y.S. Limaye, D.K. Agrawal, R. Roy, Y. Mehrotra, Synthesis, sintering and thermal expansion of $Ca_{1-x}Sr_xZr_4P_6O_{24}$-an ultra-low thermal expansion ceramic system, Journal of materials science. 26 (1991) 93-98. https://doi.org/10.1007/BF00576037

[3] P. Rado, An introduction to the technology of pottery, 2nd ed., Pergamon Press publishing, Oxford, 1988.

[4] T. Ekström, M. Nygren, SiAION ceramics, Journal of the American Ceramic Society. 75 (2005) 259-276. https://doi.org/10.1111/j.1151-2916.1992.tb08175.x

[5] A.W. Weimer, Carbide, nitride, and boride materials synthesis and processing, 1st ed., Chapman & Hall publishing, London, 1997.

[6] O. Odawara, Long ceramic-lined pipes with high resistance against corrosion, abrasion and thermal shock, Materials and Manufacturing Processes. 8 (1993) 203-218. https://doi.org/10.1080/10426919308934825

[7] G. Barbezat, A.R. Nicol, A. Sickinger, Abrasion, erosion and scuffing resistance of carbide and oxide ceramic thermal sprayed coatings for different applications, Wear. 162 (1993) 529-537. https://doi.org/10.1016/0043-1648(93)90538-W

[8] W.G. Cady, Piezoelectricity: an introduction to the theory and applications of electromechanical phenomena in crystals, 1st ed., Tata McGraw-Hill publishing, New York, 1946.

[9] X.K. Wei, N. Domingo, Y. Sun, N. Balke, R.E. Dunin- Borkowski, J. Mayer, Progress on emerging ferroelectric materials for energy harvesting, storage and conversion, Advantage Energy Matererials. (2022) 2201199. https://doi.org/10.1002/aenm.202201199

[10] E.A. Wood, Polymorphism in potassium niobate, sodium niobate, and other ABO_3 compounds, Acta Crystallographica. 4 (1951) 353-362. https://doi.org/10.1107/S0365110X51001112

[11] K. Uchino, Ferroelectric Devices, 1st ed., Marcel Dekker publishing, New York, 2000.

[12] P. Vousden, The structure of ferroelectric sodium niobate at room temperature, Acta Crystallographica. 4 (1951) 545-551. https://doi.org/10.1107/S0365110X51001768

[13] B.T. Matthias, New ferroelectric crystals, Physical Review. 75 (1949) 1771. https://doi.org/10.1103/PhysRev.75.1771

[14] B.T. Matthias, J. Remeika, Dielectric properties of sodium and potassium niobates, Physical Review. 82 (1951) 727-729. https://doi.org/10.1103/PhysRev.82.727

[15] C. Kittel, Introduction to solid state physics, 1st ed., Wiley publishing, New Jersey, 1956.

[16] F. Jona, G. Shirane, Ferroelectric crystals, International Series of Monographs on Solid State Physics, 1st ed., Pergamon Press publishing, Oxford, 1962.

[17] L.L. Altgilbers, J. Baird, B.L. Freeman, C.S. Lynch, S.I. Shkuratov, Explosive pulsed power, 1st ed., Imperial college press publishing, London, 2011.

[18] C. Kittel, Theory of antiferroelectric crystals, Physical Review. 82(5) (1951) 729-732. https://doi.org/10.1103/PhysRev.82.729

[19] K.H. Chew, Recent applications of landau-ginzburg theory to ferroelectric superlattices: A review, Solid State Phenomena, 189 (2012) 145-167. https://doi.org/10.4028/www.scientific.net/SSP.189.145

[20] B.S. Semwal, Studies of Lattice Anharmonicity and Isotopic Imperfection in Crystals, D.Phil. Thesis, Allahabad University, Allahabad, 1972.
[21] B.S. Semwal, P.K. Sharma, Thermal conductivity of an anharmonic crystal, Physical Review. B5 (1972) 3909-3914. https://doi.org/10.1103/PhysRevB.5.3909
[22] B.S. Semwal, P.K. Sharma, Thermal conductivity of an isotopically disordered harmonic crystal, Journal of Mathematical Physics. 15 (1974) 648-653. https://doi.org/10.1063/1.1666701
[23] N.S. Panwar, Structural Phase Transition in Perovskite Type Crystals, D. Phil. Thesis, HNB Garhwal University, Srinagar (Garhwal), 1989.
[24] F. Jona, R. Pepinsky, G. Shirane, Ferroelectricity in the Alums, Physical Review. 102 (1956) 1181-1182. https://doi.org/10.1103/PhysRev.102.1181
[25] R.A. Cowley, Lattice dynamics and phase transitions of strontium Titanate, Physical Review. 134 (1964) A981-A997. https://doi.org/10.1103/PhysRev.134.A981
[26] M. Tokunaga, T. Matsubara, Theory of Ferroelectric Phase Transition in KH2PO4 Type Crystals. I, Progress of Theoretical Physics. 35 (1966) 581-599. https://doi.org/10.1143/PTP.35.581
[27] H. Nagta, N. Chikoshi, T. Takenaka, Ferroelectric properties of bismuth layer-structured compound $Sr_xBi_{4-x}Ti_{3-x}Ta_xO_{12}$ ($0 \leqq x \leqq 2$), Journal of Applied Physics. 38 (1999) 5497. https://doi.org/10.1143/JJAP.38.5497
[28] Z. Cheng, J. Lin, Layered organic-inorganic hybrid perovskites: structure, optical properties, film preparation, patterning and templating engineering, CrystEngComm. 12 (2010) 2646. https://doi.org/10.1039/C001929A
[29] G.A. Samara, Effects of pressure on the dielectric properties and phase transitions of the alkali metal tantalates and niobates, Ferroelectrics. 73 (1987) 145-159. https://doi.org/10.1080/00150198708227914
[30] M.L. Keith, R. Roy, Structural relations among double oxides of trivalent elements, American Mineralogist. 39 (1954) 1-23.
[31] V.M. Goldschmidt, The laws of crystallochemistry, The Natural Sciences. 14 (1926) 477-485. https://doi.org/10.1007/bf01507527
[32] H.D. Megaw, Crystal structure of double oxides of the perovskite type, Proceedings of the Physical Society. 58 (1946) 133-152. https://doi.org/10.1088/0959-5309/58/2/301
[33] M.G. Harwood, The Crystal Structure of Lanthanum-Strontium Manganites, Proceedings of the Physical Society. Section B. B68 (1955) 586-592. https://doi.org/10.1088/0370-1301/68/9/302
[34] H. Granicher, Dielectric properties of perovskite-type substances, Helvetica Physica Acta. 24 (1951) 619-622.
[35] H.D. Megaw, Structure and transitions in perovskites, Journal of Physics Colloques. 33 (1971) C2-1-C2-5. https://doi.org/10.1051/jphyscol:1972201
[36] A.M. Glazer, The classification of tilted octahedra in perovskites, Acta Crystallographica. B28 (1972) 3384-3392. https://doi.org/10.1107/S0567740872007976
[37] A.F. Devonshire, Theory of barium Titanate, The London, Edinburgh, and Dublin Philosophical Magazine and Journal of Science. 40 (1949) 1040-1063. https://doi.org/10.1080/14786444908561372
[38] W. Cochran, Crystal stability and the theory of ferroelectricity, Physical Review Letters. 3 (1959) 412-414. https://doi.org/10.1103/PhysRevLett.3.412

[39] P.W. Anderson, izika dielekrikov, G. I. Skanavi, ed., Academic Nauk USSR publishing, Moscow, 1960: pp. 290.
[40] G. Venkataraman, Soft modes and structural phase transitions, Bulletin of Materials Science. 1 (1979) 129-170. https://doi.org/10.1007/BF02743964
[41] R. Comes, M. Lambert, A. Guinier, Solid State Communications. 6 (1968) 715-719. https://doi.org/10.1016/0038-1098(68)90571-1
[42] R. Currat, R. Comes, B. Domer, E. Wiesendanger, Inelastic neutron scattering in orthorhombic $KNbO_3$, Journal of Physics C: Solid State Physics. 7 (1974) 2521. https://doi.org/10.1088/0022-3719/7/14/016
[43] M.D. Fontana, G. Metrat, J.L. Servoin, F. Gervais, Infrared spectroscopy in $KNbO_3$ through the successive ferroelectric phase transitions, J. Phys. C, 16 (1984) 483. https://doi.org/10.1088/0022-3719/17/3/020
[44] W. Cochran, Crystal stability and the theory of ferroelectricity, Advances in Physics. 9 (1960) 387-423. https://doi.org/10.1080/00018736000101229
[45] G. Shirane, Y. Yamada, Lattice-Dynamical Study of the 110°K Phase Transition in $SrTiO_3$, Physical Review. 177 (1969) 858-863. https://doi.org/10.1103/PhysRev.177.858
[46] E. Pytte, J. Feder, Theory of a structural phase transition in perovskite-type crystals, Physical Review. 187 (1969) 1077-1088. https://doi.org/10.1103/PhysRev.187.1077
[47] R. Blinc, B. Zeks, Soft Modes in Ferroelectrics and Anti- ferroelectrics, 1st ed., North Holland publishing, Amsterdam, 1974.
[48] A.D. Bruce, R.A. Cowley, Structural Phase Transitions, 1st ed., Taylor and Francis publishing, London, 1981.
[49] P.A. Fleury, K. Lyons, Optical Studies of Structural Phase Transitions, In: K.A. Müller, H. Thomas, (eds) Structural Phase Transitions I. Topics in Current Physics, Spinger publishing, Berlin, 1981: pp. 9-92. https://doi.org/10.1007/978-3-642-81531-7_2
[50] B. Dorner, Investigation of Structural Phase Transitions by Inelastic Neutron Scattering, In: K.A. Müller, H. Thomas, (eds) Structural Phase Transitions I. Topics in Current Physics, Spinger publishing, Berlin, 1981: pp. 93-130. https://doi.org/10.1007/978-3-642-81531-7_3
[51] K.K. Kobayashi, Dynamical theory of the phase transition in KH_2PO_4-type ferroelectric crystals, Journal of the Physical Society of Japan, 24 (1968) 497-508. https://doi.org/10.1143/JPSJ.24.497
[52] R.A. Cowley, W.J.L. Buyers, G. Dolling, Relationship of normal modes of vibration of strontium titanate and its antiferroelectric phase transition at 110 ^oK, Solid State Communications. 7 (1969) 181-184. https://doi.org/10.1016/0038-1098(69)90720-0
[53] W. Cochran, A. Zia, Structure and dynamics of perovskite-type crystals, Physica Status Solidi (b), 25 (1968) 273-283. https://doi.org/10.1002/pssb.19680250126
[54] R.A. Cowley, Temperature dependence of a transverse optic mode in strontium Titanate, Physical Review Letters. 9 (1962) 159-161. https://doi.org/10.1103/PhysRevLett.9.159
[55] W.C. Spitzer, R.C. Miller, D.A. Kleiman, L.E. Howarth, Far Infrared Dielectric Dispersion in $BaTiO_3$, $SrTiO_3$, and TiO_2, Physical Review. 126 (1962) 1710-1721. https://doi.org/10.1103/PhysRev.126.1710
[56] G. Shirane, R. Nathans, V.J. Minkiewicz, Temperature dependence of the soft ferroelectric mode in $KTaO_3$, Physical Review. 157 (1967) 396-399. https://doi.org/10.1103/PhysRev.157.396

[57] G. Shirane, B.C. Frazer, V.J. Minkiewicz, J.A. Leak, A. Linz, Soft optic modes in barium Titanate, Physical Review Letters. 19 (1967) 234-235. https://doi.org/10.1103/PhysRevLett.19.234
[58] E. Fatuzzo, W.J. Merz, Ferroelectricity, 1st ed., North Holland publishing, Amsterdam, 1967.
[59] A.S. Barker, M. Tinkham, Far-Infrared Ferroelectric Vibration Mode in $SrTiO_3$, Physical Review. 125 (1962) 1527-1530. https://doi.org/10.1103/PhysRev.125.1527
[60] T.S. Benedict, J.L. Durand, Physical Review. 109 (1958) 1091-1093. https://doi.org/10.1103/PhysRev.109.1091
[61] G. rupprecht, R.O. Bell, B.D. Silverman, Nonlinearity and microwave losses in cubic strontium-titanate, Physical Review. 123 (1961) 97-98. https://doi.org/10.1103/PhysRev.123.97
[62] G. rupprecht, R.O. Bell, Microwave losses in strontium titanate above the phase transition, Physical Review. 125 (1962) 1915-1920. https://doi.org/10.1103/PhysRev.125.1915
[63] B.D. Silverman, Microwave absorption in cubic strontium titanate, Physical Review. 125 (1962) 1921-1930. https://doi.org/10.1103/PhysRev.125.1921
[64] R. Bahadur, P.K. Sharma, Impurity dependence of the Curie temperature and microwave absorption in ferroelectric crystals, Physical Review B. 12 (1975) 448-457. https://doi.org/10.1103/PhysRevB.12.448
[65] E. Pytte, Theory of perovskite ferroelectrics, Physical Review B. 5 (1972) 3758-3769. https://doi.org/10.1103/PhysRevB.5.3758
[66] N.S. Panwar, T.C. Upadhyay, B.S. Semwal, Soft mode dynamics of perovskite type crystals, Pramana. 33 (1989) 603-614. https://doi.org/10.1007/BF02845811
[67] B.S. Semwal, N.S. Panwar, Dielectric properties of perovskite crystals, Bulletin of Materials Science. 15 (1992) 237-250. https://doi.org/10.1007/BF02927502
[68] H.D. Megaw, A simple theory of the off-centre displacement of cations in octahedral environments, Acta Crystallographica. B24 (1968) 149-153. https://doi.org/10.1107/S0567740868001834
[69] S. Premkumar, S. Radhakrishnan, V.L. Mathe, Understanding A and B-site engineered lead-free $Ba_{(1-x)}Ca_xZr_yTi_{(1-y)}O_3$ piezoceramics: a perspective from DFT, Journal of Materials Chemistry C. 9 (2021) 4248-4259. https://doi.org/10.1039/D0TC05724J
[70] A.M. Glazer, H.D. Megaw, The structure of sodium niobate (T_2) at 600 ^oC, and the cubic-tetragonal transition in relation to soft-phonon modes, Philosophical Magazine. 25 (1972) 1119-1135. https://doi.org/10.1080/14786437208226856
[71] K. Ishida, G. Honjo, Soft modes and superlattice structures in $NaNbO_3$, Journal of the Physical Society of Japan. 34 (1973) 1279-1288. https://doi.org/10.1143/JPSJ.34.1279
[72] W.B. Yelon, W. Cochran, G. Shirane, A. Linz, Neutron scattering study of the soft modes in cubic potassium tantalate-niobate, Ferroelectrics. 2 (1971) 261-269. https://doi.org/10.1080/00150197108234100
[73] N. Uchida, T. Ikeda, Studies on $Pb(Zr\text{-}Ti)O_3$ ceramics with addition of Cr_2O_3, Japanese Journal of Applied Physics. 6 (1967) 1079. https://doi.org/10.1143/JJAP.6.1292
[74] Y. Guo, K. Kakimoto, H. Ohsato, Ferroelectric-relaxor behavior of $(Na_{0.5}K_{0.5})NbO_3$-based ceramics, Journal of Physics and Chemistry of Solids. 65 (2004) 1831-1835. https://doi.org/10.1016/j.jpcs.2004.06.018

[75] T. Takenakaa, K. Sakataa, Dielectric, piezoelectric and pyroelectric properties of $(BiNa)_{1/2}TiO_{3-}$ based ceramics, Ferroelectrics. 95 (1989) 153-156. https://doi.org/10.1080/00150198908245194
[76] Y. Saito, H. Takao, T. Tani, T. Nonoyama, K. Takatori, T. Homma, T. Nagaya, M. Nakamura, Lead-free piezoceramics, Nature. 432 (2004) 84-87. https://doi.org/10.1038/nature03028
[77] N.M. Shorrocks, R.W. Whatmore, P.C. Osbond, Lead scandium tantalate for thermal detector applications, Ferroelectrics. 106 (1990) 387-392. https://doi.org/10.1080/00150199008214614
[78] A. Ono, High-pressure synthesis of perovskite-derived compounds in the Sr-Y-Cu-O system, Physica C: Superconductivity. 198 (1992) 287-292. https://doi.org/10.1016/0921-4534(92)90203-O
[79] Y. Liu, Y.H. Lin, B.P. Zhang, H.M. Zhu, C.W. Nan, J. Lan, J.F. Li, High-Temperature Thermoelectric Properties in the $La_{2-x}R_xCuO_4$ (R: Pr, Y, Nb) Ceramics, Journal of the American Ceramic Society. 92 (2009) 934-937. https://doi.org/10.1111/j.1551-2916.2009.02952.x
[80] E.A. Smith, I.N. Lokuhewa, S.T. Misture, D.D. Edwards, p-Type thermoelectric properties of the oxygen-deficient perovskite $Ca_2Fe_2O_5$ in the brownmillerite structure, Journal of Solid State Chemistry. 183 (2010) 1670-1977. https://doi.org/10.1016/j.jssc.2010.05.016
[81] J. Takahashia, H. Nakanoa, K. Kageyama, Fabrication and dielectric properties of barium titanate-based glass ceramics for tunable microwave LTCC application, Journal of the European Ceramic Society. 26 (2006) 2123-2127. https://doi.org/10.1016/j.jeurceramsoc.2005.09.070
[82] D.W. Chapman, Some thin-film properties of a new ferroelectric composition, Journal of Applied Physics. 40 (1969) 2381. https://doi.org/10.1063/1.1657999
[83] M.H. Francombe, Ferroelectric films and their device applications, Thin Solid Films. 13 (1972) 413-433. https://doi.org/10.1016/0040-6090(72)90314-8
[84] B.S. Sharma, S.F. Vogel, P.I. Prentky, Retention in thin ferroelectric films, Ferroelectrics. 5 (1973) 69-75. https://doi.org/10.1080/00150197308235781
[85] Y. Tomioka, T. Okuda, Y. Okimoto, R. Kumai, K.I. Kobayashi, Magnetic and electronic properties of a single crystal of ordered double perovskite Sr_2FeMoO_6, Physical Review B. 61 (2000) 422-427. https://doi.org/10.1103/PhysRevB.61.422
[86] S. Liu, X. Tan, K. Li, R. Hughes, Synthesis of strontium cerates-based perovskite ceramics via water-soluble complex precursor routes, Ceramics International. 28 (2002) 327-335. https://doi.org/10.1016/S0272-8842(01)00098-0
[87] K. Uchino, Ceramic actuators: principles and applications, MRS Bulletin. 18 (1993) 42-48. https://doi.org/10.1557/S0883769400037349
[88] W.B. Li, D. Zhou, L.X. Pang, R. Xu, H.H. Guoa, Novel barium titanate based capacitors with high energy density and fast discharge performance, Journal of the Materials Chemistry A. 5 (2017) 19607-19612. https://doi.org/10.1039/C7TA05392D
[89] W.B. Li, D. Zhou, L. X. Pang, Enhanced energy storage density by inducing defect dipoles in lead free relaxor ferroelectric $BaTiO_3$-based ceramics, Applied Physics Letters. 110 (2017) 132902. https://doi.org/10.1063/1.4979467
[90] P.K. Panda, B. Sahoo, PZT to lead free piezo ceramics: a review, Ferroelectrics. 474 (2015) 128-143. https://doi.org/10.1080/00150193.2015.997146

[91] P. Kantha, K. Pengpat, Phase formation and electrical properties of BNLT-BZT lead-free piezoelectric ceramic system, Current Applied Physics. 9 (2009) 460-466. https://doi.org/10.1016/j.cap.2008.04.004
[92] Y. Tian, Y. Gong, D. Meng, Y. Li, B. Kuang, Dielectric dispersion, diffuse phase transition, and electrical properties of BCT-BZT ceramics sintered at a low-temperature, Journal of Electronic Materials. 44 (2015) 2890-2897. https://doi.org/10.1007/s11664-015-3727-3
[93] E. Cross, Lead-free at last, Nature. 432 (2004) 24-25. https://doi.org/10.1038/nature03142
[94] A.M. Glazer, P.A. Thomas, K.Z.B. Kishi, G.K.H. Pang, C.W. Tai, Influence of short-range and long-range order on the evolution of the morphotropic phase boundary in $Pb(Zr_{1-x}Ti_x)O_3$, Physical Review B. 70 (2004) 184123. https://doi.org/10.1103/PhysRevB.70.184123
[95] K. Kakimoto, K. Akao, Y. Guo, H. Ohsato, Raman scattering study of piezoelectric $(Na_{0.5}K_{0.5})$ NbO3-LiNbO3 ceramics, Japanese Journal of Applied Physics. 44 (2005) 7064-7067. https://doi.org/10.1143/JJAP.44.7064
[96] B. Jaffe, W.R.J. Cook, H. Jaffe, Piezoelectric ceramics, 1st ed., Academic Press publishing, London, 1971.
[97] A.J. Moulson, J.M. Herbert, Electroceramics: Materials, Properties, Applications, 2nd ed., John Wiley & Sons publishing, England, 2003.
[98] Y. Ishibashia, M. Iwata, A theory of morphotropic phase boundary in solid-solution systems of perovskite-type oxide ferroelectrics, Japanese Journal of Applied Physics. 38 (1999) 800. https://doi.org/10.1143/JJAP.38.800
[99] N. Klein, E. Hollenstein, D. Damjanovic, H.J. Trodahl, N. Setter, M. Kuball, A study of the phase diagram of (K, Na, Li)NbO_3 determined by dielectric and piezoelectric measurements, and Raman spectroscopy, Japanese Journal of Applied Physics. 102 (2007) 014112. https://doi.org/10.1063/1.2752799
[100] D. Biswas, G. S. Kathait, P. Thapliyal, V. Rohilla, S. Singh, and J. Negi, Converse piezoelectric properties of K and Na-modified $(Na_{1-x}K_x)NbO_3$ lead free ceramics for x = 0.08 and 0.17, Ferroelectrics. 550 (2019) 228-232. https://doi.org/10.1080/00150193.2019.1652511
[101] D. Biswas, P. Sharma, N.S. Panwar, Composition dependent electrical properties of $(Ba_{1-x}Ca_xZr_{0.1}Ti_{0.9})O_3$ ceramics, near morphotropic phase boundary ($0.140 \leq x \leq 0.160$), ECS Journal of Solid State Science and Technology. 10 (2021) 033002. https://doi.org/10.1149/2162-8777/abea61
[102] D. Biswas, N.S. Panwar, P. Sharma, Temperature dependent dielectric and structural properties of $(Ba_{1-x}Ca_x)(Zr_{0.1}Ti_{0.9})O_3$, ($0.140 \leq x \leq 0.160$) ceramics, ECS Journal of Solid State Science and Technology. 11 (2022) 033002. https://doi.org/ 10.1149/2162-8777/ac62f3
[103] T.R. Shrout, S.J. Zhang, Lead-free piezoelectric ceramics: Alternatives for PZT?, Journal of Electroceramics. 19 (2007) 113-126. https://doi.org/10.1007/s10832-007-9047-0
[104] D. Biswas, N.S. Panwar, P. Sharma, Converse piezoelectric properties of lead free $Ba_{1-x}Ca_xZr_{0.1}Ti_{0.9}O_3$ (x = 0.055) ceramics using double sintered method, Ferroelectrics. 568 (2020) 95-103. https://doi.org/10.1080/00150193.2020.1811032
[105] X.B. Ren, Large electric-field-induced strain in ferroelectric crystals by point-defect-mediated reversible domain switching, Nature Materials. 3 (2004) 91-94. https://doi.org/10.1038/nmat1051

[106] M. McQuarrie, F.W. Behnke, Structural and dielectric studies in the system (Ba, Ca)(Ti, Zr)O_3, Journal of the American Ceramic Society. 37 (1954) 539-543. https://doi.org/10.1111/j.1151-2916.1954.tb13986.x
[107] W.F. Liu, X.B. Ren, Large piezoelectric effect in Pb-free ceramics, Physical Review Letters. 103 (2009) 257602. https://doi.org/10.1103/PhysRevLett.103.257602
[108] W. Li, Z. Xu, R. Chu, P. Fu, G. Zang, Piezoelectric and Dielectric Properties of $(Ba_{1-x}Ca_x)(Ti_{0.95}Zr_{0.05})O_3$ Lead-Free Ceramics, Journal of the American Ceramic Society. 93 (2010) 2942-2944. https://doi.org/10.1111/j.1551-2916.2010.03907.x
[109] W. Li, Z. Xu, R. Chu, P. Fu, G. Zang, High piezoelectric d_{33} coefficient in $(Ba_{1-x}Ca_x)(Ti_{0.98}Zr_{0.02})O_3$ lead-free ceramics with relative high Curie temperature, Materials Letters. 64 (2010) 2325-2327. https://doi.org/10.1016/j.matlet.2010.07.042
[110] S.W. Zhang, H.L. Zhang, B.P. Zhang, S. Yang, Phase-transition behavior and piezoelectric properties of lead-free $(Ba_{0.95}Ca_{0.05})(Ti_{1-x}Zr_x)O_3$ ceramics, Journal of alloys and compounds. 506 (2010) 131-135. https://doi.org/10.1016/j.jallcom.2010.06.157
[111] S. Ye, J. Fuh, L. Lu, Effects of Ca substitution on structure, piezoelectric properties, and relaxor behavior of lead-free $Ba(Ti_{0.9}Zr_{0.1})O_3$ piezoelectric ceramics, Journal of Alloys and Compounds. 541 (2012) 396-402. https://doi.org/10.1016/j.jallcom.2012.06.084
[112] A. Kaushal, S.M. Olheroa, B. Singh, D.P. Fagg, I. Bdikin, J.M.F. Ferreira, Impedance analysis of $0.5Ba(Zr_{0.2}Ti_{0.8})O_3$-$0.5(Ba_{0.7}Ca_{0.3})TiO_3$ ceramics consolidated from micro-granules, Ceramics International. 40 (2014) 10593-10600. https://doi.org/10.1016/j.ceramint.2014.03.038
[113] M.A. Rafiq, M.N. Rafiq, K.V. Saravanan, Dielectric and impedance spectroscopic studies of lead-free barium-calcium-zirconium-titanium oxide ceramics, Ceramics International. 41 (2015) 11436-11444. https://doi.org/10.1016/j.ceramint.2015.05.107
[114] A. Srinivas, R.V. Krishnaiah, V.L. Niranjani, S.V. Kamat, T. Karthik, S. Asthana, Ferroelectric, piezoelectric and mechanical properties in lead free $(0.5)Ba(Zr_{0.2}Ti_{0.8})O_3$-$(0.5)(Ba_{0.7}Ca_{0.3})TiO_3$ electroceramics, Ceramics International. 41 (2015) 1980-1985. https://doi.org/10.1016/j.ceramint.2014.08.127
[115] P. Wang, Y. Li, Y. Lu, Enhanced piezoelectric properties of $(Ba_{0.85}Ca_{0.15})(Zr_{0.1}Ti_{0.9})O_3$ lead-free ceramics by optimizing calcination and sintering temperature, Journal of the European Ceramic Society. 31 (2011) 2005-2012. https://doi.org/10.1016/j.jeurceramsoc.2011.04.023
[116] S. Hunpratu, S. Maensiri, P. Chindaprasirt, Synthesis and characterization of $Ba_{0.85}Ca_{0.15}Ti_{0.9}Zr_{0.1}O_3$ ceramics by hydrothermal method, Ceramics International. 40 (2014) 13025-13031. https://doi.org/10.1016/j.ceramint.2014.04.166
[117] S. Sen, R. Choudhay, Effect of doping Ca ions on structural and electrical properties of $Ba(Zr_{0.05}Ti_{0.95})O_3$ electroceramics, Journal of Materials Science: Materials in Electronics. 15 (2004) 671-675. https://doi.org/10.1023/B:JMSE.0000038922.74021.d6
[118] G. Shirane, H. Danner, A. Pavlovic, R. Pepinsky, Phase transitions in ferroelectric $KNbO_3$, Physical Review. 93 (1954) 672-673. https://doi.org/10.1103/PhysRev.93.672
[119] D. Fu, Y. Kamai, N. Sakamoto, N. Wakiya, H. Suzuki, M. Itoh, Phase diagram and piezoelectric response of $(Ba_{1-x}Ca_x)(Zr_{0.1}Ti_{0.9})O_3$ solid solution, Journal of Physics: Condensed Matter. 25 (2013) 425901. https://doi.org/10.1088/0953-8984/25/42/425901
[120] J. Tellier, B. Malic, B. Dkhil, D. Jenko, J. Cilensek, and M. Kosec, Crystal structure and phase transitions of sodium potassium niobate perovskites, Solid State Sciences. 11 (2009) 320-324. https://doi.org/10.1016/j.solidstatesciences.2008.07.011

[121] L.E. Cross, Ferroelectric ceramics: tailoring properties for specific applications, Birkhäuser Basel, 1993: pp. 1-85. https://doi.org/10.1007/978-3-0348-7551-6_1
[122] E.I. Bondarenko, V. Yu. Topolov, A.V. Turik, The role of 90° domain wall displacements in forming physical properties of perovskite ferroelectric ceramics, Ferroelectrics Letter Section. 13 (1991) 13-19. https://doi.org/10.1080/07315179108203316
[123] T. Furukawa, E. Fukada, Piezoelectric relaxation in composite epoxy-PZT system due to tonic conduction, Japanese Journal of Applied Physics. 16 (1977) 453. https://doi.org/10.1143/JJAP.16.453
[124] B. Jaffe, R.S. Roth, S. Marzullo, Piezoelectric properties of lead zirconate-lead titanate solid-solution ceramics, Journal of Applied Physics. 25 (1954) 809. https://doi.org/10.1063/1.1721741
[125] D. Damjanovic, Ferroelectric, dielectric and piezoelectric properties of ferroelectric thin films and ceramics, Reports on Progress in Physics. 61 (1998) 1267-1324. https://doi.org/10.1088/0034-4885/61/9/002
[126] D.W. Baker, P.A. Thomas, N. Zhangb, A.M. Glazer, Structural study of $K_xNa_{1-x}NbO_3$ (KNN) for compositions in the range $x = 0.24$-0.36, Acta Crystallographica. B65 (2009) 22-28. https://doi.org/10.1107/S0108768108037361
[127] G.H. Kwei, A.C. Lawson, S.J.L. Billinge, S.W. Cheong, Structures of the ferroelectric phases of barium Titanate, The Journal of Physical Chemistry. 97 (1993) 2368-2377. https://doi.org/10.1021/j100112a043
[128] Q.M. Zhang, H. Wang, N. Kim, L.E. Cross, Direct evaluation of domain-wall and intrinsic contributions to the dielectric and piezoelectric response and their temperature dependence on lead zirconate-titanate ceramics, Journal of Applied Physics. 75 (1994) 454. https://doi.org/10.1063/1.355874
[129] Q.M. Zhang, W.Y. Pan, S.J. Jang, L.E. Cross, Domain wall excitations and their contributions to the weak-signal response of doped lead zirconate titanate ceramics, Journal of Applied Physics. 64 (1988) 6445. https://doi.org/10.1063/1.342059
[130] P. Gerthsen, K.H. Ha¨rdtl, N.A. Schmidt, Correlation of mechanical and electrical losses in ferroelectric ceramics, Journal of Applied Physics. 51(1980) 1131. https://doi.org/10.1063/1.327722
[131] D. Berlincourt, H.H.A. Krueger, Domain processes in lead titanate zirconate and barium titanate ceramics, Journal of Applied Physics. 30 (1959) 1804. https://doi.org/10.1063/1.1735059
[132] G. Arlt, N.A. Pertsev, Force constant and effective mass of 90 domain walls in ferroelectric ceramics, Journal of Applied Physics. 70 (1991) 2283. https://doi.org/10.1063/1.349421
[133] S. Li, W. Cao, L.E. Cross, The extrinsic nature of nonlinear behavior observed in lead zirconate titanate ferroelectric ceramic, Journal of Applied Physics. 69 (1991) 7219. https://doi.org/10.1063/1.347616
[134] G. Arlt, H. Dederichs, R. Herbeit, 90°-domain wall relaxation in tetragonally distorted ferroelectric ceramics, Ferroelectrics. 74 (1987) 37-53. https://doi.org/10.1080/00150198708014493
[135] A. Schnell, Nonlinear charge release of piezoelectric ceramics under uniaxial pressure. Ferroelectrics. 28 (1980) 351-353. https://doi.org/10.1080/00150198008227106
[136] M.E. Lines, A.M. Glass, Principles and applications of ferroelectrics and related materials, 1st ed., Clarendon publishing, Oxford, 1979.

[137] R. Z. Zuo, J. Fu, D. Y. Lv, Phase transformation and tunable piezoelectric properties of lead-free $(Na_{0.52}K_{0.48-x}Li_x)(Nb_{1-x-y}Sb_yTa_x)O_3$ system, Journal of the American Ceramic Society. 92 (2009) 283-285. https://doi.org/10.1111/j.1551-2916.2008.02871.x
[138] J.F. Li, D.D. Viehland, T. Tani, C.D.E. Lakeman, D.A. Payne, Piezoelectric properties of sol-gel-derived ferroelectric and antiferroelectric thin layers, Journal of Applied Physics. 75 (1993) 442. https://doi.org/10.1063/1.355872
[139] D.L. Polla, R.S. Muller, R.M. White, Integrated multisensor chip, IEEE Electron Device Letters, 7 (1986) 254-256. https://doi.org/10.1109/EDL.1986.26363
[140] S.W. Wenzel, R.M. White, A multisensor employing an ultrasonic Lamb-wave oscillator, IEEE Transactions on Electron Devices, 35 (1988) 735-743. https://doi.org/10.1109/16.2525
[141] R.M. Morney, R.M. White, R.T. Howe, Fluid motion produced by ultrasonic Lamb waves, IEEE Symposium on Ultrasonics, Honolulu, 1989, pp. 355-358. https://doi.org/10.1109/ULTSYM.1990.171385
[142] D. Bondurant, F. Gnadinger. Ferroelectrics for nonvolatile RAMs, IEEE Spectrum. 26 (1989) 30-33. https://doi.org/10.1109/6.29346
[143] M.H. Frey, D.A. Payne, Nanocrystalline barium titanate: evidence for the absence of ferroelectricity in sol-gel derived thin-layer capacitors, Applied Physics Letters. 63 (1993) 2753. https://doi.org/10.1063/1.110324
[144] K. Nilsson, J. Lidman, K. Ljungström, C. Kjellman, Biocompatible material for implants, WO Patent. 99 (1999) 54266.
[145] C.P. de Araujo, J.F. Scott, G.W. Taylor, Ferroelectric thin films: synthesis and basic properties, 1st ed., Gordon and Breach publishing, Amsterdam, 1996.
[146] R. Ramesh, Thin film ferroelectric materials and devices, 1st ed., Springer publishing, New York, 1997.
[147] N. Setter, Electroceramic based MEMS: Fabrication-technology and applications, 2nd ed., Springer publishing, New York, 2005.
[148] J.F. Scott, C.A.P. de Araujo, Ferroelectric memories, Science. 246 (1989) 1400-1405. https://doi.org/10.1126/science.246.4936.1400
[149] M. Dawber, K.M. Rabbe, J.F. Scott, Physics of thin-film ferroelectric oxides, Review of Modern Physics. 77 (2005) 1083-1130. https://doi.org/10.1103/RevModPhys.77.1083
[150] A. Kingon, P. Muralt, N. Setter, R. Waser, Electroceramic thin films for microelectronics and microsystems, 3rd ed., CRC press publishing, Boca Raton, 2004: pp. 465-526.

CHAPTER-2

Morphotropic phase boundary in $(Ba_{1-x}Ca_x)(Zr_{1-y}Ti_y)O_3$, (x = 0.140-0.160, y = 0.9)

Brief summary

The composition-dependent dielectric and structural properties were described in this chapter. Ceramic pellet samples of $(Ba_{1-x}Ca_x)(Zr_{0.1}Ti_{0.9})O_3$, ($0.140 \leq x \leq 0.160$) were prepared using a solid-state reaction route followed by double sintering. The dielectric and structural properties of the prepared samples were measured from room temperature to 450 ^oC at different frequencies in the range 10-1000 kHz. A peak shifting anomaly in the X-ray diffraction peaks patterns, an anomalous change in the slope of the c/a *vs* x plot, and the observed minimum values of dielectric constant, loss and conductivity of the prepared compositions show a strong compositional dependent dielectric and structural properties, indicating a morphotropic phase transition type behaviour, at the composition with x = 0.150.

CHAPTER-2

Morphotropic phase boundary in $(Ba_{1-x}Ca_x)(Zr_{1-y}Ti_y)O_3$, (x = 0.140- 0.160, y = 0.9)

2.1 Introduction

Perovskite ABO_3 type ferroelectric compounds are technologically essential and have significant electrical and optical properties [1]. A series of binary and tertiary perovskite solutions can be prepared by replacing A- and or B-site atoms, with compatible valence and tolerance. Among these ferroelectric materials, barium calcium zirconate titanate (BCZT) based system may have the potential to replace lead-based ceramics used in various dielectric and ferroelectric devices [2-4]. Solid solutions of $(Ba_{1-x}Ca_x)(Zr_yTi_{1-y})O_3$ (BCZT) system may be produced for all values of x and y (x, y = 0 to 1), permitting a great extent of tailorability in dielectric and piezoelectric properties. Ca can replace Ba, and Ti with Zr, in the BCZT system to form binary solid solutions. In the solid solutions of perovskite type compounds, a composition- dependent transition in physical properties is termed as a morphotropic phase boundary (MPB) [5], which shows an irregular change in lattice parameters with extremal physical properties [6]. The extremal physical properties near the MPB have the significant technological potential [7,8]. Due to the symmetry-allowed polarization extension, the large electromechanical response has been attributed to the MPB [9-11]. Jaffe et al. [12] observed the anomaly in the dielectric and piezoelectric properties in lead zirconate titanate (PZT) ceramics, near the MPB, which appeared due to the separation of the tetragonal and rhombohedral phases across the MPB. The morphotropic phase region contained mixed tetragonal and rhombohedral phases. The tetragonal and rhombohedral structures have 6 and 8 possible polarization directions, respectively. Therefore, a morphotropic phase boundary, consisting of both phases has 14 possible polarization directions, significantly contributing to electromechanical coupling factor (k_s) and extremal remanent polarization [13]. An extermal dielectric constant may be associated with the extremal remanent polarization near MPB.

For $(Ba_{1-x}Ca_x)(Zr_{0.1}Ti_{0.9})O_3$ ceramics, the orthorhombic to tetragonal (O-T) phase transition point (T_{O-T} ~ 90 ^oC) was reportedly found shifting towards lower temperature with the increase in x,

from 0.140 to 0.160 [14]. With a variation in Ba/Ca ratio, the composition-dependent behaviour of electrical properties suggested the existence of a typical MPB, in $(Ba_{1-x}Ca_x)(Zr_{0.1}Ti_{0.9})O_3$ ceramics, near x = 0.150 [14]. The reported anomalous dielectric behaviour was found composition dependent rather than temperature and frequency, in $(Ba_{1-x}Ca_x)(Zr_{0.1}Ti_{0.9})O_3$, near x = 0.150 [16]. In the MPB region, factors like polarization extension, polarization rotation, and elastic lattice softening significantly contribute to the dielectric properties of BCZT ceramics, near MPB [14,15]. Mondal et al. [16] observed increased resistivity by substituting Ba by Ca in BCZT compounds. A decrease in the mobility of the charge carriers was observed, which was attributed to the lattice distortion in BCZT $(Ba_{1-x}Ca_x)(Zr_{0.1}Ti_{0.9})O_3$ ceramics, at x = 0.150. An anomalous peak shifting in X-ray diffraction patterns has been reported close to the MPT (Morphotropic phase transition) region [17]. The dielectric and structural properties of $Ba_{1-x}Ca_xTiO_3$- $BaZr_yTi_{1-y}O_3$ (BCT- BZT) system has been explored by Tuan et al. [18] near MPB. Hanani et al. [19] reported enhanced dielectric properties of $(Ba_{1-x}Ca_xZr_{0.1}Ti_{0.9})O_3$ ceramics, at x = 0.150. This system has reported a considerable enhancement in electrical properties with longer sintering time [20-22]. The enhanced dielectric and piezoelectric properties of the BCZT system near MPB, have been attributed to the coexistence of two different phases [23-25]. The dielectric constant and electric conductivity were reportedly found extremal, in the $(Na,K)(Nb,Ta)O_3$ system, near MPB [17,26,27].

The electrical properties of the perovskite materials significantly altered with the change in the preparation conditions and compositions of solid solution systems. In MPB, separating two different ferroelectric phases with different lattice parameters, which may significantly enhance electrical properties [28,29]. From the composition-property diagram of solid solution systems, at the morphotropic phase boundary (MPB), the ferro-composition has two- or more phases and has extremal electro-physical properties [15,30-33]. The width of the coexistence region has also been attributed to the particle size [34] and depends on the processing conditions. On change of composition, MPT exhibits anomalous dielectric and piezoelectric properties [17].

In the present study, ceramic samples of $(Ba_{1-x}Ca_x)(Zr_{0.1}Ti_{0.9})O_3$, $(0.140 \leq x \leq 0.160)$, were prepared near the morphotropic phase boundary, using the solid-state reaction route followed by double sintering. The dielectric constant (ε), loss tangent ($\tan \delta$), and electric conductivity (σ) of the prepared composition samples were measured at 10, 100 and 1000 kHz. X-ray diffraction (XRD) and scanning electron microscopy (SEM) measurements of the prepared compositions

were carried out at room temperature (RT). The observed composition dependent dielectric behavior of the prepared pellet samples is presented.

2.2 Material preparation and characterization

2.2.1 Preparation

In this study, high-purity (> 99.5 %) powders of barium carbonate ($BaCO_3$), calcium carbonate ($CaCO_3$), titanium oxide (TiO_2) and zirconium oxide (ZrO_2) were utilized as raw materials. The compositions of BCZT ceramics were prepared using a solid-state reaction route with double sintering [35]. The dissolved moisture was removed from the raw powders by drying them in an oven, at 200 ^oC for 2 hours, and then the dried powders were weighed in the stoichiometric ratio to prepare the desired $(Ba_{1-x}Ca_x)(Zr_{0.1}Ti_{0.9})O_3$, $(0.140 \leq x \leq 0.160)$ compositions. The mixture was manually dry mixed and ground for 4 hrs, and then with methanol for nest 2 hrs. The agate mullet mortar and pestle were used for grinding. The mixed ground powder was calcined in the ambient air at 1100 ^oC, in the alumina crucible, to remove carbon dioxide. The calcined power was taken out from the furnace when it cooled to RT. The calcined power was weighed to check complete carbon dioxide removal. The calcined power was pressed into pellets with a longitudinal pressure of 0.2 GPa. The pellets of the prepared compositions were sintered at 1300 °C, for 4 hours. The sintered pellets were crushed and ground further into powder. This ground powder was further pressed into pellets (~ 2 mm thickness and 8 mm diameter), at 0.2 GPa. These pellets were further sintered at 1300 ^oC, for 4 hours. The BCZT ceramic samples reportedly show maximum density when double sintered at 1300 ^oC [36,37].

The XRD patterns of all prepared powder samples were measured, at room temperature (RT), with the help of PANalytical PW340 X-ray diffractometer, having a wavelength 1.5406 Å. The XRD data was taken at a scan speed of 0.3 sec per step with the step size of 0.025°. For all the prepared ceramics, the dielectric properties (ε, tan δ, and σ) were observed, near the MPB region $(0.140 \leq x \leq 0.160)$. For dielectric measurements, specimens were electroded, with conducting silver paste, in a metal-insulator-metal (MIM) arrangement. With RLC meter (PM 6306, Fluke), the dielectric measurements were carried out with increasing temperature, from RT to 450 ^oC, and in the frequency range from 10 to 1000 kHz. SEM images were observed to study surface morphology and grain size using CARL ZEISS, model no. EVO 18 Special Edition.

2.2.2 Characterization

2.2.2.1 X-ray diffraction studies

The observed room temperature XRD patterns of the prepared $(Ba_{1-x}Ca_x)(Zr_{0.1}Ti_{0.9})O_3$, $(0.140 \leq x \leq 0.160)$ pellet samples have been given in Fig. 2.1. The XRD patterns show perovskite structure of the prepared BCZT compositions with orthorhombic symmetry. The observed XRD data are consistent with the Inorganic Crystal Structure Database (ICSD) - (code 00-056-1033) records of $(Ba_{1-x}Ca_x)(Zr_{0.1}Ti_{0.9})O_3$, with peaks corresponding to (020), (221), (402), and (330), etc. [38].

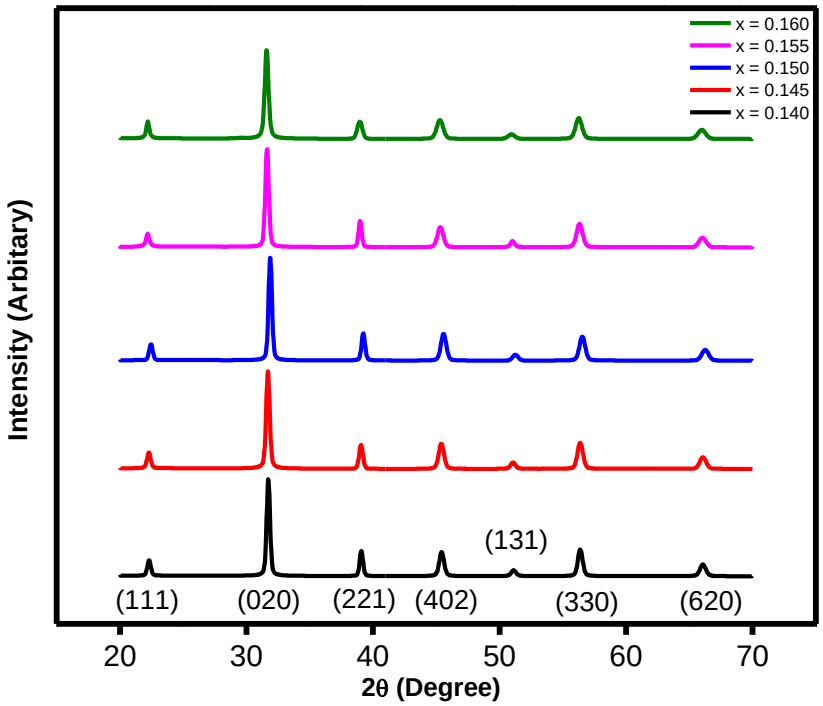

Fig. 2.1 XRD patterns of $(Ba_{1-x}Ca_x)(Zr_{0.1}Ti_{0.9})O_3$, $(0.140 \leq x \leq 0.160)$ powder samples, at RT.

2.2.2.2 Scanning electron microscopic (SEM) analysis

The SEM images of the prepared pellet samples of $(Ba_{1-x}Ca_xZr_{0.1}Ti_{0.9})O_3$, $(0.140 \leq x \leq 0.160)$ have been shown in Fig. 2.2. All the samples were found homogeneous and fine-grained. The average grain size of the prepared BCZT ceramics was determined by dividing the length of the SEM photograph in terms of the scale by the number of grains in that length. The grain size and density significantly influence the dielectric properties of ceramics [39-41].

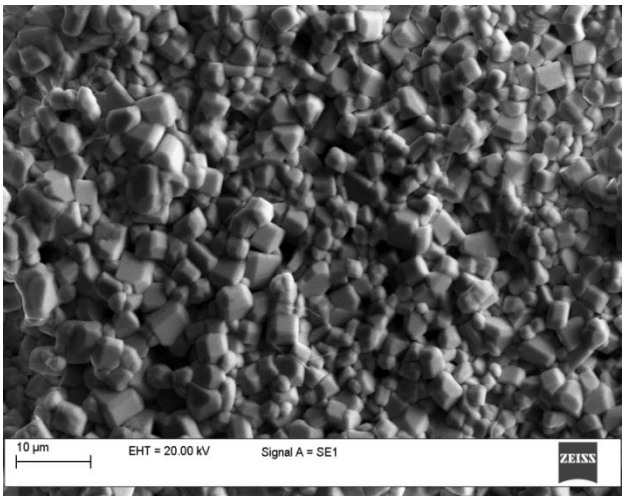

(a)

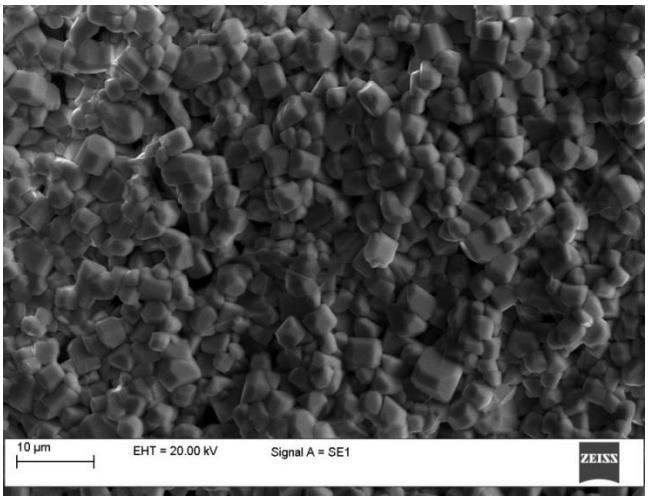

(b)

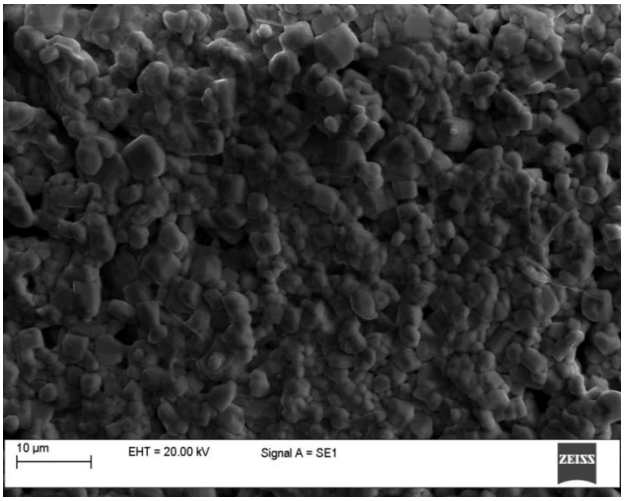

(c)

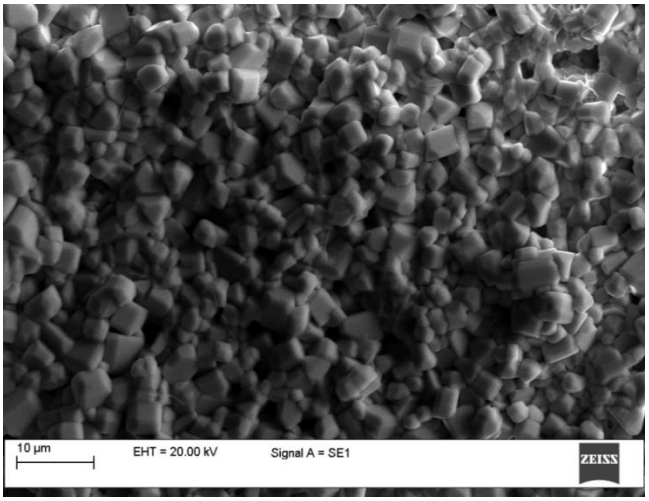

(d)

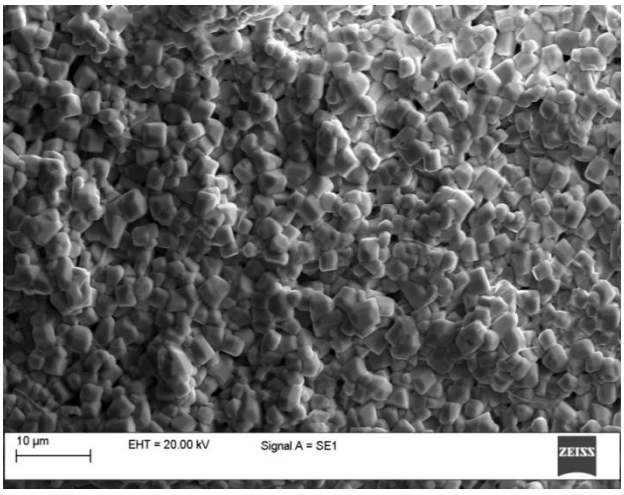

(e)

Fig. 2.2 SEM images of $(Ba_{1-x}Ca_x)(Zr_{0.1}Ti_{0.9})O_3$, for x = 0.140 (a), 0.145 (b), 0.150 (c), 0.155 (d), 0.160 (e).

2.2.2.3 Energy dispersive X- ray analysis (EDX)

An X-ray method called "Energy Dispersive X-Ray Analysis" (EDX), also known as EDS or EDAX, is often utilized to compute the elemental analysis of materials. Scanning electron microscopes (SEM) can be equipped with EDX, which utilizes the SEM's imaging capabilities to locate the desired object. The EDX system generates spectra with peaks corresponding to the elemental analysis of the specimen. Additionally, image processing and elemental mapping of a specimen or material are possible. EDX becomes extremely effective when employed in a multi-technique approach, especially in industrial forensic science studies and contamination assessment. The approach may map out the spatial distribution of the elements and be qualitative, semi-quantitative, or quantitative.

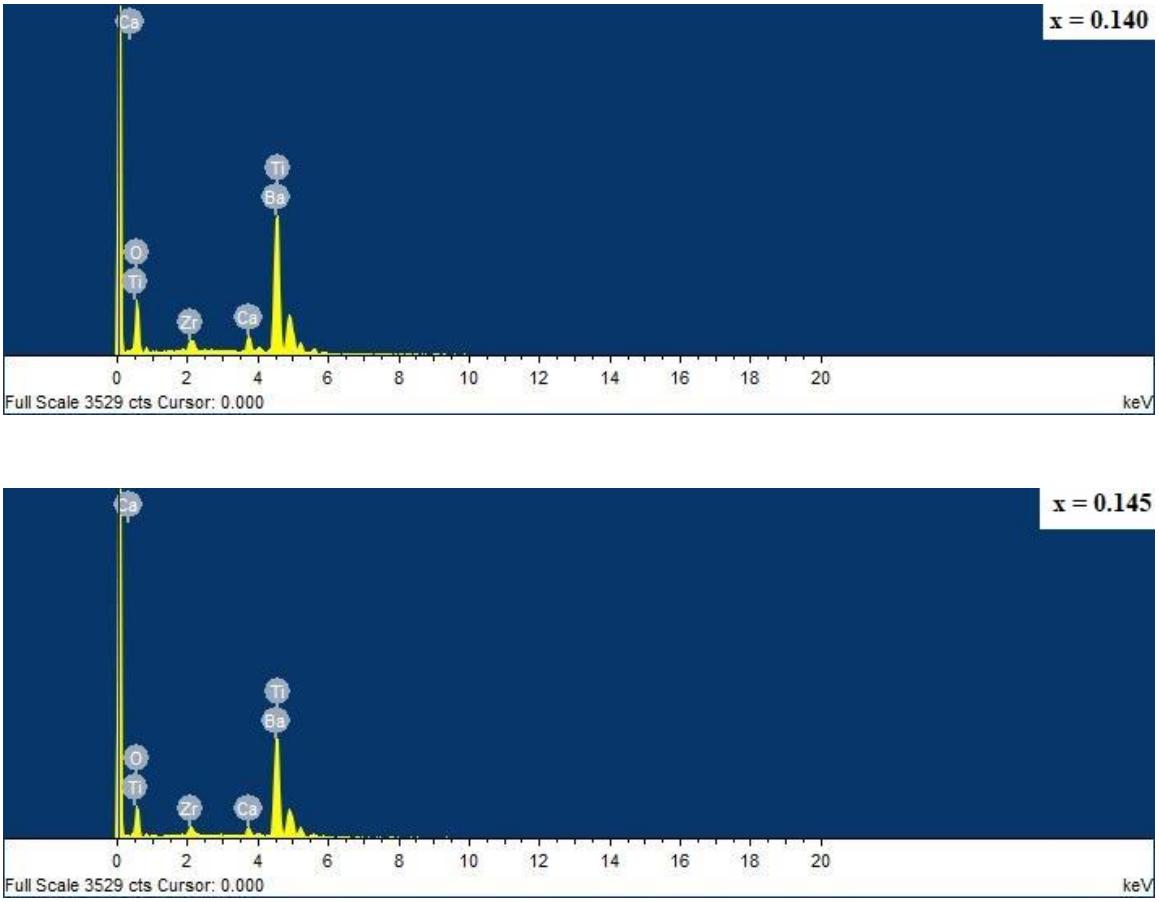

Fig. 2.3 EDX results of $(Ba_{1-x}Ca_x)(Zr_{1-y}Ti_y)O_3$, (x = 0.140-0.160, y = 0.9), samples for different x values.

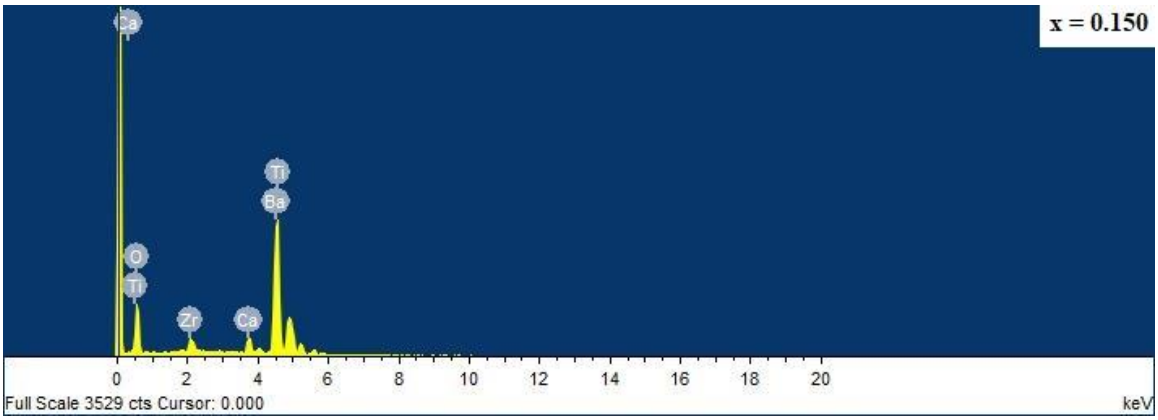

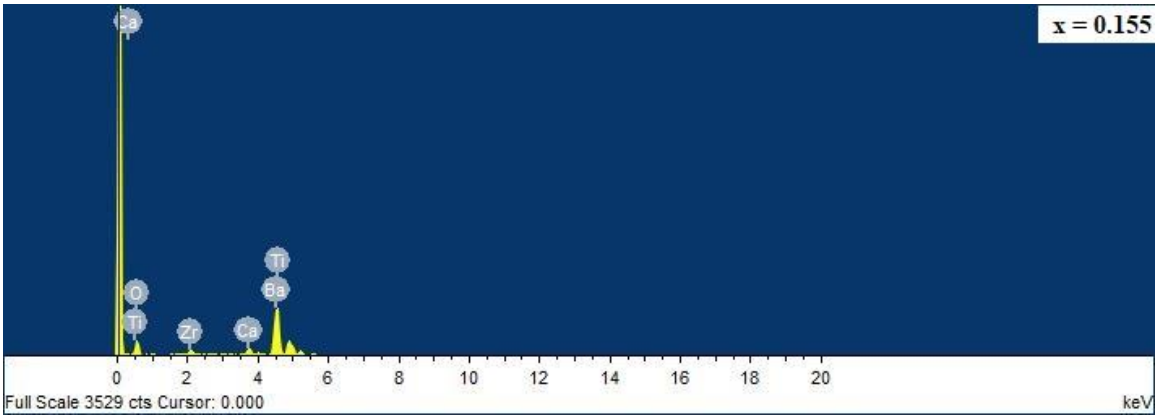

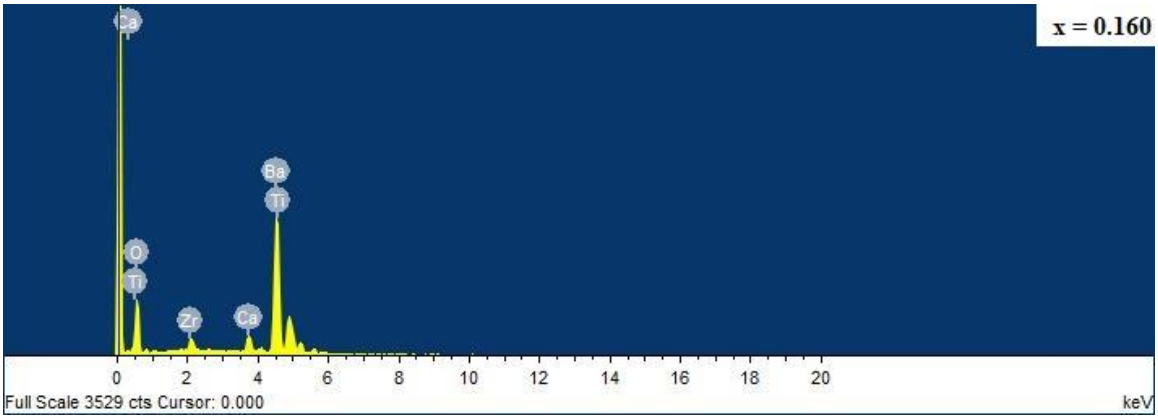

Fig. 2.3 Continued.

Energy- dispersive X- ray spectroscopy (EDX) is extensively employed for quality control and test investigation in several industrial applications, viz., metals, semiconductors, cement, paper and polymers; medical field, in the analysis of blood, tissues, bones, and organs; in pollution

control, ore prospecting, archaeology, and oceanography; etc. Chemical analysis of $(Ba_{1-x}Ca_x)(Zr_{1-y}Ti_y)O_3$, (x = 0.140-0.160, y = 0.9), samples was done by CARL ZEISS, model no. EVO18 special edition. The observed EDX results of the $(Ba_{1-x}Ca_x)(Zr_{0.1}Ti_{0.9})O_3$ system have been shown in Fig. 2.3.

Table 2.1 EDX results of $(Ba_{1-x}Ca_x)(Zr_{0.1}Ti_{0.9})O_3$, $(0.140 \leq x \leq 0.160)$ compositions.

Composition (x)	Atomic % (Measured)				Atomic % (Calculated)				Escaping of Ba and Ca (%)	
	Ba/Ca	Ba	Ca	O	Ba/Ca	Ba	Ca	O	Ba	Ca
0.140	6.04	13.90	2.30	64.66	6.14	17.2	2.8	60	19.18	17.85
0.145	6.15	14.47	2.35	65.15	5.89	17.1	2.9	60	15.38	18.96
0.150	6.18	15.21	2.46	66.10	5.66	17.0	3.0	60	10.52	18.00
0.155	6.43	14.92	2.32	63.29	5.45	16.9	3.1	60	11.71	25.16
0.160	6.47	13.99	2.17	68.04	5.25	16.8	3.2	60	16.72	32.80

The EDX results show considerable escaping of alkaline metal (Ba and Ca) ions from the prepared compositions of BCZT $(Ba_{1-x}Ca_xZr_{0.1}Ti_{0.9})O_3$, $(0.140 \leq x \leq 0.160)$ ceramics, with a lowest for the compositions with x = 0.150, Table 2.1. The EDX analysis shows more escaping of calcium (Ca) than barium (Ba), which may be due to the higher equilibrium vapor pressure of the former [42]. A slight variation in stoichiometry triggers a sensitive effect in the density, grain size, and morphology of BCZT ceramics [43].

2.3 Dielectric measurements

Measurements were taken for the prepared samples with a similar method to study dielectric properties' temperature, frequency and composition (x) dependence. The dielectric constant (ε) was measured using the relation [44]

$$\varepsilon = C/C_o, \qquad (2.1)$$

where C_o and C, respectively, represent the capacitances of the electrodes without and with a dielectric; C_o is shown by,

$$C_o = (0.0885\pi r^2/d)\ pF, \qquad (2.2)$$

where d (cm) is the distance between them and r (cm) is the radius of the electrodes. Electric conductivity (σ) was obtained using Eq. [44],

$$\sigma = \varepsilon_o \omega \varepsilon \tan\delta, \qquad (2.3)$$

where $\omega = 2\pi f$, f is the applied frequency, tan δ is the dissipation factor, and ε_o is the permittivity of free space.

2.4 Morphotropic phase boundary in $(Ba_{1-x}Ca_x)(Zr_{1-y}Ti_y)O_3$, at x = 0.150

The measured XRD patterns of different prepared compositions of $(Ba_{1-x}Ca_x)(Zr_{0.1}Ti_{0.9})O_3$ are given in Fig. 2.4. The XRD data indicate the polycrystalline nature of the prepared compositions. They are consistent with the "Inorganic Crystal Structure Database" (ICSD) - (code 00-056-1033) data of $(Ba_{0.85}Ca_{0.15})(Zr_{0.1}Ti_{0.9})O_3$ with peaks corresponding to (020), (221), (402), and (330), etc.

Among the prepared compositions, a continuous peak shifting was observed in the most intense peaks (020), (221), (402), and (330), with the increment in the value of calcium concentration (x). In the XRD patterns of BCZT ceramics, the most intense peaks were found shifting to a lower angle with increasing x, except for the composition with x = 0.150, where the peaks moved to the higher angle, indicating anomalous structural behaviour at this composition- a break was noticed in the peak shifting tendency. A similar tendency was also observed by other workers [17,26,27]. The lattice parameters were calculated from the observed XRD data. The variation of lattice parameters (a, b, and c), and c/a ratio with composition (x), was shown in Fig. 2.5. The slope of the c/a *vs* x graph changed, from negative to positive, at the composition with x = 0.150, which exhibits a structural abnormality, at this composition- a composition-dependent behaviour, an MPB region. Sen et al. [38] reported a change in the lattice parameters with the varying composition (x), in $(Ba_{1-x}Ca_x)(Zr_{0.1}Ti_{0.9})O_3$ ceramics. A similar break in the peaks shifting tendency has been reportedly found in $Na_{1-x}K_xNbO_3$, near x = 0.17, 0.32, and 0.50 compositions [17,26,27].

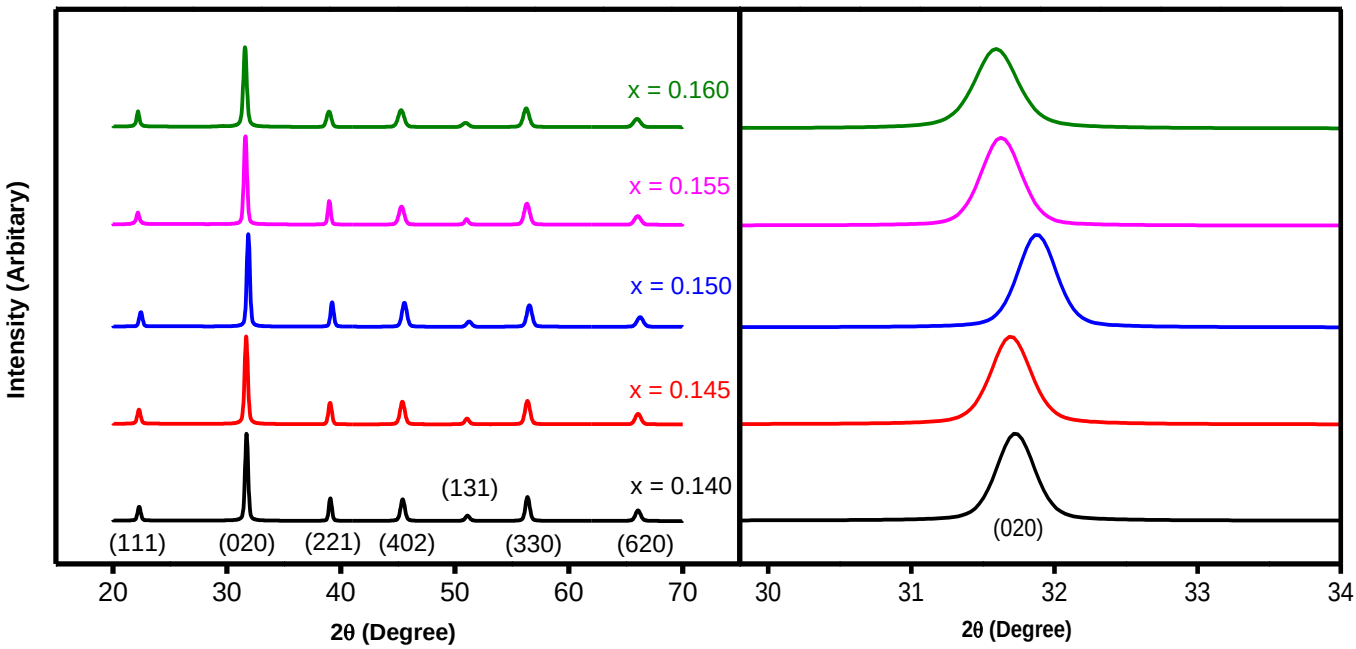

Fig. 2.4 XRD patterns of $(Ba_{1-x}Ca_x)(Zr_{0.1}Ti_{0.9})O_3$, $(0.140 \leq x \leq 0.160)$ powder samples, at RT, showing break in peaks shifting tendency, at x = 0.150 composition.

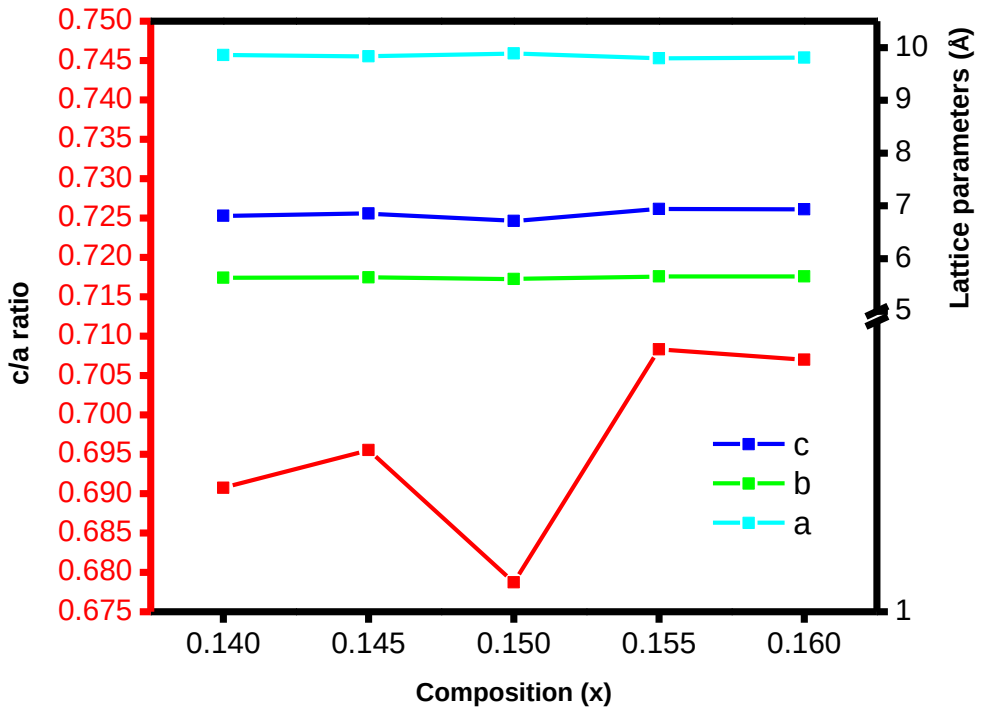

Fig. 2.5 Lattice parameters and c/a (ratio of lattice parameters, c and a) change with composition (x), in $(Ba_{1-x}Ca_x)(Zr_{0.1}Ti_{0.9})O_3$, $(0.140 \leq x \leq 0.160)$ ceramics.

2.4.1 Density and grain size

The density of the sintered pellets was measured using the Archimedes method. Generally, the density of the pellets was found proportionally varying with grain size, except for the composition with x = 0.150, where the density was found to be maximum and grain size minimum, among the prepared compositions, Fig. 2.6. Among the prepared compositions, minimum grain size (1.03 µm) was found for x = 0.150 and maximum for x = 0.145 (1.7 µm). Maximum density was found for x = 0.150 (4.2 g/cc, 65 to 78% of theoretical value), whereas minimum density for x = 0.140 (3.8 g/cc). The porosity and density significantly influence the dielectric properties of the compositions [45].

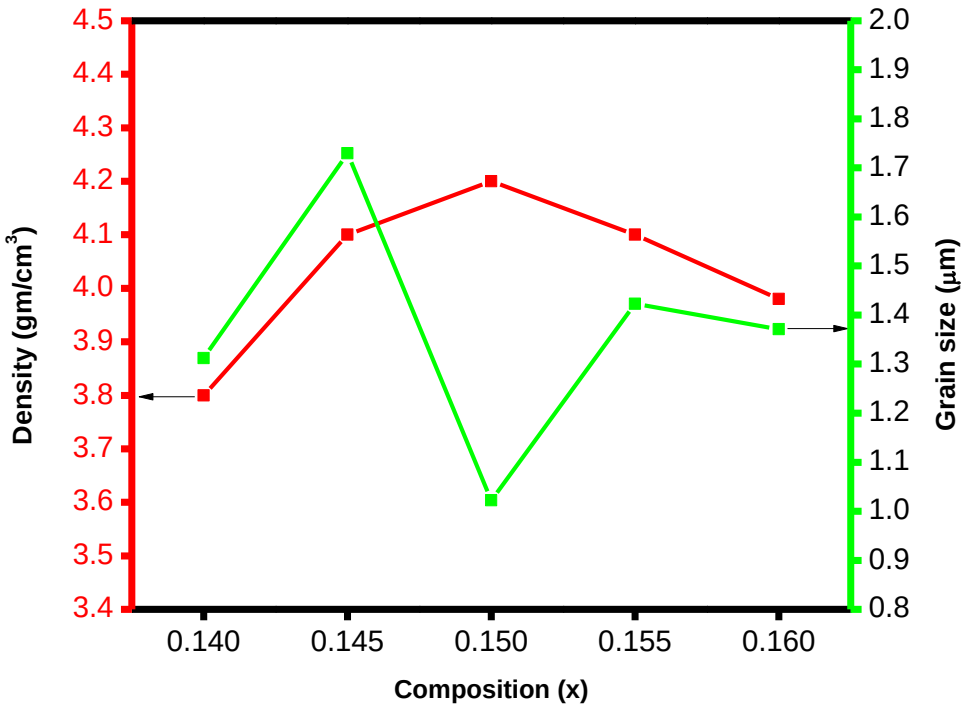

Fig. 2.6 Composition (x) variation of grain size and density, in $(Ba_{1-x}Ca_x)(Zr_{0.1}Ti_{0.9})O_3$, ($0.140 \leq x \leq 0.160$).

Fig. 2.6 exhibits the maximum density for the samples with x = 0.150, among the prepared samples. During the sintering process, the mechanism of densification and grain growth needs material transportation and that may happen via grain boundary diffusion, lattice diffusion, surface diffusion, evaporation, and viscous flow [45]. A two-stage sintering method was chosen

to achieve the densification of ceramic bodies without significant grain growth [46]. Ceramics of intermediate density and fine grain size have been reported for perovskite compounds, like $BaTiO_3$, using a two-stage sintering method [47,48]. The double-sintered ceramic samples show a significant increase in dielectric constant than those prepared with usual single sintering. Double sintering is a simple and cost-effective method to obtain higher-density materials with controlled grain growth without adding dopants. Sintering significantly affects ceramics' densification and their dielectric properties [49]. The double sintering process was applied in the present study to improve the density of the ceramics inhibiting grain growth. It triggers different sintering mechanisms in different temperature ranges. After the first sintering (at 1300 ^oC), pellets with poor density with developed cracks were obtained. The minimum activation energy of surface diffusion exhibits excessive grain growth during the start of the sintering process, which triggers grain coarsening, and the total surface area reduces because of larger grains. The driving force is the observed change in surface area.

Moreover, due to early grain growth, the reduced driving force appears before the composition enters the primary sintering process [50,51]. Once that coarsening occurs, the pore removal becomes quite difficult, resulting in poor densification, in the single sintering. The double sintering was chosen to activate different sintering processes in different temperature ranges, and to suppress grain growth and improve densification. After the second sintering stage, the pellet samples were hard enough with improved density.

The material grain growth, free surfaces, the reaction of grain boundaries, and the change in lattice may be significantly altered with the function of sintering and the involvement of different mechanisms. Every diffusing species, whether it is volatile or non-volatile, are ions of different charges and is responsible for contributing different diffusion rates. Different diffusing species or ions may have different vapour pressures, diffusion paths, and different diffusion rates. Their collective effort significantly alters the measured density and grain size of the prepared compositions.

2.4.2 Dielectric measurements near the MPB region

At RT, the observed composition dependence ($0.140 \leq x \leq 0.160$) of dielectric properties (ε, tan δ, and σ) of $(Ba_{1-x}Ca_x)(Zr_{0.1}Ti_{0.9})O_3$ ceramics, at different frequencies, has been shown in Figs. 2.7-2.9. With the increase in frequency, normally, ε and tan δ were found decreasing, and σ

increasing, for the prepared compositions. These observations are in consistency with the previous publications [17,26,27,35]. Figs. 2.10-2.11 show the measured composition dependence ($0.140 \leq x \leq 0.160$) of ε, tan δ, and σ of BCZT ceramics, at different temperatures, at 1 MHz. With the increase in temperature, the dielectric constant (ε) was found increasing, and electric conductivity (σ) and loss tangent (tan δ) decreasing, for all the prepared compositions. Among the prepared compositions, an irregular decrease was found in the dielectric properties, near MPB, with anomalously lower values of ε, tan δ, and σ, at $x = 0.150$. The measured composition ($0.140 \leq x \leq 0.160$) dependence of ε, tan δ, and σ, at different frequencies with RT, were shown in Figs. 2.12-2.13. A drastic change was observed in the dielectric properties (ε, tan δ, and σ) at $x = 0.150$, at all the measured frequencies. Figs. 2.10-2.13 show that the dielectric properties of the BCZT are significantly composition dependent. A drastic minimum in the dielectric properties (ε, tan δ, and σ), shows a typical morphotropic phase transition type behavior, at the compositions with $x = 0.150$, which is composition dependent rather than temperature and frequency [16]. However, the microstructure, grain size, voids, porosity and density greatly affect the dielectric properties of the pellet samples [39-41]. The contribution of escaping of alkaline ions and composition-dependent structural anomaly may be the responsible factors for the observed dielectric anomaly in the prepared BCZT ceramics. The dielectric constant decreases with decreasing grain size, which arises because of the increased occurrence of non-ferroelectric low permittivity grain boundaries [39]. With increasing grain size, number of grain boundaries decreases and results in the decreased loss. Also, the presence of liquid phase, internal stress, etc. may contribute to the observed dielectric behaviour in BCZT samples.

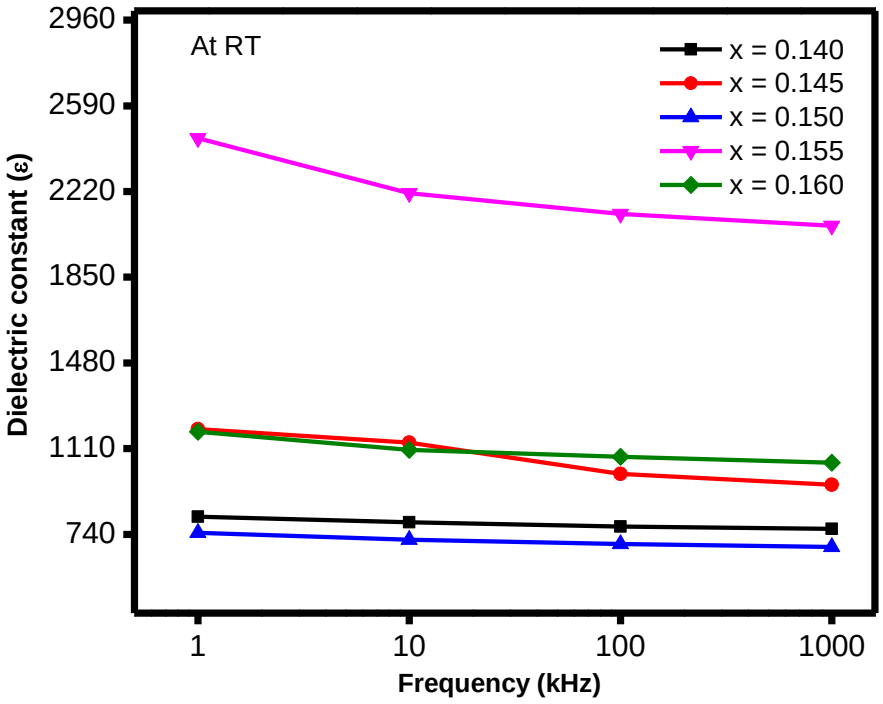

Fig. 2.7 Variation of dielectric constant (ε) with frequency, in $(Ba_{1-x}Ca_x)(Zr_{0.1}Ti_{0.9})O_3$, ($0.140 \leq x \leq 0.160$), at RT.

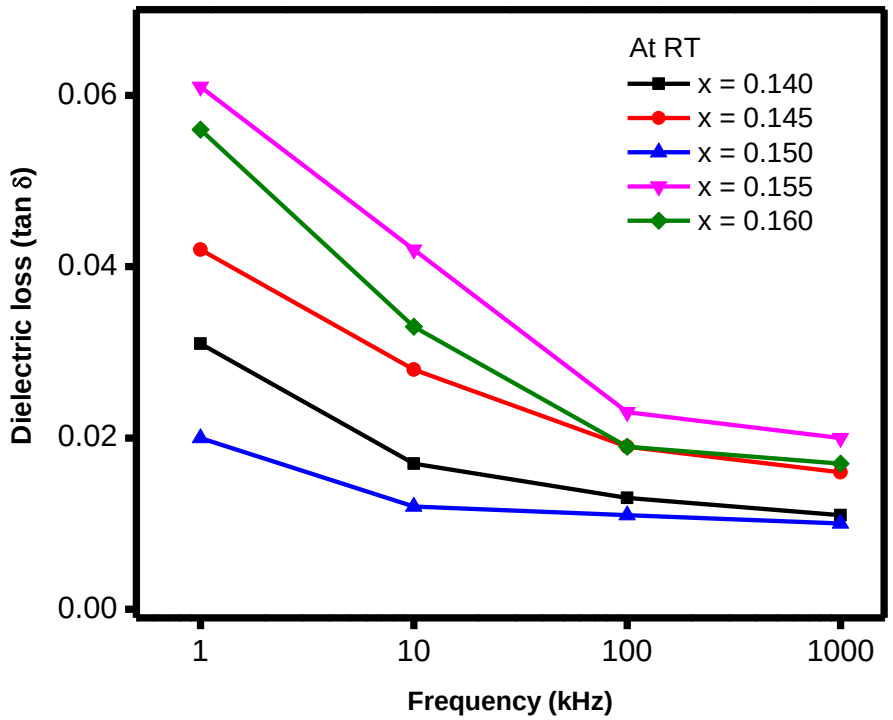

Fig. 2.8 Variation of dielectric loss (tan δ) with frequency, in $(Ba_{1-x}Ca_x)(Zr_{0.1}Ti_{0.9})O_3$, ($0.140 \leq x \leq 0.160$), at RT.

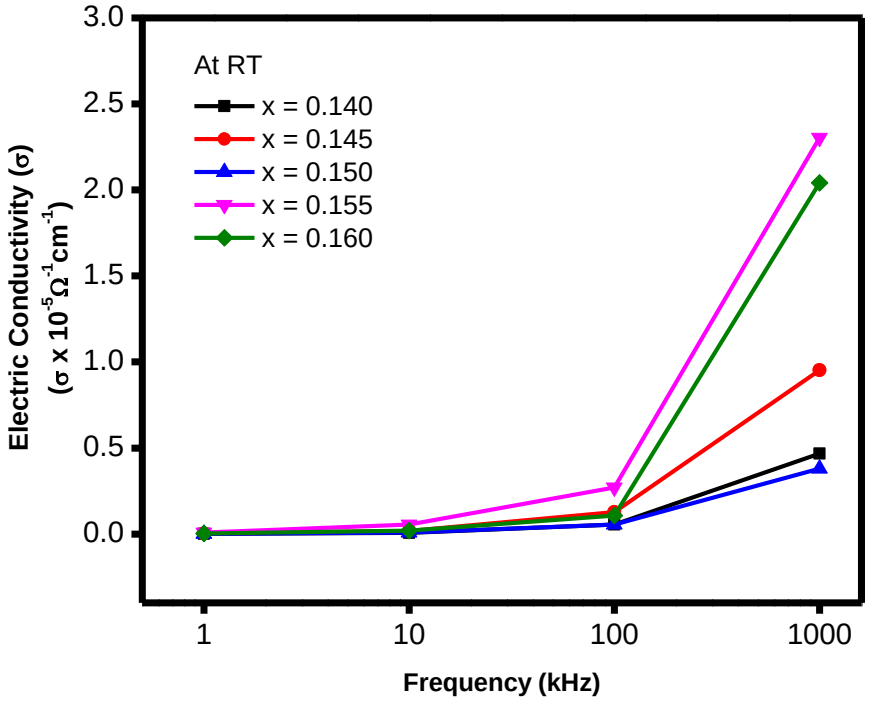

Fig. 2.9 Variation of electric conductivity (σ) with frequency, in $(Ba_{1-x}Ca_x)(Zr_{0.1}Ti_{0.9})O_3$, ($0.140 \leq x \leq 0.160$), at RT.

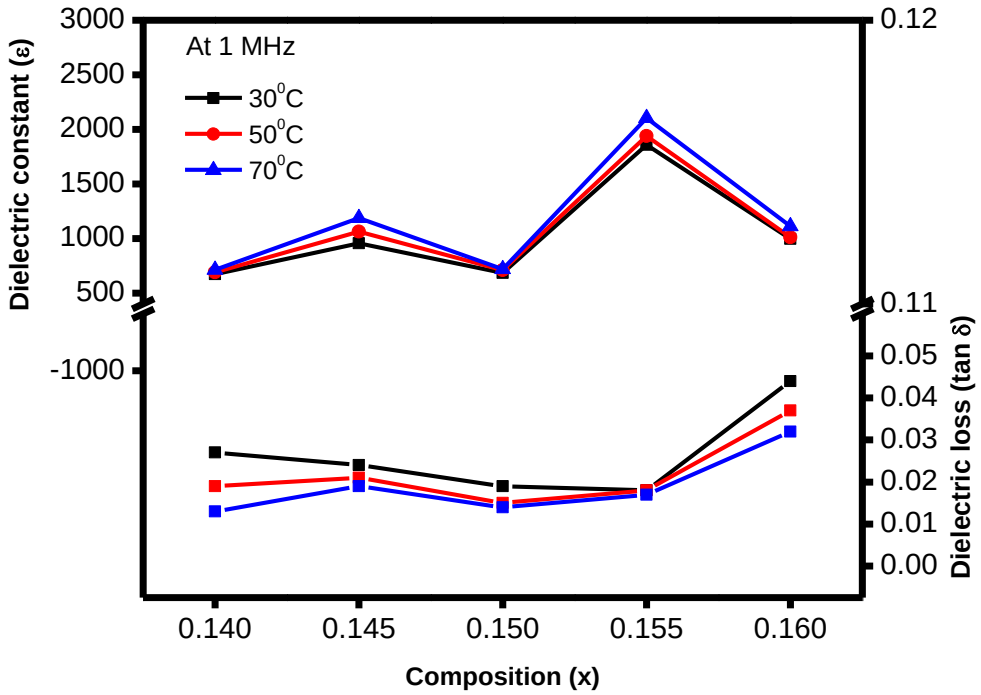

Fig. 2.10 Composition variation of dielectric constant (ε) and dielectric loss (tan δ), in $(Ba_{1-x}Ca_x)(Zr_{0.1}Ti_{0.9})O_3$, ($0.140 \leq x \leq 0.160$), at different temperatures.

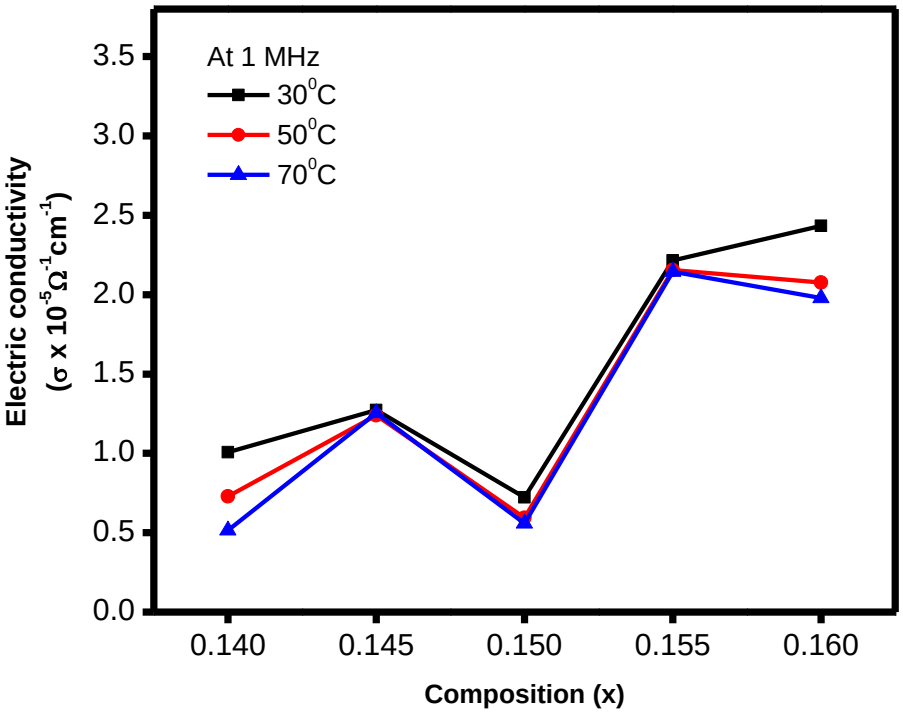

Fig. 2.11 Composition variation of electric conductivity (σ), in $(Ba_{1-x}Ca_x)(Zr_{0.1}Ti_{0.9})O_3$, $(0.140 \leq x \leq 0.160)$, at different temperatures.

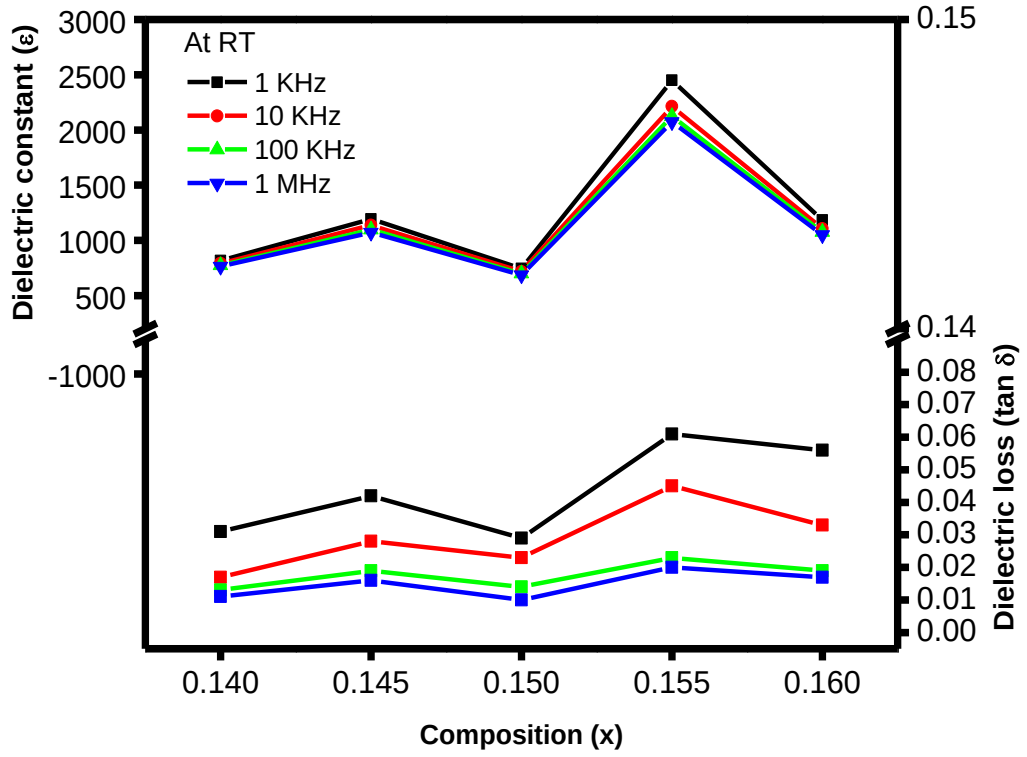

Fig. 2.12 Composition variation of dielectric constant (ε) and dielectric loss (tan δ), in $(Ba_{1-x}Ca_x)(Zr_{0.1}Ti_{0.9})O_3$, $(0.140 \leq x \leq 0.160)$, at different frequencies.

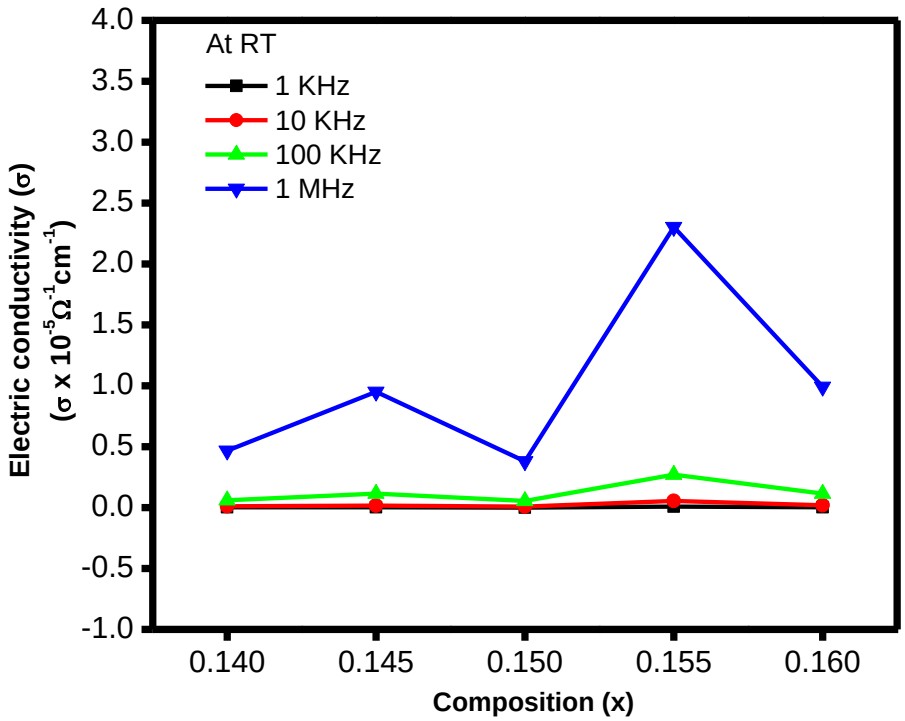

Fig. 2.13 Composition variation of electric conductivity (σ), in $(Ba_{1-x}Ca_x)(Zr_{0.1}Ti_{0.9})O_3$, ($0.140 \leq x \leq 0.160$), at different frequencies.

2.5 Discussion

There are two types of defects found in perovskite ABO_3 type compounds, viz., vacancies at A- and O-sites [28]. These vacancies significantly affect the electrical properties [17,26,27,40] of oxides. The conduction process in these oxides may be understood with the behaviour of the majority of acceptor or donor concentration. In ABO_3 type perovskite compounds, A- site vacancy behaves as an electron acceptor, which is equivalent to saying that it may donate a hole for conduction, and the O-site vacancy behaves as an electron donor, it may donate electron for conduction. If the number of vacancies at the A-site is more than that at O-site, the solids may behave as p-type, or if there is the majority of O-site vacancy, it may behave as the n-type. The majority of A- or O-site vacancies will decide whether a solid will behave as p- or n-type. More A-site vacancies will donate more holes for conduction, and the hole conductivity will increase. In contrast, more O-site vacancies will contribute more electrons for conduction, and the electron conductivity of the solid will increase. The EDX results of the prepared $(Ba_{1-x}Ca_x)(Zr_{0.1}Ti_{0.9})O_3$ ceramics show considerable escaping of alkaline (Ba and Ca) ions from the samples, having minimum for the composition with x = 0.150, Table 2.1. The oxygen escaping was lower than the escaping of alkaline (Ba and Ca) ions. Therefore, A-site vacancies are in excess than that at

O-site, envisaging the dominance of p-type conduction in the present $(Ba_{1-x}Ca_x)(Zr_{0.1}Ti_{0.9})O_3$ ceramics. The deficiency of A-site vacancies is lowest, so fewer holes are available for conduction. The conductivity is minimum for the samples with x = 0.150, than the other prepared compositions.

Many researchers reported the p- type conductivity in various oxides, viz., ZrO_2, $Na_{1-x}K_xNbO_3$, etc. [17,26,52]. In the present study, a distinct conductivity minimum was observed, with a decrease in A- site vacancy concentration, near MPB, with x = 0.150. Among the prepared compositions, it appears that during the sintering of the pellet samples, the intensification of diffusion processes distinctively decreases the possibility of escaping of volatile alkaline ions near the MPB region [17,26].

With the increase in density, the dielectric constant of ceramics increases [53,54]. In the present study, the dielectric constant was found to be minimum even though the density was maximum, for the composition with x = 0.150, among the prepared compositions, which indicates the control of composition more than the density near MPB region. The dielectric properties of ceramics may depend on the preparation process, because of its mechanical distinctions in the forming process, inhomogeneity in microchemistry, varying shrinkage, and chemical modification during sintering.

These observations indicate that the composition, structure, and preparation process significantly affect the electrical properties of BCZT ceramics. For the composition near MPB, the structural anomaly and a decrease in A- site vacancy concentration in the p-type oxides may be responsible for the observed minimum values of ε, tan δ, and σ, at x = 0.150, among the prepared compositions.

References

[1] G.A. Samara, Effects of pressure on the dielectric properties and phase transitions of the alkali metal tantalates and niobates, Ferroelectrics. 73 (1987) 145-159. https://doi.org/10.1080/00150198708227914

[2] Y. Saito, H. Takao, T. Tani, T. Nonoyama, K. Takatori, T. Homma, T. Nagaya, M. Nakamura, Lead-free piezoceramics, Nature. 432 (2004) 84-87. https://doi.org/10.1038/nature03028

[3] M. Dawber, K.M. Rabe, J.F. Scott, Physics of thin-film ferroelectric oxides, Reviews of modern physics. 77 (2005) 1083-1130. https://doi.org/10.1103/RevModPhys.77.1083

[4] P. Kantha, K. Pengpat, P. Jarupoom, U. Intatha, G. Rujijanagul, T. Tunkasiri, Phase formation and electrical properties of BNLT-BZT lead-free piezoelectric ceramic system, Current Applied Physics. 9 (2009) 460-466. https://doi.org/10.1016/j.cap.2008.04.004

[5] M. Ahtee, A.M. Glazer, Lattice parameters and tilted octahedra in sodium-potassium niobate solid solutions, Acta Crystallographica Section A. A32 (1976) 434-446. https://doi.org/10.1107/S0567739476000983

[6] R. Guo, L.E. Cross, S.E. Park, B. Noheda, D.E. Cox, G. Shirane, origin of the high piezoelectric response in $PbZr_{1-x}Ti_xO_3$, Physical Review Letters. 84 (2000) 5423-5426. https://doi.org/10.1103/PhysRevLett.84.5423

[7] S.E. Park, T.R. Shrout, Ultrahigh strain and piezoelectric behavior in relaxor based ferroelectric single crystals, Journal of Applied Physics. 82 (1997) 1804. https://doi.org/10.1063/1.365983

[8] B. Noheda, Structure and high-piezoelectricity in lead oxide solid solutions, Current Opinion Solid State and Materials Science. 6 (2002) 27-34. https://doi.org/10.1016/S1359-0286(02)00015-3

[9] H. Fu, R.E. Cohen, Polarization rotation mechanism for ultrahigh electromechanical response in single-crystal piezoelectrics, Nature. 403 (2000) 281-283. https://doi.org/10.1038/35002022

[10] R.E. Cohen, Relaxors go critical, Nature. 441 (2006) 941-942. https://doi.org/10.1038/441941a

[11] M. Ahart, M. Somayazulu, R.E. Cohen, P. Ganesh, P. Dera, H.K. Mao, R.J. Hemley, Y. Ren, P. Liermann, Z. Wu, Origin of morphotropic phase boundaries in ferroelectrics, Nature. 451 (2008) 545-548. https://doi.org/10.1038/nature06459

[12] B. Jaffe, R.S. Roth, S. Marzullo, Properties of piezoelectric ceramics in the solid-solution series lead titanate-lead zirconate-lead oxide: tin oxide and lead titanate-lead hafnate, Journal of research of the National Bureau of Standards. 55 (1955) 239-254.

[13] S. Somiya, Ceramics, In: R.A. Meyers (ed) Encyclopedia of physical science and technology, Academic press publishing, New York, 2003: pp. 569-619. https://doi.org/10.1016/B0-12-227410-5/00092-2

[14] Y. Tian, L. Wei, X. Chao, Z. Liu, Z. Yang, Phase transition behavior and large piezoelectricity near the morphotropic phase boundary of lead-Free $(Ba_{0.85}Ca_{0.15})(Zr_{0.1}Ti_{0.9})O_3$ ceramics, Journal of the American Ceramic Society. 96 (2013) 496-502. https://doi.org/10.1111/jace.12049

[15] D. Xue, Y.M. Zhou, H.X. Bao, C. Zhou, J.H. Gao, X.B. Ren, Elastic, piezoelectric, and dielectric properties of $Ba(Zr_{0.2}Ti_{0.8})O_3$-50$(Ba_{0.7}Ca_{0.3})TiO_3$ Pb-free ceramic at the morphotropic phase boundary, Journal of Applied Physics. 109 (2011) 054110. https://doi.org/10.1063/1.3549173

[16] T. Mondal, S. Das, T. Badapanda, T.P. Sinha, P.M. Sarun, Effect of Ca^{2+} substitution on impedance and electrical conduction mechanism of $Ba_{1-x}Ca_xZr_{0.1}Ti_{0.9}O_3$ ($0.00 \leq x \leq 0.20$) ceramics, Physica B: Condensed Matter. 508 (2017) 124-135. https://doi.org/10.1016/j.physb.2016.12.021

[17] S. Singh, J. Negi, N.S. Panwar, Dielectric properties of $Na_{1-x}K_xNbO_3$, near x = 0.5 morphotropic phase region, Journal of Physics and Chemistry of Solids. 123 (2018) 311-327. https://doi.org/10.1016/j.jpcs.2018.08.018

[18] D.A. Tuan, V. Tung, T.V. Choung, N.T. Tinh, N.T.M. Huong, Structure, microstructure and dielectric properties of lead-free BCT-*x*BZT ceramics near the morphotropic phase boundary, Indian Journal of Pure and Applied Physics. 53 (2015) 409-415. http://nopr.niscpr.res.in/handle/123456789/31600

[19] Z. Hanani, D. Mezzane, M.Amjoud, S. Fourcade, A.G. Razumnaya, I.A. Luk'yanchuk, M. Gouné, Enhancement of dielectric properties of lead-free BCZT ferroelectric ceramics by grain size engineering, Superlattices and Microstructures. 127 (2019) 109-117. https://doi.org/10.1016/j.spmi.2018.03.004

[20] P. Wang, Y. Li, Y. Lu, Enhanced piezoelectric properties of $(Ba_{0.85}Ca_{0.15})(Zr_{0.1}Ti_{0.9})O_3$ lead-free ceramics by optimizing calcination and sintering temperature, Journal of the European Ceramic Society. 31 (2011) 2005-2012. https://doi.org/10.1016/j.jeurceramsoc.2011.04.023

[21] J. Wu, D. Xiao, B. Wu, W. Wu, J. Zhu, Z. Yang, J. Wang, Sintering temperature-induced electrical properties of $(Ba_{0.90}Ca_{0.10)(}Ti_{0.85}Zr_{0.15})O_3$ lead-free ceramics, Materials Research Bulletin. 47 (2012) 1281. https://doi.org/10.1016/j.materresbull.2012.01.032

[22] J. Wu, D. Xiao, W. Wu, J. Zhu, J. Wang, Effect of dwell time during sintering on piezoelectric properties of $(Ba_{0.85}Ca_{0.15})(Zr_{0.1}Ti_{0.9})O_3$ lead-free ceramics, Journal of Alloys and Compounds. 509 (2011) L359-L361. https://doi.org/10.1016/j.jallcom.2011.08.024

[23] W. Li, Z. Xu, R. Chu, P. Fu, G. Zang, Piezoelectric and Dielectric Properties of $(Ba_{1-x}Ca_x)(Ti_{0.95}Zr_{0.05})O_3$ Lead-Free Ceramics, Journal of the American Ceramic Society. 93 (2010) 2942-2944. https://doi.org/10.1111/j.1551-2916.2010.03907.x

[24] W. Li, Z. Xu, R. Chu, P. Fu, G. Zang, High piezoelectric d_{33} coefficient in $(Ba_{1-x}Ca_x)(Ti_{0.98}Zr_{0.02})O_3$ lead-free ceramics with relative high Curie temperature, Materials Letters. 64 (2010) 2325-2327. https://doi.org/10.1016/j.matlet.2010.07.042

[25] S.W. Zhang, H.L. Zhang, B.P. Zhang, S. Yang, Phase-transition behavior and piezoelectric properties of lead-free $(Ba_{0.95}Ca_{0.05})(Ti_{1-x}Zr_x)O_3$ ceramics, Journal of alloys and compounds. 506 (2010) 131-135. https://doi.org/10.1016/j.jallcom.2010.06.157

[26] D. Biswas, P. Sharma, N. S. Panwar, Dielectric properties of $Na_{1-x}K_xNbO_3$ (NKN) ($0.160 \leq x \leq 0.200$) ceramics synthesized by double sintered method, Ferroelectrics. 571 (2021) 214-229. https://doi.org/10.1080/00150193.2020.1853757

[27] J. Negi, S. Singh, N.S. Panwar, Structural and dielectric anomaly in $Na_{1-x}K_xNbO_3$, at $x = 0.315$, Phase Transitions, 92 (2019) 149-158. https://doi.org/10.1080/01411594.2018.1563789

[28] B. Jaffe, R.S. Roth, S. Marzullo, Piezoelectric properties of lead zirconate-lead titanate solid-solution ceramics, Journal of Applied Physics. 25 (1954) 809. https://doi.org/10.1063/1.1721741

[29] D. Damjanovic, Ferroelectric, dielectric and piezoelectric properties of ferroelectric thin films and ceramics, Reports on Progress in Physics. 61 (1998) 1267-1324. https://doi.org/10.1088/0034-4885/61/9/002

[30] A.M. Glazer, P.A. Thomas, K.Z.B. Kishi, G.K.H. Pang, C.W. Tai, Influence of short-range and long-range order on the evolution of the morphotropic phase boundary in $Pb(Zr_{1-x}Ti_x)O_3$, Physical Review B. 70 (2004) 184123. https://doi.org/10.1103/PhysRevB.70.184123
[31] B. Jaffe, W.R. Cook, J.H. Jaffe, Piezoelectric ceramics, 1st ed., Academic press publishing, New York, 1971.
[32] A.J. Moulson, J.M. Herbert, Electroceramics: Materials, Properties, Applications, 2nd ed., John Wiley & Sons publishing, England, 2003.
[33] Y. Ishibashia, M. Iwata, A theory of morphotropic phase boundary in solid-solution systems of perovskite-type oxide ferroelectrics, Japanese Journal of Applied Physics. 38 (1999) 800. https://doi.org/10.1143/JJAP.38.800
[34] W. Cao, L.E. Cross, Theoretical model for the morphotropic phase boundary in lead zirconate-lead titanate solid solution, Physical Review B. 47 (1993) 4825-4830. https://doi.org/10.1103/PhysRevB.47.4825
[35] D. Biswas, P. Sharma, N.S. Panwar, Structural and electrical properties of lead free $Na_{1-x}K_xNbO_3$ ($0.160 \leq x \leq 0.200$) ceramics, Ceramics International. 47 (2021) 13814-13819. https://doi.org/10.1016/j.ceramint.2021.01.246
[36] D. Biswas, N.S. Panwar, P. Sharma, Converse piezoelectric properties of lead free $Ba_{1-x}Ca_xZr_{0.1}Ti_{0.9}O_3$ ($x = 0.055$) ceramics using double sintered method, Ferroelectrics. 568 (2020) 95-103. https://doi.org/10.1080/00150193.2020.1811032
[37] N. Buatip, N. Promsawat, N. Pisitpipathsin, O. Namsar, P. Pawasri, K. Ounsung, K. Phabsimma, S.T. Rattanachan, P. Janphuang, S. Projprapai, Investigation on electrical properties of BCZT ferroelectric ceramics prepared at various sintering conditions, Integrated Ferroelectrics. 187 (2018) 45-52. https://doi.org/10.1080/10584587.2018.1445395
[38] S. Sen, R. Choudhay, Effect of doping Ca ions on structural and electrical properties of $Ba(Zr_{0.05}Ti_{0.95})O_3$ electroceramics, Journal of Materials Science: Materials in Electronics. 15 (2004) 671-675. https://doi.org/10.1023/B:JMSE.0000038922.74021.d6
[39] M.H. Frey, Z. Xu, P. Han, D.A. Payne, The role of interfaces on an apparent grain size effect on the dielectric properties for ferroelectric barium titanate ceramics, Ferroelectrics. 206 (1998) 337-353. https://doi.org/10.1080/00150199808009168
[40] E.V. Bursyan, Nonlinear Crystal-Barium Titanate, Nauka Press publishing, Moskva, 1974.
[41] K. Yan, X. Ren, Multi-phase transition behaviour and large electrostrain in lead-free (K, Na, Li)NbO_3 ceramics, Journal of Physics D: Applied Physics. 47 (2014) 015309. https://doi.org/10.1088/0022-3727/47/1/015309
[42] J. Bohdanskya, H.E.J. Schins, Vapor pressure of different metals in the pressure range of 50 to 4000 torr, The Journal of Physical Chemistry. 71 (1967) 215-217. https://doi.org/10.1021/j100861a001
[43] N. Pisitpipathsin, P. Kantha, K. Pengpat, and G. Rujijanagul, Influence of Ca substitution on microstructure and electrical properties of Ba $(Zr,Ti)O_3$ ceramics, Ceramics International. 39 (2013) S35-S39. https://doi.org/10.1016/j.ceramint.2012.10.031
[44] V. Lingwal, B.S. Semwal, N.S. Panwar, Dielectric properties of $Na_{1-x}K_xNbO_3$ in orthorhombic phase, Bulletin of Materials Science. 26 (2003) 619-625. https://doi.org/10.1007/BF02704326

[45] B. Malic, J. Koruza, J. Hrescak, J. Bernard, K. Wang, J. Fisher, A. Bencan, Sintering of lead-free piezoelectric sodium potassium niobate ceramics, Materials. 8 (2015) 8117-8146. https://doi.org/10.3390/ma8125449
[46] I.W. Chen, X.H. Wang, Sintering dense nanocrystalline ceramics without final-stage grain growth, Nature. 404 (2000) 168-171. https://doi.org/10.1038/35004548
[47] H.T. Kim, Y.H. Han, Sintering of nanocrystalline $BaTiO_3$, Ceramics International. 30 (2004) 1719-1723. https://doi.org/10.1016/j.ceramint.2003.12.141
[48] W. Chaisan, R. Yimnirun, S. Ananta, Two-stage sintering of barium titanate ceramic and resulting characteristics, Ferroelectrics, 346 (2007) 84-92. https://doi.org/10.1080/00150190601180380
[49] U. Sutharsini, M. Thanihaichelvan, R. Singh, Sintering of functional materials, 2nd ed., Intechopen publishing, London, United Kingdom, 2017.
[50] J. Koruza, B. Malic, Initial stage sintering mechanism of $NaNbO_3$ and implications regarding the densification of alkaline niobates, Journal of the European Ceramic Society. 34 (2014) 1971-1979. https://doi.org/10.1016/j.jeurceramsoc.2014.01.035
[51] R.M. German, Z.A. Munir, Surface area reduction during isothermal sintering, Journal of the American Ceramic Society. 59 (1976) 379-383. https://doi.org/10.1111/j.1151-2916.1976.tb09500.x
[52] J.Z. Rudolph, About the conduction mechanism of oxidic semiconductors at high temperatures, Naturforsch. 14a (1959) 727.
[53] H. Chen, C. Yang, C. Fu, L. Zhao, Z. Gao, The size effect of $Ba_{0.6}Sr_{0.4}TiO_3$ thin films on the ferroelectric properties, Applied Surface Science. 252 (2006) 4171-4177. https://doi.org/10.1016/j.apsusc.2005.06.027
[54] Q. Xu, X.F. Zhang, H.X. Liu, W. Chen, M. Chen, B.H. Kim, Effect of sintering temperature on dielectric properties of $Ba_{0.6}Sr_{0.4}TiO_3$-MgO composite ceramics prepared from fine constituent powders, Materials and Design. 32 (2011) 1200-1204. https://doi.org/10.1016/j.matdes.2010.10.018

CHAPTER-3

Temperature-dependent dielectric properties of $(Ba_{1-x}Ca_x)(Zr_{0.1}Ti_{0.9})O_3$, $(0.140 \leq x \leq 0.160)$ ceramics

---

Brief summary

The temperature-dependent dielectric and structural properties were described in this chapter. Dielectric properties (ε, tan δ, and σ) of the prepared compositions were measured, in the temperature range from RT (room temperature) to 450 ^{o}C, at various frequencies (12-1000 kHz). The dielectric measurements show a single phase transition, around 100 ^{o}C, for the prepared $(Ba_{1-x}Ca_x)(Zr_{1-y}Ti_y)O_3$ (BCZT) compositions, in the measured temperature range. The structural variation was studied using high-temperature X-ray diffraction (HT-XRD) measurements of the compositions with x = 0.150 and 0.155. The HT-XRD results were consistent with the dielectric measurements, showing structural anomaly at around 100 ^{o}C; showing tetragonal phase, between RT and around 100 ^{o}C; and cubic phase, above 100 ^{o}C, in the measured temperature range.

CHAPTER-3

Temperature-dependent dielectric properties of $(Ba_{1-x}Ca_x)(Zr_{0.1}Ti_{0.9})O_3$, ($0.140 \leq x \leq 0.160$) ceramics

3.1 Introduction

Perovskite ferroelectric barium calcium zirconate titanate $(Ba_{1-x}Ca_x)(Zr_{0.1}Ti_{0.9})O_3$, (x = 0.140-0.160, y = 0.9) is attractive due to its no. of ferroelectric phases [1-4]. It shows the cubic structure at a high-temperature range. Tian et al. [4] reported the phase schematic of $(Ba_{1-x}Ca_x)(Zr_{1-y}Ti_y)O_3$ (x, y = 0 to 1) solid solutions. When Ca ions replace Ba ions at the A- site and Ti by Zr at the B-site of the $BaTiO_3$, two different solid solutions can be formed [5-10]. One is $Ba_{1-x}Ca_xTiO_3$ (BCT) system, and the other is $BaZr_yT_{1-y}O_3$ (BZT). The perovskite ferroelectric $BaTiO_3$ compound undergoes three distinct structural phase transformations sequence, viz., ferroelectric rhombohedral (R) on cooling, ferroelectric orthorhombic (O) ~ -90 ^oC, ferroelectric tetragonal (T) ~ 0 ^oC, and paraelectric cubic (C) phase ~ 125 ^oC [4]. For $Ba_{1-x}Ca_xTiO_3$ (BCT) system, the Curie temperature (T_C) rises with a rise in x concentration [5-7], whereas the (O) → (T) phase transition has been moved to the lower temperature range [5-7]. Further, for $BaZr_yT_{1-y}O_3$ (BZT) system, the Curie temperature (T_C) shifts down with the increase in y, whereas T_{R-O} and T_{O-T} shift towards the higher temperature range [5-7]. A condition arrives when all three transition points come closer to each other. The condition is achieved when y increases to 0.10 [8-10]. The BCT and BZT systems may show distinct phases from the reported phase transition characteristics. The Ti-shift in the BO_6 octahedron may contribute to the ferroelectricity of the $BaTiO_3$ system, suggesting three different ferroelectric structures in the lattice, viz., a T (tetragonal) structure with polarization vector direction [001] followed by a O (orthorhombic) structure with [011] and a R (rhombohedral) structure with [111] [11].

In the previous Chapter, dielectric properties (ε, tan δ, and σ) of $(Ba_{1-x}Ca_x)(Zr_{1-y}Ti_y)O_3$, (x = 0.140-0.160, y = 0.9) were found lowest for the samples with x = 0.150, among the prepared compositions, at all measured temperatures and frequencies [12]. The obtained findings exhibit a strong composition dependence of dielectric properties- a morphotropic-like phase boundary in $(Ba_{1-x}Ca_x)(Zr_{1-y}Ti_y)O_3$, (x = 0.140-0.160, y = 0.9), ceramics, at x = 0.150. The composition variation of this system also shows structural anomaly near x = 0.150. The polarization rotation

and extension, and the elastic softening of the lattice may be the potential factors for the composition-dependent anomaly near the MPB [13]. Also, near the MPB, the presence of two or more phases can significantly change the physical or structural properties of the $(Ba_{1-x}Ca_x)(Zr_{1-y}Ti_y)O_3$ ceramics [14,15]. Depending on the composition (x), $(Ba_{1-x}Ca_x)(Zr_{1-y}Ti_y)O_3$, the system shows cubic, tetragonal or orthorhombic phases [16]. The $(Ba_{1-x}Ca_x)(Zr_{1-y}Ti_y)O_3$ ceramics also exhibit polymorphic phases depending on the temperature and composition (x) [17]. The sintering-dependent density and dielectric properties of $(Ba_{1-x}Ca_x)(Zr_{1-y}Ti_y)O_3$ compositions were reported [12,18]. The study was further extended, and the observed temperature-dependent dielectric and structural properties of the double-sintered $(Ba_{1-x}Ca_x)(Zr_{1-y}Ti_y)O_3$ compositions are being reported presently.

In the present study, the temperature variation of dielectric properties of BCZT samples near the morphotropic phase boundary was carried out from room temperature (RT) to 450 ^oC. $(Ba_{1-x}Ca_x)(Zr_{0.1}Ti_{0.9})O_3$, $(0.140 \leq x \leq 0.160)$ pellet samples were prepared by solid-state reaction method followed by double sintering. The prepared samples' temperature dependence of dielectric constant, loss tangent, and electric conductivity was measured at various frequencies (12-1000 kHz). The HT-XRD measurements were carried out for two compositions, with x = 0.150 and 0.155, in the temperature range from RT to 450 ^oC. Consistent with the dielectric behaviour, high temperature X-ray diffraction (HT-XRD) measurements of the prepared samples, with x = 0.150 and 0.155, indicated tetragonal phase, between room temperature and 100 ^oC, and cubic phase above 100 ^oC, in the measured temperature range.

3.2 Experimentation

The preparation methodology of the $(Ba_{1-x}Ca_x)(Zr_{1-y}Ti_y)O_3$ pellet samples, their X- ray diffraction (XRD) patterns, scanning electron micrograph (SEM) images, composition-dependent dielectric properties, density, etc. were described in a previous communication [12]. The dielectric constant, loss tangent and electric conductivity of the prepared compositions are measured at different frequencies in the temperature range, from RT to 450 ^oC, using an impedance analyzer (Keysight, E49990), have been reported. For dielectric measurements, specimens were electroded, with air-drying conducting silver paste, in a metal-insulator-metal (MIM) arrangement.

To study different phases of the prepared BCZT ceramics, HT- XRD were measured, from RT to 450 ^{o}C, for the compositions with x = 0.150 and 0.155, by an X-ray diffractometer (PANalytical, X'PERT PRO), using Cu$K_{\alpha 1}$ radiation of wavelength 1.5406 Å. The scan speed of the diffractometer was 0.1 sec per step with a step size of 0.01^{o}. The composition was heated up at a heating rate of 5 ^{o}C/s. At each measuring temperature, the desired temperature was held for 2 minutes before the XRD measurement.

3.3 Dielectric measurements

Presently, the thermal variation of the dielectric properties, the dielectric constant (ε), tangent loss (tan δ) and electric conductivity (σ) of the prepared $(Ba_{1-x}Ca_x)(Zr_{1-y}Ti_y)O_3$ ceramics, (x = 0.140-0.160, y = 0.9), were measured, in the temperature range from RT to 450 ^{o}C, at different frequencies (12-1000 kHz). Figs. 3.1, 3.2 and 3.3 show the measured temperature-dependence of ε, tan δ, and σ of the BCZT ceramics. The dielectric constant (ε) was found to increase with an increase in temperature but with an anomalously large value at around 100 ^{o}C, indicating a phase transition at this temperature. Similarly, the tangent loss and electric conductivity anomaly, Figs. 3.2 and 3.3, respectively, confirm the occurrence of phase transition at around 100 ^{o}C, in these compositions. The insets of Figs. 3.1- 3.2 show the anomaly. The wide dielectric constant peaks were observed at 99, 99, 84, 99, and 94 ^{o}C, Fig. 3.1; and electric conductivity peaks at 104, 104, 89, 99, and 94 ^{o}C, Fig. 3.3, for the compositions with x = 0.140, 0.145, 0.150, 0.155, 0.160, respectively. The dielectric constant, loss tangent and electric conductivity anomaly were observed at all the measuring frequencies for an individual composition, Figs. 3.1-3.3. However, for the compositions with $x \leq 0.150$, the dielectric constant and electric conductivity peaks were not observed at the same temperature for an individual composition. The observed wide dielectric peaks indicate the relaxor-type behaviour, whereas the occurrence of frequency-independent transition temperature shows the non-relaxor nature of the prepared material [19]. For a relaxor, the wide dielectric constant peak shifts to higher temperature with increasing frequency, owing to the increasing relaxation time with temperature [19]. The occurrence of wide dielectric constant and electric conductivity peaks and slight variation in the temperature of these peaks may be the resulting effect of the structural change, barrier heights at the grain boundary, activation energy and other interactions [20], resulting maximum for one grain at one temperature and for another grain at another temperature, in the ceramic sample, near the

transition temperature of that composition. Near x = 0.150, the BCZT ceramics shows morphotropic-type phase boundary (MPB) comprising two or more phases [21]. A combination of these phases may initiate different polarization directions, which might have also contributed to the observed wide dielectric peaks for the compositions near MPB. With the increase in the measuring frequency, the observed decrease in dielectric constant (ε) and loss tangent (tan δ) and increase in the electric conductivity were found to be consistent with the reported results [12,22,23], which may be attributed to the damping out of successive relaxation modes in the lattice [24].

The Curie point indicates the transition temperature where the material observes paraelectric to ferroelectric transition. The paraelectric phase is a high symmetry phase, and the ferroelectric is a low symmetry phase. Thus, this phase transition is attributed to the structural phase transition in the perovskite- type ferroelectrics [25]. The dielectric properties of the perovskites are attributed to a significant temperature-dependent vibrational mode-the soft mode [26]. The frequency of vibrational modes in a crystal depends on the long- and short-range interactions among the vibrating species. At the transition temperature, the soft mode frequency tends to zero, and the lattice observes a displacement leading to the structural anomaly-the structural phase transition [26,27]. According to the soft mode theory, the dielectric permittivity of perovskites is proportional to the inverse of the square of the soft mode frequency [28]. When Ba atoms are replaced by Ca atoms, in the ABO_3 type $Ba(Zr, Ti)O_3$, the change in the mass, force constant and other interactions result in a change in the soft mode frequency. With the random allocation of varied (Ca) mass at different lattice sites (A-site), the force constant and other interactions vary randomly, resulting change in the soft mode frequency accordingly and, thereby to the change in the observed dielectric constant with the substitution of Ba by Ca in the lattice.

Fig. 3.4 shows the temperature-dependence of dielectric permittivity and conductivity, at 1 MHz, in the measured temperature range. The dielectric anomaly was observed near 100 ^{o}C, for the prepared BCZT compositions. The observed anomaly in the dielectric properties indicates the transition temperature [25]. This transition is attributed to the tetragonal to cubic structural change [29]. The dielectric anomaly was observed varying with the Ca doping (x), at the A- site, in the $(Ba_{1-x}Ca_x)(Zr_{1-y}Ti_y)O_3$, (x = 0.140-0.160, y = 0.9) ceramics, as shown in Figs. 3.1-3.3. Apart from the softening of the active phonon mode, the polarization extension and rotation

mechanism, porosity, microstructure and grain morphology of $(Ba_{1-x}Ca_x)(Zr_{1-y}Ti_y)O_3$ ceramic samples of a composition may contribute to its observed dielectric nature [30].

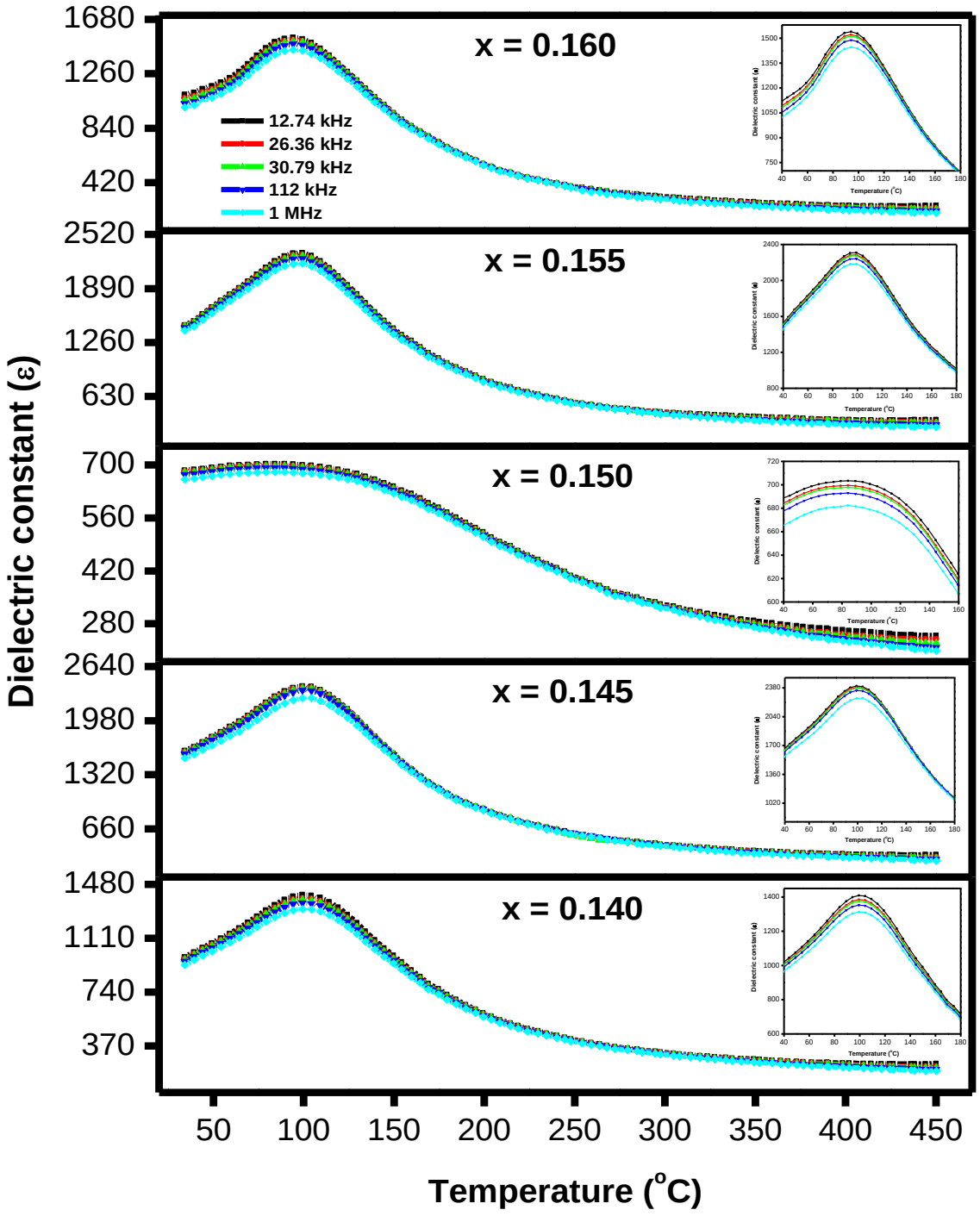

Fig. 3.1 Temperature variation of dielectric constant (ε), in $(Ba_{1-x}Ca_x)(Zr_{1-y}Ti_y)O_3$, (x = 0.140-0.160, y = 0.9), at different frequencies.

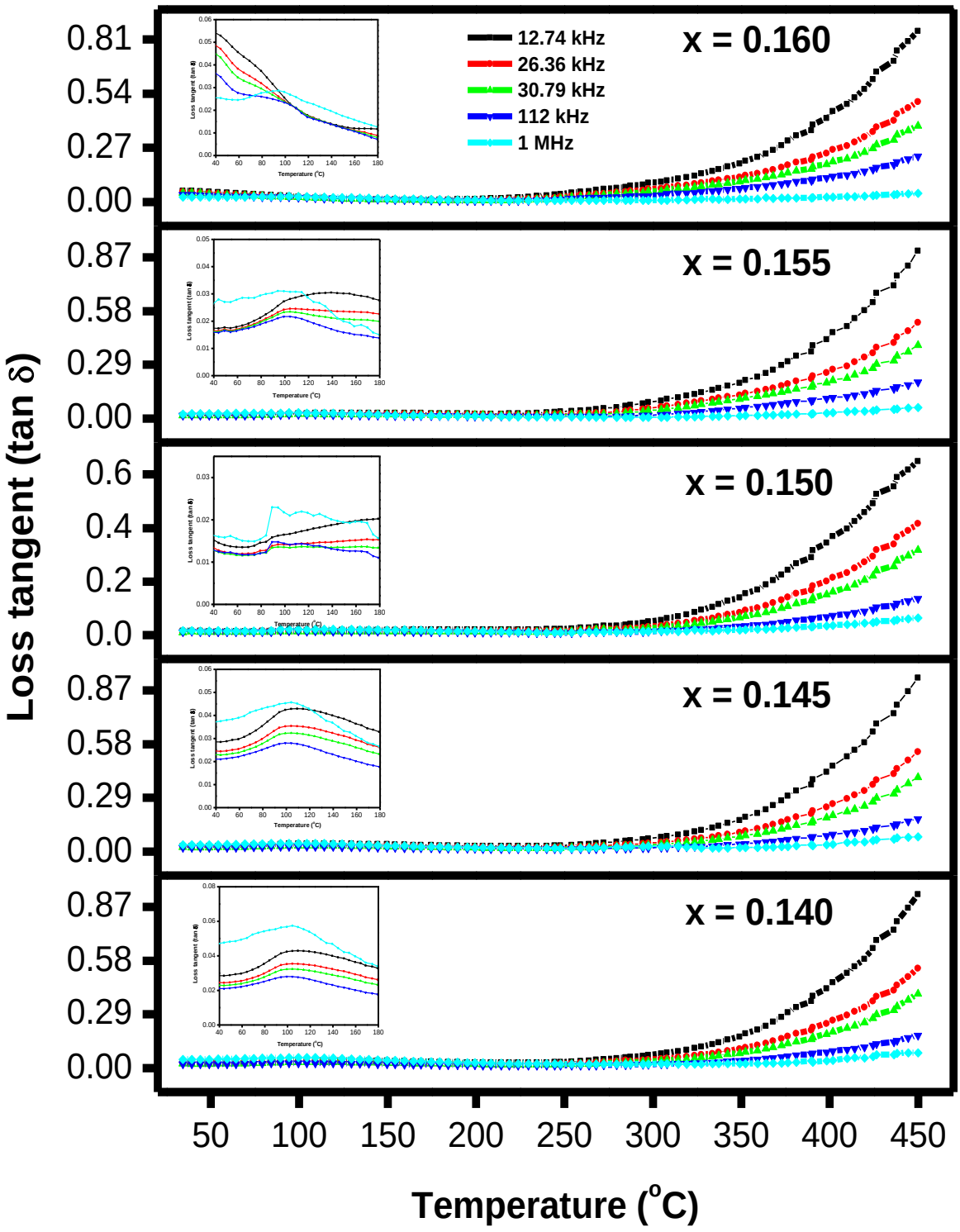

Fig. 3.2 Temperature variation of dielectric loss (tan δ), in $(Ba_{1-x}Ca_x)(Zr_{1-y}Ti_y)O_3$, (x = 0.140-0.160, y = 0.9), at different frequencies.

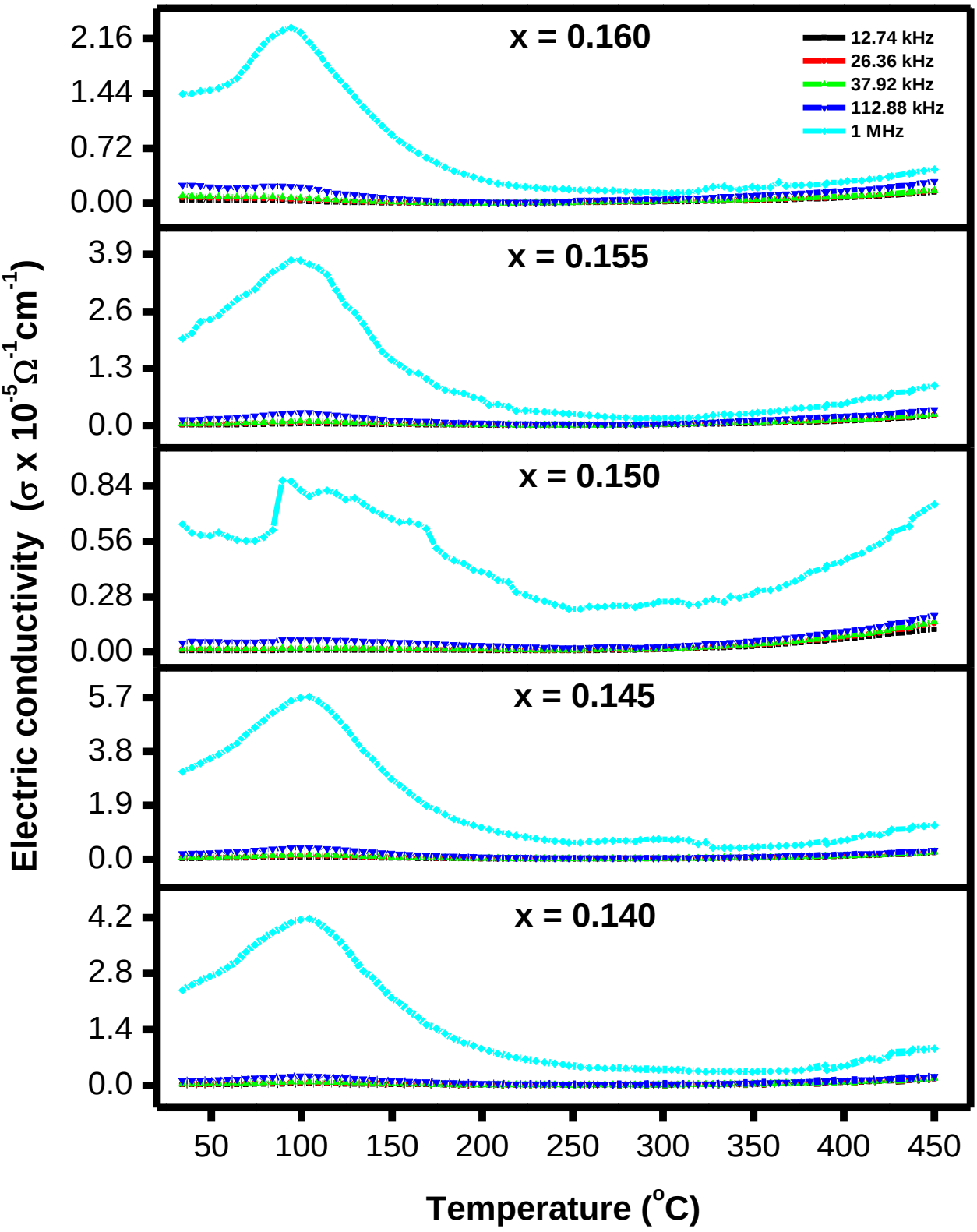

Fig. 3.3 Temperature variation of electric conductivity (σ), in $(Ba_{1-x}Ca_x)(Zr_{1-y}Ti_y)O_3$, (x = 0.140- 0.160, y = 0.9), at different frequencies.

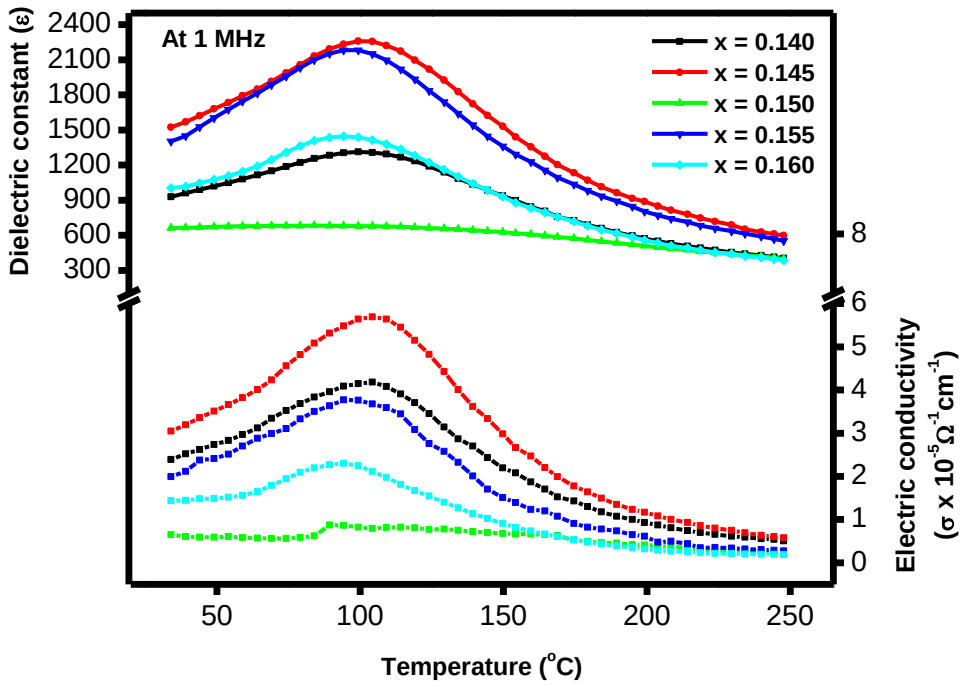

Fig. 3.4 Variation of dielectric constant (ε) and electric conductivity (σ) with temperature, in $(Ba_{1-x}Ca_x)(Zr_{1-y}Ti_y)O_3$, (x = 0.140- 0.160, y = 0.9), at 1 MHz**.**

3.4 X-Ray diffraction measurements

The dielectric measurements of the prepared BCZT compositions indicate the phase transition at around 100 ^oC. To study the structural variation with temperature, the high-temperature X-ray diffraction (HT-XRD) measurements were carried out on the samples with composition x = 0.150 and 0.155, in the temperature range from RT to 450 ^oC. These two compositions (x = 0.150 and 0.155) were selected as the representatives of the prepared compositions due to their similar observed dielectric anomaly, near T_c. The HT-XRD patterns obtained for $(Ba_{1-x}Ca_x)(Zr_{1-y}Ti_y)O_3$, x = 0.150 and 0.155, pellet samples have been shown in Figs. 3.5 and 3.6, respectively. The measured XRD peaks have been indexed with the help of the Inorganic Crystal Structure Database (ICSD). The HT-XRD of the ceramics indicates polycrystalline nature. The HT-XRD patterns measured near the transition temperatures were compared with the observed dielectric anomaly. The observed phase transition from the HT-XRD data and the dielectric anomaly were found to be consistent with each other. The lattice parameters of BCZT ceramics were refined using the Rietveld method. The space groups for these refinements were P4mm and Pm-3m, respectively [31-33,35].

From the observed XRD patterns of these compositions exhibit a tetragonal phase, between room temperature and about 100 ^oC, which is compatible with the ICSD - (code 01-083-1875) and

(code 01-079-2265) data [31,32]; and above about 100 ^{o}C, they exhibit cubic symmetry, consistent with ICSD- (01-074-1962) [33], ICSD - (01-075-0216) [34], and ICSD - (01-078-4475) data [35].

In the HT- XRD patterns of $(Ba_{1-x}Ca_x)(Zr_{1-y}Ti_y)O_3$, (x = 0.150), a continuous shifting of the most intense peaks (101), (111), (002), and (211), to the lower angle was observed with increasing temperature, in the measured temperature range, Fig. 3.5. A similar fashion was also observed for the composition x = 0.155, Fig. 3.6. The measured HT- XRD patterns exhibit a structural transition, from tetragonal (ferroelectric) to cubic (paraelectric) phase, at around 100 ^{o}C, which is consistent with the dielectric measurements. The peaks' profiles were refined using a pseudo-Voigt function, and the background was modeled using the Legendre polynomial. Furthermore, lattice parameters were refined by High Score Plus software using the Rietveld analysis [36]. Ba and Ca ions were located and shared at the same A-site (0,0,0), Ti and Zr ions were shared at B-site (½,½,½) and oxygen ions were located at the O-site (½,½,0), respectively [29]. Furthermore, the occupancies of Ba : Ca ions shared at the same location were fixed as 85 : 15 (for x = 0.150), and 845 : 155 (for x = 0.155), and for Ti : Zr ions 90 : 10, according to their molar ratios. The observed temperature variations in lattice parameters are shown in Figs. 3.7 and 3.8, for the compositions with x = 0.150 and 0.155, respectively.

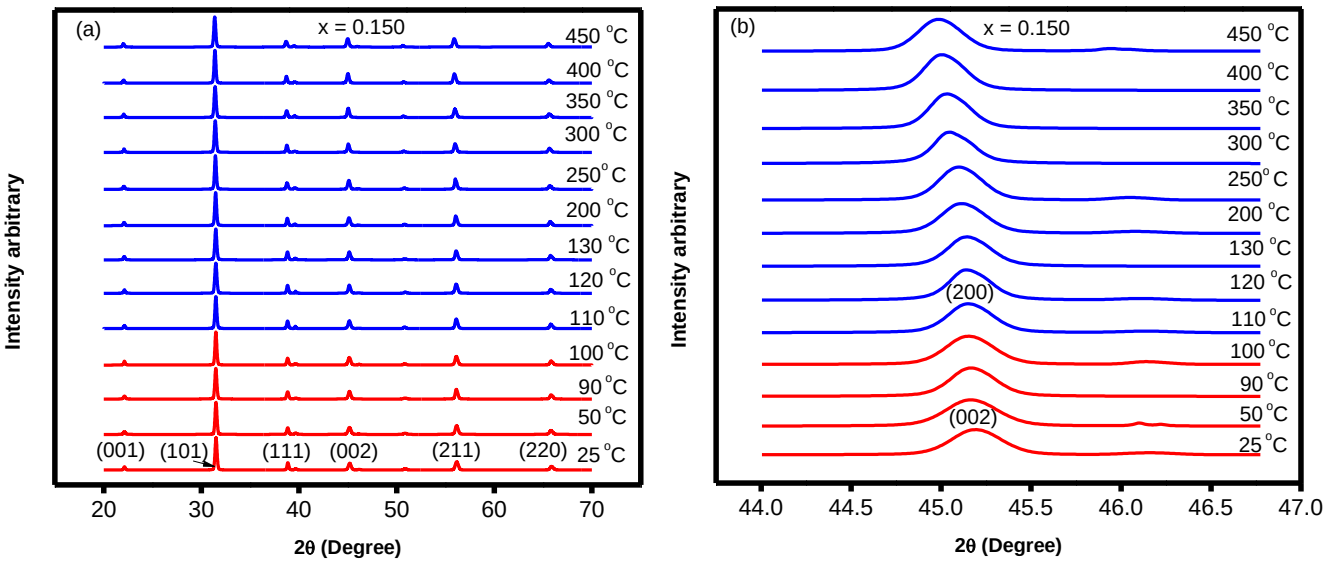

Fig. 3.5 (a) HT-XRD patterns of $(Ba_{0.85}Ca_{0.15})(Zr_{0.1}Ti_{0.9})O_3$ ceramics, (b) expanded angle view (44^{o}- 47^{o}).

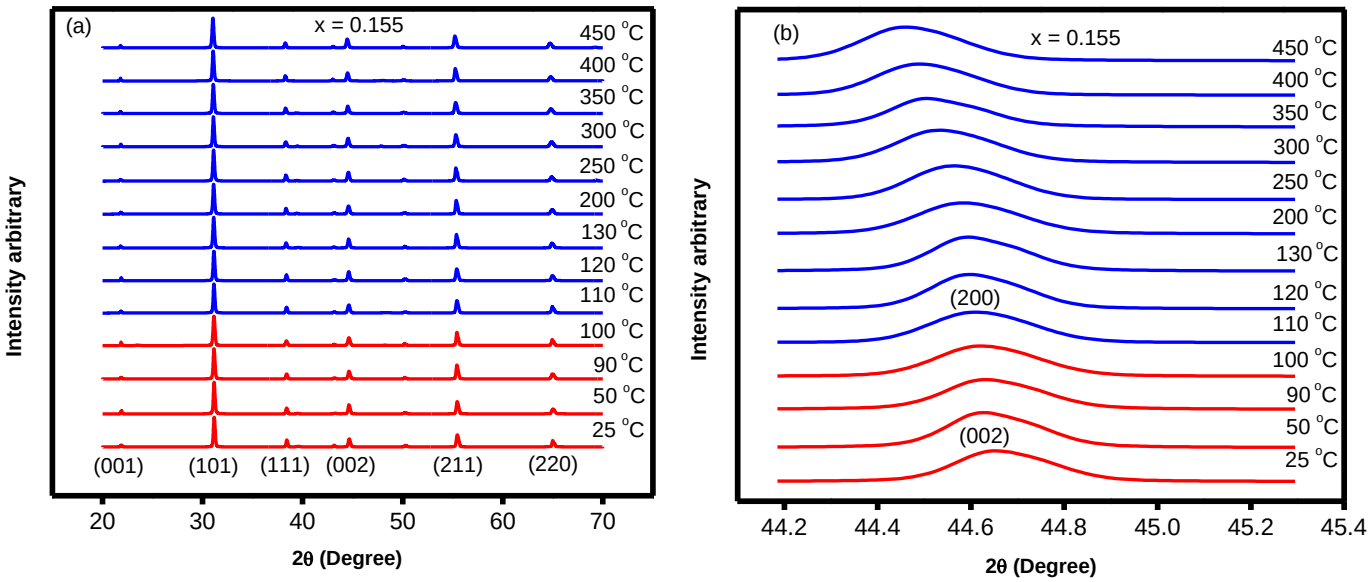

Fig. 3.6 (a) HT-XRD patterns of $(Ba_{0.845}Ca_{0.155})(Zr_{0.1}Ti_{0.9})O_3$ ceramics, (b) expanded angle view (44^o- 47^o).

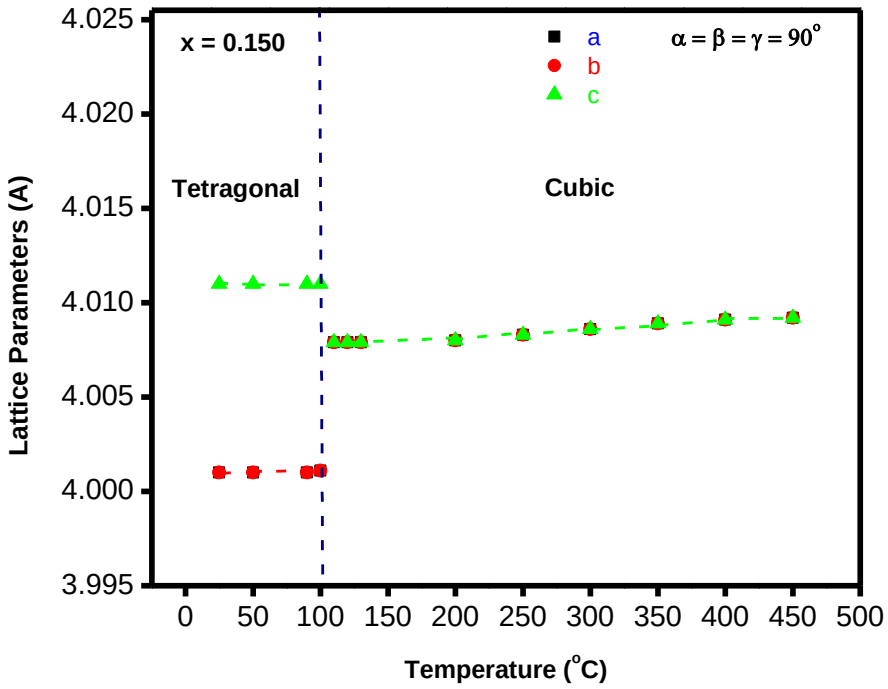

Fig. 3.7 Variation of lattice parameters with temperature, in $(Ba_{1-x}Ca_x)(Zr_{1-y}Ti_y)O_3$, (x = 0.150, y = 0.9).

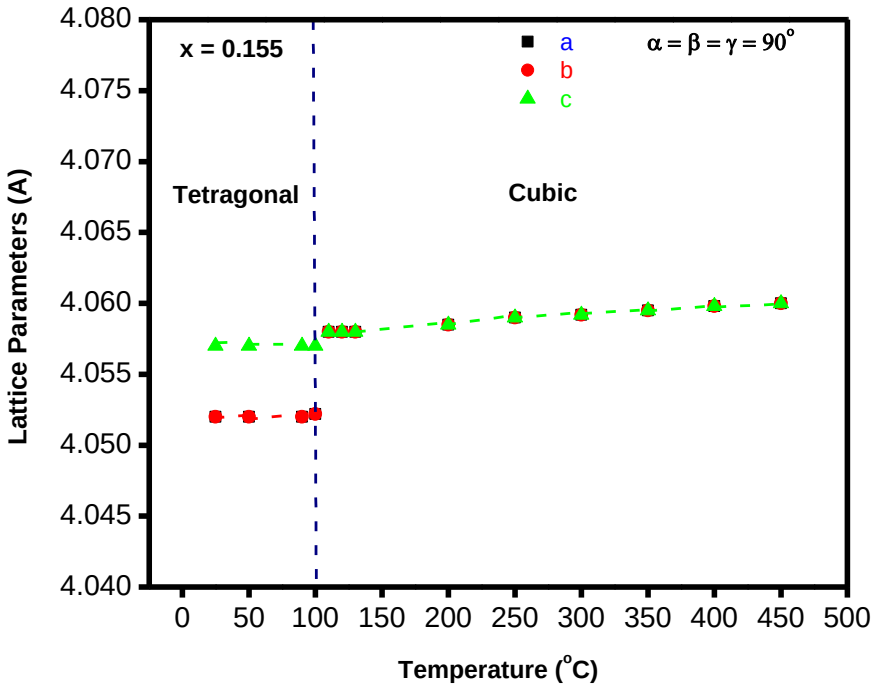

Fig. 3.8 Variation of lattice parameters with temperature, in $(Ba_{1-x}Ca_x)(Zr_{1-y}Ti_y)O_3$, (x = 0.155, y = 0.9).

3.5 Discussion

The dielectric properties and high-temperature X-ray diffraction (HT-XRD) of the $(Ba_{1-x}Ca_x)(Zr_{1-y}Ti_y)O_3$, (x = 0.140-0.160, y = 0.9) ceramics were measured. At all the measured frequencies, the observed electric conductivity and dielectric constant exhibit minimum values for the compositions with x = 0.150, among the prepared compositions. The HT-XRD of the BCZT ceramic samples with x = 0.150 and 0.155 were measured. The HT-XRD measurements show a distinct phase transition, from tetragonal to cubic phase, at around 100 ^oC, consistent with the dielectric measurements.

References

[1] T. Mitsui, W.B. Westphal, Dielectric and X-ray studies of $Ca_xBa_{1-x}TiO_3$ and $Ca_xSr_{1-x}TiO_3$, Physical Review. 124 (1961) 1354-1359. https://doi.org/10.1103/PhysRev.124.1354

[2] D. Fu, M. Itoh, S. Koshihara, T. Kosugi, S. Tsuneyuki, Anomalous phase diagram of ferroelectric (Ba,Ca)TiO_3 single crystals with giant electromechanical response, Physical Review Letters. 100 (2008) 227601. https://doi.org/10.1103/PhysRevLett.100.227601

[3] D. Fu, Y. Kamai, N. Sakamoto, N. Wakiya, H. Suzuki, M. Itoh, Phase diagram and piezoelectric response of $(Ba_{1-x}Ca_x)(Zr_{0.1}Ti_{0.9})O_3$ solid solution, Journal of Physics: Condensed Matter. 25 (2013) 425901. https://doi.org/10.1088/0953-8984/25/42/425901

[4] Y. Tian, L. Wei, X. Chao, Z. Liu, Z. Yang, Phase transition behavior and large piezoelectricity near the morphotropic phase boundary of lead-Free $(Ba_{0.85}Ca_{0.15})(Zr_{0.1}Ti_{0.9})O_3$ ceramics, Journal of the American Ceramic Society. 96 (2013) 496-502. https://doi.org/10.1111/jace.12049

[5] D. Biswas, N.S. Panwar, P. Sharma, Temperature dependent dielectric and structural properties of $(Ba_{1-x}Ca_x)(Zr_{0.1}Ti_{0.9})O_3$, $(0.140 \leq x \leq 0.160)$ ceramics, ECS Journal of Solid State Science and Technology. 11 (2022) 033002. https://doi.org/ 10.1149/2162-8777/ac62f3

[6] X. Wang, H. Yamada, C.N. Xu, Large electrostriction near the solubility limit in $BaTiO_3$-$CaTiO_3$ ceramics, Applied Physics Letters. 86 (2005) 022905. https://doi.org/10.1063/1.1850598

[7] R.C. Pullar, Y. Zhang, L. Chen, S. Yang, J.R.G. Evans, A.N. Salak, D.A. Kiselev, A.L. Kholkin, V.M. Ferreira, N.M. Alford, Dielectric measurements on a novel $Ba_{1-x}Ca_xTiO_3$ (BCT) bulk ceramic combinatorial library, Journal of Electroceramics. 22 (2009) 245-251. https://doi.org/10.1007/s10832-008-9430-5

[8] D. Hennings, A. Schnell, Diffuse ferroelectric phase transitions in $Ba(Ti_{1-y}Zr_y)O_3$ ceramics, Journal of the American Ceramic Society. 65 (1982) 539-544. https://doi.org/10.1111/j.1151-2916.1982.tb10778.x

[9] Z. Yu, C. Ang, R. Guo, A.S. Bhalla, Piezoelectric and strain properties of $Ba(Ti_{1-x}Zr_x)O_3$ ceramics, Journal of Applied Physics. 92 (2002) 1489. https://doi.org/10.1063/1.1487435

[10] X.G. Tang, K.H. Chew, H.L.W. Chan, Diffuse phase transition and dielectric tunability of Ba $(Zr_yTi_{1-y})O_3$ relaxor ferroelectric ceramics, Acta Materialia. 52 (2004) 5177-5183. https://doi.org/10.1016/j.actamat.2004.07.028

[11] A.V. Hippel, Ferroelectricity, domain structure, and phase transitions of barium titanate, Reviews of Modern Physics. 22 (1950) 221-237. https://doi.org/10.1103/RevModPhys.22.221

[12] D. Biswas, P. Sharma, N.S. Panwar, Composition dependent electrical properties of $(Ba_{1-x}Ca_xZr_{0.1}Ti_{0.9})O_3$ ceramics, near morphotropic phase boundary $(0.140 \leq x \leq 0.160)$, ECS Journal of Solid State Science and Technology. 10 (2021) 033002. https://doi.org/10.1149/2162-8777/abea61

[13] Y. Ishibashi, Theory of the morphotropic phase boundary, Ferroelectrics. 264 (2001) 197-206. https://doi.org/10.1080/00150190108008570

[14] W. Li, Z. Xu, R. Chu, P. Fu, G. Zang, Piezoelectric and dielectric properties of $(Ba_{1-x}Ca_x)(Ti_{0.95}Zr_{0.05})O_3$ lead-free ceramics, Journal of the American Ceramic Society. 93 (2010) 2942-2944. https://doi.org/10.1111/j.1551-2916.2010.03907.x

[15] W. Li, Z. Xu, R. Chu, P. Fu, G. Zang, High piezoelectric d_{33} coefficient in $(Ba_{1-x}Ca_x)(Ti_{0.98}Zr_{0.02})O_3$ lead-free ceramics with relative high curie temperature, Materials Letters. 64 (2010) 2325-2327. https://doi.org/10.1016/j.matlet.2010.07.042
[16] W.F. Liu, X.B. Ren, Large piezoelectric effect in Pb-free ceramics, Physical Review Letters. 103 (2009) 257602. https://doi.org/10.1103/PhysRevLett.103.257602
[17] G. Singh, V.S. Tiwari, P.K. Gupta, Evaluating the polymorphic phase transition in calcium-doped Ba $(Zr_{0.05}Ti_{0.95})O_3$: a lead-free piezoelectric ceramic, Journal of Applied Crystallography. 46 (2013) 324-331. https://doi.org/10.1107/S0021889813000666
[18] D. Biswas, N.S. Panwar, P. Sharma, Converse piezoelectric properties of lead free $Ba_{1-x}Ca_xZr_{0.1}Ti_{0.9}O_3$ (x = 0.055) ceramics using double sintered method, Ferroelectrics. 568 (2020) 95-103. https://doi.org/10.1080/00150193.2020.1811032
[19] A. Peláiz-Barranco, F. Calderón-Piñar, O. García-Zaldívar, Y. González-Abreu, Relaxor behaviour in ferroelectric ceramics, In: A. Peláiz-Barranco (ed) Advances in Ferroelectrics, Intech open publishing, London, 2012: pp. 85-107. https://doi.org/10.5772/52149
[20] J. Negi, N.S. Panwar, Structural and electrical properties of lead-free $Na_{0.685}K_{0.315}Nb_{1-y}Ta_yO_3$ ($0 \leq y \leq 0.05$) ceramics, Journal of Physics and Chemistry of Solids. 151 (2021) 109853. https://doi.org/10.1016/j.jpcs.2020.109853
[21] S. Somiya, Ceramics, In: R.A. Meyers (ed) Encyclopedia of physical science and technology, Academic press publishing, New York, 2003: pp. 569-619. https://doi.org/10.1016/B0-12-227410-5/00092-2
[22] S. Singh, J. Negi, N.S. Panwar, Dielectric properties of $Na_{1-x}K_xNbO_3$, near x = 0.5 morphotropic phase region, Journal of Physics and Chemistry of Solids. 123 (2018) 311-327. https://doi.org/10.1016/j.jpcs.2018.08.018
[23] A.S. Kandari, K. Kandari, V Lingwal, A.A. Bourai, N.S. Panwar, Composition dependent dielectric anomaly in $Na_{1-x}K_xNbO_3$, at x = 0.475, Ferroelectrics. 393 (2009) 121-129. https://doi.org/10.1080/00150190903413190
[24] V. Lingwal, B.S. Semwal, N.S. Panwar, Relaxational behavior of mixed $NaNbO_3$-$KNbO_3$ system, Ferroelectrics. 332 (2011) 219-225. https://doi.org/10.1080/00150190600732777
[25] S. Singh, J. Negi, N.S. Panwar, Temperature dependent dielectric properties of (Na, K)NbO_3, near equimolar composition, Ceramics International. 45 (2019) 13067-13071. https://doi.org/10.1016/j.ceramint.2019.03.238
[26] N.S. Panwar, T.C. Upadhyay, B.S. Semwal, Soft mode dynamics of perovskite type crystals, Pramana. 33 (1989) 603-614. https://doi.org/10.1007/BF02845811
[27] E. Pytte, Theory of perovskite ferroelectrics, Physical Review B. 5 (1972) 3758-3769. https://doi.org/10.1103/PhysRevB.5.3758
[28] X. Gonze, C. Lee, Dynamical matrices, born effective charges, dielectric permittivity tensors, and interatomic force constants from density-functional perturbation theory, Physical Review B. 55 (1997) 10355-10368. https://doi.org/10.1103/PhysRevB.55.10355
[29] K.N.D.K. Muhsen, R.A.M. Osman, M.S. Idris, Structure refinement and impedance analysis of $Ba_{0.85}Ca_{0.15}Zr_{0.10}Ti_{0.90}O_3$ ceramics sintered in air and nitrogen, Journal of Materials Science: Materials in Electronics. 30 (2019) 20673-20686. https://doi.org/10.1007/s10854-019-02433-3
[30] R.C. Buchanan, Ceramic Materials for Electronics: Processing, Properties, and Applications, 1st ed., Marcel Dekker Inc publishing, New York, 1986.

[31] R. Waesche, W. Denner, H. Schulz, Influence of high hydrostatic pressure on the crystal structure of barium titanate ($BaTiO_3$), Materials Research Bulletin. 16 (1981) 497-500. https://doi.org/10.1016/0025-5408(81)90113-6
[32] R.H. Buttner, E.N. Maslen, Structural parameters and electron difference density in $BaTiO_3$, Acta Crystallographica Section B. 48 (1992) 764-769. https://doi.org/10.1107/S010876819200510X
[33] S. Miyake, R. Ueda, On phase transformation of $BaTiO_3$, Journal of the Physical Society of Japan. 2 (1947) 93-97. https://doi.org/10.1143/JPSJ.2.93
[34] J.W. Edwards, R. Speiser, H.L. Johnston, Structure of barium titanate at elevated temperatures, Journal of the American Chemical Society. 73 (1951) 2934-2935. https://doi.org/10.1021/ja01150a149
[35] H.D. Megaw, Crystal structure of barium titanate, Nature. 155 (1945) 484. https://doi.org/10.1038/155484b0
[36] L.V. Azaroff, Elements of X- ray Crystallography, 1st ed., McGraw Hill publishing, New York, 1968.

CHAPTER-4

Piezoelectric properties of $(Ba_{1-x}Ca_x)(Zr_{0.1}Ti_{0.9})O_3$ ($0.140 \leq x \leq 0.160$), near morphotropic phase boundary

---

Brief summary

The composition-dependent piezoelectric properties were described in this chapter. Piezoelectric measurements of the prepared compositions were carried out at room temperature (RT). For the compositions with $x \leq 0.150$, the converse piezoelectric constant (d_{33}*), strain (%), coercive field (E_c) and remnant polarization (P_r) were found to increase with x, which were found anomalously to decrease with further increase in x above 0.150. Among the prepared compositions, the maximum value of d_{33}* was found 342 pm/V, for the samples with x = 0.150. The measured maximum values of strain (%), piezoelectric constant (d_{33}*) and break in XRD peak shifting patterns of the prepared samples indicate composition-dependent piezoelectric properties, showing morphotropic-like phase boundary (MPB), near x = 0.150 composition. The prepared compositions of lead-free BCZT ceramics will extend the possibilities to use this compound in the field of piezoelectric sensors.

CHAPTER-4

Piezoelectric properties of $(Ba_{1-x}Ca_x)(Zr_{0.1}Ti_{0.9})O_3$ $(0.140 \leq x \leq 0.160)$, near morphotropic phase boundary

4.1 Introduction

Certain solid materials generate electrical charges on their surfaces due to the applying mechanical stress (direct piezoelectric effect). The applied stress alters the polarization density within the volume of the material, resulting in the observed potential. The incident was first observed in quartz crystal by the Curie brothers in 1880. It was named the direct piezoelectric effect. Since this effect is reversible, the material will mechanically deform in response to the application of a voltage. It's known as the converse piezoelectric effect. Gabriel Lippmann investigated the converse piezoelectric effect in 1881. The converse effect is used for displacement and actuator devices, while the direct piezoelectric effect is used for force, pressure, acceleration and vibration transducers. The 32-point groups have 7 fundamental crystal structures, which are triclinic, monoclinic, rhombohedral (trigonal), hexagonal, orthorhombic, tetragonal, and cubic in order of increasing symmetry. There is a total of 32 point groups and out of which 21 classes are not centrosymmetric (for piezoelectric materials, it should be non-centrosymmetric); and in 20 of these classes [point group (432) is the only exception], relevant stresses result in the generation of positive and negative charges on the crystal surfaces. These substances are referred to as piezoelectrics. Despite not having a centre of symmetry, the point group (432) or the cubic group has no piezoelectric effect. The piezoelectric charges produced along its [111] axes cancel out each other. All ferroelectric materials are pyroelectric.

The piezoelectric phenomena have been used to design a piezoelectric sensor. The piezoelectric sensor can convert a pressure signal into an electrical signal or vice versa. One important member is the quartz crystal, among the piezoelectric family. A material is electrically neutral owing to equal positive and negative charges. However, when pressure is created on the material's surface, a voltage signal is found between the material's surfaces owing to separating the negative and positive charges, contributing to the net generated dipoles. The piezoelectric crystal is deformed, and potential is produced due to the displacement of the ions. The piezoelectric property essentially relies on the symmetry of the crystal structure. Under the

influence of an external mechanical force, electric polarization results from a sufficiently low degree of symmetry in a crystal.

Crystals cannot generate the piezoelectric effect with central symmetry from the 11-point group. All classes lacking a centre of symmetry, except for point group 432, are piezoelectric.

An external electric field and mechanical stress may polarize a class of materials known as piezoelectrics. The relationship between stress (X_{ik}) applied to a piezoelectric material, and the resulting charge density (D_i) is known as the direct piezoelectric phenomenon, and it can be written as

$$D_i = d_{ijk} X_{jk} \tag{4.1}$$

where d_{ijk} (CN^{-1}) is the piezoelectric coefficient. The piezoelectric materials have an additional attractive property. They can alter their dimensions in an electric field E. (a contraction or expansion). The converse piezoelectric phenomenon, which denotes the strain, occurs as a result of the external electric field in a piezoelectric material:

$$S_{ij} = d_{kij}E_k = d^*_{ijk}E_k \tag{4.2}$$

$$d^*_{ijk} = S_{ij} / E_k \tag{4.3}$$

where d^* ($m.V^{-1}$) is the converse piezoelectric coefficient. The direction of the mechanical and electric fields, determines the sign of the piezoelectric charge D_i and strain S_{ij}. Both positive and negative values of the piezoelectric coefficient (d*) are possible.

Ferroelectric materials exhibit hysteresis in the variation of polarization (P) with the applied electric field (E). Fig. 4.1 depicts an ideal ferroelectric P-E loop (hysteresis). Polarization has reached saturation with a gradually increasing applied electric field (P_s). P_s is the maximum polarization the specimen can achieve. Polarization decreases with decreasing electric field, and some polarization is still present at zero applied electric field, known as the remnant polarization (P_r).

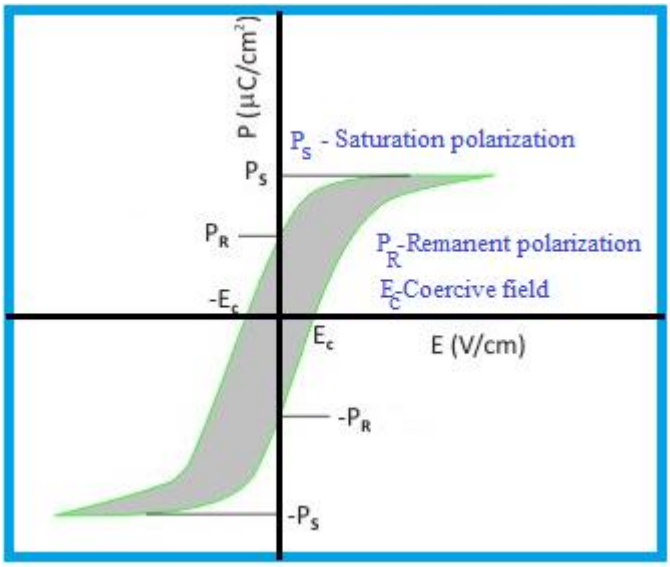

Fig. 4.1 A typical P-E loop (hysteresis).

Piezoelectric materials are employed in various fields, such as piezoelectric motors, power transformers, strain gauges, piezoelectric actuators, detection and generation of sonar waves, scanning force microscopes, loudspeakers, underwater microphones and speakers, inkjet printers and quartz clocks etc. Precise linear or rotational movements have been measured using piezoelectric materials to achieve micrometer precision in precision engineering applications. Gases can be ignited by piezoelectric material by producing a spark with the help of an electric current. The investigations in this field have a broad scope.

Piezoelectric ceramics have been widely used in many applications. A piezoelectric ceramic can generate a voltage from mV to V range, depending upon the material properties, on applying pressure. Further, using an operational amplifier, the voltage signal can be amplified and may be used to switch on a buzzer, LED on applying a load. The output voltage may be calibrated with other units like sound intensity, light intensity or weight, etc. Fig. 4.2 exhibits the block diagram of a piezoelectric sensor.

Load cell-type sensors may be prepared using piezoelectric ceramics. The prepared BCZT ceramics are piezoelectric as well as a good dielectric material. They can be configured in M-P-M (metal- piezo material- metal) structure. A load cell is a transducer that converts mechanical force, i.e., tensile and compressive force, into a measurable electrical unit. Piezoelectric-type load cell operates on the idea of accumulation of charges, which is a system's ability to hold a charge. When pressure or force is exerted on the prepared ceramic pellet sample, a difference in

charge is formed, which may lead to an output voltage. Therefore, the applied load (force) may be calibrated regarding voltage. Also, it can be used as a door knock sensor, etc.

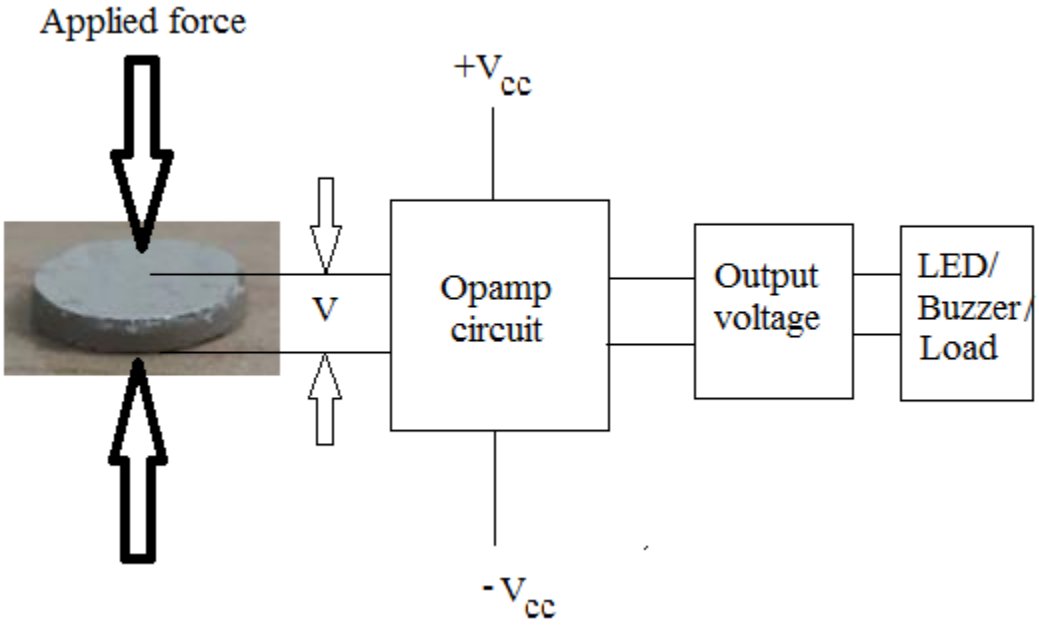

Fig. 4.2 Block diagram of piezoelectric sensor (load cell, door knock sensor etc.).

ABO_3 type barium-calcium zirconate-titanate (BCZT) ferroelectric ceramics are interesting due to their wide electrical properties and non-toxic nature [1-3]. Though the large piezoelectric constant lead- based perovskite ferroelectric compounds, e.g., lead zirconate titanate (PZT) and $Pb(B'B'')O_3$, (B' = Zn, Mg, In and Sc and B'' = Nb, Mo, Ta, and W), [4-5] are available, but due to their toxic nature, they are less preferred to utilize, and the search for high piezoelectric constant lead- free compounds has attracted the attention recently [1,6-10].

Significant piezoelectric constant has been found in $(Ba_{1-x}Ca_x)(Zr_{1-y}Ti_y)O_3$, (x, y = 0 to 1) ceramics, near the morphotropic phase boundary [11,12]. The structural and electrical properties of the BCZT system have been investigated by Hennings [13] and Yu et al. [14]. Tian et al. [15] studied the composition variation of piezoelectric and structural properties by varying the Ba/Ca ratio in $(Ba_{1-x}Ca_x)(Ti_{0.9}Zr_{0.1})O_3$, for the compositions with x = 0 to 0.20, and reported the existence of a typical MPB, near x = 0.150. The mechanism of the enhanced piezoelectricity around the MPB is of considerable significance. The polarization extension and rotation, presence of intermediate phases, and elastic softening of lattice contribute to large piezoelectricity in $(Ba_{1-x}Ca_x)(Ti_{0.9}Zr_{0.1})O_3$ ceramics, at morphotropic phase boundary [15]. As a

result, much time and energy has been spent researching the causes of the high level of piezoelectricity. The $(Ba_{1-x}Ca_x)(Ti_{0.9}Zr_{0.1})O_3$ ceramic systems receive significant attention because of the development of several possible polarization directions, at MPB, which may contribute to a large extremal remanent polarization and electromechanical coupling factor (k_s) [5]. Mondal et al. [16] observed enhanced electrical properties in BCZT ceramics due to the cell deformation near the MPB region. An anomalous break in the peak shifting pattern has been reportedly observed at MPB [17]. Hanani et al. [18] found technologically potential piezoelectric properties of $(Ba_{1-x}Ca_x)(Ti_{0.9}Zr_{0.1})O_3$ compositions, near x = 0.150. Wang et al. [19] observed significant piezoelectric properties of $(Ba_{1-x}Ca_x)(Ti_{0.9}Zr_{0.1})O_3$ lead-free ceramics with x = 0.150. Wu et al. [20,21] observed the effect of sintering dwell time on piezoelectric properties of $(Ba_{1-x}Ca_x)(Ti_{0.9}Zr_{0.1})O_3$ compounds, near x = 0.150, the morphotropic phase boundary. The enhanced electrical properties of the $(Ba_{1-x}Ca_x)(Ti_{0.9}Zr_{0.1})O_3$ compounds, near morphotropic phase boundary (MPB), may be attributed to the separation of two ferroelectric phases with different crystallographic parameters [22-24]. Therefore, ABO_3 type compounds are attracting considerable attention due to the significant hike in their piezoelectric properties near the MPB.

Presently, $(Ba_{1-x}Ca_xZr_{1-y}Ti_y)O_3$ (x = 0.140-0.160, y = 0.9), samples of BCZT ceramics have been prepared by solid-state reaction method following double sintering, at 1300 ^oC, for 4 hrs, each cycle. The structural behaviour and piezoelectric properties of the prepared $(Ba_{1-x}Ca_xZr_{1-y}Ti_y)O_3$ compositions were observed. The composition dependence of structure, converse piezoelectric constant (d_{33}*), strain (%), coercive field, polarization current, and remnant polarization of the BCZT samples were measured for the compositions near MPB, x = 0.150. The preparation methodology of the $(Ba_{1-x}Ca_x)(Zr_{1-y}Ti_y)O_3$ pellet samples, their X-ray diffraction (XRD) patterns, scanning electron micrograph (SEM) images, composition-dependent dielectric properties, density, etc. were described in Chapter-2. For piezoelectric measurements, the sintered pellet samples were electroded, with air-drying silver paste, in metal-insulator-metal (MIM) configuration. Further, to measure the prepared samples' polarization and piezoelectric constant (d_{33}*), a P-E loop tracer (aixACCT Systems GmbH, aixPES) with a piezometer was used.

4.2 Piezoelectric measurements

The polarization *vs* the electric field (P-E) hysteresis loops of the prepared BCZT samples were measured at room temperature, at 1 Hz frequency (triangular wave), with an applied peak electric field of 8.28 kV/cm (breakdown limit field). The observed P-E hysteresis loops for the prepared compositions have been shown in Fig. 4.3. The hysteresis loops show a good ferroelectric nature of the prepared ceramics. Fig. 4.4 shows the observed strain (%) *vs* electric field characteristics of the prepared BCZT samples. The observed butterfly loops show the soft domain reorientation characteristic of the prepared samples [28].

Generally, electroceramics have two main categories. They are called dielectric and conductive ceramics. Electroceramics may show mechanical strain upon applying an electric field and vice versa. The observed electric field-induced strain experiences two types of contribution. The intrinsic contributions are responsible for exhibiting electrostriction and piezoelectric effects, while the irrelevant contributions may show domain wall movement in materials having ferroelectric domain structures. The converse piezoelectric effect exhibits a mechanical strain upon applying an electric field. The converse effect consists of a linear dependence of the strain upon the applied electric field, which can be elongation or contraction depending on the relative direction of the applied electric field and the material's polarity [28]. The ferroelectric domain may change when an electric field is applied to the prepared ceramics. The domain walls simultaneously contribute to the changes in polarization and strain. The observed strain is firmly negative, exhibiting that the compositions experience elongation along the electric field direction. Furthermore, strain response, piezoelectric effect and electrostriction incorporate the contribution of domain wall movement, which contributes to a complex nonlinear and hysteretic nature, with a typical strain-electric field loop similar to a butterfly-like shape [28].

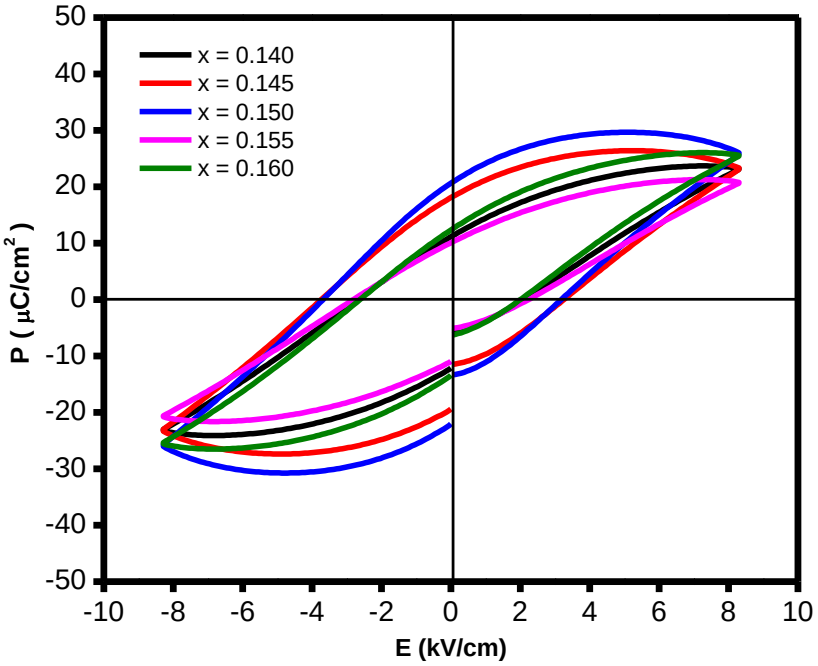

Fig. 4.3 Polarization *vs* electric field (P- E) hysteresis loops of $(Ba_{1-x}Ca_x)(Zr_{1-y}Ti_y)O_3$, (x = 0.140- 0.160, y = 0.9) ceramics.

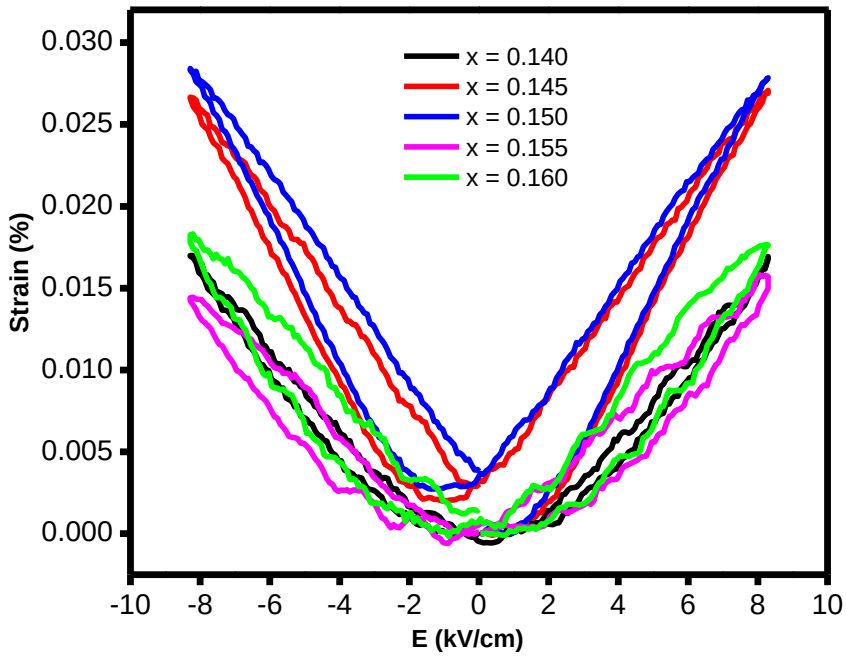

Fig. 4.4 Plot of strain (%) with electric field, in $(Ba_{1-x}Ca_x)(Zr_{1-y}Ti_y)O_3$, (x = 0.140- 0.160, y = 0.9) ceramics.

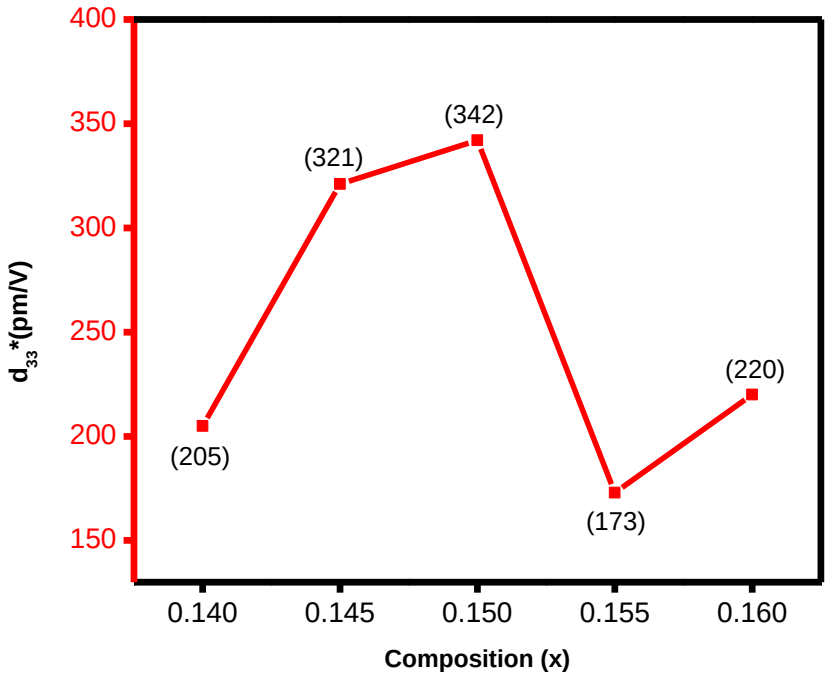

Fig. 4.5 Plot of converse piezoelectric constant (d_{33}^*) with sample (x), in $(Ba_{1-x}Ca_x)(Zr_{1-y}Ti_y)O_3$, (x = 0.140- 0.160, y = 0.9) ceramics.

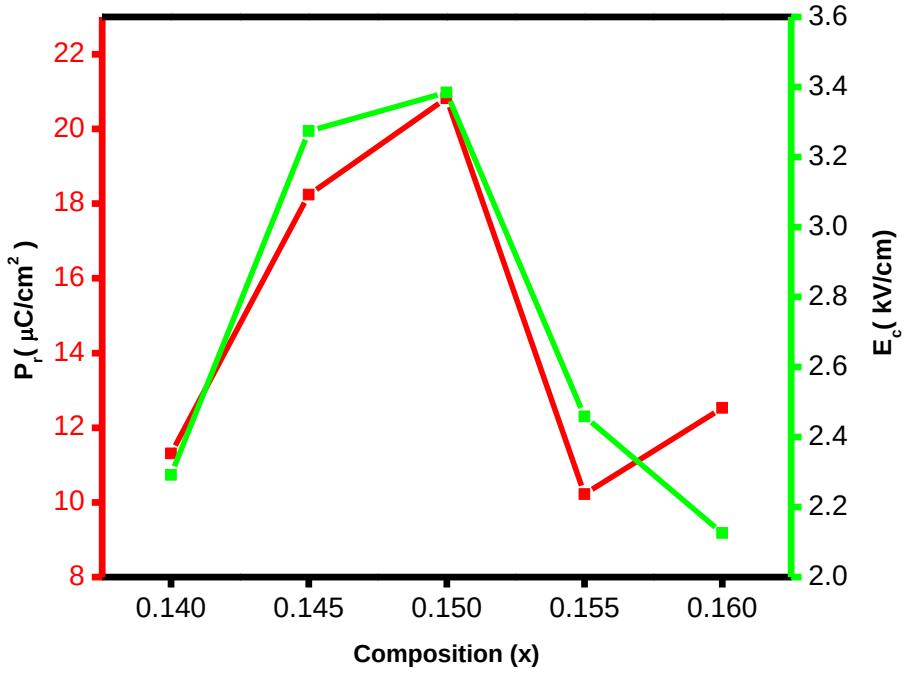

Fig. 4.6 Variations of coercive field (E_c) and remnant polarization (P_r) with sample (x), in $(Ba_{1-x}Ca_x)(Zr_{1-y}Ti_y)O_3$, (x = 0.140- 0.160, y = 0.9) ceramics.

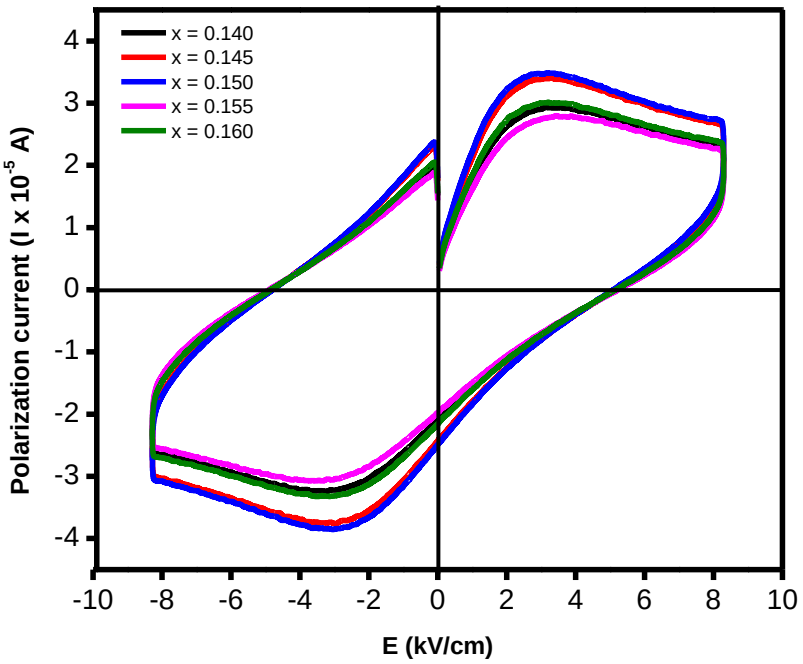

Fig. 4.7 Variations of polarization current with an electric field, in $(Ba_{1-x}Ca_x)(Zr_{1-y}Ti_y)O_3$, (x = 0.140- 0.160, y = 0.9) ceramics.

For the prepared compositions, the highest strain value (%) was observed for the composition with x = 0.150. The converse piezoelectric constant (d_{33}*) is obtained as the ratio of the strain (maximum) to the electric field (maximum), i.e., S_{max}/E_{max} [29], and was calculated from the butterfly characteristics of the BCZT ceramics. For the prepared compositions, a plot of the piezoelectric constant (d_{33}*) with composition (x), at RT, has been shown in Fig. 4.5. The value of (d_{33}*) was found maximum to be 342 pm/V, for the compositions with x = 0.150, among the prepared compositions. Singh et al. [30] observed similar piezoelectric characteristics for the pellet samples of (Na, K)NbO_3 ceramics near MPB. The observed distinct change in converse piezoelectric properties, at x = 0.150, may be attributed to the lattice change near the MPB.

For the prepared BCZT compositions, the observed variation of coercive field (E_c) and remnant polarization (P_r) with Ca content (x) have been shown in Fig. 4.6. In the prepared composition range, the maximum value of remnant polarization (P_r) was found 20.82 μC/cm^2; and maximum coercive field (E_c), 3.384 kV/cm, for the samples with x = 0.150. These observations may be attributed to the greater deformation in the lattice of the BCZT ceramics, near MPB, at x = 0.150 [15,31]. The variation of polarization current with the applied electric field is shown in Fig. 4.7.

The highest magnitude (3.48×10^{-5} A) was observed for the compositions with x = 0.150, among the prepared samples.

The internal stress, defects, and morphology of the ceramics considerably depend on the processing conditions [32], the purity, and the grain size of the starting materials [33]. The electrical properties considerably depend on the prepared samples' crystallographic information, grain size and density [34,35]. The low permittivity of the grain boundary contributes to low polarization in the ferroelectrics. Also, the available space charges at the grain boundary may help to exclude polarization charges on the grain surface, and may result in polarization discontinuity. Therefore, a depolarization field appears, and further, the polarization reduces, in the smaller grain ceramics. With increasing Ca component (x), the density of the BCZT ceramics was reportedly found to increase, reaching a maximum for x = 0.150, which decreases with a further increase in x. In contrast, the grain size had the opposite variation, i.e., it decreased with increasing x, reaching a minimum for x = 0.150, and increased with further increase in x [36]. The increase or decrease in the number of grain boundaries depends on the grain size of the ceramics, while larger grains result in less no. of grain boundaries and vice versa. The smaller grain size, for the compositions with x = 0.150, would have more grain boundaries, resulting in reduced polarization in the BCZT ceramics. But the observed remnant polarization (P_r) and coercive field (E_c) were found to be maximum for the sample with x = 0.150, which shows that these parameters are a composition-dependent property rather than the density or the grain size of the BCZT ceramics. A similar observation on the dielectric properties of BCZT ceramics has been reported in a previous communication [36].

4.3 Discussion

For the prepared BCZT ceramics, a continuous XRD peaks shifting pattern was observed with varying x, with a break for the samples with x = 0.150, indicating a strong composition-dependent structural anomaly. Among the prepared compositions, the piezoelectric constant (d_{33}*), strain (%), remnant polarization, polarization current and coercive field were observed maximum, for the sample with x = 0.150. The structural anomaly, and extremal values of converse piezoelectric constant (d_{33}*), strain (%), remnant polarization, and coercive field show a MPB-like composition, near x = 0.150, in the prepared BCZT ceramics.

References

[1] Y. Saito, H. Takao, T. Tani, T. Nonoyama, K. Takatori, T. Homma, T. Nagaya, M. Nakamura, Lead-free piezoceramics, Nature. 432 (2004) 84-87. https://doi.org/10.1038/nature03028

[2] M. Dawber, K.M. Rabe, J.F. Scott, Physics of thin-film ferroelectric oxides, Reviews of modern physics. 77 (2005) 1083-1130. https://doi.org/10.1103/RevModPhys.77.1083

[3] P. Kantha, K. Pengpat, P. Jarupoom, U. Intatha, G. Rujijanagul, T. Tunkasiri, Phase formation and electrical properties of BNLT-BZT lead-free piezoelectric ceramic system, Current Applied Physics. 9 (2009) 460-466. https://doi.org/10.1016/j.cap.2008.04.004

[4] X. Du, J. Zheng, U. Belegundu, K. Uchino, Crystal orientation dependence of piezoelectric properties of lead zirconate titanate near the morphotropic phase boundary, Applied Physics Letters. 72 (1998) 2421. https://doi.org/10.1063/1.121373

[5] S. Somiya, Ceramics, Encyclopedia of physical science and technology, 3rd ed., Academic press publishing, New York, 2003: pp. 569-619. https://doi.org/10.1016/B0-12-227410-5/00092-2.

[6] E. Cross, Materials Science: Lead-Free at Last, Nature. 432 (2004) 24-25. https://doi.org/10.1038/nature03142

[7] W.F. Liu, X.B. Ren, Large piezoelectric effect in Pb-free ceramics, Physical Review Letters. 103 (2009) 257602. https://doi.org/10.1103/PhysRevLett.103.257602

[8] H.X. Bao, C. Zhou, D.Z. Xue, J.H. Gao, X.B. Ren, A modified lead-free piezoelectric BZT-xBCT system with higher T_C, Journal of Physics D: Applied Physics. 43 (2010) 465401. https://doi.org/10.1088/0022-3727/43/46/465401

[9] J. Fu, R. Zuo, Z. Xu, High piezoelectric activity in (Na,K)NbO_3 based lead-free piezoelectric ceramics: Contribution of nanodomains, Applied Physics Letters. 99 (2011) 062901. https://doi.org/10.1063/1.3624704

[10] D. Xue, Y.M. Zhou, H.X. Bao, C. Zhou, J.H. Gao, X.B. Ren, Elastic, piezoelectric, and dielectric properties of $Ba(Zr_{0.2}Ti_{0.8})O_3$-$50(Ba_{0.7}Ca_{0.3})TiO_3$ Pb-free ceramic at the morphotropic phase boundary, Journal of Applied Physics. 109 (2011) 054110. https://doi.org/10.1063/1.3549173

[11] A.B. Swain, S.D. Kumar, V. Subramanian, P. Murugavel, Influence of external electric field on the physical characteristics of lead free BZT-BCT piezoceramic, Journal of Alloys and Compounds. 787 (2019) 990-995. https://doi.org/10.1016/j.jallcom.2019.02.197

[12] Y. Tian, Y. Gong, D. Meng, Y. Li, B. Kuang, Dielectric dispersion, diffuse phase transition, and electrical properties of BCT-BZT ceramics sintered at a low-temperature, Journal of Electronic Materials. 44 (2015) 2890-2897. https://doi.org/10.1007/s11664-015-3727-3

[13] D. Hennings, A. Schnell, Diffuse Ferroelectric Phase Transitions in $Ba(Ti_{1-y}Zr_y)O_3$ Ceramics, Journal of the American Ceramic Society. 65 (1982) 539-544. https://doi.org/10.1111/j.1151-2916.1982.tb10778.x

[14] Z. Yu, C. Ang, R. Guo, A.S. Bhalla, Piezoelectric and strain properties of $Ba(Ti_{1-x}Zr_x)O_3$ ceramics, Journal of Applied Physics. 92 (2002) 1489. https://doi.org/10.1063/1.1487435

[15] Y. Tian, L. Wei, X. Chao, Z. Liu, Z. Yang, Phase Transition Behavior and Large Piezoelectricity Near the Morphotropic Phase Boundary of Lead-Free $(Ba_{0.85}Ca_{0.15})(Zr_{0.1}Ti_{0.9})O_3$ Ceramics, Journal of the American Ceramic Society. 96 (2013) 496-502. https://doi.org/10.1111/jace.12049

[16] T. Mondal, S. Das, T. Badapanda, T.P. Sinha, P.M. Sarun, Effect of Ca^{2+} substitution on impedance and electrical conduction mechanism of $Ba_{1-x}Ca_xZr_{0.1}Ti_{0.9}O_3$ ($0.00 \leq x \leq 0.20$) ceramics, Physica B: Condensed Matter. 508 (2017) 124-135. https://doi.org/10.1016/j.physb.2016.12.021

[17] S. Singh, J. Negi, N.S. Panwar, Dielectric properties of $Na_{1-x}K_xNbO_3$, near x = 0.5 morphotropic phase region, Journal of Physics and Chemistry of Solids, 123 (2018) 311-317. https://doi.org/10.1016/j.jpcs.2018.08.018

[18] Z. Hanani, D. Mezzane, M. Amjoud, S. Fourcade, A.G. Razumnaya, I.A. Luk'yanchuk, M. Gouné, Enhancement of dielectric properties of lead-free BCZT ferroelectric ceramics by grain size engineering, Superlattices and Microstructures, 127 (2019) 109-117. https://doi.org/10.1016/j.spmi.2018.03.004

[19] P. Wang, Y. Li, Y. Lu, Enhanced piezoelectric properties of $(Ba_{0.85}Ca_{0.15})(Zr_{0.1}Ti_{0.9})O_3$ lead-free ceramics by optimizing calcination and sintering temperature, Journal of the European Ceramic Society. 31 (2011) 2005-2012. https://doi.org/10.1016/j.jeurceramsoc.2011.04.023

[20] J. Wu, D. Xiao, B. Wu, W. Wu, J. Zhu, Z. Yang, J. Wang, Sintering temperature-induced electrical properties of $(Ba_{0.90}Ca_{0.10})(Ti_{0.85}Zr_{0.15})O_3$ lead-free ceramics, Materials Research Bulletin. 47 (2012) 1281. https://doi.org/10.1016/j.materresbull.2012.01.032

[21] J. Wu, D. Xiao, W. Wu, J. Zhu, J. Wang, Effect of dwell time during sintering on piezoelectric properties of $(Ba_{0.85}Ca_{0.15})(Zr_{0.1}Ti_{0.9})O_3$ lead-free ceramics, Journal of Alloys and Compounds. 509 (2011) L359-L361. https://doi.org/10.1016/j.jallcom.2011.08.024

[22] W. Li, Z. Xu, R. Chu, P. Fu, G. Zang, Piezoelectric and Dielectric Properties of $(Ba_{1-x}Ca_x)(Ti_{0.95}Zr_{0.05})O_3$ Lead-Free Ceramics, Journal of the American Ceramic Society. 93 (2010) 2942-2944. https://doi.org/10.1111/j.1551-2916.2010.03907.x

[23] W. Li, Z. Xu, R. Chu, P. Fu, G. Zang, High piezoelectric d_{33} coefficient in $(Ba_{1-x}Ca_x)(Ti_{0.98}Zr_{0.02})O_3$ lead-free ceramics with relative high Curie temperature, Materials Letters. 64 (2010) 2325-2327. https://doi.org/10.1016/j.matlet.2010.07.042

[24] S.W. Zhang, H.L. Zhang, B.P. Zhang, S. Yang, Phase-transition behavior and piezoelectric properties of lead-free $(Ba_{0.95}Ca_{0.05})(Ti_{1-x}Zr_x)O_3$ ceramics, Journal of alloys and compounds. 506 (2010) 131-135. https://doi.org/10.1016/j.jallcom.2010.06.157

[25] D. Biswas, P. Sharma, N.S. Panwar, Structural and electrical properties of lead free $Na_{1-x}K_xNbO_3$ ($0.160 \leq x \leq 0.200$) ceramics, Ceramics International. 47 (2021) 13814-13819. https://doi.org/10.1016/j.ceramint.2021.01.246

[26] S. Sen, R. Choudhay, Effect of doping Ca ions on structural and electrical properties of $Ba(Zr_{0.05}Ti_{0.95})O_3$ electroceramics, Journal of Materials Science: Materials in Electronics. 15 (2004) 671-675. https://doi.org/10.1023/B:JMSE.0000038922.74021.d6

[27] J. Negi, N.S. Panwar, Structural and electrical properties of lead-free $Na_{0.685}K_{0.315}Nb_{1-y}Ta_yO_3$ ($0 \leq y \leq 0.05$) ceramics, Journal of Physics and Chemistry of Solids. 151 (2021) 109853. https://doi.org/10.1016/j.jpcs.2020.109853

[28] G. Viola, T. Saunders, X. Wei, K.B. Chong, H. Luo, M.J. Reece, H. Yan, Contribution of piezoelectric effect, electrostriction and ferroelectric/ferroelastic switching to strain-electric field response of dielectrics, Journal of Advanced Dielectrics. 3 (2013) 1350007. https://doi.org/10.1142/S2010135X13500070

[29] A. Jalalian, A.M. Grishin, X.L. Wang, Z.X. Cheng, S.X. Dou, Large piezoelectric coefficient and ferroelectric nanodomain switching in $Ba(Ti_{0.80}Zr_{0.20})O_3$-$0.5(Ba_{0.70}Ca_{0.30})TiO_3$ nanofibers and thin films, Applied Physics Letters. 104 (2014) 103112. https://doi.org/10.1063/1.4867013

[30] S. Singh, N.S. Panwar, Piezoelectric properties of $Na_{1-x}K_xNbO_3$, near x = 0.500 morphotropic phase region, Ferroelectrics. 558 (2020) 240-245. https://doi.org/10.1080/00150193.2020.1735907

[31] G. Xu, J. Wen, C. Stock, P.M. Gehring, Phase instability induced by polar nanoregions in a relaxor ferroelectric system, Nature Materials. 7 (2008) 562-566. https://doi.org/10.1038/nmat2196

[32] S. Mitra, A.R. Kulkarni, O. Prakash, Diffuse phase transition and electrical properties of lead-free piezoelectric $(Li_xNa_{1-x})NbO_3$ $(0.04 \leq x \leq 0.20)$ ceramics near morphotropic phase boundary, Journal of Applied Physics. 114 (2013) 064106. https://doi.org/10.1063/1.4817815

[33] H.S. Nalwa, Handbook of nanostructured materials and nanotechnology, 1st ed., Academic Press publishing, New York, 1999.

[34] V.R. Mudinepalli, L. Feng, W.C. Lin, B.S. Murty, Effect of grain size on dielectric and ferroelectric properties of nanostructured $Ba_{0.8}Sr_{0.2}TiO_3$ ceramics, Journal of Advanced Ceramics. 4 (2015) 46-53. https://doi.org/10.1007/s40145-015-0130-8

[35] Z.Y. Shen, J.F. Li, Enhancement of piezoelectric constant d_{33} in $BaTiO_3$ ceramics due to nano-domain structure, Journal of the Ceramic Society of Japan. 118 (2010) 940-943. https://doi.org/10.2109/jcersj2.118.940

[36] D. Biswas, P. Sharma, N.S. Panwar, Composition dependent electrical properties of $(Ba_{1-x}Ca_xZr_{0.1}Ti_{0.9})O_3$ ceramics, near morphotropic phase boundary $(0.140 \leq x \leq 0.160)$, ECS Journal of Solid State Science and Technology. 10 (2021) 033002. https://doi.org/10.1149/2162-8777/abea61

CHAPTER-5

Optical properties of $(Ba_{1-x}Ca_x)(Zr_{1-y}Ti_y)O_3$, (x = 0.155, y = 0.9), thin films

---

Brief summary

The optical properties of the prepared thin films have been described in this chapter. Thin films were deposited, on quartz and p-Si (100) substrates, by radio frequency (RF) sputtering of ceramic barium calcium zirconate titanate $[(Ba_{1-x}Ca_x)(Zr_{0.1}Ti_{0.9})O_3]$, (x = 0.155), target. The as-deposited films were annealed for one hour at different temperatures, between 500 and 800 ^oC. The occurrence of film crystallization was observed on annealing at and above 600 ^oC. However, films peeled out on annealing at 800 ^oC. The structure and optical transmittance of the prepared films (hereafter referred to as $BCZT_{0.9}$ films), annealed at different temperatures, were measured. Refractive index and optical bandgap were obtained from the measured optical transmittance of the films deposited on quartz substrates and annealed at different temperatures. The optical bandgap of the $BCZT_{0.9}$ films was found to reduce from 4.24 to 3.87 eV with the increase in annealing temperature.

CHAPTER-5

Optical properties of $(Ba_{1-x}Ca_x)(Zr_{1-y}Ti_y)O_3$, (x = 0.155, y = 0.9), thin films

5.1 Introduction

The study of thin films deals with systems whose dimensions are very small. The distinct and unique characteristics of a thin film are not conferred simply by its thinness but rather by the microstructure resulting from the unique arrangement of the atoms by gradually adding the basic building blocks one by one. The study of bulk form analyses of the physical properties of three-dimensional forms. These characteristics are generally considered independent of volume, even though many characteristic qualities are associated with unit volume. This idea is reasonable because the sizes are roughly within macroscopic bounds, still, once one dimension is so tiny, it is no longer valid that the surface-to-volume ratio noticeably increases. In a bulk material, the particles are influenced by forces from all directions. However, these forces are reduced when merely surface area is considered. Because of their obvious symmetry, the force exerted on the particles at the surface varies from those of the bulk. Thus, one speaks of the existence of surface states because energy levels at the surface may differ significantly from the internal axis.

When a substance's thin film is considered, a situation arises where the two surfaces are so near one another that it may significantly affect the substance's internal physical characteristics and mechanisms. As a result, their internal physical properties and processes diverge significantly from those of bulk material. The surfaces' proximity and interaction with one another can give rise to whole new phenomena. Additionally, reducing a material's one dimension to an order of only a few atomic layers produces a structure that is halfway between macro- and molecular-scale systems, offering a way to investigate the microphysical underpinnings of many processes.

It is impossible to precisely answer what limits a film should be considered 'thin'. It is feasible to state that the thickness beneath which the described anomalies arise determines the limit; however, this varies for various physical processes. The technology and physics of thin films deal with films that range in thickness from tenths of a nanometer to several micrometers. Thin film materials' surface-to-volume ratio, thickness, microchemistry, and microstructure impact their physical characteristics, and the growth process strongly influences these factors.

Optical phenomena are specialized ones related to thin films. Recently, the vast demand and wide tailor-made applications extraordinarily promoted studies on thin films' electrical properties and electron emission. The optical characteristics deal with the properties of materials when exposed to electromagnetic radiation and, more specifically, to visible light. Thin films were initially used for their optical characteristics. Metal films have good reflecting properties. They are utilized in different components of high-precision optical equipment. Coated lenses are used in optical imaging devices, like microscopes, binoculars, cameras, telescopes, etc. Selective absorbers, optical filters, and dielectric mirrors all utilize coatings similar coatings [1].

Apart from the standard optical components, optical films have a variety of new emerging applications, like solar cell coatings [2], energy storage applications [3], end mirrors for lasers [4] etc. In contrast, a predetermined wavelength dependence of transmittance or reflectance can be achieved by combining several films with different thicknesses and refractive indices. Almost all applications for optical films are found in the region of the electromagnetic spectrum from the ultraviolet range to the infrared range and far beyond.

The several dielectric materials incorporated in optical coatings include fluorides [5] (e.g., MgF_2, CeF_3), oxides [6] (e.g., Al_2O_3, TiO_2, SiO_2, Ta_2O_5), sulfides [5] (e.g., CdS, ZnS), assorted materials [7] (e.g., ZnTe, ZnSe), etc. A fundamental property of optical thin film is their minimum absorption coefficient [8] ($\alpha < 10^3$ cm^{-1}), which makes them virtually transparent in some important wavelength regions of the spectrum (higher wavelength region).

One of the important optical characteristics in constructing optical coatings is the refractive index (n_o). A phase shift is created between the incident and forward-scattered beams due to the refracted beam moving in various mediums at numerous speeds. The difference in velocities of the incident and refracted beams can be used to interpret this phase shift. It is anticipated that the value of n_o may be affected owing to the change in the strength of the refracted beam. The density of electrons may also affect the value of n_o. For numerous optical applications, ferroelectric materials [9,10], such as $LiNbO_3$, $KNbO_3$, $Ba(ZrTi)O_3$, $PbTiO_3$ and their family, are widely used. Various optical applications such as optical waveguide devices [11,12], frequency doublers for diode lasers [13-17], infrared detectors [18,19], spatial light modulators [20], optical memories [21,22] and displays, etc., will require suitable optical materials. Nonmetallic materials can be transparent or opaque to visible light, often appearing coloured when transparent to visible light. The three main ways that a set of materials can absorb light are, in theory,

electronic polarization, electronic transitions across the band gap, and electronic excitations to impurity or defect levels, which also impact the materials' transmission characteristics. Electronic polarization's absorption becomes significant at light frequencies close to the constituent atoms' relaxation frequency. The final two processes involve electron transitions, which are dependent on the materials' electronic energy band structures; one of these absorption processes includes the absorption as a consequence of electron excitations across the band-gap; the other is associated with electron excitations to impurity or defect levels that are located within the band gap.

Absorption of a photon can introduce or excite an electron, across the band gap, from the adjacently filled valence band to an empty state within the conduction band, generating a free electron in the conduction band and a hole in the valence band. The excitation energy (E_g) is related to the absorbed photon frequency (ν), i.e., $E_g = h\nu$. These excitations with the accompanying absorption may only occur if the photon energy is larger than the band gap, E_g, i.e. if $h\nu > E_g$, or $hc/\lambda > E_g$.

Electromagnetic radiations are categorized as microwaves, infrared light, ultraviolet light, x-rays, visible light and gamma rays. The optical property of a material is defined as the response due to the introduction of electromagnetic radiation. It is conveniently studied by using visible radiation. The optical phenomenon relies on the frequency of the light incident on the materials. The band gap energy falls under ultraviolet radiation for numerous materials, so the solid does not absorb visible light. For example, materials with excitation energy $E_g = 3.1$ eV and $\lambda = 400$ nm show minimum wavelength in the visible range. Therefore, the nonmetallic materials having band gap energy greater than 3.1 eV exhibit colourless and transparent characteristics.

An extremely efficient way to ascertain the inter-band structure of the materials is through optical measurements. Between various bands, photon-induced inter-band electronic transitions may take place. Lattice vibrations can also be studied using optical properties. Mainly, measuring the absorption coefficient for different energies gives information about the band gaps of the materials [23]. Thin films' optical and electrical characteristics are significant due to their technological applications in sensors. Studying the band gap of the optical thin films is also essential for various applications.

Recently, there has been a marked rise in the interest in large dielectric constant (K) materials for memory components. To scale down the size of the memory devices, silicon oxynitride

(SiN_xO_y), the most common semiconductor memory dielectric, due to its high leakage current [24] and small relative permittivity [25,26], has to be replaced by high dielectric constant and low leakage current material. Many binary oxides with relatively higher dielectric constant, e.g., tantalum pentoxide (Ta_2O_5) [27-31], titanium oxide (TiO_2), zirconium oxide (ZrO_2) [32-34], and their solid solutions, etc., have been found compatible with the current fabrication procedures, and are therefore attracting significant attention in miniaturization of silicon memory devices. Numerous oxides with high dielectric constant have been proposed to improve performance and reduce the size of memory devices [35-38]. The high dielectric constant perovskite solutions, such as strontium zirconate titanate ($Sr(Zr,Ti)O_3$), barium zirconate titanate ($Ba(Zr,Ti)O_3$), calcium zirconate titanate ($Ca(Zr,Ti)O_3$), and their solid solutions, e.g., $(Ba,Ca)(Zr,Ti)O_3$, etc. [39-41] have tremendous potential in memory devices. However, they must be tested to be non-toxic and compatible with current fabrication procedures in the microelectronic industry. These lead-free perovskite solid solutions have attracted researchers due to their large dielectric- and piezo-constant, etc., in general, and exceptionally extreme properties at certain compositions near the morphotropic phase boundary (MPB) [42-49]. Near the MPB, a composition-dependent transition and irregular variation in lattice parameters cause the extremal physical properties [42-49]. A MPB has been reportedly observed, at composition $(Ba_{1-x}Ca_x)(Zr_{0.1}Ti_{0.9})O_3$, in the barium calcium zirconate titanate ($(Ba,Ca)(Zr,Ti)O_3$) system (BCZT system) [42]. With varying x, different $(Ba_{1-x}Ca_x)(Zr_{0.1}Ti_{0.9})O_3$ compositions may be prepared, which may exhibit many possibilities to substitute the lead-based ceramics in several ferroelectric and dielectric devices [50-54].

Thin films of BCZT system offer various potential uses, including integrated circuits and piezoelectric micro- system devices, etc. [55]. Ferroelectric thin films are mostly coated using physical techniques, such as radio frequency sputtering, pulsed laser deposition, etc. [56,57], and chemical solution deposition techniques, for example, the sol-gel method, etc. [58]. Ferroelectric thin films may have highly compact surfaces and exhibit significant dielectric and piezoelectric properties. Luo et al. [55] investigated the dielectric characteristics of BCZT thin films produced using the radio frequency sputtering. Lin et al. [51] and Bhardwaj et al. [52] studied the dielectric constant of BCZT thin films produced by the sol-gel and pulsed laser deposition methods. Annealing treatment remarkably influences the films' electrical characteristics, crystallographic phase, and microchemistry [59-61]. The leakage current characteristics of BCZT thin films have

been reported to improve with a rise in annealing temperature [55]. The stoichiometry and microstructure considerably affect the electrical properties of BCZT films. Hence the optimized annealing may improve the dielectric and leakage current characteristics of thin film composition.

Previously, the maximum dielectric constant of bulk $(Ba_{1-x}Ca_x)(Zr_{0.1}Ti_{0.9})O_3$ pellets was observed for x = 0.155, among the prepared compositions near MPB [42]. In the present study, ceramic pellet target of $(Ba_{1-x}Ca_x)(Zr_{0.1}Ti_{0.9})O_3$, (x = 0.155), was prepared by solid- state reaction process through double sintering. Thin films were deposited by radio-frequency (RF) sputtering of the prepared ceramic target, using argon as sputtering gas (hereafter referred to as $BCZT_{0.9}$ films). To investigate the optical and electrical properties, thin films were deposited, onto both sides polished quartz (refractive index, 1.51, and transmittance in the visible region = 92 %), and silicon [p- Si (100)] substrates, respectively. All films were deposited at ambient temperature and then annealed in ambient air, each at 500, 600, 650, 700, 750 and 800 ^oC, for 1 hr. The effect of annealing on the measured structural, optical and electrical properties of the prepared $BCZT_{0.9}$ thin films has been presented in this paper.

5.2 Preparation

A target (ceramic pellet) of BCZT $(Ba_{0.845}Ca_{0.155})(Zr_{0.1}Ti_{0.9})O_3$ was prepared by solid-state reaction process followed by double sintering. The preparation method of the target was similar to that used to prepare pellet samples for bulk measurements, which is discussed in Chapter-2. High purity (> 99.5%) powders of Ba_2CO_3, Ca_2CO_3, ZrO_2 and TiO_2, were taken for the current study. The materials were dried separately to remove the absorbed moisture, at 200 °C for 2 hrs. The composition was made by weighing the materials in an accurate stoichiometric ratio. The mixture was well mixed, wet and dry ground, and calcined as described in Chapter-2. The calcined powder was pressed into a target (~ 4 mm thickness and 2-inch diameter) with a longitudinal pressure of 0.5 GPa. The composition was sintered at 1300 ^oC, for 4 hrs. The sintered target was crushed and ground further into powder. This ground powder was pressed into a target (pellet) at 0.5 GPa. According to Chapter-2, maximum density was observed for BCZT ceramics at 1300 ^oC, which is also lower than their corresponding melting point. So, the sintering temperature of $(Ba_{0.845}Ca_{0.155})(Zr_{0.1}Ti_{0.9})O_3$ composition was chosen at 1300 ^oC, according to its optimized density and melting point [42], and the target was sintered for 4 hrs.

This sintered target was crushed further, fine ground and pressed into ~ 4 mm thickness and 2-inch diameter target at 0.5 GPa, and further sintered at the chosen temperature 1300 ^{o}C, for 4 hours [42]. $BCZT_{0.9}$ thin films were deposited by magnetron RF sputtering of the prepared target. The quartz substrates (15 mm × 10 mm × 0.5 mm) were shake cleaned using an ultrasonic cleaner, for 4-5 minutes in the laboratory detergent mixed with de-ionized water, then rinsed with de-ionized water and lastly wiped with soft dry cloth with a little trace of acetone. When exposed to air, within seconds, oxide layer forms on the surface of the silicon substrate. To remove the formed oxide layer, silicon substrates were shaken well in dilute hydrogen fluoride (HF), 3-4 drops in 250 ml de-ionized water, for 4-5 minutes, using ultrasonic cleaner, which were further rinsed with de-ionized water and finally wiped by clean and dry trace paper, and were instantly placed within the chamber, which was immediately evacuated. The vacuum pumping unit combined with a 300 litre/sec diffusion pump with a 200 liter/ min rotary vacuum pump was used to achieve an ultimate vacuum of 1×10^{-5} mbar. The Pirani-penning gauge combination was used to monitor the vacuum. The vacuum chamber, open at both ends, from Hind High Vacuum Co. (P) Ltd. Bangalore (India), was formed with a 300 mm diameter stainless steel cylinder. The target was fastened with a water-cooled magnetron assembly and was arranged to facilitate the sputtering in sputter-down mode. The target- substrate distance was kept 30 mm. Argon (Sigma Aldrich, 99.99% purity), the sputtering gas, pressure in the chamber was controlled using a needle valve. The radio frequency power used for depositing the $BCZT_{0.9}$ films was kept at 60 W. The as-deposited film samples were taken out of the vacuum chamber and were annealed, each at 500, 600, 650, 700, 750 and 800 ^{o}C, for 1 h, in air. Films annealed at 800 ^{o}C were found to peel out of the substrates, and were not suitable for any further measurements.

X-ray diffraction (XRD) measurements were taken with the help of an X-ray diffractometer (PANalytical, X'PERT PRO) to find the structural data of the prepared thin films. Elemental identification and quantification in the deposited film samples and the ceramic target were done using a scanning electron microscope (Carl Zeiss, EVO 18 Special Ed.) integrated with energy dispersive spectrometer (Oxford instruments). Transmittance of the films, deposited onto quartz substrates, was measured in the wavelength range, from 900 to 200 nm, with a 1 nm step, using a UV-Vis-NIR spectrophotometer (Agilent, Cary 5000).

5.3 Characterization

5.3.1 X- ray diffraction patterns

The structural characteristics of thin films, prepared on the silicon substrates were measured with X-ray diffraction (XRD) at room temperature (RT). The XRD patterns of the prepared films were measured by a X-ray diffractometer (PANalytical, X'PERT PRO), having $CuK_{\alpha 1}$ radiation of wavelength 1.5406 Å. The XRD data was measured at a scanning rate of 1.8º/minute, in a wide range of 2θ ($20° \leq 2\theta \leq 65°$). Peak indexing was done using the Inorganic Crystal Structure Database (ICSD). The structural properties of $BCZT_{0.9}$ oxide films depend on their growth and post-annealing process [62]. Generally, oxide films deposited at room temperature have an amorphous character, while higher annealing temperatures are required for crystallization [23,62-66]. The measured XRD patterns of the $BCZT_{0.9}$ films are shown in Fig. 5.1. The films deposited at RT and annealed at 500 ºC show amorphous structure. Films annealed at 600 and 650 ºC show crystal structure with a single (020) orientation, and films annealed at 700 and 750 ºC exhibit multi-orientation crystallization with orthorhombic structure and are consistent with the ICSD-(00-056-1033). The height of the XRD peaks increases with increasing annealing temperature, up to 750 ºC, indicating increased crystallite size and improved oxygen stoichiometry, with increasing annealing temperature [67].

From the measured XRD data, stress (S) in the prepared films was calculated using the relation [68,69], $S = Y(b-b_o)/2\nu b_o$, where Y is Young's modulus (59.2 GPa), ν, the Poisson ratio (0.3), b_o the lattice constant (5.6522 nm) [68,70] of bulk $BCZT_{0.9}$, and b is the observed lattice constant of the prepared $BCZT_{0.9}$ film. From the XRD data, Fig. 5.1, the lattice constant b is measured 5.6643, 5.6647, 5.6649 and 5.6717 nm for films annealed at 600, 650, 700 and 750 ºC, respectively. The changing lattice constant may be related to the change in stress on annealing. Variation of the calculated stress with annealing temperature is shown in Fig. 5.2. In the prepared $BCZT_{0.9}$ films, the drastically increasing stress with rising annealing temperature might have resulted in the peeling out and failure of the films on annealing at 800 ºC.

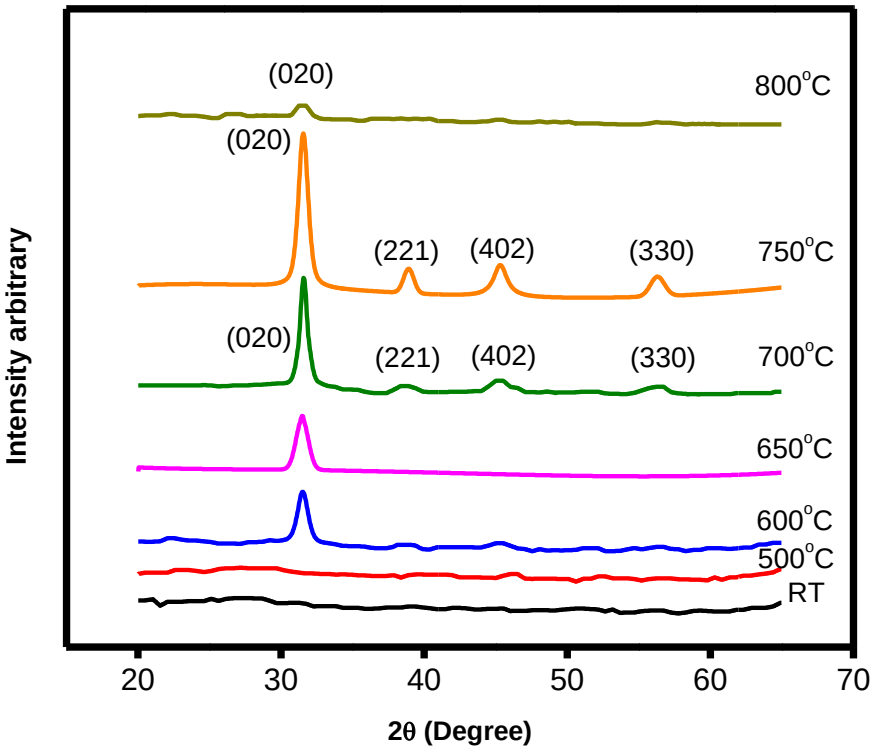

Fig. 5.1 XRD patterns of $BCZT_{0.9}$ thin films.

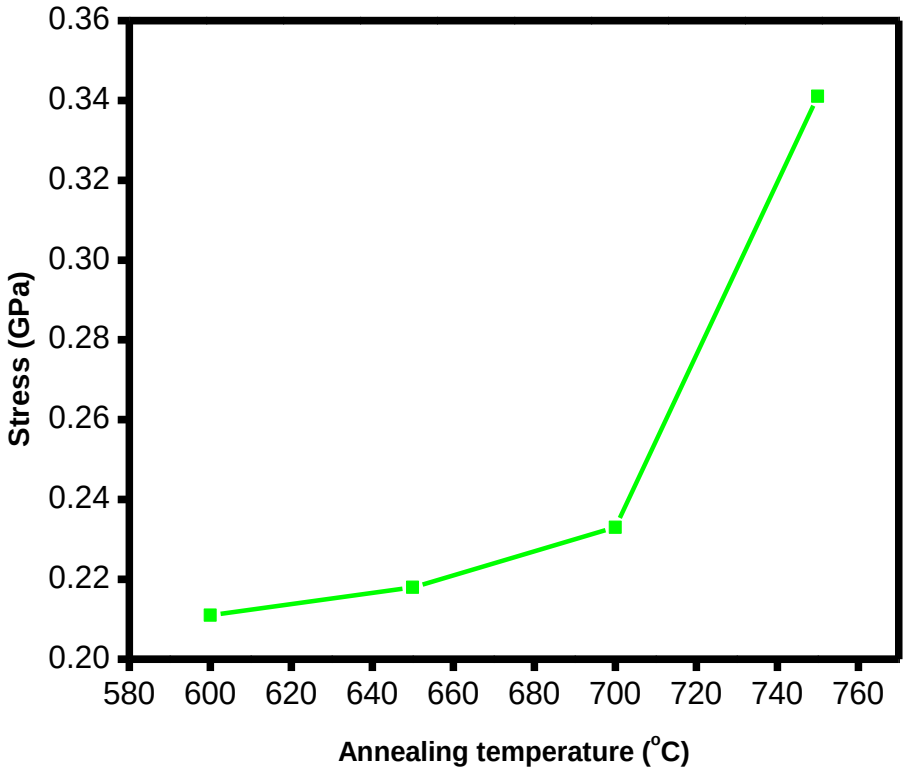

Fig. 5.2 Stress variation with annealing temperature in $BCZT_{0.9}$ films, annealed at 600, 650, 700 and 750 °C.

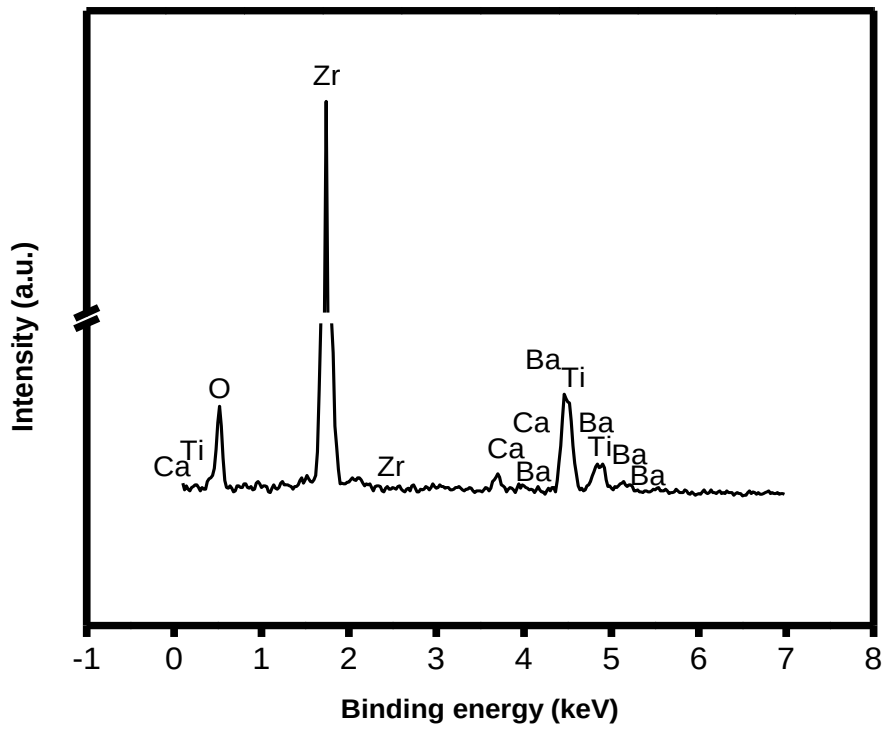

Fig. 5.3 EDS spectrum of $BCZT_{0.9}$ thin films.

5.3.2 Energy dispersive spectroscopy (EDS) results

Fig. 5.3 exhibits the featured distinctive Ba, Ca, Ti, Zr, and O peaks in the energy dispersive spectrum of $BCZT_{0.9}$ films deposited at room temperature (RT). The EDS measurements showed consistency of the elemental composition in the bombarded target and the deposited films.

5.3.3 Optical measurements

The optical transmission of the $BCZT_{0.9}$ films, deposited on quartz substrates, was measured in the wavelength range 900-200 nm. Fig. 5.4 exhibits the measured transmission spectra of the prepared films, deposited at RT and annealed at 500, 600, 650, 700, and 750 ^{o}C. For the films deposited at RT and annealed at 500 and 600 ^{o}C, high transmittance (~79-80%), near the transmittance of blank quartz (i.e., 92%), was found above 400 nm, in the measured wavelength range. It was found that the transmittance of the amorphous films increased with annealing temperature (up to 600 ^{o}C), which may be a result of improved film quality with better oxygen stoichiometry on annealing [36]. However, the observed improvement in the transmittance of amorphous films was smaller with rising annealing, up to 600 ^{o}C. The transmittance was measured to decrease (~73-87%) with further increase in annealing temperature (between 650 and 750 ^{o}C), which may be associated with the multi-orientation of the crystallites on annealing

(XRD data, Fig. 5.1), which may cause in the scattering of incident photons and hence reduced transmittance [36].

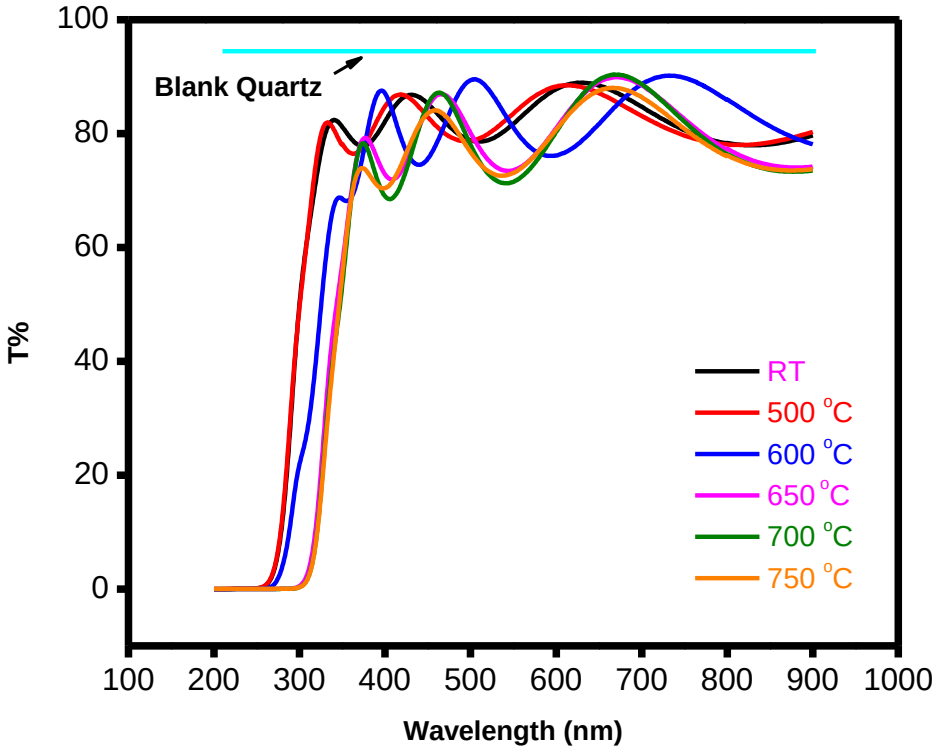

Fig. 5.4 Wavelength variation of optical transmittance (T%) of $BCZT_{0.9}$ films deposited on the quartz substrate.

The optical transmittance plots were used to compute the thickness (d) and refractive index (n_o), and other optical parameters of the prepared $BCZT_{0.9}$ films, deposited on a quartz substrate (transmittance = 92%, n_o = 1.51), applying Swanepoel's envelope method [23]. Fringes were observed in the transmittance plot. In the optical transmission the fringes appear due to the interference phenomenon arising from the reflections at the film, and film-substrate interface, as in the Fabry Perot interferometer [23]. The occurrence of the fringes observed at different wavelengths in different samples depends on their slightly different thickness.

5.3.4 Refractive index

According to Swanpole's envelope method, the refractive index (n_o) at the wavelength λ, is shown by

$$n(\lambda) = \left(N + \left(N^2 - n_s^2 \right)^{1/2} \right)^{1/2}; \qquad (5.1)$$

where n_s is the refractive index of the substrate, at wavelength λ; and

$$N = \frac{2\,n_s\left[T_M(\lambda) - T_m(\lambda)\right]}{T_M(\lambda)\,T_m(\lambda)} + \frac{n_s^2 + 1}{2}; \qquad (5.2)$$

where $T_M(\lambda)$ and $T_m(\lambda)$ are the transmission maxima and minima, respectively, corresponding to wavelength λ obtained from the envelope, for example, as shown in Fig. 5.5.

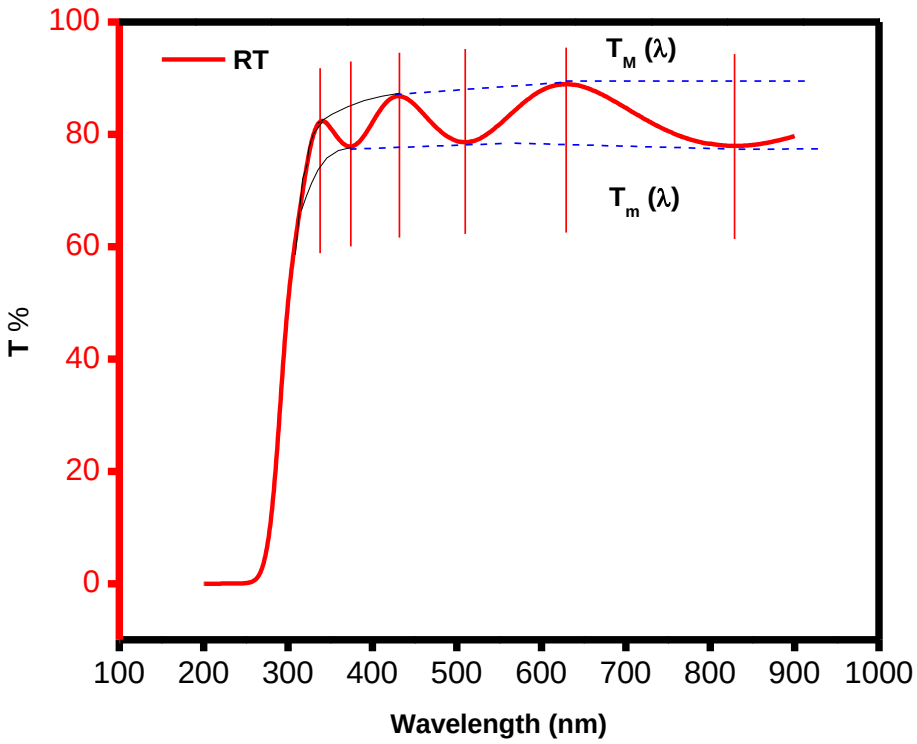

Fig. 5.5 Envelope of the transmission spectra of the $BCZT_{0.9}$ film deposited at RT.

The reported value of the refractive index for $BaTiO_3$ thin film was 2.05 [71], and for $BaCaTiZrO_3$ thin film, 2.32 [72]; at 632.8 nm.

5.3.5 Film thickness

The thickness (d) of the film is shown by [23],

$$d = \frac{\lambda_1\,\lambda_2}{2\left(n_1\lambda_2 - n_2\lambda_1\right)}, \qquad (5.3)$$

where λ_1 and λ_2 are the wavelengths of two successive maxima and minima; n_1 and n_2 are the refractive indices, at λ_1 and λ_2, respectively.

Thickness (d) of the RT deposited $BCZT_{0.9}$ films and the films annealed at 500-750 ^oC, were calculated 330 ± 10 nm. The refractive index was generally noticed to reduce as the wavelength increased, which is consistent with the reported results for other oxides [72,73]. On the increase in annealing temperature, the value of n of the prepared films increased from 1.896 to 2.090, at 633 nm wavelength, Fig. 5.6. A significant difference in the refractive indices of amorphous and crystalline films was observed, Fig. 5.6. The magnitudes of n of the crystalline films were higher than that of the amorphous films, which may be due to the increased density of the former on annealing [74]. The processing conditions, presence of voids, defects, film-substrate interaction and crystal structure of the prepared film may influence the measured variations in n_o [74,75].

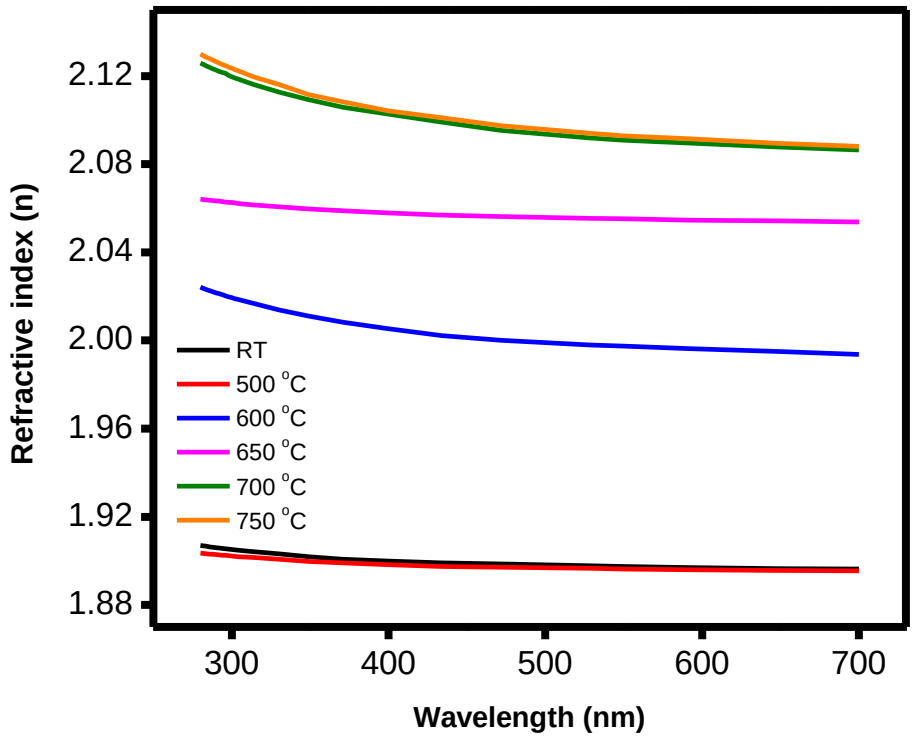

Fig. 5.6 Wavelength dependence of refractive index, in $BCZT_{0.9}$ films, for as-deposited and the films annealed at different temperatures.

5.3.6 Absorption and extinction coefficient

The amount of energy a material can absorb is determined by its absorption coefficient. The absorption coefficient (α) of the material film is shown by [76,77],

$$\alpha = -\log(x)/d, \tag{5.4}$$

where, $$x = \frac{E_m - \left[E_m^2 - (n^2-1)^3 (n^2 - n_s^4)\right]^{1/2}}{(n-1)^3 (n - n_s^2)}, \tag{5.5}$$

with $$E_m = \frac{8\, n^2\, n_s}{T_M} + (n^2 - 1)(n^2 - n_s^2), \tag{5.6}$$

n and n_s are the refractive indices of the film and substrate, respectively; d is the film thickness, and T_m is the maximum transmission of the film.

For the prepared $BCZT_{0.9}$ films (room temperature deposited films and the films annealed at various temperatures), the measured α was observed decreasing with increasing wavelength in ambient atmosphere, Fig. 5.7. The calculated value of α has been obtained to be 1.670, 1.665, 1.908, 2.153, 2.386 and 2.389 cm^{-1} for the samples deposited at RT, annealed at 500, 600, 650, 700 and 750 ^oC, respectively, at 400 nm wavelength. Fringes were observed in the transmittance plot. In the optical transmission, the fringes appear due to the interference phenomenon arising from the reflections at the film, and film-substrate interface, as in the Fabry Perot interferometer [23]. The occurrence of the fringes observed at different wavelengths in different samples depends on their slightly different thickness. The interference fringes vanish in the strong absorption region, so the values of n in the strong absorption region were extrapolated from those calculated in the other spectral regions [23].

The extinction coefficient (k) is defined as the reduction of the intensity of radiation as a result of absorption or scattering by matter, and at the wavelength λ, is given by [23],

$$k = \alpha\lambda/4\pi. \tag{5.7}$$

With rising annealing temperature, the k was observed to increase from 0.044 to 0.049 at 633 nm, Fig. 5.8. The values of k did not change significantly after annealing (up to 750 ^oC). The higher annealing temperature may cause more absorption due to atom reorientation and more oxygen loss in the crystal area [78], which could make crystalline films' extinction coefficient greater than amorphous films'.

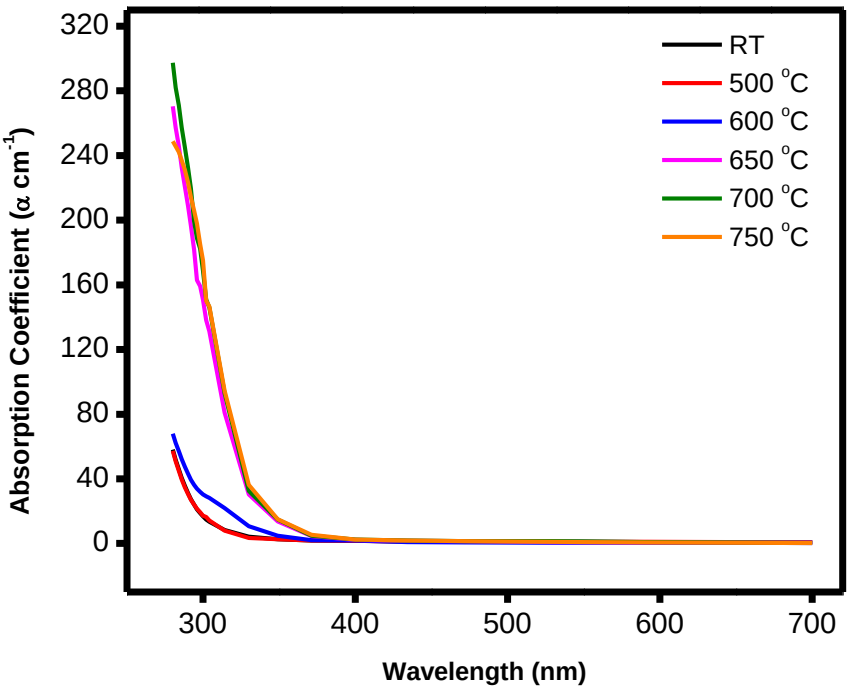

Fig. 5.7 Wavelength dependence of absorption coefficient (α in the unit of 10^3) of $BCZT_{0.9}$ films, annealed at different temperatures.

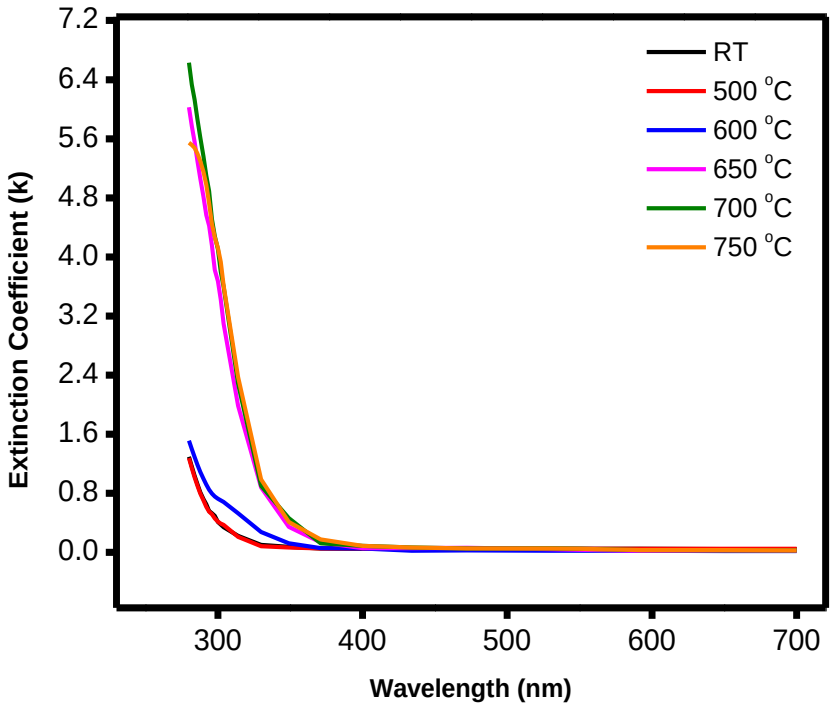

Fig. 5.8 Variation of extinction coefficient with wavelength of the $BCZT_{0.9}$ films prepared at different conditions.

5.3.7 Optical band gap and inter band transitions

The optical transmission plots of the prepared thin films show a sharp absorption edge with the appearance of the ultraviolet (UV) region, which is about to end in the visible region of the spectrum at short wavelengths. The films deposited at RT and annealed at 500, 600, 650, 700 and 750 ^{o}C show the sharp absorption edge or critical wavelength (λ_c) at 272, 271, 278, 273 and 281 nm, respectively. The valence band is the top nearly filled band, and the conduction band is the lowest nearly empty band. The band gap is the distance between them, which represent the electronic transitions from the valence band to the conduction band. At higher wavelengths, the large optical transmission is constrained by absorption owing to the vibration of lattice ions in resonance with the incident radiation. The frequency of maximum absorption is correlated to the mass of vibrating cations and anions and the force constant. The incident photon energy can be used to explain the absorption coefficient, hν and fulfills Eq. (5.8) [78],

$$\alpha(h\nu) = A\,(h\nu - E_g)^m, \qquad (5.8)$$

where m and A are constants. The value of constant m decides the nature of transition in the thin film samples. The observations may be analyzed according to Eq. (5.8).

The value of E_g has been calculated both at and outside the absorption edge. The relationship between the absorption coefficient variation and incident photon energy was plotted to evaluate the energy gap. The band gap of the dielectric films relies on their composition, stoichiometry, presence of defects, voids etc. [78-80].

The atoms are temporarily displaced from their mean positions in the lattice by absorbing some external energy at all temperatures above absolute zero. This result in the vibration of atoms about their mean locations in the solid, and these vibrations have quantized energy values. These quantized lattice vibrations are called phonons. A solid with absorbed radiation may undergo elastic vibrations that start photon-electron, photon-phonon, and other interactions.

The direct transition probability may be observed due to photon-electron interaction in the films and calculated using Eq. (5.8), with m = ½. Figs. 5.9(a), 5.10(a), 5.11(a), 5.12(a), 5.13(a) and 5.14(a) show $(\alpha)^2$ *vs* hν plots, for the RT deposited films and the films annealed at 500, 600, 650, 700 and 750 ^{o}C, respectively. Extrapolation of the straight portion of the curve, $(\alpha)^2$ *vs* hν, gives the directly allowed energy band gap (E_g) of the $BCZT_{0.9}$ films. The value of the directly permitted energy band gap was estimated from the intersection of the tangent, drawn near the

absorption edge, in the $(\alpha)^2$ *vs* hν curve (the straight line section), with the energy axis. Values of the directly allowed energy band gap were obtained as 4.18 eV for the $BCZT_{0.9}$ films deposited at RT and 4.17, 4.13, 4.00, 3.93 and 3.87 eV for the films annealed at 500, 600, 650, 700 and 750 ^oC, respectively. The structural change in the lattice may be used to explain how post-annealing affects the film band gap. On crystallization the band gap decreases drastically on the rise in annealing temperature. The structural change in the lattice, phase separation [81], enhanced crystallographic orientation [82], and the increased density with increasing annealing temperature can be attributed to the measured change in band gap on annealing.

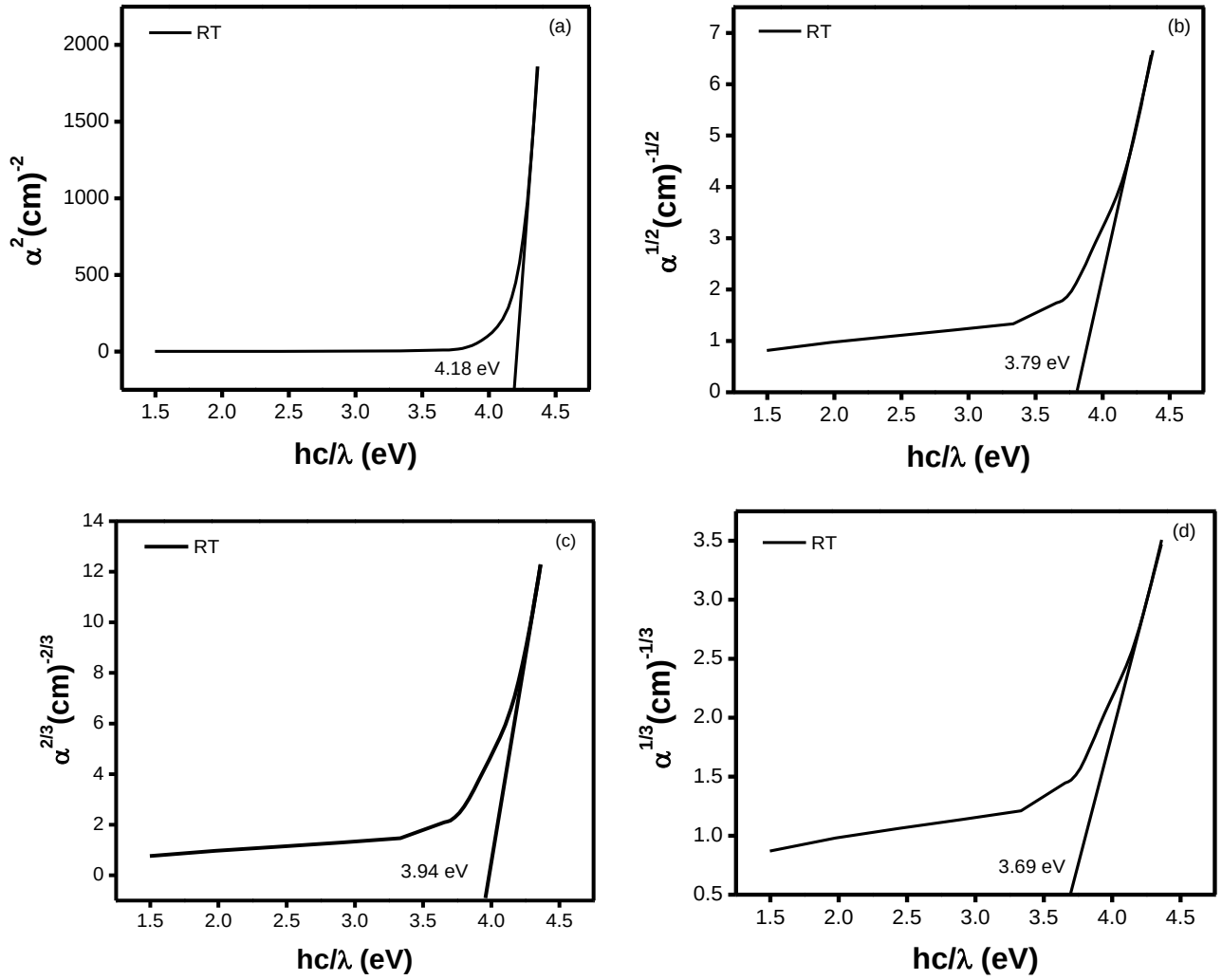

Fig. 5.9 $(\alpha)^2$ *vs* hc/λ curves, for $BCZT_{0.9}$ thin films, deposited at RT [m = 0.5, Fig. 5.9 (a), m = 2, Fig. 5.9 (b), m = 3/2, Fig. 5.9 (c), m = 3, Fig. 5.9 (d)].

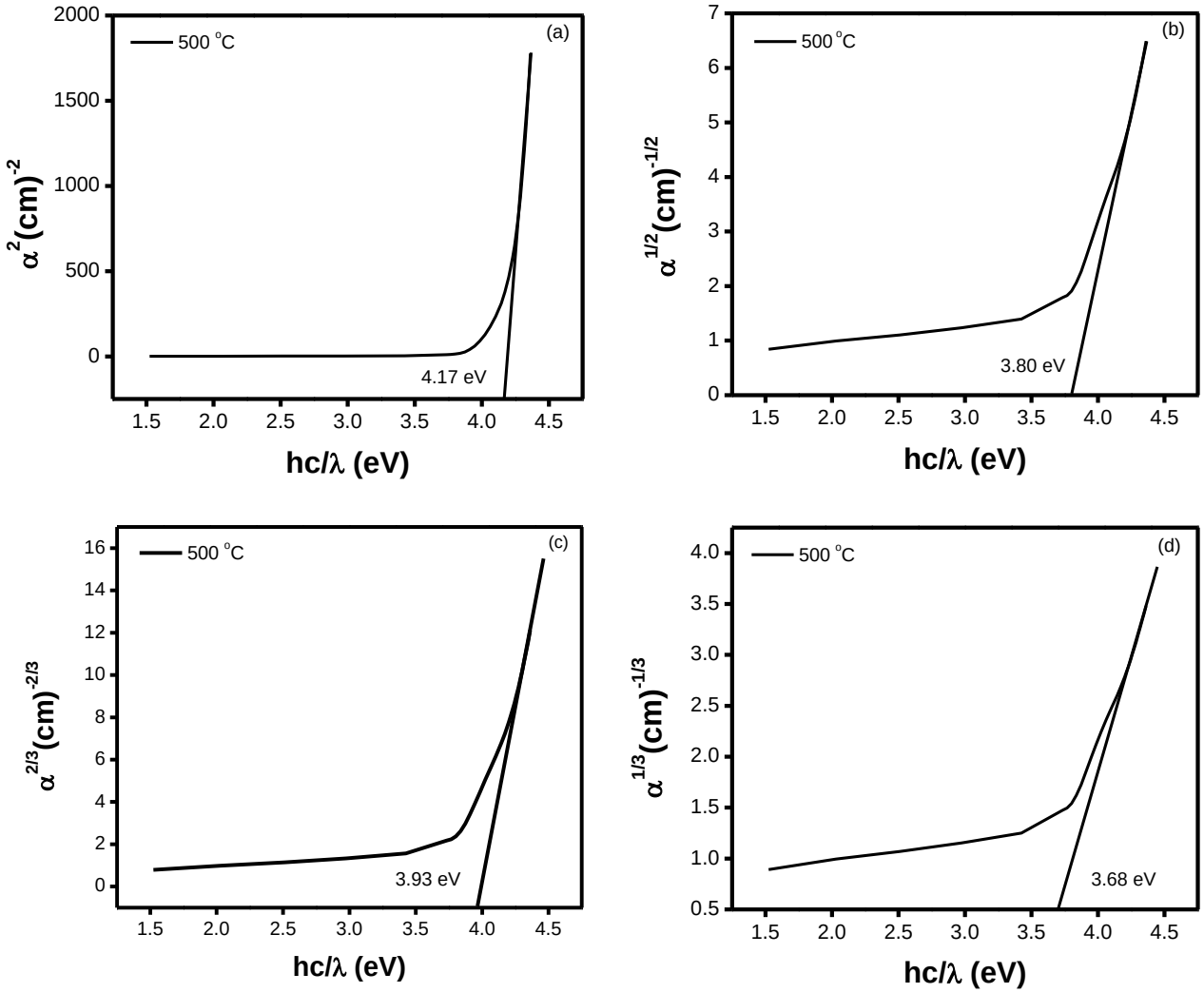

Fig. 5.10 $(\alpha)^2$ *vs* hc/λ curves, for $BCZT_{0.9}$ thin films, deposited at 500 ºC [m = 0.5, Fig. 5.10 (a), m = 2, Fig. 5.10 (b), m = 3/2, Fig. 5.10 (c), m = 3, Fig. 5.10 (d)].

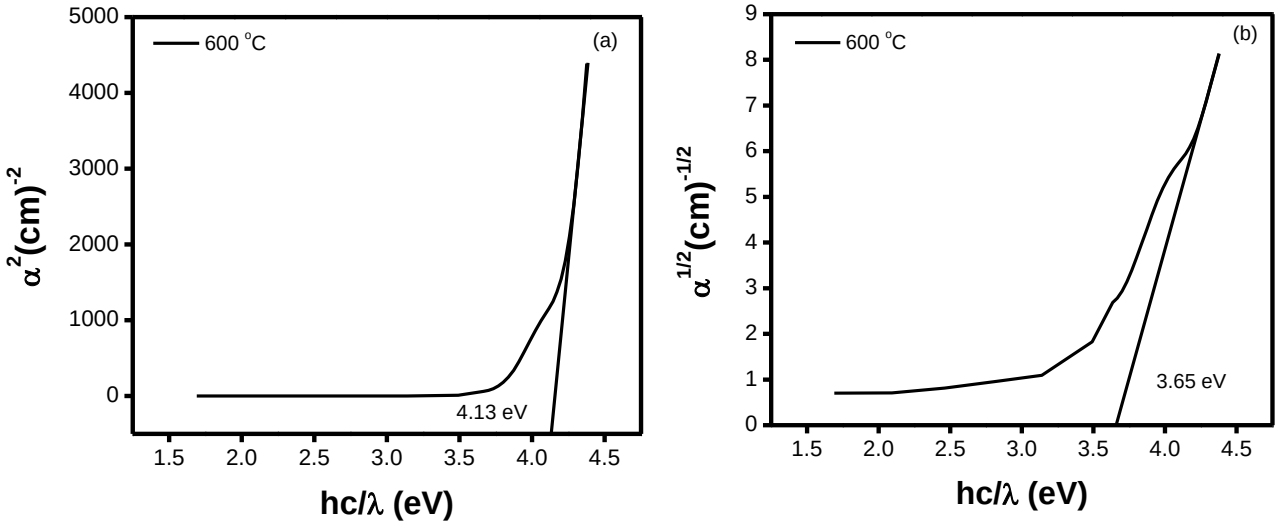

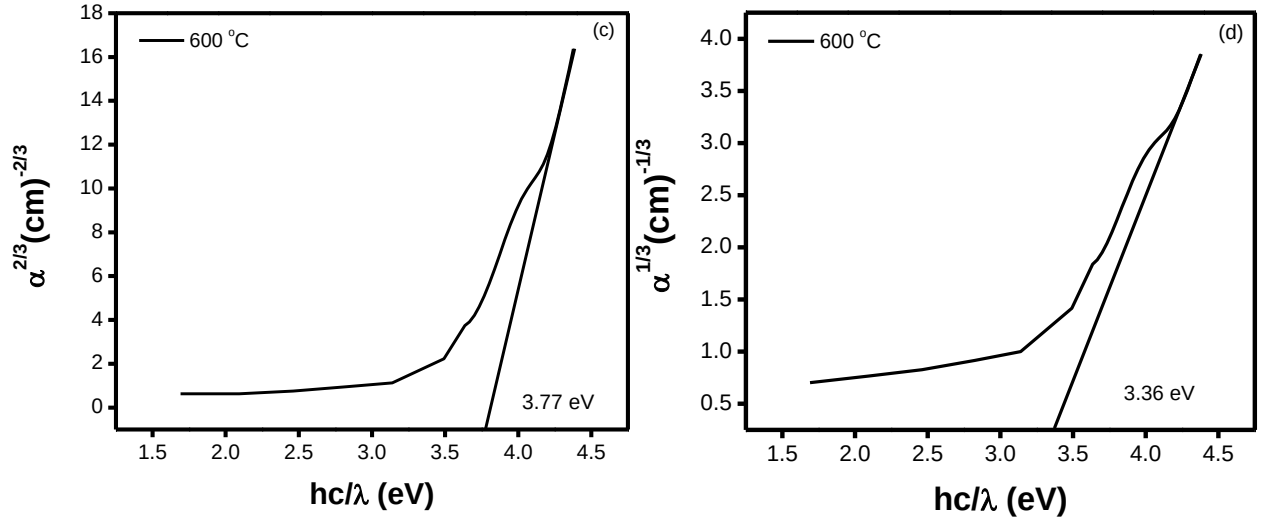

Fig. 5.11 $(\alpha)^2$ *vs* hc/λ curves, for $BCZT_{0.9}$ thin films, deposited at 600 ºC [m = 0.5, Fig. 5.11 (a), m = 2, Fig. 5.11 (b), m = 3/2, Fig. 5.11 (c), m = 3, Fig. 5.11 (d)].

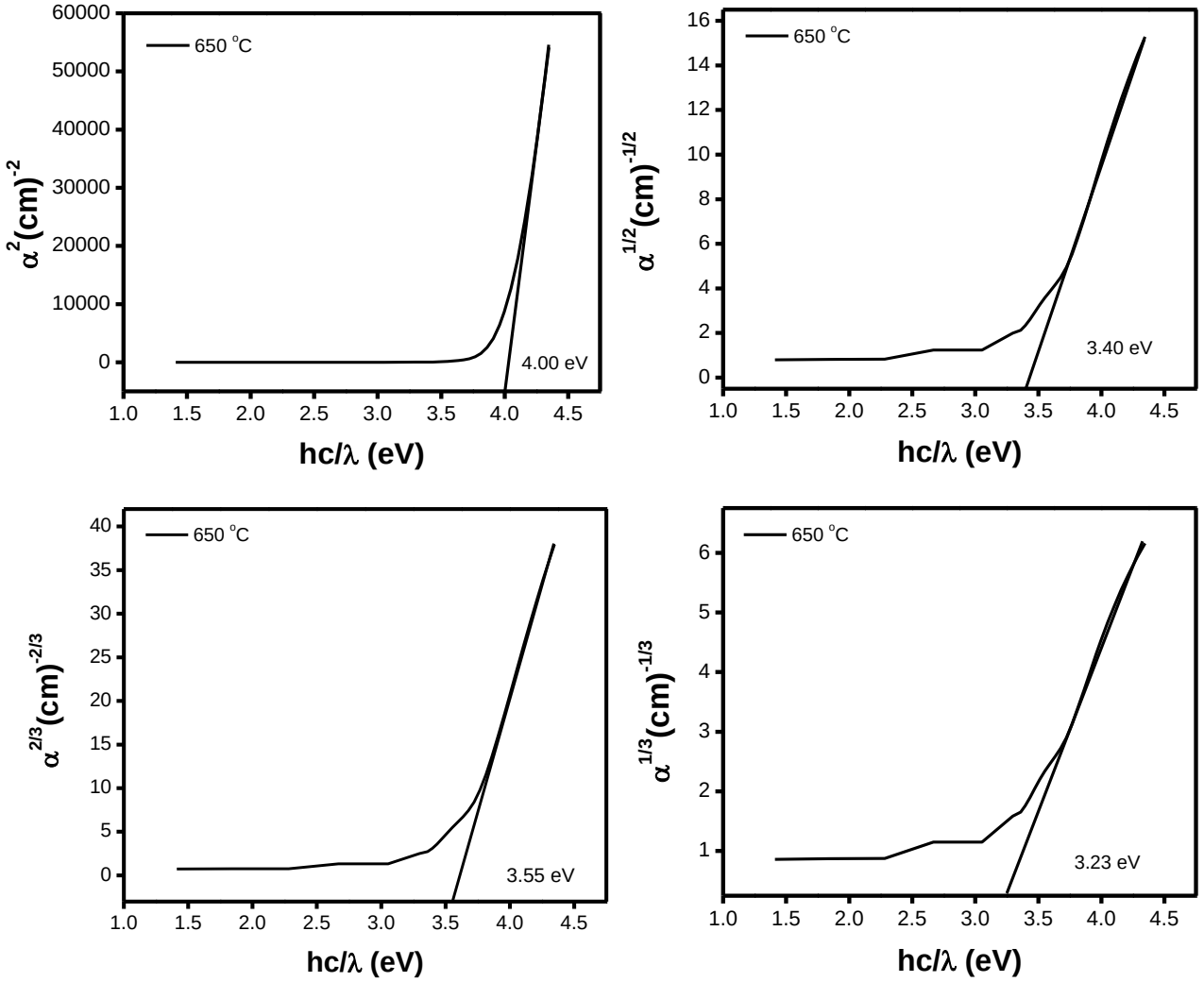

Fig. 5.12 $(\alpha)^2$ *vs* hc/λ curves, for $BCZT_{0.9}$ thin films, deposited at 650 ºC [m = 0.5, Fig. 5.12 (a), m = 2, Fig. 5.12 (b), m = 3/2, Fig. 5.12 (c), m = 3, Fig. 5.12 (d)].

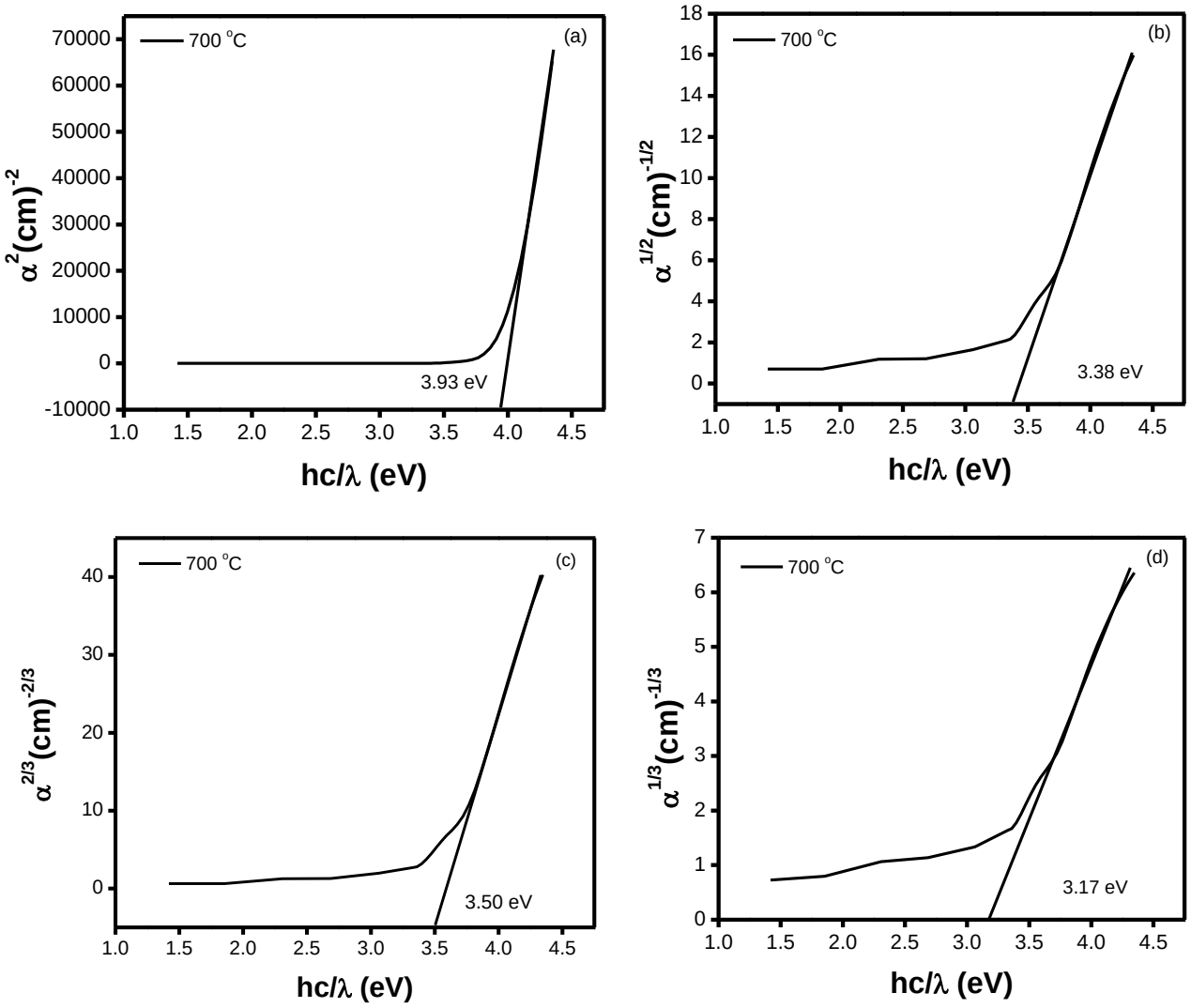

Fig. 5.13 $(\alpha)^2$ *vs* hc/λ curves, for $BCZT_{0.9}$ thin films, deposited at 700 ºC [m = 0.5, Fig. 5.13 (a), m = 2, Fig. 5.13 (b), m = 3/2, Fig. 5.13 (c), m = 3, Fig. 5.13 (d)].

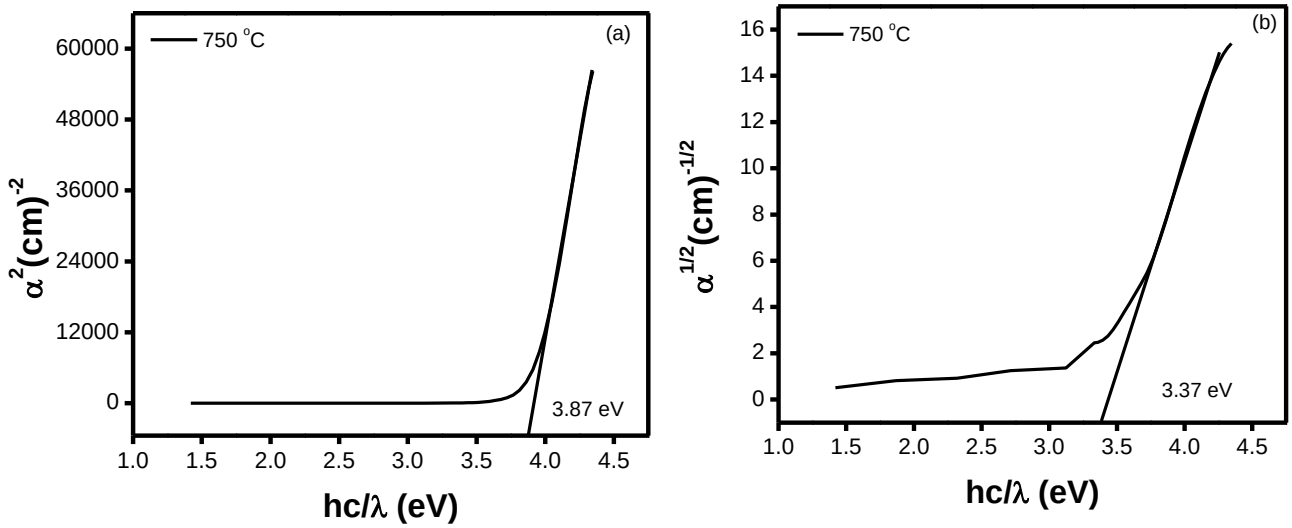

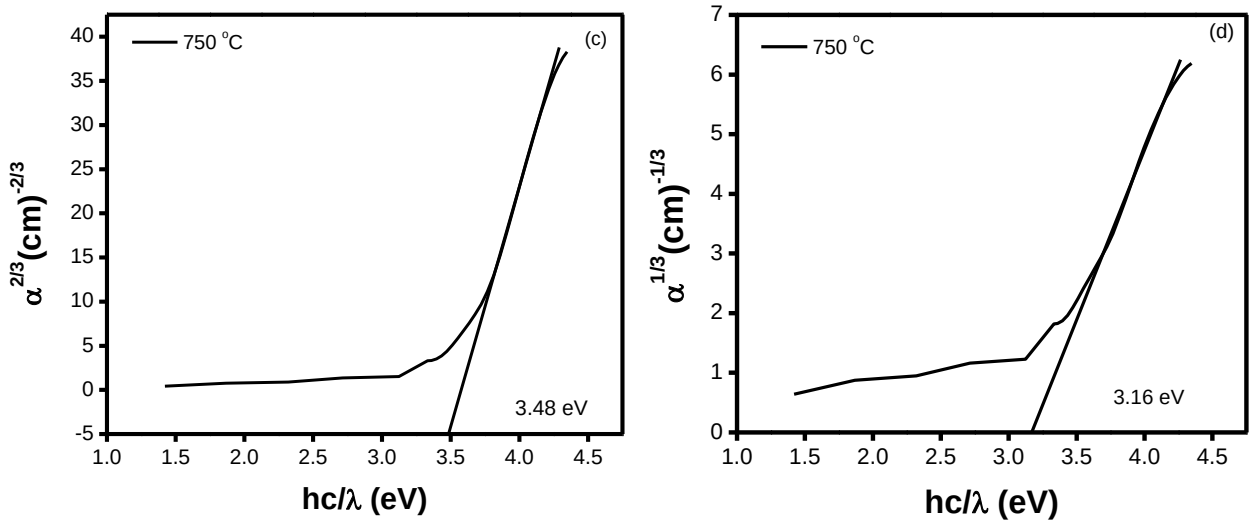

Fig. 5.14 $(\alpha)^2$ *vs* hc/λ curves, for $BCZT_{0.9}$ thin films, deposited at 750 °C [m = 0.5, Fig. 5.14 (a), m = 2, Fig. 5.14 (b), m = 3/2, Fig. 5.14 (c), m = 3, Fig. 5.14 (d)].

The indirectly allowed transition probability may be observed due to the photon-phonon interaction. The photon-phonon interaction is satisfied by Eq. (5.8) with m = 2. Figs. 5.9(b), 5.10(b), 5.11(b), 5.12(b), 5.13(b), and 5.14(b), exhibit the plot of $\alpha^{1/2}$ *vs* hν. The E_g (indirect band gap) obtained 3.79 eV for RT deposited films and 3.80, 3.65, 3.40, 3.38, and 3.37 eV for the films annealed at 500, 600, 650, 700 and 750 °C, respectively.

Besides photon-assisted electronic transitions, the phonon-assisted interaction probabilities are probable due to the inter-band absorptions in the films that correspond to the energy levels in the forbidden band. Excitons can be developed by direct photons alone or with help from photon-phonon interactions. Eq. (5.8) gives this direct absorption probability with m = 3/2, and the $\alpha^{2/3}$ *vs* hν curves were presented in Figs. 5.9(c), 5.10(c), 5.11(c), 5.12(c), 5.13(c), and 5.14(c), for films deposited at RT and the films annealed at 500, 600, 650, 700 and 750 °C, respectively. For the prepared films, the direct forbidden gap energy (E_g, attributed to this mechanism) value was calculated using the $\alpha^{2/3}$ *vs* hν curves. The direct forbidden gap energy were obtained 3.94 eV for RT films, and 3.93, 3.77, 3.55, 3.50, and 3.48 eV for the films annealed at 500, 600, 650, 700 and 750 °C, respectively.

Photon-phonon interactions can also result in the formation of excitons. Eq. (5.8) with m = 3 illustrates the probability of phonon-assisted indirect absorption. The $\alpha^{1/3}$ *vs* hν curves were presented in Figs. 5.9(d), 5.10(d), 5.11(d), 5.12(d), 5.13(d) and 5.14(d), for films deposited at RT and the films annealed at 500, 600, 650, 700 and 750 °C, respectively. For the prepared films, the

values of the indirect forbidden energy gap, E_g, were calculated using the $\alpha^{1/3}$ *vs* hν curves. The values of indirect forbidden energy gap attributed to this method, E_g, were calculated 3.69 eV for the room temperature (RT) films, and 3.68, 3.36, 3.23, 3.17 and 3.16 eV for the films annealed at 500, 600, 650, 700 and 750 ^oC, respectively.

5.4 Discussion

$BCZT_{0.9}$ films were sputter deposited using the ceramic $(Ba_{0.845}Ca_{0.155})(Zr_{0.1}Ti_{0.9})O_3$ target. The as-deposited films were annealed at 500, 600, 650, 700, 750 and 800 ^oC. However, films annealed at 800 ^oC peeled out, possibly due to the extraordinarily increased stress upon annealing. X-ray diffraction measurements showed the formation of orthorhombic $BCZT_{0.9}$ structure on annealing at 600, 650, 700, and 750 ^oC. It was found that the annealing temperature significantly impacted the optical characteristics of the prepared thin films. The optical band gap was decreased with an increase in annealing temperature. Burstein [83] explained the broadening (red shift) and narrowing (blue shift) effect of the measured band gap. Based on these observations, the most satisfactory representation for the α^2 *vs* hν curve was found, which recommends direct transition probability in the deposited $BCZT_{0.9}$ films via photon-electron interaction.

References

[1] E.V. Bursian, Nonlinear Crystal-Barium Titanate, 1st ed., Nauka Press publishing, Moscow, 1974.

[2] K.L. Chopra, S.R. Das, Properties of Thin Films for Solar Cells. In: Thin film solar cells, 1st ed., Springer publishing, Boston, 1983.

[3] J.F. Wager, Transparent electronics, Science. 300 (2003) 1245-1246. https://doi.org/10.1126/science.108527

[4] P.K. Das, Lasers and optical engineering, 1st ed., Springer publishing, New York, 1990.

[5] D. Smith, P. Baumeister, Refractive index of some oxide and fluoride coating materials, Applied Optics. 18 (1979) 111-115. https://doi.org/10.1364/AO.18.000111

[6] M.F. Al- Kuhaili, Optical properties of hafnium oxide thin films and their application in energy-efficient windows, Optical Materials. 27 (2004) 383-387. https://doi.org/10.1016/j.optmat.2004.04.014

[7] A.M. Ledger, Inhomogeneous interface laser mirror coatings, Applied Optics. 18 (1979) 2979-2989. https://doi.org/10.1364/AO.18.002979

[8] T.F. Deutsch, Absorption coefficient of infrared laser window materials, Journal of Physics and Chemistry of Solids. 34 (1973) 2091-2104. https://doi.org/10.1016/S0022-3697(73)80057-5

[9] M. Lines, A. Glass, Principles and applications of ferroelectrics and related materials, Clarendon Press publishing, Oxford, 1979.

[10] M.A. Aegerter, Ferroelectric thin coatings, Journal of Non-Crystalline Solids. 151 (1992) 195-202. https://doi.org/10.1016/0022-3093(92)90029-J

[11] N.A. Clark, M.A. Handschy, Surface-stabilized ferroelectric liquid-crystal electro-optic waveguide switch, Applied Physics Letters. 57 (1990) 1852. https://doi.org/10.1063/1.104037

[12] F.J. Walker, R.A. McKee, H.W. Yen, D.E. Zelmon, Optical clarity and waveguide performance of thin film perovskites on MgO, Applied Physics Letters. 65 (1994) 1495. https://doi.org/10.1063/1.112023

[13] P. Gunther, Nonlinear optical crystals for optical frequency doubling with laser diodes, Proceedings of SPIE, 236 (1981) 8-18. https://doi.org/10.1117/12.958976

[14] G.H. Hewig, K. Jain, Frequency doubling in a $LiNbO_3$ thin film deposited on sapphire, Journal of Applied Physics. 54 (1983) 57. https://doi.org/10.1063/1.331686

[15] J.C. Baumert, J. Hoffnagle, P. Gunther, Nonlinear optical effects in $KNbO_3$ crystals at $Al_xGa_{1-x}As$, Dye, Ruby and Nd:YAG laser wavelengths., Proceedings of SPIE. 492 (1984) 374-384. https://doi.org/10.1117/12.943728

[16] H. Hu, S.B. Krupanidhi, Multi-ion-beam reactive sputter deposition of ferroelectric $Pb(Zr,Ti)O_3$ thin films, Journal of Applied Physics. 71 (1992) 376. https://doi.org/10.1063/1.350719

[17] H. Tamada, A. Yamada, M. Saitoh, $LiNbO_3$ thin-film optical waveguide grown by liquid phase epitaxy and its application to second-harmonic generation, Journal of Applied Physics. 70 (1991) 2536. https://doi.org/10.1063/1.349409

[18] R.W. Whatmorea, P.C. Osbonda, N.M. Shorrocks, Ferroelectric materials for thermal IR detectors, Ferroelectrics. 76 (1987) 351-367. https://doi.org/10.1080/00150198708016956

[19] R. Watton, Ferroelectric materials and devices in infrared detection and imaging, Ferroelectrics. 91 (1989) 87-108. https://doi.org/10.1080/00150198908015731

[20] J.T. Evans, An experimental 512-bit nonvolatile memory with ferroelectric storage cell, IEEE Journal of Solid-State Circuits. 23 (1988) 1171-1175. https://doi.org/10.1109/4.5940
[21] R. Bez, A. Pirovano, Non-volatile memory technologies: emerging concepts and new materials, Materials Science in Semiconductor Processing. 7 (2004) 349-355. https://doi.org/10.1016/j.mssp.2004.09.127
[22] G. Lucovsky, A. Mooradian, W. Taylor, G.B. Wright, Identification of the fundamental vibrational modes of trigonal, α-monoclinic and amorphous selenium, Solid State Communications. 5 (1967) 113-117. https://doi.org/10.1016/0038-1098(67)90006-3
[23] G. Moddel, K.M. Johnson, W. Li, R.A. Rice, L.A.P. Stauffer, M.A. Handschy, Applied Physics Letters. 55 (1989) 537.
[24] R. Swanepoel, Determination of the thickness and optical constants of amorphous silicon, Journal of Physics E: Scientific Instruments. 16 (1983) 1214. https://doi.org/10.1088/0022-3735/16/12/023
[25] K.W. Kwon, C.S. Kang, S.O. Park, H.K. Kang, S.T. Ahn, Thermally robust Ta/sub 2/O/sub 5/capacitor for the 256-Mbit DRAM, IEEE Transactions on Electron Devices. 43 (1996) 919-923. https://doi.org/10.1109/16.502124
[26] Y. Shi, L. He, F. Guang, L. Li, Z. Xin, R. Liu, A review: preparation, performance, and applications of silicon oxynitride film, Micromachines. 10 (2019) 552. https://doi.org/10.3390/mi10080552
[27] K. Ohta, K. Yamada, K. Shimizu, Y. Tarui, Quadruply self-aligned stacked high-capacitance RAM using Ta_2O_5 high-density VLSI dynamic memory, IEEE Transactions on Electron Devices. 29 (1982) 368-376. https://doi.org/10.1109/T-ED.1982.20711
[28] S. Roberts, J. Ryan, L. Nesbit, Selective Studies of Crystalline Ta_2O_5 Films, Journal of the Electrochemical Society, 133 (1986) 1405. https://doi.org/10.1149/1.2108899
[29] R.F. Cava, W.F. Peck Jr, J.J. Krajewski, Enhancement of the dielectric constant of Ta_2O_5through substitution with TiO_2, Nature. 377 (1995) 215-217. https://doi.org/10.1038/377215a0
[30] K. Nomura, H. Ogawa, Some Properties of RF Sputtered Al_2O_3-Ta_2O_5 Composite Thin Films, Journal of the Electrochemical Society. 138 (1991) 3701. https://doi.org/10.1149/1.2085483
[31] G.B. Alers, D.J. Werder, Y. Chabal, H.C. Lu, E.P. Gusev, E. Garfunkel, T. Gustafsson, R.S. Urdahl, Applied Physics Letters. 73 (1998) 1517. https://doi.org/10.1063/1.4921416
[32] N. Rausch, E.P. Burte, Thin TiO_2 films prepared by low pressure chemical vapor deposition, Journal of the Electrochemical Society. 140 (1993) 145. https://doi.org/10.1149/1.2056076
[33] J.S. Lee, H.W. Song, W.J. Lee, B.G. Yu, K. No, Effects of process parameters on titanium dioxide thin film deposited using ECR MOCVD, Thin Solid Films. 287 (1996) 120-124. https://doi.org/10.1016/S0040-6090(96)08784-6
[34] M. Kadoshima, M. Hiratani, Y. Shimamoto, K. Torii, H. Miki, S. Kimura, T. Nabatame, Rutile-type TiO_2 thin film for high-k gate insulator, Thin Solid Films. 424 (2003) 224-228. https://doi.org/10.1016/S0040-6090(02)01105-7
[35] A.I. Kingon, J.P. Maria, S.K. Streiffer, Alternative dielectrics to silicon dioxide for memory and logic devices, Nature. 406 (2000) 1032-1038. https://doi.org/10.1038/35023243
[36] P. Thapliyal, A.S. Kandari, V. Lingwal, N.S. Panwar, G.M. Rao, Annealing temperature-dependent structural and electrical properties of $(Ta_2O_5)_{1-x}$-$(TiO_2)_x$ thin films, $x \leq 0.11$, Ceramics International. 47 (2021) 12066-12071. https://doi.org/10.1016/j.ceramint.2021.01.050

[37] M. Wang, R. Zuo, S. Qi, L. Liu, Synthesis and characterization of sol-gel derived (Ba,Ca)(Ti,Zr)O_3 nanoparticles, Journal of Materials Science: Materials in Electronics. 23 (2012) 753-757. https://doi.org/10.1007/s10854-011-0484-9
[38] M. Kumar, M. Kumar, D. Kumar, The deposition of nanocrystalline TiO_2 thin film on silicon using Sol-Gel technique and its characterization, Microelectronic Engineering. 87 (2010) 447-450. https://doi.org/10.1016/j.mee.2009.08.025
[39] C.S. Hwang, S.O. Park, H.J. Cho, C.S. Kang, H.K. Kang, S.I. Lee, M.Y. Lee, Deposition of extremely thin (Ba,Sr)TiO_3 thin films for ultra-large-scale integrated dynamic random access memory application, Applied Physics Letters. 67 (1995) 2819. https://doi.org/10.1063/1.114795
[40] T. Kawahara, M. Yamamuka, A. Yuuki, K. Ono, Surface morphologies and electrical properties of (Ba,Sr)TiO_3 films prepared by two-step deposition of liquid source chemical vapor deposition, Japanese Journal of Applied Physics. 34 (1995) 5077. https://doi.org/10.1143/JJAP.34.5077
[41] T. Kawahara, M. Yamamuka, T. Makita, J. Naka, A. Yuuki, N. Mikami, and K. Ono, Step coverage and electrical properties of (Ba,Sr)TiO_3 films prepared by liquid source chemical vapor deposition using $TiO(DPM)_2$, Japanese Journal of Applied Physics. 33 (1994) 5129. https://doi.org/10.1143/JJAP.33.5129
[42] D. Biswas, P. Sharma, N.S. Panwar, Composition dependent electrical properties of $(Ba_{1-x}Ca_xZr_{0.1}Ti_{0.9})O_3$ ceramics, near morphotropic phase boundary ($0.140 \leq x \leq 0.160$), ECS Journal of Solid State Science and Technology. 10 (2021) 033002. https://doi.org/10.1149/2162-8777/abea61
[43] S. Singh, J. Negi, N.S. Panwar, Dielectric properties of $Na_{1-x}K_xNbO_3$, near x = 0.5 morphotropic phase region, Journal of Physics and Chemistry of Solids. 123 (2018) 311-317. https://doi.org/10.1016/j.jpcs.2018.08.018
[44] A.M. Glazer, P.A. Thomas, K.Z.B. Kishi, G.K.H. Pang, C.W. Tai, Influence of short-range and long-range order on the evolution of the morphotropic phase boundary in $Pb(Zr_{1-x}Ti_x)O_3$, Physical Review B. 70 (2004) 184123. https://doi.org/10.1103/PhysRevB.70.184123
[45] K. Kakimoto, K. Akao, Y. Guo, H. Ohsato, Raman scattering study of piezoelectric $(Na_{0.5}K_{0.5})$ NbO3-LiNbO3 ceramics, Japanese Journal of Applied Physics. 44 (2005) 7064-7067. https://doi.org/10.1143/JJAP.44.7064
[46] B. Jaffe, W.R. Cook, J.H. Jaffe, Piezoelectric ceramics, 1st ed., Academic press publishing, New York, 1971.
[47] A.J. Moulson, J.M. Herbert, Electroceramics: Materials, Properties, Applications, John Wiley & Sons publishing, United Kingdom, 2003.
[48] Y. Ishibashia, M. Iwata, A theory of morphotropic phase boundary in solid-solution systems of perovskite-type oxide ferroelectrics, Japanese Journal of Applied Physics. 38 (1999) 800. https://doi.org/10.1143/JJAP.38.800
[49] N. Klein, E. Hollenstein, D. Damjanovic, H.J. Trodahl, N. Setter, M. Kuball, A study of the phase diagram of (K, Na, Li)NbO_3 determined by dielectric and piezoelectric measurements, and Raman spectroscopy, Japanese Journal of Applied Physics. 102 (2007) 014112. https://doi.org/10.1063/1.2752799
[50] A. Piorra, A. Petraru, H. Kohlstedt, M. Wuttig, E. Quandt, Piezoelectric properties of $0.5(Ba_{0.7}Ca_{0.3}TiO_3)$-$0.5[Ba(Zr_{0.2}Ti_{0.8})O_3]$ ferroelectric lead-free laser deposited thin films, Japanese Journal of Applied Physics. 109 (2011) 104101. https://doi.org/10.1063/1.3572056

[51] Y. Lin, G. Wu, N. Qin, D. Bao, Structure, dielectric, ferroelectric, and optical properties of (1-x)$Ba(Zr_{0.2}Ti_{0.8})O_3$-x$(Ba_{0.7}Ca_{0.3})TiO_3$ thin films prepared by sol-gel method, Thin Solid Films. 520 (2012) 2800-2804. https://doi.org/10.1016/j.tsf.2011.12.030

[52] C. Bhardwaj, B.S.S. Daniel, D. Kaur, Pulsed laser deposition and characterization of highly tunable (1-x)$Ba(Zr_{0.2}Ti_{0.8})O_3$-x$(Ba_{0.7}Ca_{0.3})TiO_3$ thin films grown on $LaNiO_3$/Si substrate, Journal of Physics and Chemistry of Solids. 74 (2013) 94-100. https://doi.org/10.1016/j.jpcs.2012.08.005

[53] G. Kang, K. Yao, and J. Wang, (1-x)$Ba(Zr_{0.2}Ti_{0.8})O_3$-x$(Ba_{0.7}Ca_{0.3})TiO_3$ Ferroelectric Thin Films Prepared from Chemical Solutions, Journal of the American Ceramic Society. 95 (2012) 986-991. https://doi.org/10.1111/j.1551-2916.2011.04877.x

[54] W. Bai, B. Shen, F. Fu, J. Zhai, Dielectric, ferroelectric, and piezoelectric properties of textured BZT-BCT lead-free thick film by screen printing, Materials Letters. 83 (2012) 20-22. https://doi.org/10.1016/j.matlet.2012.05.114

[55] B.C. Luo, D.Y. Wang, M.M. Duan, S. Li, Growth and characterization of lead-free piezoelectric $BaZr_{0.2}Ti_{0.8}O_3$-$Ba_{0.7}Ca_{0.3}TiO_3$ thin films on Si substrates, Applied Surface Science. 270 (2013) 377-381. https://doi.org/10.1016/j.apsusc.2013.01.033

[56] D.Y. Wang, N.Y. Chan, S. Li, S.H. Choy, H.Y. Tian, L.W. Chan Helen, Enhanced ferroelectric and piezoelectric properties in doped lead-free $(Bi_{0.5}Na_{0.5})_{0.94}Ba_{0.06}TiO_3$ thin films, Applied Physics Letters. 97 (2010) 212901. https://doi.org/10.1063/1.3518484

[57] D.Y. Wang, D.M. Lin, K.W. Kwok, N.Y. Chan, J.Y. Dai, S. Li, H.L.W. Chan, Ferroelectric, piezoelectric, and leakage current properties of $(K_{0.48}Na_{0.48}Li_{0.04})(Nb_{0.775}Ta_{0.225})O_3$ thin films grown by pulsed laser deposition, Applied Physics Letters. 98 (2011) 022902. https://doi.org/10.1063/1.3535608

[58] T. Matsuda, W. Sakamoto, B.Y. Lee, T. Lijima, J. Kumagai, M. Moriya, T. Yogo, Electrical properties of lead-free ferroelectric Mn-doped $K_{0.5}Na_{0.5}NbO_3$-$CaZrO_3$ thin films prepared by chemical solution deposition, Japanese Journal of Applied Physics. 51 (2012) 09LA03. https://doi.org/10.1143/JJAP.51.09LA03

[59] J. Ihlefeld, B. Lauglhin, A.H. Lowery, W. Borland, A. Kingon, J.P. Maria, Copper compatible barium titanate thin films for embedded passives, Journal of Electroceramics. 14 (2005) 95-102. https://doi.org/10.1007/s10832-005-0866-6

[60] B. Malic, I. Boerasu, M. Mandeljc, M. Kosec, V. Sherman, T. Yamada, N. Setter, M. Vukadinovic, Processing and dielectric characterization of $Ba_{0.3}Sr_{0.7}TiO_3$ thin films on alumina substrates, Journal of the European Ceramic Society. 27 (2007) 2945-2948. https://doi.org/10.1016/j.jeurceramsoc.2006.11.020

[61] D.M. Tahan, A. Safari, L.C. Klien, Preparation and Characterization of Ba_xSr_{1-x}, TiO_3 Thin Films by a Sol-Gel Technique, Journal of the American Ceramic Society. 79 (1996) 1593-1598. https://doi.org/10.1111/j.1151-2916.1996.tb08769.x

[62] K. Sreenivas, A. Mansingh, M. Sayer, Structural and electrical properties of rf sputtered amorphous barium titanate thin films, Journal of Applied Physics. 62 (1987) 4475. https://doi.org/10.1063/1.339037

[63] P. Thapliyal, N.S. Panwar, G.M. Rao, Optical properties and current conduction in annealed $(Ta_2O_5)_{0.94}$ - $(TiO_2)_{0.06}$ thin films, Superlattices and Microstructures. 158 (2021) 107008. https://doi.org/10.1016/j.spmi.2021.107008

[64] M. Okuyama, Y. Matsui, H. Nakano, Y. Hamakawa, $PbTiO_3$ ferroelectric thin film gate fet for infrared detection, Ferroelectrics. 33 (1981) 235-241. https://doi.org/10.1080/00150198108008091

[65] K. Iijimo, Y. Tomita, R. Takayama, I. Ueda, Preparation of c-axis oriented $PbTiO_3$ thin films and their crystallographic, dielectric, and pyroelectric properties, Journal of Applied Physics. 60 (1986) 361. https://doi.org/10.1063/1.337654
[66] S.B. Krupanidhi, G.M. Rao, Pulsed laser deposition of strontium titanate thin films for dynamic random access memory applications, Thin Solid Films. 249 (1994) 100-108. https://doi.org/10.1016/0040-6090(94)90093-0
[67] H. Kang, W. Tian, J. Wu, Y. Zhang, Z. Li, G. Pang, Effect of annealing on microstructure and capacitance properties of sol-gel TiO_2 film on aluminum, International Journal of Electrochemical Science. 16 (2021) 150963. https://doi.org/10.20964/2021.01.21
[68] M. Ohring, The material science of thin films, 1st ed., Academic press publishing, San Diego, 1995.
[69] V. Lingwal, N.S. Panwar, Scanning magnetron-sputtered TiN coating as diffusion barrier for silicon devices, Journal of Applied Physics. 97 (2005) 104902. https://doi.org/10.1063/1.1896433
[70] S. Sen, R. Choudhay, Effect of doping Ca ions on structural and electrical properties of $Ba(Zr_{0.05}Ti_{0.95})O_3$ electroceramics, Journal of Materials Science: Materials in Electronics. 15 (2004) 671-675. https://doi.org/10.1023/B:JMSE.0000038922.74021.d6
[71] J. Xu, D. P. Durisin, G.W. Auner, Optical properties of pulsed-laser deposited $BaTiO_3$ thin films, Photon Processing in Microelectronics and Photonics IV: Proceedings of SPIE, 5713 (2005) 305-310. https://doi.org/10.1117/12.584639
[72] S.P.P. Sadhu, M. Rath, S. Posam, S. Muthukumar V., M.S.R. Rao, K.B.R. Varma, Large nonlinear refraction in pulsed laser deposited BCZT thin films on quartz substrates, Journal of the Optical Society of America B. 35 (2018) 2625. https://doi.org/10.1364/JOSAB.35.002625
[73] C. Corbella, M. Vives, A. Pinyol, I. Porqueras, C. Person, E. Bertran, Influence of the porosity of RF sputtered Ta_2O_5 thin films on their optical properties for electrochromic applications, Solid State Ionics. 165 (2003) 15-22. https://doi.org/10.1016/j.ssi.2003.08.018
[74] P.C. Joshi, M.W. Cole, Influence of postdeposition annealing on the enhanced structural and electrical properties of amorphous and crystalline Ta_2O_5 thin films for dynamic random access memory applications, *Journal of Applied Physics.* 86 (1999) 871. https://doi.org/10.1063/1.370817
[75] Md. M. -ur- Rahman, G. Yu, T. Soga, T. Jimbo, H. Ebisu, M. Umeno, Refractive index and degree of inhomogeneity of nanocrystalline TiO_2 thin films: Effects of substrate and annealing temperature, Journal of Applied Physics. 88 (2000) 4634. https://doi.org/10.1063/1.1290456
[76] R.A. Smith, Wave Mechanics of Crystalline Solids, 2nd ed., Chapman and Hall publishing, London, 1969.
[77] C.R. Sekhar, Preparation of copper oxide thin film by the sol-gel-like dip technique and study of their structural and optical properties, Solar Energy Materials and Solar Cells, 68 (2001) 307-312. https://doi.org/10.1016/S0927-0248(00)00364-0
[78] S.M. Sze, Physics of Semiconductor Devices, 2nd ed., Wiley Publishing, New York, 1981.
[79] I.P. Raevskii, M.A. Malitskaya, O.I. Prokopalo, V.G. Smotrakovm, E.G. Fesenko, Photoconductivity and thermally stimulated conductivity of potassium and sodium niobate single crystal, Soviet Physics, Solid State. 19 (1977) 283-284.
[80] M. Shur, Physics of Semiconductor Devices, 1st ed., Prentice Hall publishing, New Jersey, 1990.

[81] D.Y. Jiang, D.Z. Shen, K.W. Liu, C.X. Shan, Y.M. Zhao, T. Yang, B. Yao, Y.M. Lu, J.Y. Zhang, Effect of post annealing on the band gap of $Mg_xZn_{1-x}O$ thin films, Semiconductor Science and Technology. 23 (2008) 035002. https://doi.org/10.1088/0268-1242/23/3/035002
[82] S.V.J. Chandra, S. Uthanna, G.M. Rao, Effect of substrate temperature on the structural, optical and electrical properties of dc magnetron sputtered tantalum oxide films, Applied Surface Science. 254 (2008) 1953-1960. https://doi.org/10.1016/j.apsusc.2007.08.005
[83] E. Burstein, Anomalous optical absorption limit in InSb, Physical Review. 93 (1954) 632-633. https://doi.org/10.1103/PhysRev.93.632

CHAPTER-6

Current-voltage characteristics of $(Ba_{1-x}Ca_x)(Zr_{1-y}Ti_y)O_3$, (x = 0.155, y = 0.9), thin films

---

Brief summary

The current-voltage characteristics of the prepared $BCZT_{0.9}$ films, annealed at different temperatures, have been described in this chapter. The current-voltage variations of the prepared films exhibit different conductions for different annealing treatments. MIS Ag/$BCZT_{0.9}$/Si/Ag assisted structure was prepared to find different dominating conduction mechanisms in the insulator, such as ohmic, Schottky emission, space-charge-limited current, Poole-Frenkel effect, tunneling, and ionic conduction. The variation of room temperature leakage current density (J) with the applied electric field (E) for the prepared MIS structures was measured for different annealing conditions. On crystallization, the leakage current density of the prepared films decreased by order of 3, from ~10^{-6} for amorphous to ~10^{-9} A/cm^2 for crystalline films. Electrical properties were observed to improve for the films annealed at 750 ^oC than other annealed films.

CHAPTER-6

Current-voltage characteristics of $(Ba_{1-x}Ca_x)(Zr_{1-y}Ti_y)O_3$, (x = 0.155, y = 0.9), thin films

6.1 Introduction

Significant development and research have been carried out to achieve applications of ferroelectric materials in semiconductor technology [1-3]. Commercial nonvolatile memories are already made using ferroelectric capacitors in silicon-based integrated circuits [4,5]. Ferroelectric random access memory (FRAM) was proposed long back [6]. Since then, improved equipment and more sophisticated techniques have undoubtedly [7], led to the preparation and characterization of higher-quality ferroelectric films for different applications [8-16].

Various applications are also expected in the field of sensors and actuators. It has indeed undoubtedly resulted in a fast advancement in the production of polycrystalline films and high-quality epitaxial via newer development methods combined with improved control over the growth characters. A lot of studies have been dedicated to ferroelectrics with perovskite structures, such as $BaTiO_3$, $PbTiO_3$, (Pb, La)TiO_3, Pb(Zr, Ti)O_3, (Ba, Sr)TiO_3, etc. [17-23].

The post-deposition annealing temperature had an odd relationship with the leakage current density and was significantly higher for crystalline films than amorphous films [24]. Additionally, the majority of applications rely on the application [25] of an external field to the ferroelectric capacitor [26-28], which can be made of single crystals, bulk ceramics, or thin films of polycrystalline or epitaxial quality [29,30], which is prone to a leakage current. Also, understanding the conduction mechanism is necessary to reduce leakage current. To recognize the conduction mechanisms responsible for the leakage current, the investigation of the charge transport phenomena in ferroelectric thin films is significant, and also for all applications involving ferroelectric capacitors exposed to an applied external field [31,32].

Numerous factors, including impurity content, oxygen vacancy, the occurrence of partially oxidized silicon at grain boundaries close to the film or substrate interface, etc., have been implicated in the increase in leakage current density. The thin film's composition, structure, impurities, stress, homogeneity, and local effects (grain boundaries, dopant segregation,

compositional variations, high defect density, pores, etc.) significantly impact the leakage current.

Ferroelectric thin films are frequently electrically characterized by current-voltage (I-V) and capacitance-voltage (C-V) measurements for microelectronic applications like memory devices. In theory, these measurements can derive information about the modes of charge transport and the charge distribution in the ferroelectric film [25,33-35]. In the present study, the I-V measurements were carried out on the $(Ba_{0.845}Ca_{0.155})(Zr_{0.1}Ti_{0.9})O_3$ thin film-assisted metal-insulator-semiconductor (MIS) structures using a piezo-meter (aixACCT Systems GmbH, aixPES). By RF magnetron sputtering of the $(Ba_{0.845}Ca_{0.155})(Zr_{0.1}Ti_{0.9})O_3$ target thin films were deposited onto silicon (Si, p-type, <100>) substrates. The as-deposited films were annealed for one hr at different temperatures, between 500 and 800 ^oC, in an ambient atmosphere. For the electrical measurements, metal-insulator-semiconductor (MIS) structures, $Ag/BCZT_{0.9}/p\text{-}Si$, were prepared, using a shadowing mask, to sputter deposit silver as the top circular electrode(s) of 1.963×10^{-3} cm^2 area. The bottom electrode for the MIS configuration was formed by depositing the silver on the back side of the silicon substrate without any mask. Further, to measure the current-voltage (I-V) characteristics of the prepared films, a P-E loop tracer with a piezo-meter was used.

6.2 Basic conduction processes in insulators

In the characterization of electrical properties of $(Ba_{0.845}Ca_{0.155})(Zr_{0.1}Ti_{0.9})O_3$ films, investigations have been performed on the conduction mechanism, leakage current, breakdown voltage measurements, etc. In an ideal MIS diode, the conduction of the insulating film is taken to be null at normal temperatures. Nevertheless, real insulators exhibit carrier conduction when the electric field or temperature is large [36]. Based on the energy band gap, the conduction mechanism may be explained in the dielectrics, amorphous or crystalline [35,36]. Compared to amorphous structures, the conductivity of a semiconductor is more vulnerable to impurities. Many localized traps are produced due to the large fluctuations in local configurations of atoms, which may trap free carriers and counteract the impact of contaminants. When sandwiched between pair of metal and semiconductor electrodes (MIS arrangement), insulating oxide films exhibit a huge electrical conduction phenomenon. The migration of electrons, holes and ions, due to the presence of an applied electric field, may rise to measurable currents. In different applied

field regions, different conductions, such as ohmic, at low fields, to Schottky [37,38] Poole-Frenkel [39], Fowler-Nordheim [40], mixed-conduction [41,42], etc. Ideally, a dielectric is expected to be a perfect insulator with infinite resistivity. When subjected to an applied voltage (V), all dielectrics have a finite resistivity, allowing the passage of current (I) through it. At an applied electric field, the Fowler-Nordheim tunneling, Poole-Frenkel emission, Schottky effect, space-charge-limited conduction, ionic conduction, or a combination of some of these mechanisms may be held responsible for current flow through an impurity-free dielectric. Only a single mechanism cannot explain the observed I-V characteristics of the deposited film at all the applied voltages; however, over a measured voltage range, any of these mechanisms may have dominating effect. The maximum electric field a dielectric can sustain without causing runaway currents is generally used to define leakage current capability. The current-voltage (C-V) properties must be analyzed between the insulator and contacts of the prepared thin film material to find the rate-limiting dominant transport method. Barrier-limited and bulk-limited transport mechanisms are two significant-categories of rate-limiting mechanisms [36,43-45].

Barrier-limited processes are effective in the locality of the contact-insulator interface. The flow of charge restricts the conduction process from the contact to the insulator; once the charge is injected, it has difficulty migrating to the other electrode. Tunneling and Schottky emission conductions come into this type of mechanism. A sufficient number of charge carriers are inserted into the insulator conduction band by tunneling or Schottky emission in a bulk-limited mechanism [41,43]. Still, bulk transport restrictions make it difficult to reach the opposite electrode. The leakage current characteristics show ohmic behaviour at the lower electric field and exponential behaviour at moderately high fields [46,47]. Poole-Frenkel (PF) and space-charge-limited (SCL) conductions are examples of this mechanism [36]. The behaviour of some common conduction mechanisms is briefly tabulated in Table 6.1.

Table 6.1 Basic conduction processes in insulators [36,48].

Process	**Expression**
Schottky emission (SC)	$J = AT^2 \exp\left[\frac{-q\left(\Phi_B - \beta\sqrt{E}\right)}{k_B T}\right]$, (6.1)

Tunnel or field emission (TE) $$J \sim E^2 \exp\left[\frac{-4\sqrt{2m^*}(q\Phi_B)^{3/2}}{3q\hbar E}\right], \quad (6.2)$$

Ohmic $$J \sim E \exp\left(-\Delta E_{ae}/k_B T\right), \quad (6.3)$$

Space-charge-limited (SCL) $$J = \frac{8\,\varepsilon_i\,\mu\,V^2}{9d^3}, \quad (6.4)$$

Poole-Frenkel emission (PF) $$J \sim E \exp\left[\frac{-q\left(\Phi_B - \frac{\beta}{r}E^{1/2}\right)}{k_B T}\right]. \quad (6.5)$$

Ionic conduction (IC) $$J \sim \frac{E}{T}\exp\left(-\Delta E_{ai}/k_B T\right). \quad (6.6)$$

---

where Φ_B = barrier height, A = effective Richardson constant, m* = effective mass of the electron, E = electric field, d = insulator thickness, ΔE_{ae} = activation energy of electrons, ΔE_{ai} = activation energy of ions, and $\beta \equiv \sqrt{q/\alpha\pi\varepsilon_0\varepsilon}$, k_B = Boltzmann's constant, q = electronic charge, V = applied voltage, T = absolute temperature, J = current density, μ = mobility of charge carriers, ε_i = insulator dynamic permittivity, ε_0 = permittivity of vacuum, ε = dielectric constant of the insulator film, α and r are described in the text.

The electrical characteristics of insulating oxide films and the conduction process in layers may be influenced by the existence of the following various charges [49]:

(i) The trapped electrons and holes in the bulk of the insulator are identified as oxide-trapped charges.

(ii) The ionic impurities that in the insulator's bulk are identified as mobile ionic charges.

(iii) The structural defects localized in the insulator, around the insulator-semiconductor, are identified as interface fixed oxide charges.

(iv) The captured holes and electrons by trapping centres localized at the insulator-semiconductor interface are identified as interface-trapped charges [36].

The thermionic emission of electrons from a heated metal into a vacuum is known as the Schottky effect. This effect occurs due to the induced image force, which lowers the potential energy for charge carrier emission on the application of the electric field. The requirement of minimum energy to escape an electron from initial energy at the Fermi level into the vacuum is known as the work function $q\Phi_m$ (Φ_m in volts), as given in Fig. 6.1 [36]. The magnitude of $q\Phi_m$ for metals is small and alters from 2 to 6 electron volts (eV). Usually, the value of $q\Phi_m$ is much more prone to surface contamination.

When an electron is at a distance x from the metal, an image positive charge (having equal and opposite charge of the electron) is induced on the metal surface [50,51]. The force of attraction between the electron and the induced positive charge corresponds to the force that would present between the electron at distance +x, and an equal positive charge located at distance -x, from the metal surface. The positive charge is referred to as the image charge, and the image charge induced to justify the basic concept is that inside a metal the electric field is zero. The force of attraction, known as the image force, is given by $-q^2/16\pi\varepsilon_o x^2$, where ε_o is the permittivity of free space. The potential energy of the electron at a distance x from the metal surface is $q^2/16\pi\varepsilon_o x$, and is measured downward from the x-axis, and this rounds the potential barrier, Fig. 6.1.

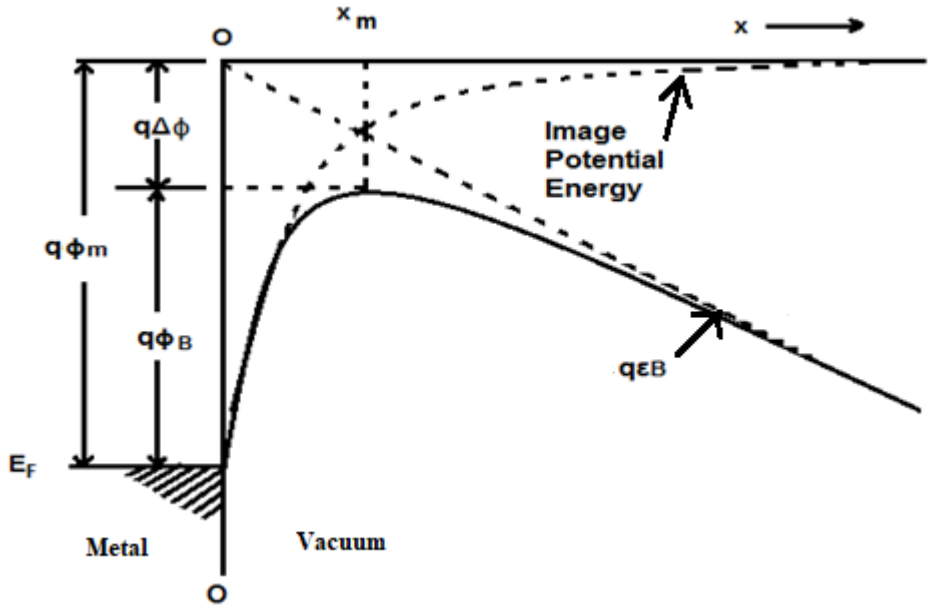

Fig. 6.1 Energy-band diagram between a metal surface and vacuum. The metal work function is $q\phi_m$. The effective work function (or barrier) is lowered when an electric field is applied to the surface. The lowering is due to the combined effect of the field and the image-force [36].

At an applied electric field, E, the total potential energy (PE), as a position function (measured downward from the x- axis), is given by Eq. (6.7),

$$PE(x) = \frac{q^2}{16\pi\varepsilon_o x} + qEx, \qquad (6.7)$$

Schottky barrier lowering (also called image-force lowering) $\Delta\Phi$ and the location of the lowering x_m (as shown in Fig. 6.1) is computed using the condition d[PE(x)]/dx = 0, which gives

$$x_m = (q/16\pi\varepsilon_o E)^{1/2}, \quad \text{and} \quad \Delta\Phi = (qE/4\pi\varepsilon_o)^{1/2} = 2Ex_m \qquad (6.8)$$

The current owing to the thermally excited electrons hopping from one isolated state to the next, at low voltage and high-temperature, results an ohmic conduction mechanism. The ohmic conduction shows a linear characteristic between J and E, Eq. (6.3). The process of ionic conduction is analogous to that of diffusion, Eq. (6.6). The space-charge-limited (SCL) current occurs owing to the non-uniform rate of flow of charge carriers from metal contact to insulating film and through the insulating film and develops a space-charge cloud, which results in slowing down the further carrier injection from contact [43]. The applied voltage squared determines the space-charge-limited current, Eq. (6.4).

Poole-Frenkel emission is involved with field-enhanced thermal excitation of trapped electrons into the conduction band of the insulator [36]. Poole-Frenkel (PF) effect follows a straight line plot in between the Ln (J/E) and $\sqrt{E}$, Eq. (6.5). The coefficient r, presented in Eq. (6.5), is referred to as the slope parameter [52] to show the impact of the trapping or acceptor centres ($1 \leq r \leq 2$) [48,53,54]. For r = 1, the conduction process is called the normal Poole-Frenkel effect [35,49]. The conduction mechanism is attributed to the modified Poole-Frenkel effect or Poole-Frenkel method with compensation [49,55], for r = 2. In the latter case, the insulator encompasses the non-negligible number of trapped carriers [49,56]. Poole-Frenkel effect is a trap-limited mechanism, in which the slope of the line of the Ln (J/E) *vs* $\sqrt{E}$ plot relies on the relative densities of the donor- and acceptor-type trapping centres [49].

The current for Poole- Frenkel and Schottky emission mechanism may be described as [49], from Table 6.1.

$$i = i_o \exp[\beta q\sqrt{E}/k_B T], \quad (6.9)$$

where $\beta = (q/\alpha\pi\varepsilon_o K_d)^{1/2}$, (6. 10)

and K_d is the high frequency or dynamic dielectric constant.

One can calculate $\beta^*_{SC} = \beta_{SC} q/k_B T$ and $\beta^*_{PF} = \beta^*_{PF}\, q/rk_B T$ from the slopes of the Ln J *vs* $\sqrt{E}$ and Ln (J/E) *vs* $\sqrt{E}$ plots, respectively. Experimentally, it is hard to differentiate Schottky and Poole-Frenkel's mechanisms. The constant β is the only term which differentiates these two mechanisms, which is twice, in Poole-Frenkel emission, of that for Schottky effect ($\beta_{PF} = 2\beta_{SC}$), owing to image-charge formation in the latter ($\beta = 1$ for Poole-Frankel effect, and 4 for Schottky emission).

The internal emission mechanism can transport bulk charge, trapped by impurity levels in the insulator band gap, to the conduction band. In Poole-Frenkel emission [57,58], the impurity is considered an ionized donor with a hydrogen-like coulomb potential. The defect centre becomes neutral with filled by an electron. Applying an electric field distorts the potential well asymmetrically [43], Fig. 6.2. The escaping of trapped electrons may occur when the thermal activation overcomes the energy barrier corresponding to that necessitated to ionize the donor. The net current flows due to successive electrons' hopping between Poole-Frenkel traps. In specific temperature and voltage ranges, any conduction mechanism may dominate, in an insulator. Furthermore, because the processes of conduction mechanisms are not independent of one another, they must be thoroughly investigated. For example, Schottky and tunneling characteristics are pretty-comparable for the huge space-charge effect [59].

Tunnel emission happens when trapped electrons are field ionized into the conduction band or electrons from the metal Fermi level tunnel into the insulator's conduction band. Tunnel emission is greatly influenced by the applied voltage, but is largely unaffected by temperature. The Fowler-Nordheim tunneling or field emission shows a straight line in the Ln (J/E^2) *vs* (1/E) plot, Eq. (6.2).

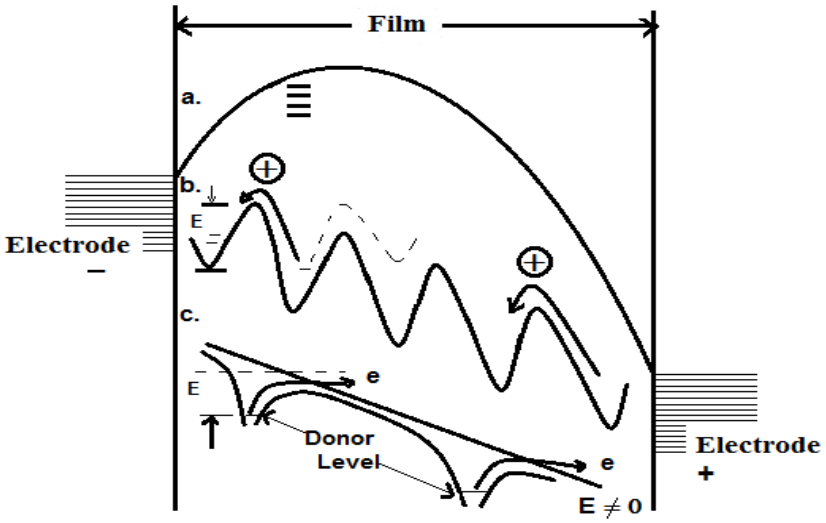

Fig. 6.2 Bulk-limited conduction methods (dotted lines refer to E = 0); (a) space-charge limited; (b) ionic conduction of cations ⊕; (c) Poole-Frenkel emission [43].

The electron may flow through tunneling from the negative electrode into unoccupied portions of the positive electrode in a very thin (few nm) film with a moderate applied field [60], Fig. 6.3(a). For a thicker film and higher voltage (field is greater than the barrier height), the electrons by the tunnel procedure are preferably conveyed into the conduction band of the dielectric somewhat than directly to the opposite electrode; Fig. 6.3(b), transition 1. For a large number of traps, the tunneling in the dielectric can take place through some of the traps, 2 in Fig. 6.3(b). The transfer probability increased significantly in this way [60]. The tunneling can also occur from some occupied traps into the conduction band, 3 in Fig. 6.3(b), or (at high applied fields) from the valence band into the conduction, i.e., Zener breakdown mechanism, Fig. 6.3(c), transition 1.

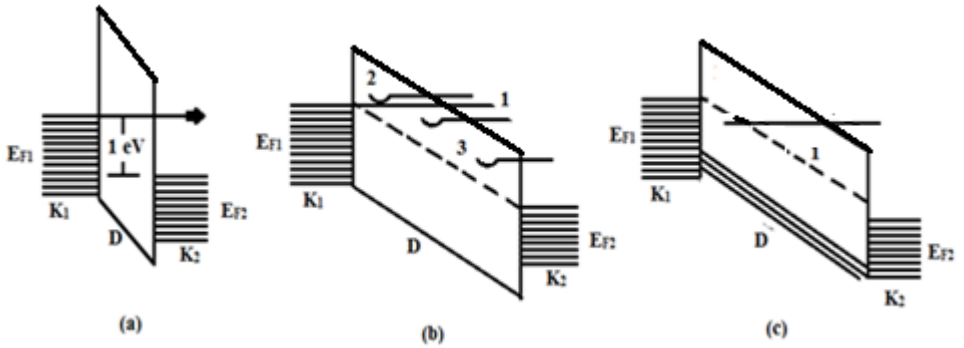

Fig. 6.3 The energy diagrams of possible mechanisms of charge transport in a dielectric film D: (a) tunneling between electrodes K_1 and K_2; (b) tunneling: 1 - into conduction band; 2, 3 – from traps; (c) 1- Zener breakdown; E_{f1} and E_{f2} – Fermi levels in K_1 and K_2 metals [60].

All the mechanisms described above depend upon the flow of free carriers into the dielectric's conduction band. The carriers have a constrained mean free path owing to the multiple interactions undergone in the dielectric. Due to the interaction with optical phonons, the carriers lose their relatively low energy, or traps can catch them. During their journey, they are accelerated by an applied electric field. In a dielectric, the space-charge-limited current is triggered by the drift mobility of charge carriers, which relies on the presence and type of traps, recombination centres, etc. The presence of shallow traps (trap levels exist between the Fermi level and the bottom of the conduction band) may drastically minimize the current. Deep traps [61,62] below the Fermi level have no impact on the current, since they are always full and hence cannot support capturing the injected carriers. The laws are made more complicated by the existence of additional types of traps. The current can increase significantly with double injection and the absence of recombination centres [63]. These recombination centres are responsible for mutually neutralizing the associated space charges. In the case of double injection, the features may illustrate a zone of negative resistance under specific circumstances. This phenomenon is caused by a sudden increase in conductivity, which could be because that the carrier lifetime relies on the injection level.

6.3 Current-voltage (I-V) characteristics

In the current study, ceramic pellet target of $(Ba_{1-x}Ca_x)(Zr_{1-y}Ti_y)O_3$, (x = 0.155, y = 0.9), was prepared by solid-state reaction process through double sintering. Thin films were deposited by radio-frequency (RF) sputtering of the prepared ceramic target, using a RF power of 60 W and argon as the sputtering gas at room temperature. The as-deposited films were annealed at different temperatures (between 500 and 800 ^oC) in the ambient air for one hour. The methods for preparing and characterizing thin films are discussed in Chapter-5. For the measurement of current-voltage (I-V) characteristics of the prepared films, metal-insulator-semiconductor (MIS) structures, Ag/$BCZT_{0.9}$/p-Si, were prepared using a shadowing mask (with circular opening of 0.5 mm diameter) to sputter deposit silver as the top circular electrode(s) of 1.963×10^{-3} cm^2 are and formed the metal-insulator-semiconductor (MIS) structures. Without a mask, silver was deposited on the silicon substrate's back side to create the bottom electrode for the MIS configuration. To measure the current-voltage (I-V) characteristics of the prepared films, a P-E loop tracer (aixACCT Systems GmbH, aixPES) with a piezometer was used. The film thickness

was calculated by optical method, and was found to be around 330 ± 10 nm, Chapter-5. In each I-V measurement, the voltage was swept from 1 to 10 volts, in 19 steps, while a delay time was set at 2 seconds. The top electrode was considered a positive polarity of the applied DC voltage concerning the bottom electrode. All the I-V measurements of $BCZT_{0.9}$ thin films were performed at room temperature. A schematic view of the prepared MIS Ag/$BCZT_{0.9}$/Si/Ag assisted structure is shown in Fig. 6.4.

Fig. 6.5 exhibits the observed current-voltage (I-V) variations of the as-deposited and annealed $BCZT_{0.9}$ films, which were measured at room temperature (RT). All of the prepared films exhibited an exponential rise in current at low voltages, accompanied by a saturation region at higher voltages, except the films annealed at 600, 650, 700, and 750 ^{o}C. No saturation region was observed in the measured applied voltage range for the films annealed at 600, 650, 700 and 750 ^{o}C.

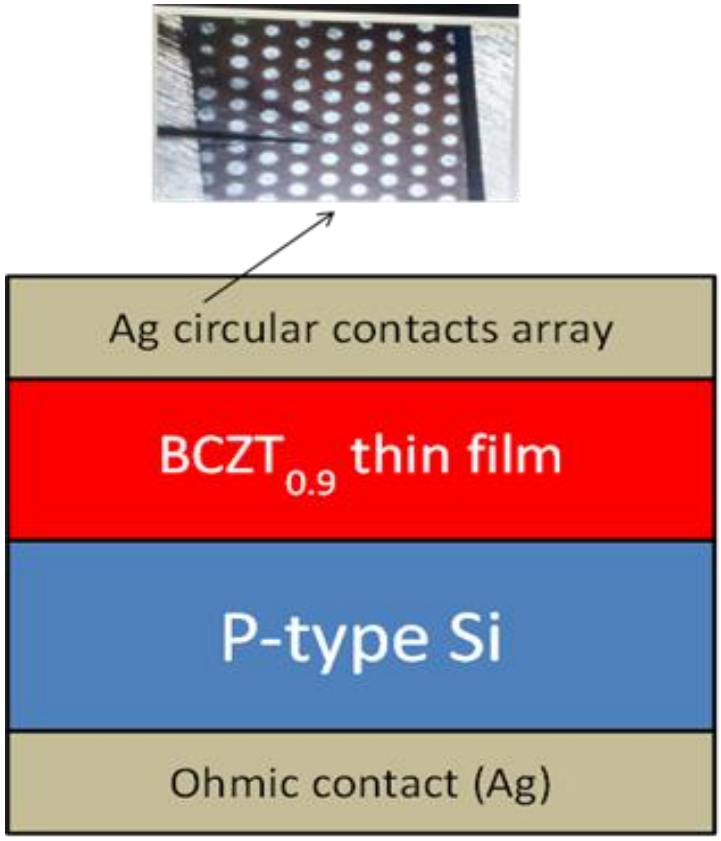

Fig. 6.4 Schematic view of the prepared MIS Ag/$BCZT_{0.9}$/Si/Ag assisted structure.

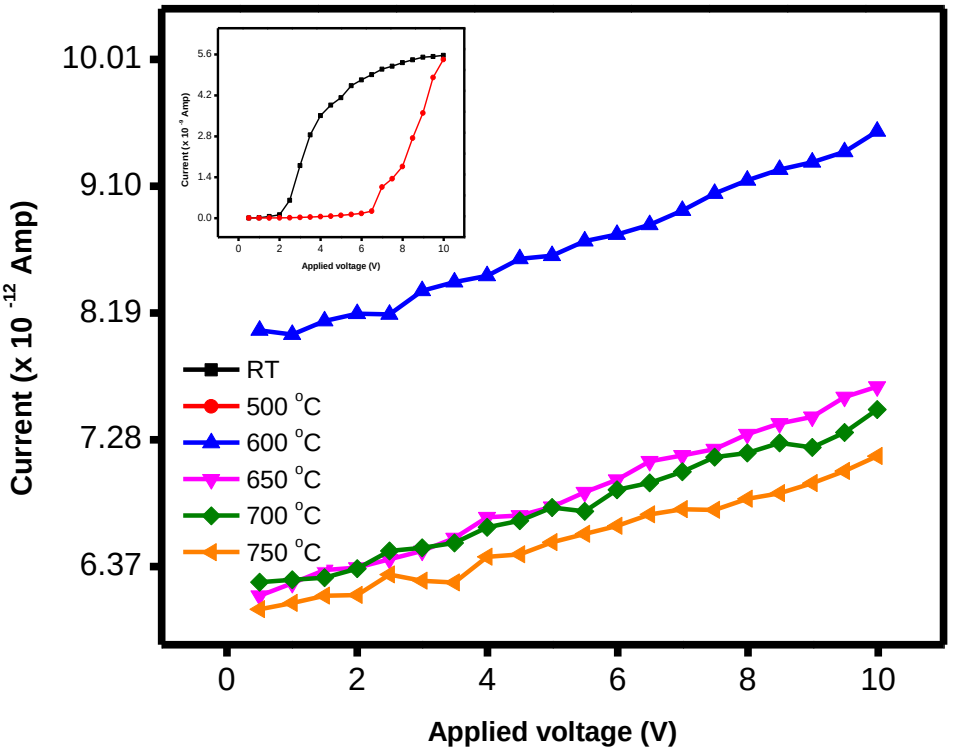

Fig. 6.5 Variation of leakage current with applied voltage (V) in $BCZT_{0.9}$ films annealed at different temperatures.

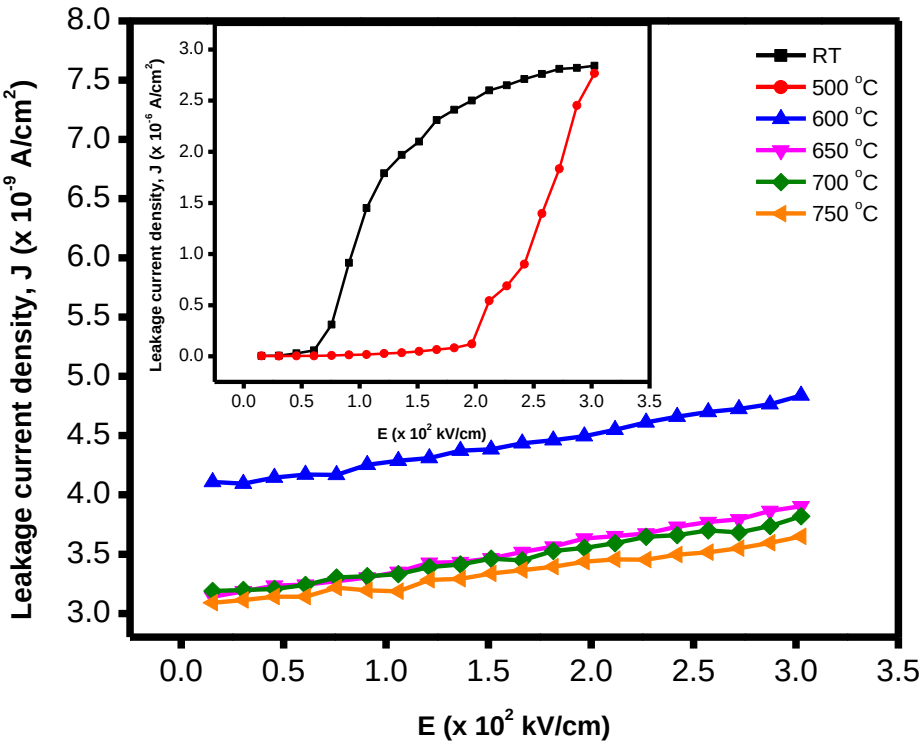

Fig. 6.6 Variation of leakage current density (J) with an applied electric field (E) in $BCZT_{0.9}$ films annealed at different temperatures.

The observed variation of room temperature leakage current density (J) with the applied field (E) for the prepared MIS structures is shown in Fig. 6.6. With higher annealing temperatures, till 750 ^{o}C, the J reduced considerably. The J was observed to be significantly reduced, by order of 10^{-3}, for the $BCZT_{0.9}$ films annealed at and above 600 ^{o}C (crystalline films), compared to that for the films annealed at a lower temperature ($\leq$ 500 ^{o}C) (amorphous films). With increasing annealing temperature ($\leq$ 750 ^{o}C), the leakage current density decreases, which may be the result of enhanced crystallization, film stress, decreased O_2 vacancies, and increased interface oxide layer (SiO_2) thickness [64]. The significant drop in the J of the crystalline $BCZT_{0.9}$ films, which were annealed at temperatures from 600 to 750 ^{o}C, may be attributed to the rise in the film quality, improved oxygen stoichiometry, and decreased weak leakage passes. Though the formation of the interfacial SiO_2 layer increases the barrier height at the interface and thereby reduces the leakage current, this might have also reduced the resultant capacitance of the structure on increasing annealing temperature. Presently, on rising annealing temperature, the capacitance of the MIS structure was found to increase (Chapter-7), which indicates an insignificant effect of the interfacial SiO_2 layer, if forms any.

From the observed I-V and J-E characteristics, different conduction mechanisms, in Ag/$BCZT_{0.9}$/p-Si/Ag MIS structures, in different applied field ranges can be envisaged, Figs. 6.5 and 6.6, respectively [36,65]. For the films annealed at 600, 650, 700 and 750 ^{o}C, the linear variation of leakage current exhibits the ohmic conduction for $E < 1.21 \times 10^2$ kV/cm (corresponding to 4 V), whereas the films deposited at RT and annealed at 500 ^{o}C, show ohmic conduction, for $E \leq 1.05 \times 10^2$ kV/cm (corresponding to 3.5 V) [36,66]. To find the probable conduction mechanisms (Fowler-Nordheim tunneling, Poole-Frenkel emission, Schottky effect, space-charge-limited conduction, or ionic conduction) in Ag/$BCZT_{0.9}$/p-Si MIS film structures, several plots have been drawn for the prepared $BCZT_{0.9}$ films. To find out the possibility of Schottky conduction (Eq. 6.1), a relationship between log (J) and the square root of the electric field was plotted and shown in Fig. 6.7. Similarly, for Poole-Frenkel conduction mechanism, Eq.6.5, log (J/E) *vs* $(E)^{½}$ plot was drawn and shown in Fig. 6.8. The leakage current density (J) was measured lowest (3.6×10^{-9} A/cm^2 at 3.0×10^2 kV/cm, i.e., at 10 V); and dielectric constant (K) maximum, at 1 MHz (148), for the films, annealed at 750 ^{o}C, exhibiting the best electrical properties among the prepared $BCZT_{0.9}$ thin films.

Table 6.2 Refractive indices obtained from Schottky and Poole-Frenkel plots.

Various parameters ($BCZT_{0.9}$ thin films)	**Obtained from SE Plot**	**Obtained from PF Plot (Normal PF) (modified PF effect)**	
		r = 1	**r = 2**
As-deposited films (n_o = 1.8975)			
$n = \sqrt{K_d}$	1.84	0.77	0.38
K_d	3.41	0.60	0.15
Films deposited at 500 ^oC (n_o= 1.8963)			
$n = \sqrt{K_d}$	1.91	0.77	0.38
K_d	3.65	0.59	0.14
Films deposited at 600 ^oC (n_o = 1.9975)			
$n = \sqrt{K_d}$	0.81	0.59	0.30
K_d	0.65	0.35	0.09
Films deposited at 650 ^oC (n_o = 2.0552)			
$n = \sqrt{K_d}$	0.79	0.58	0.29
K_d	0.63	0.34	0.08
Films deposited at 700 ^oC (n_o = 2.0909)			
$n = \sqrt{K_d}$	0.79	0.58	0.29
K_d	0.62	0.34	0.08
Films deposited at 750 ^oC (n_o = 2.0929)			
$n = \sqrt{K_d}$	0.78	0.59	0.29
K_d	0.62	0.34	0.08

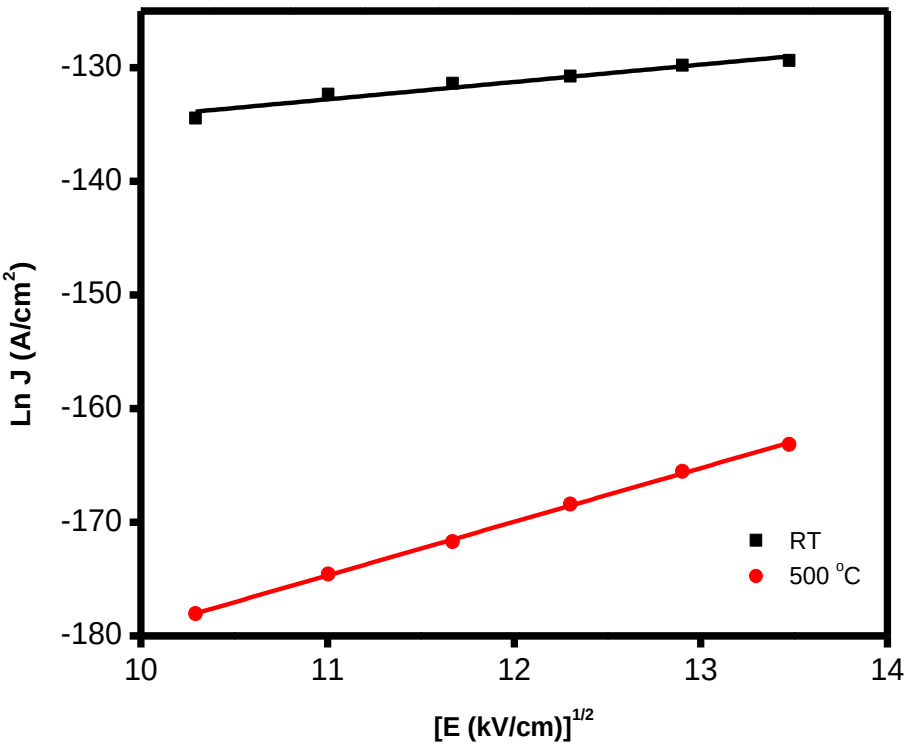

Fig. 6.7 Ln J *vs* √E plot for $BCZT_{0.9}$ films, deposited at RT and annealed at 500 °C (Schottky emission).

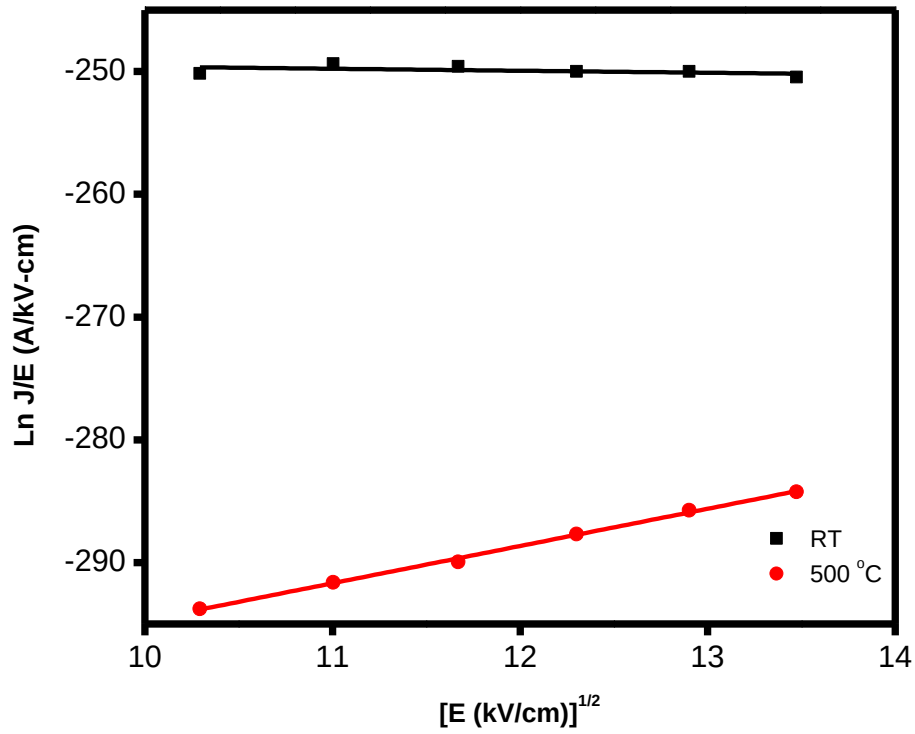

Fig. 6.8 Ln J/E *vs* √E plot for $BCZT_{0.9}$ films, deposited at RT and annealed at 500 °C (suspected Poole-Frenkel conduction).

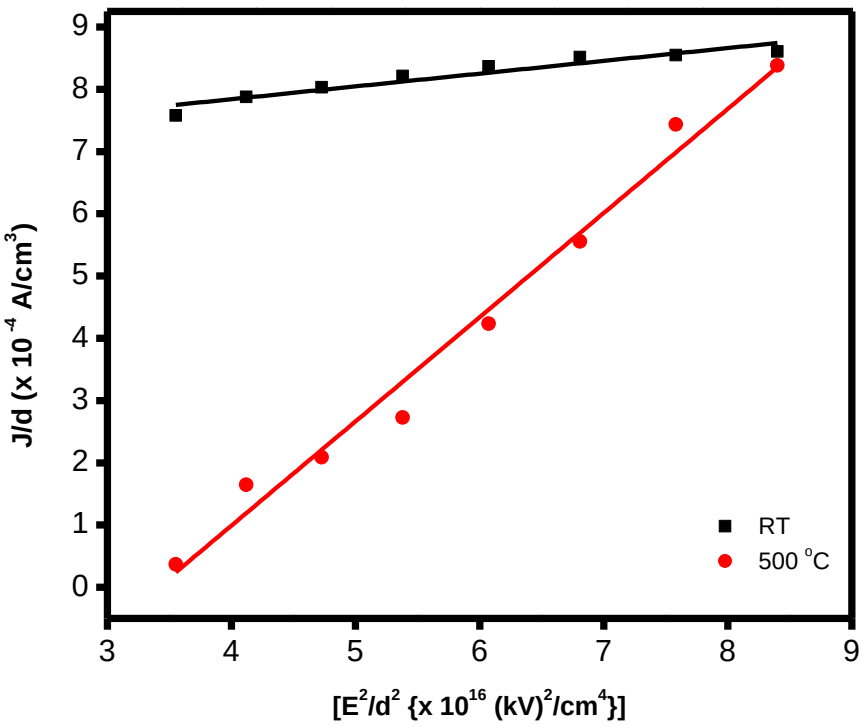

Fig. 6.9 J/d *vs* E^2/d^2 plot for $BCZT_{0.9}$ films, deposited at RT and annealed at 500 °C (Space-charge-limited conduction).

For films deposited at RT and annealed at 500 °C, the linear Ln J *vs* √E plots, Fig. 6.7, indicates the dominance of Schottky emission (SE) [36,65], whereas the linearity in the Ln J/E *vs* √E plot, Fig. 6.8, exhibits prominence of Poole-Frenkel (PF) type conduction [36,65], in the applied field ranging from 1.05 x 10^2 kV/cm to 1.81 x 10^2 kV/cm. Out of the two mechanisms, the SE and PF, the dominating mechanism is determined from the consistency of the refractive index (n_o) obtained from the optical measurements and the refractive index ($n = \sqrt{K_d}$), where K_d is the dynamic dielectric constant obtained from electrical measurements, and the refractive index (n_o) calculated from the optical data (at 550 nm), Table 6.2 [36,65]. The consistency of the refractive index, obtained from the two methods, supports the dominance of SE [67] and discards the possibility of PF-type conduction in the applied field between 1.05 x 10^2 kV/cm and 1.81 x 10^2 kV/cm for these films. Further, in the higher measured field range (E > 1.81 x 10^2 kV/cm), the linearity between J/d *vs* E^2/d^2 plot, exhibited the dominance of space-charge-limited type conduction [68,69], in the films deposited at RT and annealed at 500 °C, Fig. 6.9.

Similarly, in the field range, 1.05 x 10^2 kV/cm < E ≤ 1.81 x 10^2 kV/cm, the linearity in Ln J *vs* √E and Ln J/E *vs* √E plots indicated the possibility of the SE and PF conduction, but the inconsistency of the refractive indices, obtained from optical and electrical measurements, discards the possibility of either of these conductions, in the films annealed at 600, 650, 700 and

750 ^{o}C; whereas the linearity of the J/d *vs* E^2/d^2 (d is the film thickness) plots exhibits the dominance of space-charge-limited (SCL) current conduction, in the measured field range, $E \geq 1.21 \times 10^2$ kV/cm, in these film, Fig. 6.10.

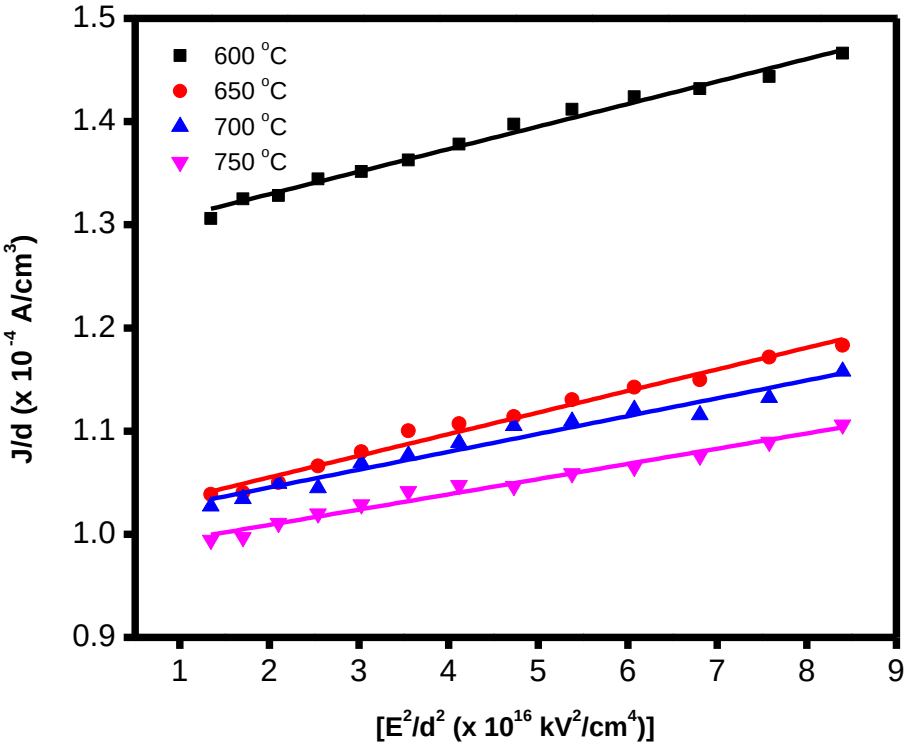

Fig. 6.10 J/d *vs* E^2/d^2 plots for the $BCZT_{0.9}$ films, annealed at 600, 650, 700 and 750 ^{o}C (Space-charge-limited conduction).

A probability of tunneling conduction was shown by the linear Ln (J/E^2) *vs* 1/E curve for the films, annealed at 600, 650, 700 and 750 ^{o}C, at the higher fields ($E \geq 1.96 \times 10^2$ kV/cm), Fig. 6.11. The tunneling conduction operation is initiated by the migration of trap carriers into the conduction band as a result of field ionization or by the tunneling of electrons from the Fermi energy extent of metal into the insulator conduction band [36,70,71]. The probability of various tunneling conduction mechanisms, including Fowler-Nordheim, direct, and double barrier, was investigated by Chaneliere et al. [49] and may contribute to the $BCZT_{0.9}$ MIS structures. The current conduction in the films that have been annealed at 600, 650, 700, and 750 ^{o}C may be influenced by these tunneling processes. The possibilities of tunneling through the film volume are meager because the deposited film thickness in the current study was relatively high (around

330 nm). Very thin films (less than 50 nm) have a high tunneling probability. The fact that the very thin interfacial SiO_2 layer forms on the silicon substrate and thickens with increasing annealing temperature may be helped to explain the observed tunneling [70,72]. The increased interfacial SiO_2 layer increases the field to notice tunneling conduction ($\geq 1.96 \times 10^2$ kV/cm) in the annealed films. Films crystallize on annealing at and above 700 ^oC. There is a probability of tunneling conduction in the films annealed films (600, 650, 700 and 750 ^oC), at the higher electric fields ($\geq 1.96 \times 10^2$ kV/cm); however, owing to the increased thickness of the interfacial SiO_2 layer, the probability of tunneling conduction becomes low in the 600-750 ^oC annealed films, Fig. 6.11. Since Schottky and Poole-Frenkel conductions are not possible within the films annealed at 600, 650, 700 and 750 ^oC, the trap-assisted tunneling (double barrier and direct) through the anode to the cathode can be excluded. These measurements indicate the dominance of Fowler-Nordheim (FN) tunneling from the Fermi level of the electrodes into the insulator conduction band, through a very thin SiO_2 interface layer, without trap electron hopping, in the 600, 650, 700 and 750 ^oC annealed $BCZT_{0.9}$ films, in the higher fields, $E \geq 1.96 \times 10^2$ kV/cm.

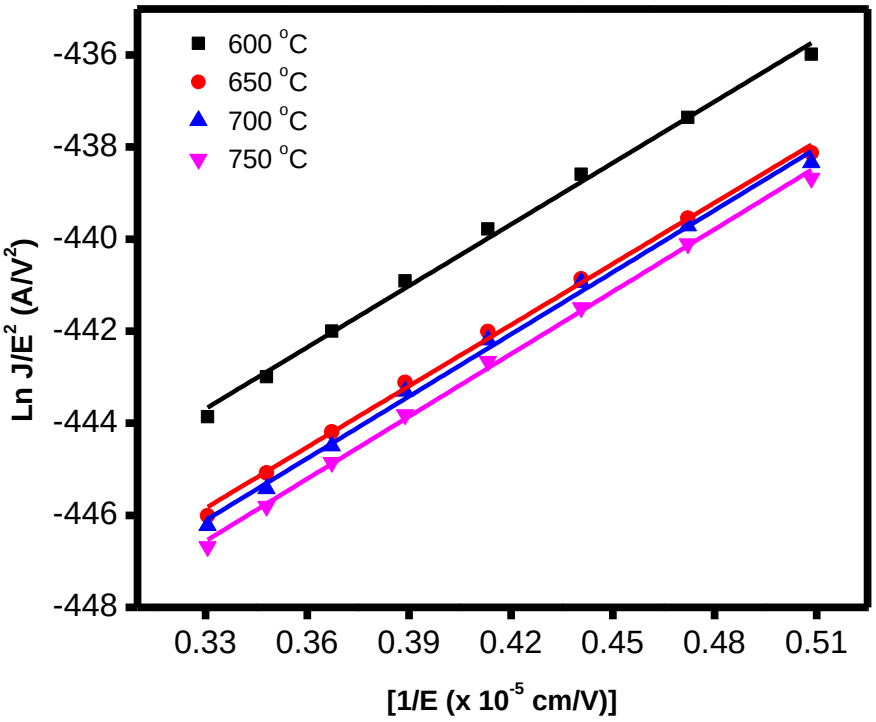

Fig. 6.11 Ln (J/E^2) *vs* 1/E plot for the $BCZT_{0.9}$ films, annealed at 600, 650, 700 and 750 ^oC (Fowler-Nordheim tunneling).

6.4 Discussion

The leakage current density (J) of the presently prepared $BCZT_{0.9}$ films was observed to vary with annealing temperature. At the measured electric field 3.0×10^2 kV/cm, among the prepared films, the minimum J was measured 3.6×10^{-9} A/cm^2 for the films annealed at 750 ^oC, Fig. 6.5. Presently, for the as-deposited and films annealed at various temperatures, the breakdown was not detected in the observed field range, i.e., up to 3.0×10^2 kV/cm. Structural imperfections and stress may influence the electrical properties of amorphous thin films. The leakage current density was measured to reduce due to the compensation of oxygen vacancies. The leakage current density was also strongly observed depending on the annealing temperature. Generally, the gradual decreasing behaviour of the leakage current was observed in the $BCZT_{0.9}$ films on annealing up to 750 ^oC, which can be owing to the enhanced crystallization and compensating oxygen vacancies during annealing. A drastic reduction in leakage current was observed for all the deposited $BCZT_{0.9}$ films, annealed from 600 to 750 ^oC, which may be attributed to the heightened barrier height at the interface due to the formation of an interfacial SiO_2 layer between silicon and oxide film.

An in-depth understanding of various conduction mechanisms in MIS structures might lower the leakage current's value. The current work investigated the different conduction mechanisms of the $BCZT_{0.9}$ films, deposited at RT and annealed at 500, 600, 650, 700 and 750 ^oC. The various conduction operations were found depending on the different annealing conditions. The developing interfacial SiO_2 layer, which depends on annealing treatment, was essential in computing the probable current conduction operations in the prepared $BCZT_{0.9}$ films.

It is still necessary to conduct further research to understand the current transport phenomena in dielectrics. More rigorous theoretical models and experimentation would explore the insights of the system examined. More work would be needed to understand the underlying process since these measurements are essential for electronic applications.

References

[1] S.S. Eaton, D.B. Butler, M. Parris, D. Wilson, H. McNeille, A Ferroelectric Nonvolatile Memory, IEEE International Solid State Circuits Conference, Digest of Technical Papers. 329 (1988) 130-131. https://doi.org/10.1109/ISSCC.1988.663665

[2] O. Auciello, C.M. Foster, Processing technologies for ferroelectric thin films and heterostructures, Annual Review of Materials Science. 28 (1998) 501-531. https://doi.org/10.1146/annurev.matsci.28.1.501

[3] H. Ishiwara, Current status and prospects of FET-type ferroelectric memories, Annual Device Research Conference Digest (IEEE 1999) 1 (2001) 6-9. https://doi.org/10.1109/DRC.1999.806306

[4] J.F. Scott, C.A. Paz de Araujo, Ferroelectric memories, Science. 246 (1989) 1400-1405. https://doi.org/10.1126/science.246.4936.140

[5] T. Sumi, N. Moriwaki, G. Nakane, T. Nakakuma, Y. Judai, Y. Uemoto, Y. Nagano, S. Hayashi, M. Azuma, T. Otsuki, G. Kano, J.D. Cuchiaro, M.C. Scott, L.D. McMillan, C.A. Paz de Araujo, 256Kb Ferroelectric nonvolatile memory technology for 1T/1C cell with 100ns read/write time at 3V, Integrated Ferroelectrics. 6 (1995) 1-13. https://doi.org/10.1080/10584589508019349

[6] D.A. Buck, Ferroelectrics for Digital Information Storage and Switching, Report R-212, MIT, 1952.

[7] K. Seshan, Thin film deposition processes and techniques, 1st ed., Noyes publishing/william andrew publishing, New York, 2002.

[8] O. Saburi, Properties of semiconductive barium titanates, Journal of the Physical Society of Jppan. 14 (1959) 1159-1174. https://doi.org/10.1143/JPSJ.14.1159

[9] K. D. Budd, S. K. Dey, D. A. Payne, Sol-gel processing of PbTiO//3, PbZrO//3, PZT, and plzt thin films, British Ceramic Proceedings, pp. 107-121, 1985.

[10] R.W. Vest, Metallo-organic decomposition (MOD) processing of ferroelectric and electro-optic films: A review, Ferroelectrics. 102 (1990) 53-68. https://doi.org/10.1080/00150199008221465

[11] G.H. Haertling, PLZT thin films prepared from acetate precursors, Ferroelectrics. 116 (1991) 51-63. https://doi.org/10.1080/00150199108007929

[12] L.M. Sheppard, Advances in processing of ferroelectric thin films, American Ceramic Society Bulletin. 71 (1992) 85-95.

[13] G. Li, Ph. D. Dissertation, Clemson University, Clemson, SC, 1995.

[14] R.W. Schwartz, T.J. Boyle, S.J. Lockwood, M.B. Sinclair, D. Dimos, C.D. Buchheit, Sol-gel processing of PZT thin films: A review of the state-of-the-art and process optimization strategies, Integrated Ferroelectrics. 7 (1995) 259-277. https://doi.org/10.1080/10584589508220238

[15] O. Auciello, A.I. Kingon, S.B. Krupanidhi, Sputter Synthesis of Ferroelectric Films and Heterostructures, MRS Bulletin. 21 (1996) 25-30. https://doi.org/10.1557/S0883769400046042

[16] J.J. Pankove, Optical Processes in Semiconductors, 1st ed., Prentice Hall, New Jersey, 1956.

[17] C. Kittel, Solid State Physics, 1st ed., John Wiley and Sons publishing, 1970.

[18] H. Tanaka, H. Tabata, T.K.T. Kawai, S.K.S. Kawai, Dominant Factors for Formation of Perovskite $PbTiO_3$ Films Using Excimer Laser Ablation, Japanese Journal of Applied Physics. 33 (1994) L451. https://doi.org/10.1143/JJAP.33.L451

[19] R. Bruchhaus, H. Huber, D. Pitzer, W. Wersing, Sputtered PZT films for ferroelectric devices, Integrated Ferroelectrics. 4 (1994) 365-370. https://doi.org/10.1080/10584589408223882
[20] Y.M. Kang, J.K. Ku, S. Baik, Crystallographic characterization of tetragonal (Pb,La)TiO_3 epitaxial thin films grown by pulsed laser deposition, Journal of Applied Physics. 78 (1995) 2601. https://doi.org/10.1063/1.360120
[21] A.R. Raju, C.N.R. Rao, Oriented ferroelectric thin films of $PbTiO_3$, (Pb,La)TiO_3, and Pb(Zr,Ti)O_3 by nebulized spray pyrolysis, Applied physics letters. 66 (1995) 896. https://doi.org/10.1063/1.113424
[22] V.R. Palkar, S.C. Purandare, S.P. Pai, S. Chattopadhyay, P.R. Apte, R. Pinto, M.S. Multani, C-axis oriented ferroelectric thin films of $PbTiO_3$ on Si by pulsed laser ablation, Applied physics letters. 68 (1996) 1582. https://doi.org/10.1063/1.116687
[23] P.C. Joshi, M.W. Cole, Influence of postdeposition annealing on the enhanced structural and electrical properties of amorphous and crystalline Ta_2O_5 thin films for dynamic random access memory applications, Journal of Applied Physics. 86 (1999) 871. https://doi.org/10.1063/1.370817
[24] J.F. Scott, Ferroelectric Memories, 1st ed., Springer-Verlag publishing, Berlin, Germany, 2000.
[25] K. Corp, N.M. Albuquweque, R. Womack, An experimental 512-bit nonvolatile memory with ferroelectric storage cell, IEEE Journal of Solid-State Circuits. 23 (1988) 1171-1175. https://doi.org/10.1109/4.5940
[26] T. Ueda, A. Noma, D. Usda, GaAs MMIC Chip-sets for mobile communication systems with on-chip ferroelectric capacitors, Integrated Ferroelectrics. 7 (1995) 45-60. https://doi.org/10.1080/10584589508220220
[27] H. Takasu, The ferroelectric memory and its applications, Journal of Electroceramics. 4 (2000) 327-338. https://doi.org/10.1023/A:1009910525462
[28] N. Izyumskaya; Y.I. Alivov, S.J. Cho, H.H. Morkoç, H. Lee, Y.S. Kang, Processing, structure, properties, and applications of PZT thin films, Critical Reviews in Solid State and Materials Sciences. 32 (2007) 111-202. https://doi.org/10.1080/10408430701707347
[29] M. Dawber, K.M. Rabbe, J.F. Scott, Physics of thin-film ferroelectric oxides, Review of Modern Physics. 77 (2005) 1083-1130. https://doi.org/10.1103/RevModPhys.77.1083
[30] M. Chentir, E. Bouyssou, L. Ventura, C. Anceau, Leakage current evolution versus dielectric thickness in lead zirconate titanate thin film capacitors, Journal of Applied Physics. 105 (2009) 061605. https://doi.org/10.1063/1.3055416
[31] W. Pabst, L.W. Martin, Y. Chu, R. Ramesh, Leakage mechanisms in thin films, Applied Physics Letters. 90 (2007) 072902. https://doi.org/10.1063/1.2535663
[32] T. Mihara, H. Watanabe, Electronic conduction characteristics of sol-gel ferroelectric Pb($Zr_{0.4}Ti_{0.6}$)O_3 thin-film capacitors: part I, Japanese Journal of Applied Physics. 34 (1995) 5664. https://doi.org/10.1143/JJAP.34.5664
[33] H. Schroeder, S. Schmitz, P. Meuffels, Applied Physics Letters. 82 (2003) 781. https://doi.org/10.1063/1.1541096
[34] B. Chen, H. Yang, L. Zhao, J. Miao, B. Xu, X.G. Qiu, B.R. Zhao, X.Y. Qi, X.F. Duan, Thickness and dielectric constant of dead layer in Pt/($Ba_{0.7}Sr_{0.3}$)TiO_3/$YBa_2Cu_3O_{7-x}$ capacitor, Applied Physics Letters. 84 (2004) 583. https://doi.org/10.1063/1.1644342
[35] J. Frenkel, Mechanism of conductivity in metal-polymermetal structures, Technical Physics of the USSR, 1938: pp. 685.

[36] S.M. Sze, Physics of Semiconductor Devices, 2nd ed., Wiley Publishing, New York, 1981.
[37] C.H. Lin, P.A. Friddle, C.H. Ma, A. Daga, H. Chen, Effects of thickness on the electrical properties of metalorganic chemical vapor deposited Pb(Zr,Ti)O_3 (25-100 nm) thin films on $LaNiO_3$ buffered Si, Journal of Applied Physics. 90 (2001) 1509. https://doi.org/10.1063/1.1383262
[38] I. Boerasu, L. Pintilie, M. Pereira, M.I. Vasilevskiy, M.J.M. Gomes, Competition between ferroelectric and semiconductor properties in Pb($Zr_{0.65}Ti_{0.35}$)O_3 thin films deposited by sol-gel, Journal of Applied Physics. 93 (2003) 4776. https://doi.org/10.1063/1.1562009
[39] Y.S. Sang, S. J. Lee, S. H. Kim, B. G. Cahe, M.S. Jang, Schottky barrier effects in the electronic conduction of sol-gel derived lead zirconate titanate thin film capacitors, Journal of Applied Physics. 84 (1998) 5005. https://doi.org/10.1063/1.368747
[40] J.F. Scott, C.A. Araujo, B.M. Melnick, L.D. McMillan, R. Zuleeg, Quantitative measurement of space-charge effects in lead zirconate-titanate memories, Journal of Applied Physics. 70 (1991) 382. https://doi.org/10.1063/1.350286
[41] K.H. Ahn, S.S. Kim, S. Baik, Thickness dependence of leakage current behavior in epitaxial (Ba,Sr)TiO_3 film capacitors, Journal of Applied Physics. 93 (2003) 1725. https://doi.org/10.1063/1.1535750
[42] G. Dietz, R. Waser, Charge injection in $SrTiO_3$ thin films, Thin Solid Films. 299 (1997) 53-58. https://doi.org/10.1016/S0040-6090(96)09073-6
[43] M. Ohring, The material science of thin films, 1st ed., Academic press publishing, San Diego, 1995.
[44] E.H. Nicollian, J.R. Brews, MOS Physics and Technology, 1st ed., Wiley Publishing, New York, 1982.
[45] V. lingwal, N.S. Panwar, Capacitance-voltage characteristics of $NaNbO_3$ thin films, Journal of Applied Physics. 94 (2003) 4571. https://doi.org/10.1063/1.1608470
[46] R. Moazzami, C. Hu, W.H. Shepherd, Electrical conduction and breakdown in sol-gel derived PZT thin films, IEEE Proceedings on Reliability Physics Symposium, New Orleans, pp. 231-236, 1990. https://doi.org/10.1109/RELPHY.1990.66092
[47] R. Moazzami, Electrical characteristics of ferroelectric PZT thin films for DRAM applications, IEEE Transactions on Electron Devices. 39 (1992) 2044-2049. https://doi.org/10.1109/16.155876
[48] E. Bertran, J.M. Lopez-Villegas, J.L. Andujar, J. Campmany, A. Canillas, J.R. Morante, Optical and electrical properties of a-Si_xN_y: H films prepared by rf plasma using N_2+SiH_4 gas mixtures, Journal of Non-Crystalline Solids. 137 (1991) 895-898. https://doi.org/10.1016/S0022-3093(05)80264-9
[49] C. Chanaliere, S. Four, J.L. Autran, R.A.B. Devine, N.P. Sandler, Properties of amorphous and crystalline Ta_2O_5 thin films deposited on Si from a Ta(OC_2H_5)$_5$ precursor, Journal of Applied Physics. 83 (1998) 4823. https://doi.org/10.1063/1.367277
[50] W. Schottky, Semiconductor theory of the barrier layer, The Natural Sciences. 26 (1938) 843. https://doi.org/10.1007/BF01774216
[51] S.M. Sze, C.R. Crowel, D. Kahng, Photoelectric determination of the image force dielectric constant for hot electrons in Schottky barriers, Journal of Applied Physics. 35 (1964) 2534. https://doi.org/10.1063/1.1702894
[52] R. Ongaro, A. Pillonnet, Poole-Frenkel (PF) effect high field saturation, Revue de Physique Appliquée. 24 (1989) 1085-1095. https://doi.org/10.1051/rphysap:0198900240120108500

[53] J.G. Simmons, Poole-Frenkel effect and Schottky effect in metal-insulator-metal systems, Physical Review. 155 (1967) 657-660. https://doi.org/10.1103/PhysRev.155.657
[54] J.R. Yeargan, H.L. Taylor, The Poole-Frenkel effect with compensation present, Journal of Applied Physics. 39 (1968) 5600. https://doi.org/10.1063/1.1656022
[55] A.K. Jonscher, Electronic properties of amorphous dielectric films, Thin Solid Films. 1 (1967) 213-234. https://doi.org/10.1016/0040-6090(67)90004-1
[56] V. Nazabal, F. Charpentier, J.L. Adam, P. Nemec, H. Lhermite, M.L.B. Anne, J. Charrier, J.P. Guin, A. Moréac, Sputtering and pulsed laser deposition for near- and mid-infrared applications: A comparative study of $Ge_{25}Sb_{10}S_{65}$ and $Ge_{25}Sb_{10}Se_{65}$ amorphous thin films, International Journal of Applied ceramic Technology. 8 (2011) 990-1000. https://doi.org/10.1111/j.1744-7402.2010.02571.x
[57] J. Frenkel, On pre-breakdown phenomena in insulators and electronic semi-conductors, Physical Review. 54 (1938) 647-648. https://doi.org/10.1103/PhysRev.54.647
[58] S.M. Sze, Current transport and maximum dielectric strength of silicon nitride films, Journal of Applied Physics. 38 (1967) 2951. https://doi.org/10.1063/1.1710030
[59] J.J. O'Dwyer, The theory of electrical conduction and breakdown in solid dielectrics, 1st ed., Clarendon Press publishing, Oxford, New York, 1973.
[60] L. Eckertova, Physics of Thin Films, 1st ed., Plenum Press publishing, New York, 1977.
[61] N.A. Chowdhury, D. Misra, Charge trapping at deep states in Hf-silicate based high-K gate dielectrics, Journal of The Electrochemical Society. 154 (2007) 30. https://doi.org/10.1149/1.2402989
[62] P. Mark, M. Allen, Electrical properties: charge injection phenomena, Annual Review of Materials Science. 3 (1973) 111-146. https://doi.org/10.1146/annurev.ms.03.080173.000551
[63] M. Silver, D. Adler, M.P. Shaw, V. Cannella, J. McGill, MRS Online Proceedings Library. 70 (1986) 119-124. https://doi.org/10.1557/PROC-70-119
[64] E. Atanassova, M. Kalitzova, G. Zollo, A. Paskaleva, A. Peeva, M. Georgieva, G. Vitali, High temperature-induced crystallization in tantalum pentoxide layers and its influence on the electrical properties, Thin Solid Films. 426 (2003) 191-199. https://doi.org/10.1016/S0040-6090(03)00027-0
[65] P. Thapliyal, N.S. Panwar, G.M. Rao, Optical properties and current conduction in annealed $(Ta_2O_5)_{0.94}$ - $(TiO_2)_{0.06}$ thin films, Superlattices and Microstructures. 158 (2021) 107008. https://doi.org/10.1016/j.spmi.2021.107008
[66] P.L. Young, dc electrical conduction in thin Ta_2O_5 films. I. Bulk-limited conduction, Journal of Applied Physics. 47 (1976) 235. https://doi.org/10.1063/1.322354
[67] R. Brazis, P. Pipinys, A. Rimeika, V. Lapeika, Electron transport in Ta_2O_5 films, Journal of materials science letters, 9 (1990) 266-267. https://doi.org/10.1007/BF00725819
[68] G.M. Rao, S.B. Krupanidhi, Study of electrical properties of pulsed excimer laser deposited strontium titanate films, Journal of Applied Physics. 75 (1994) 2604. https://doi.org/10.1063/1.356235
[69] D. Landheer, K. Rajesh, D. Masson, J.E. Huise, G.I. Sproule, T. Quance, Factors affecting interface-state density and stress of silicon nitride films deposited on Si by electron-cyclotron resonance chemical vapor deposition, Journal of Vacuum Science & Technology A. A16 (1998) 2931. https://doi.org/10.1116/1.581442

[70] E. Atanassova, N. Novkovski, A. Paskaleva, M. Pecovska-Gjorgjevich, Oxygen annealing modification of conduction mechanism in thin rf sputtered Ta_2O_5 on Si, Solid State Electrons. 46 (2002) 1887-1898. https://doi.org/10.1016/S0038-1101(02)00134-X

[71] G.Q. Lo, D.L. Kwong, S. Lee, Metal-oxide-semiconductor characteristics of chemical vapor deposited Ta_2O_5 films, Applied Physics Letters. 60 (1992) 3286. https://doi.org/10.1063/1.106721

[72] C. Chaneliere, J.L. Autran, R.A.B. Devine, B. Balland, Tantalum pentoxide (Ta_2O_5) thin films for advanced dielectric applications, Materials Science and Engineering: R: Reports. 22 (1998) 269-322. https://doi.org/10.1016/S0927-796X(97)00023-5

CHAPTER-7

Capacitance-voltage characteristics of $(Ba_{1-x}Ca_x)(Zr_{1-y}Ti_y)O_3$, (x = 0.155, y = 0.9), thin films

---

Brief summary

The capacitance-voltage characteristics of the prepared $BCZT_{0.9}$ films, annealed at different temperatures, have been described in this chapter. MIS Ag/$BCZT_{0.9}$/Si/Ag assisted structure was prepared to measure the capacitance-voltage characteristics of the prepared $BCZT_{0.9}$ films. The variation of room temperature dielectric constant (K) with annealing temperature (^oC) for the prepared MIS structures was measured. With a rise in annealing temperature, the improved density and increase in grain size may be attributed to the observed increase in the dielectric constant (K) of the $BCZT_{0.9}$ films. The dielectric constant was obtained maximum, 148 (at 1 MHz), and leakage current density minimum, 3.6×10^{-9} A/cm^2 (at 3.0×10^2 kV/cm electric field), for the films, annealed at 750 ^oC. Dielectric characteristics were observed to improve for the films annealed at 750 ^oC than other annealed films.

CHAPTER-7

Capacitance-voltage characteristics of $(Ba_{1-x}Ca_x)(Zr_{1-y}Ti_y)O_3$, (x = 0.155, y = 0.9), thin films

7.1 Introduction

Over the past few years, ferroelectric materials have been integrated into semiconductor technology through extensive research and development. Integrated circuits built on silicon have already been constructed with ferroelectric capacitors. Electrical characterization of the ferroelectric capacitor is a significant part of gate stack characterization of the insulating films and the semiconductor surface research [1-5]. Capacitance-voltage (C-V) measurements are one of the most accepted methods for getting information on the interface states, oxide charges, ion move through the insulator and the silicon impurity [6-9]. Frankl [10] described the utilization of metal-insulator-semiconductor (MIS) capacitor capacitance-voltage curves to examine such devices. Terman [11] studied C-V variations to determine surface state densities. Grove et al. [12] first published papers on these studies, which contributed an important role in understanding and developing metal-insulator-semiconductor (MIS) technology. Deal et al. [13] used C-V variations to illustrate the barrier heights for various gate metals. Zaininger and Heiman [14] described the variety of material/device variables that may be calculated from C-V variations. Both low and high frequencies are used to measure MIS capacitance. Castagne [15], Kuhn [16], Kappallo and Walsh [17] demonstrated the low-frequency C-V variations, which are mentioned as quasi-static calculations to measure interface traps. The MIS capacitor characteristics are well documented in the popular books by Sze [18] and Nicollian and Brews [7].

C-V variations in a semiconductor device are performed by using two simultaneous voltage sources; an applied small alternating current (AC) voltage and a direct current (DC) voltage (V_{dc}) [19]. The measurement of capacitance is based on the variations in the magnitude of direct current (DC) voltage for a fixed AC signal. The direct current (DC) voltage bias is used to enable the sampling of the material at various depths in the device. The alternating current (AC) bias presents the small-signal bias so that the capacitance measurements may be conducted at a given depth in the device.

7.2 Typical capacitance-voltage (C-V) characteristics

The numerous charges may be computed by the capacitance-voltage (C-V) characteristics of metal-insulator-semiconductor capacitors (MIS-C) [20,21]. The energy band diagrams of an ideal and a practical MIS capacitor with a p- or an n-type substrate has been shown in Fig. 7.1 [20,21].

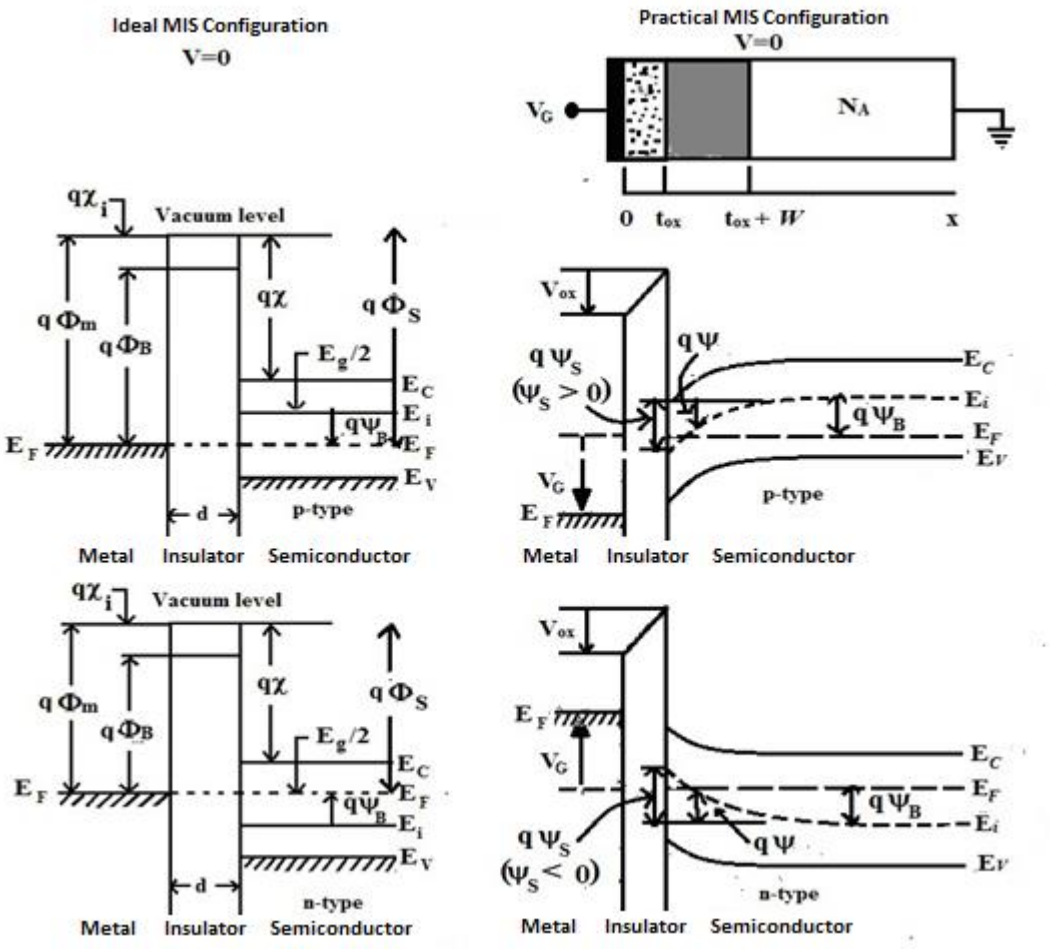

Fig. 7.1 An ideal and practical MIS capacitor's energy band diagram [21].

The intrinsic energy level E_i or voltage ψ in the neutral region of the device is selected as the zero reference potential. At the semiconductor surface, $\psi = \psi_s$, where ψ_s is called the surface potential. The work function of the metal (or semiconductor) Φ_m (or Φ_s) is the energy essential for an electron within the metal (or semiconductor) to shift from the Fermi level to the vacuum

level. The two work functions are the same in the ideal MIS structure $\Phi_{ms} \equiv \Phi_m - \Phi_s = 0$, as shown in Fig. 7.1.

Observations of C-V variation for p-type substrates are generally measured by 'sweeping' the bias voltage at fixed high AC frequency and simultaneously measuring capacitance, which changes owing to accumulation, depletion, and inversion of charge carrier in the semiconductor substrate adjacent to the dielectric interface, as given in Fig. 7.2. When the metal electrode is biased negatively (i.e., $\psi_s < 0$) concerning "p-type" semiconductor (Si in the present case), the band bending results in an accumulation of the majority of p-type carriers, and a negative surface voltage appear adjacent to the semiconductor surface, Fig. 7.2(b(i)); this is the charge accumulation situation. In this situation, the capacitance, C, is determined by the thickness of the dielectric alone, whereas, when a less positive voltage is applied onto the metal (i.e., $\psi_B > \psi_s > 0$), the band bends downwards, Fig. 7.2(b(ii)), and the semiconductor surface potential becomes more positive, and majority carriers (holes) are repelled away from the film/substrate interface layer, to a depletion depth; this is the charge depletion situation. In the depletion case, the rate of electron-hole pair recombination is highest near the semiconductor surface [22]. Additionally, raising the gate (metal) voltage ($\psi_s > \psi_B$) in the positive direction, the bands bend even more downward. Further, the intrinsic level E_i at the surface crosses over the Fermi level E_F, Fig. 7.2 b(iii). In the present study, the number of electrons (minority carriers) at the surface is higher than that of the holes, the surface is thus inverted, and this is the 'inversion' case. In the inversion region, capacitance is computed by the thickness of that film and depletion depth, which is, therefore, lower. At a very large positive bias potential, the concentration of electrons in the inversion becomes high. Deep depletion (DD), as shown in Fig. 7.2(a), occurs in the MIS capacitor when the high-frequency capacitance is measured, i.e., while the gate voltage is swept 'rapidly'. 'Rapidly' means that the gate voltage must change fast enough so the structure is not in thermal equilibrium [23].

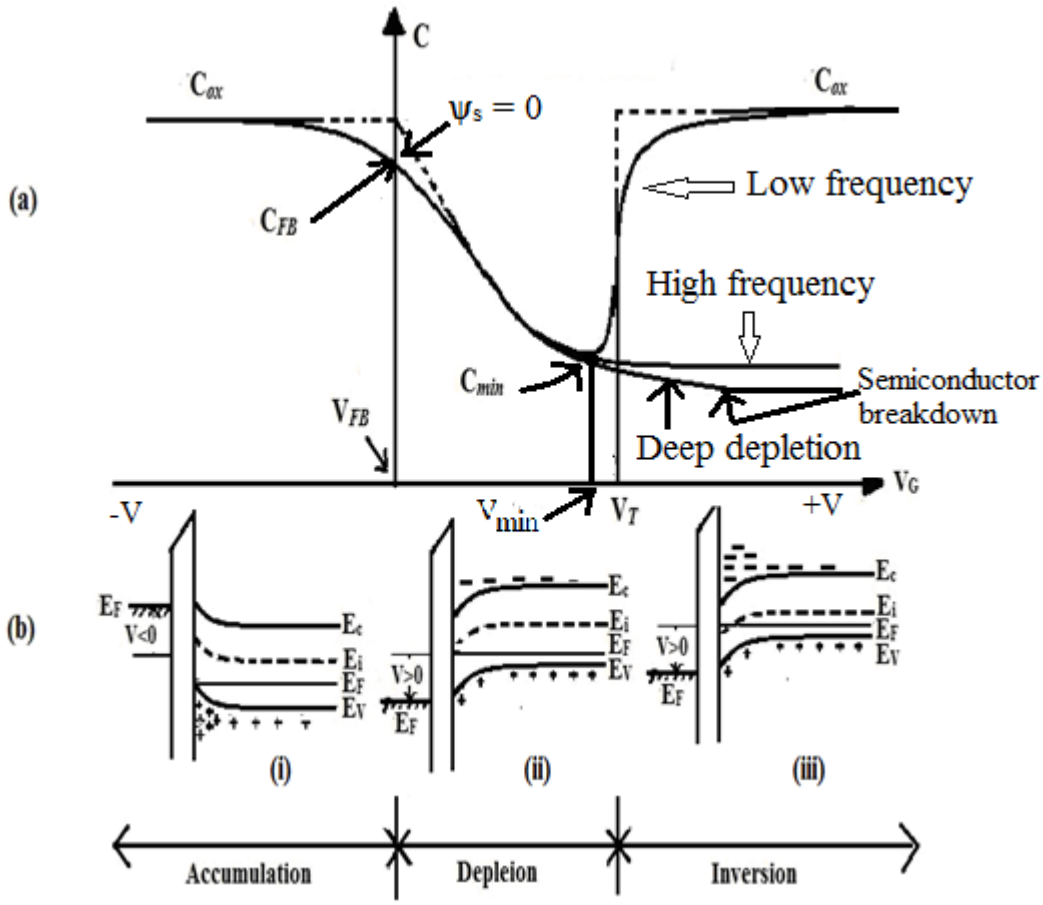

Fig. 7.2 Typical MIS, on p- type substrate, (a) capacitance- voltage curves for low frequency (LF), high frequency (HF) and deep depletion (DD) [24], and (b) band diagram for HF [19, 25-26].

When dealing with practical MIS systems (on p- type substrates), one must consider the effects of actual surfaces. First, the choice of metal and semiconductor results in a non-zero work function difference ($\Phi_{ms} = \Phi_m \sim \Phi_s \neq 0$), as shown in Fig. 7.3(a). Second, there are charges inside the oxide and at the film/substrate interface. In this case, the band diagram at equilibrium has a tilt in the oxide conduction band to align the Fermi levels, given in Fig. 7.3(b). Consequently, the bands bend close to the semiconductor surface to accommodate the difference in work function. To achieve the flat-band condition, Fig. 7.3(c), in which the surface potential of the semiconductor goes away ($\psi_s = 0$), a bias voltage is needed on the gate. This bias is referred to as the flat band potential [19] $V_{FB} = \Phi_{ms}$.

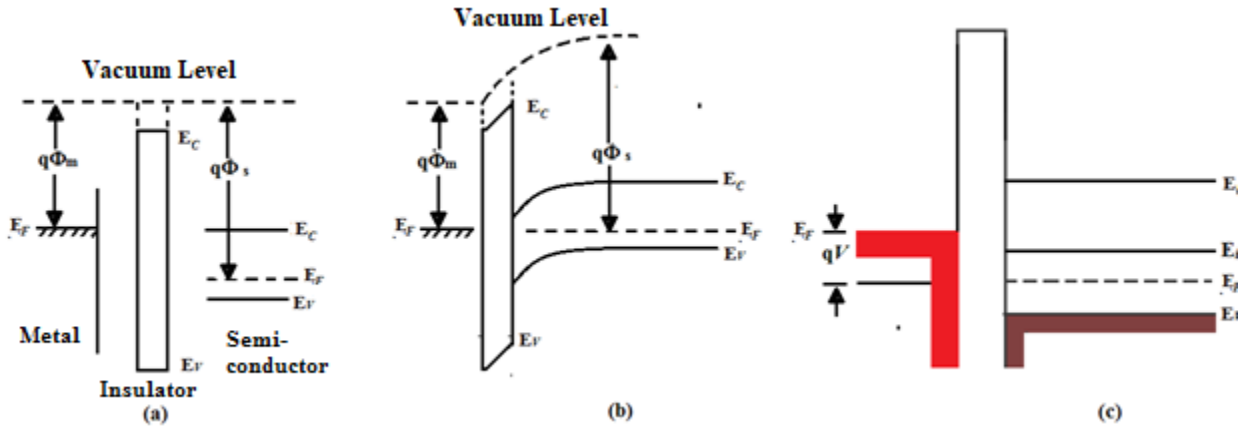

Fig. 7.3 Energy band diagrams (at V = 0) of (a) ideal MIS, (b) practical MIS stacks on p- type substrate, and (c) flat- band voltage in practical MIS stacks.

Practically, sometimes a distorted and stretched-out C-V plot is observed, i.e., accumulation, depletion and inversion phenomena are not found in the C-V variations. In that case, interface quantum states might have arisen generally because of its broken symmetry resulting from the crystal lattice's termination at a surface [26,27]. These states may also involve energies that are contained within the bulk crystal's band gap. Physically, interface traps and fast surface states [28] may be assumed as originating from unfulfilled, i.e., dangling bonds, which lie owing to the transition from single crystal silicon to amorphous insulator/SiO_2 films. The density and energy distribution of interface traps and fast surface states are typically highly process and/or material-dependent [29]. Although the semantic distinction between interface traps and fast surface states is not entirely clear, one can make a useful distinction by considering time constants. In this situation, a fast surface state has a charging time constant quick enough for a high-frequency C-V measurement to pick up on its response. As seen in Fig. 7.4, this causes the resulting C-V plot to be stretched out and distorted.

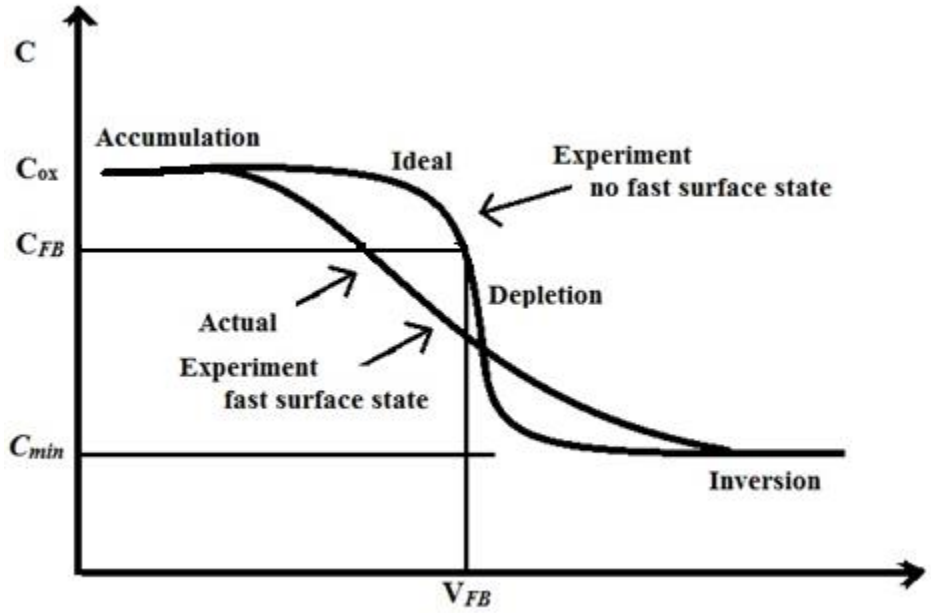

Fig. 7.4 Distortion due to fast surface states (p- type substrate, accumulation at left).

In equilibrium, MIS structure is also influenced by the presence of charges in the insulator, and at the interface between the oxide and semiconductor, Fig. 7.5 [18]. The charges associated with the oxide-semiconductor system, such as fixed oxide, interface trapped, oxide trapped charge, mobile ionic, etc., have been summarized into (1) fixed oxide interface and are immobile under an applied electric field. (2) Oxide-trapped charges Q_{ot}, which may be observed owing to the X-ray radiation or hot electron injection: these traps are contained inside the insulating layer. (3) Mobile ionic charges (Q_m), like barium and calcium ions. (4) Interface trapped charge Q_{it} at the insulator interface [30].

Interface traps are electrically active defects with an energy distribution across the Si band gap. They serve as for generation and recombination and contribute to the leakage current, decreased mobility, drain current, low-frequency noise, and transconductance [19]. Interface traps at the oxide-semiconductor interface are acceptor-like in the upper half and donor-like in the lower half of the band gap [31]. As electrons or holes occupy interface traps, the interface traps become charged and donate to threshold voltage shifts. Studies have shown that the periodic lattice structure is thought to be disrupted by impurities and defects near the interface, resulting in the existence of the interface charge, Q_{it}, within the forbidden gap [7,32].

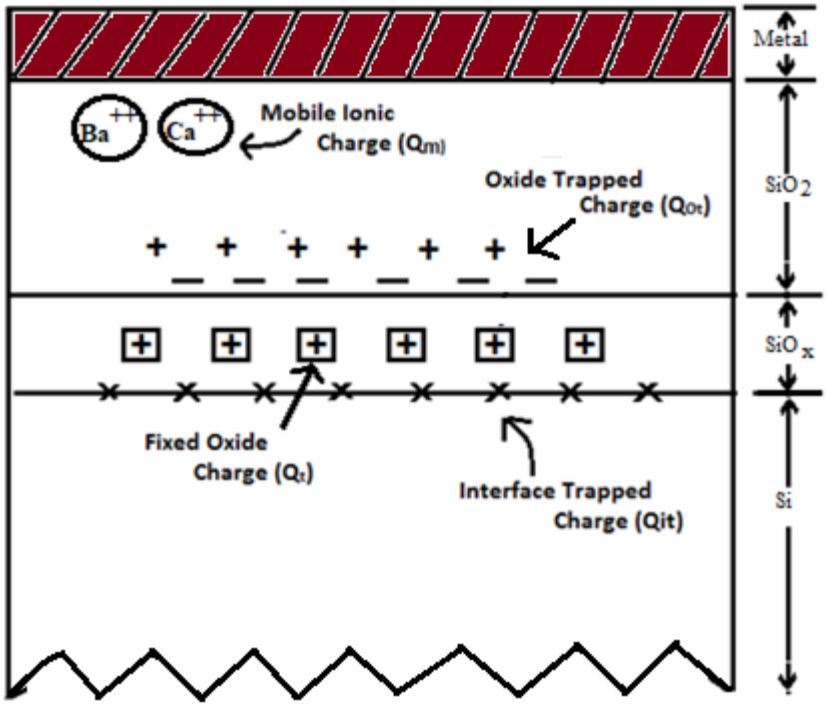

Fig. 7.5 Terminology for charges attributed to thermally oxidized silicon [19].

When a voltage is applied, the interface-trap level moves up or down with the valence and conductance bands while the Fermi level remains fixed. A charge modification in the interface trap happens when it crosses the Fermi level. This charge modification donates to the MIS capacitance and varies the ideal MIS plot. Even on a clean surface, in a UHV system, Q_{it} can be extremely high [33]. Proper surface passivation and post-deposition annealing may help to minimize Q_{it}. At high frequencies, the interface cannot follow the AC voltage swing, which yields high-frequency plot free of capacitance owing to the interface traps [18].

Oxide charges (Q_{ox}) include the oxide fixed charge (Q_f), the oxide trapped charge (Q_{ot}) and the mobile ionic charge (Q_m), as shown in Fig. 7.5. Oxide fixed charge, Q_f, is fixed and cannot be charged or discharged over a wide variation of surface potential. It is located within the order of 80 Å at the Si-insulator interface [19]. Its density is not potentially influenced by the oxide thickness or the type or concentration of impurities in the silicon. It is typically positive and depends on oxidation and annealing conditions, and silicon orientation. It has been recommended that excess silicon (trivalent silicon) or the loss of an electron from excess oxygen centres close to the semiconductor-insulator interface is the source of fixed oxide charges [19]. In the

electrical measurements, Q_f can be regarded as a charge sheet at the semiconductor-insulator interface. Oxide-trapped charges (Q_{ot}) are associated with defects in the oxide film. The oxide traps are generally electrically neutral but may be charged by introducing electrons and holes into the oxide. Snow et al. [34] explained that alkaline earth metal ions, such as calcium, cause significant flat-band voltage shifts, and device instability.

In the accumulation case, the semiconductor capacitance, C_s, is too large, because the slope of space charge density (Q_s) *vs* ψ_s plot is very steep, as shown in Fig. 7.6. At the surface of the semiconductor, the surface potential (ψ_s) depends only on the characteristics of the semiconductor, e.g., band gap, dielectric constant, doping level, etc. Hence, the series capacitance in the accumulation case is just the oxide capacitance (C_{ox}). The physical thickness (d) of the oxide, calculated by optical method [35] (Chapter-5); the capacitance (C_{ox}), in the accumulation case, obtained from C-V variations may be used to compute the dielectric constant of the oxide [20],

$$C_{ox} = \frac{A\varepsilon_{ox}}{d} \quad . \qquad (7.1)$$

As the gate voltage becomes less negative, the semiconductor surface is depleted. The depletion layer capacitance C_d is added in series with C_{ox} [20],

$$\frac{1}{C_\infty} = \frac{1}{C_{ox}} + \frac{1}{C_d} \qquad and \qquad C_d = \frac{\varepsilon_S A}{W} \qquad (7.2)$$

where ε_s permittivity of the substrate, A is the surface area of the electrode, and W is the depletion width in the semiconductor substrate.

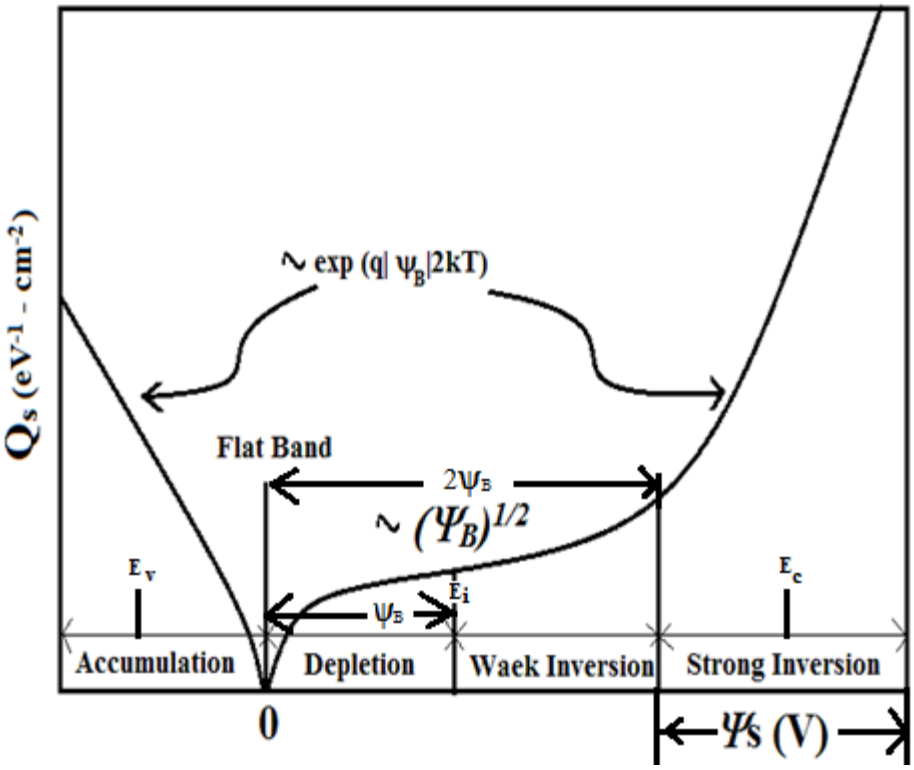

Fig. 7.6 Space-charge density (Q_s) as a function of the surface potential (ψ_s), for typical p-type semiconductor (Ge), at RT [19].

The depletion width (W) increases with rising gate voltage across the capacitor in the depletion region. When flat- band condition has arrived, the MIS capacitance, C_{FB}, is shown by [20],

$$\frac{C_{ox} - C_{FB}}{C_{Ox} - C_{\infty}} = \frac{C_O}{C_O + 6C_{\infty}}, \tag{7.3}$$

The metal-semiconductor work function difference (Φ_{ms}) is used to calculate the flat-band voltage of real MIS structures. The flat band voltage (V_{FB}) distinguishes the accumulation regime from the depletion regime. The amount of charge in the oxide or charge at the oxide-semiconductor interface affects the flat-band voltage. The flat-band voltage is still known as the voltage, which yields a flat energy band in the semiconductor when applied to the gate electrode. Any charge impacts the flat-band voltage, whether it is in the oxide or at the interface [36]. On biasing, the effective trapped charge (Q_i), is then known as the addition of oxide charges (Q_f, Q_m and Q_{ot}) and interface charges (Q_{it}). It effectively shifts the ideal MIS curve along the voltage axis, depending on the existence of positive or negative Q_i, at the interface [7,20].

The magnitude of the flat- band voltage shift (ΔV_f) is caused by fixed oxide charge (Q_f), is given by

$$\Delta V_f = \frac{Q_f}{C_{ox}} \quad , \tag{7.4}$$

where C_{ox} is oxide capacitance. The flat- band voltage shift, owing to the mobile ionic charge (Q_m), from Gauss's law, is shown by

$$\Delta V_m = \frac{Q_m}{C_{ox}} = \frac{1}{C_{ox}}\left[\frac{1}{d}\int_0^d x\rho_m(x)dx\right] \tag{7.5}$$

where $\rho_m(x)$ is the volume charge density. The oxide traps are associated with defects in insulating film and are generally electrically neutral, which, by introducing electrons or holes, may be changed into the oxide-trapped charge. The flat band voltage shift owing to the oxide-trapped charge [37], is shown by

$$\Delta V_{ot} = \frac{Q_{ot}}{C_{ox}} = \frac{1}{C_{ox}}\left[\frac{1}{d}\int_0^d x\rho_{ot}(x)dx\right] \tag{7.6}$$

where Q_{ot} is the effective net charge of mobile ions per unit area at the semiconductor-insulator interface and $\rho_{ot}(x)$ is the volume charge density. The overall voltage shift owing to all the oxide charges is shown by (summing equations. (7.4), (7.5) and (7.6),

$$\Delta V_{FB} = \Delta V_f + \Delta V_m + \Delta V_{ot} = \frac{Q_i}{C_{ox}} \tag{7.7}$$

Where Q_i (= Q_f + Q_m + Q_{ot}) is the addition of the effective net oxide charges per unit area, at insulator- semiconductor interface. If the value of Φ_{ms} is not zero, and if the oxide charge Q_i exists, Eq. (7.7) (assuming negligible interface traps), the experimental C-V plot, will be shifted from the ideal theoretical plot by an amount [18],

$$V_{FB} = \phi_{ms} - \frac{Q_i}{C_{ox}}. \quad (7.8)$$

The flat-band voltage shift is obtained concerning an ideal C-V plot, for which $Q_i = 0$. For both n- and p-type substrates, positive Q_i causes the C-V plot to shift to more negative values of gate bias concerning the ideal C-V plot, while negative Q_i causes the C-V plot to shift to the more positive gate voltage.

While the gate voltage becomes more positive than the flat-band voltage, the MIS capacitance keeps decreasing until strong inversion is achieved at the threshold voltage V_T; at this point, the surface potential is twice the Fermi potential, i.e.,

$$\psi_S(inv) = 2\psi_B. \quad (7.9)$$

Strong inversion with a maximum depletion width, W_d, occurs at higher voltages than the threshold voltage, V_T. In the current work, the high frequency measurements were performed; a small-signal measuring voltage at high frequency (1 MHz) was used. The gate voltage varies more quickly than the generation-recombination rate of the minority carriers in the inversion layer, and the interface traps do not follow the AC gate voltage [19]. The charge in the inversion layer cannot change in response and does not affect the capacitance in any way. As a result, the MIS capacitance remains at its minimum, C_{min}, corresponding to the minimum depletion-layer capacitance (C_{d_min}), resulting from the maximum depletion width W_D [20].

$$\frac{1}{C_{\min}} = \frac{1}{C_{ox}} + \frac{1}{C_{d\_\min}} \quad (7.10)$$

If the C-V variations are carried out at low frequency [15-17], the MIS capacitance in the strong inversion case, at low-frequency, will become very dissimilar from that discovered by high-frequency measurements. Because the gate voltage varies gradually at low frequency [38], there is enough time for minority carriers to get produced in bulk, to drift across the depletion region to the inversion layer, or to go back to the substrate and recombine. 'Low frequency' means the AC probe frequency at which the interface traps and minority carrier inversion charges must be able to react to the measurement. The charge in the inversion layer also contributes to the capacitance. The charge in the inversion layer also contributes to the capacitance. In an ideal

MIS capacitor, this is the space charge, Q_S, induced by the electric field. The semiconductor capacitance (C_S) is substantial in the case of strong inversion because the space-charge density increases exponentially, Fig. 7.6. Again, the MIS series capacitance at low frequency is C_{ox}. The low frequency (LF) curve in Fig. 7.2(a) shows C_{ox} in the strong inversion region. In a practical MIS system, the interface charge also contributes to the capacitance in the potential inversion case. The deep depletion region is shown as the DD curve in Fig. 7.2(a). It corresponds to the experimental situation in which both the gate voltage and the low-signal measuring voltage alter too quickly to form an inversion layer in the surface depletion range. As a result, the depletion layer becomes wider than WD, and there is no capacitance minimum in deep depletion. A thin SiO_2 layer is usually, formed onto the Si substrate due to the reaction of Si with ambient oxygen. When the film of the dielectric material is deposited on this Si substrate, the interfacial SiO_2 layer also contributes to the obtained (effective) relative permittivity of the material. In the relative permittivity measurements, the adequate thickness of the insulating material in the MIS structure has involved the contribution of the SiO_2 layer and the thickness of the deposited material film. Therefore, to measure the material's actual relative permittivity, the actual thickness of the deposited material film and the contribution of the interfacial SiO_2 layer must be considered.

7.3 Capacitance-voltage (C-V) characteristics

The dielectric constant of bulk $(Ba_{0.845}Ca_{0.155})(Zr_{0.1}Ti_{0.9})O_3$ composition was found to be maximum among the prepared compositions, at room temperature, Chapter-2. In the present study, the Si- based MIS capacitors of $(Ba_{0.845}Ca_{0.155})(Zr_{0.1}Ti_{0.9})O_3$ were fabricated. Thin layers of $(Ba_{0.845}Ca_{0.155})(Zr_{0.1}Ti_{0.9})O_3$ system were sputter deposited onto p- type Si (100) wafer, at 60 W forward power and 1 W reverse power, for 30 min., at RT, using a RF sputtering vacuum system. All the samples were deposited in similar conditions, at room temperature, as described in Chapter-5. The RT-deposited films were annealed at 500, 600, 650, 700 and 750 ^oC, for 1 hour, in an ambient atmosphere. The physical thickness of thin films of $BCZT_{0.9}$ was determined by optical method, as mentioned in Chapter-5. An array of silver (Ag) dots (1.963×10^{-3} cm^2 area) as metal gates was sputter deposited onto the prepared films to make MIS structures. Electrical measurements were carried out on the MIS Ag/$BCZT_{0.9}$/Si/Ag structures using the deposited films. The capacitance-voltage (C-V) variations were measured by to and fro sweep of

the applied DC voltage (between +10 and −10 V), using a 50 mV (peak to peak), 1 MHz signal. To carry out the capacitance-voltage (C-V) characteristics of the prepared films, a multi-frequency LCR meter (Fluke, PM 6306) was used at a frequency of 1 MHz.

In the MIS configuration, Krupanidhi and Rao [39] have observed that the existence of interface states results in frequency-dependent capacitance characteristics. This was explained by the frequency dispersion of permittivity of the insulator, a high density of interface states, and the existence of a high resistive interfacial layer [40]. The measured variation of capacitance with frequency for the prepared $BCZT_{0.9}$ films is depicted in Fig. 7.7. Fig. 7.8 displays the variation of tan δ (dissipation factor) *vs* f (frequency). It was found that capacitance reduces with rising frequency, for all the prepared samples. Dissipation factor was found minimum in the films annealed at 750 ^{o}C, which can be associated with the oxygen incorporation in the stoichiometry of the film and enhancement in density. Fig. 7.9 exhibits the measured C-V variations of $BCZT_{0.9}$ assisted MIS configuration, deposited at RT, and annealed at 500, 600, 650, 700 and 750 ^{o}C, respectively. For all the prepared films, the measured capacitance was found rising with a rise in annealing temperature. However, the films were peeled out at temperature 800 ^{o}C. The occurrence of film crystallization was observed on annealing at and above 600 ^{o}C. On crystallization, the capacitance was found to increase. The release of compressive stress with rising annealing temperature may be associated with the increased polarization, and hence to the increased capacitance. The C-V characteristics show inversion, depletion, and accumulation zones for all the prepared thin films. For negative bias voltage, the negative charge of electrons, at the gate, is compensated by the positive charge of holes accumulated at the surface of the semiconductor (p-type), which measures the capacitance of the deposited film (C_{ox}). When the bias voltage is switched to a positive direction the surface of the semiconductor becomes depleted from the holes, and the resulted in extra space charge capacitance (C_{sp}) is added in series to the C_o. In the strong inversion region, the change in the potential at the gate depends on the number of negative charges at the metal-semiconductor interface. The obtained low hysteresis C-V curves of most of the prepared compositions indicate low trap densities. The C-V curves of prepared $BCZT_{0.9}$, assisted MIS structures show clockwise hysteresis. The clockwise, and anti- clockwise hysteresis, in the C-V plots, are the signs of electron and hole ejection into the film, respectively [21].

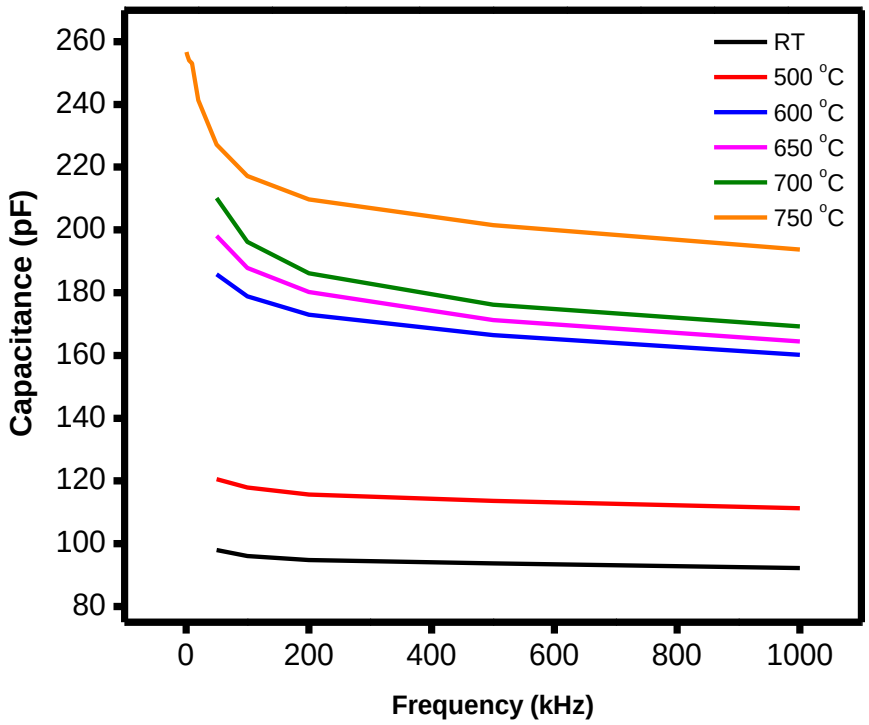

Fig. 7.7 Frequency variation of capacitance of $BCZT_{0.9}$ film assisted MIS.

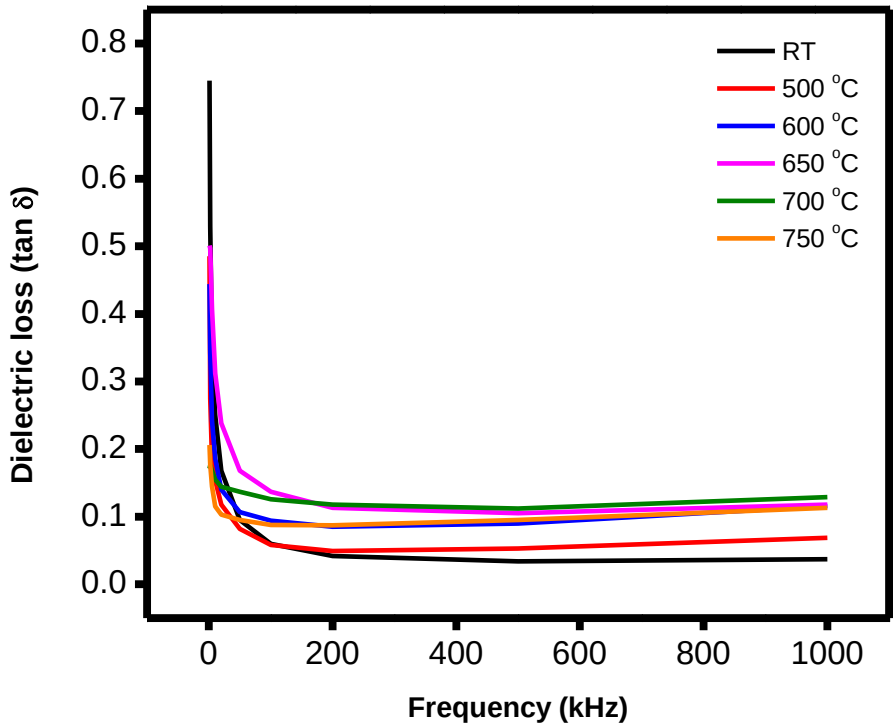

Fig. 7.8 Frequency variation of dielectric loss (tan δ) in $BCZT_{0.9}$ films, annealed at different temperatures.

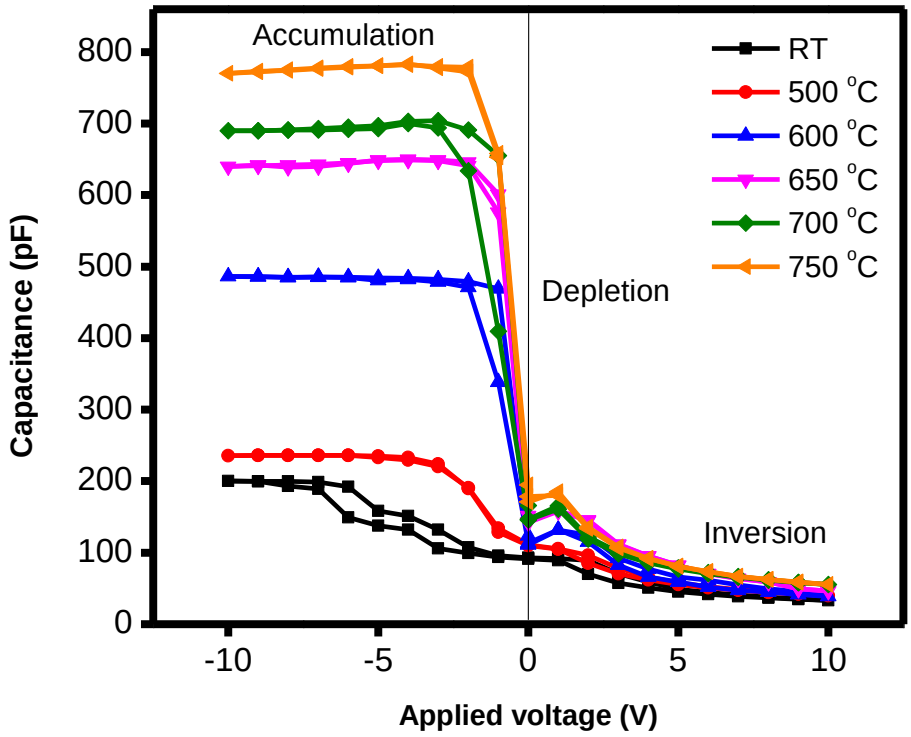

Fig. 7.9 C-V characteristic of $BCZT_{0.9}$ assisted MIS configuration, films deposited at RT and annealed at 500, 600, 650, 700 and 750 ^{o}C.

Chanaliere et al. [41] suggested that the hysteresis exhibits anti-clockwise behavior for orthorhombic symmetry and clockwise for hexagonal symmetry. They also suggested that the direction of the hysteresis loop in MIS capacitors may be anti-clockwise due to surface-state trapping [42]. The anti-clockwise hysteresis behavior occurs due to negative Q_i, which shifts the C-V curve to a more positive side along the voltage axis [43,44]. The low hysteresis in the C-V curves exhibits low trap density at the film-substrate interface [45]. The observed C-V characteristics were moving towards a larger negative bias, indicating the existence of a positive fixed oxide charge ($+Q_f$) at the interface of the deposited film and the silicon [18].

The dielectric constant (K) of the deposited films was calculated from the C-V plots using the capacitance at the charge accumulation. In Table 7.1, C_o is the capacitance in the accumulation region, which was found increasing with the annealing temperature upto 750 ^{o}C. The flat-band capacitance (C_{FB}), calculated from the Eq. (7.3), was found increasing with an increase in annealing temperature. It was found 117.01 pF for the as-deposited films, and 273.63 pF for the films annealed at 750 ^{o}C, in $BCZT_{0.9}$ thin films. The value of flat band voltage (V_{FB}) corresponding to C_{FB} was observed shifting from the relatively larger negative (-2.33 V, for the films deposited at RT) to the smaller negative value with increasing annealing temperature (-0.32

V, for the films annealed at 750 ºC), Table 7.1. For all the prepared films, the flat band voltage (V_{FB}) shifted towards the left side with respect to ideal one, Fig. 7.4. The observed shifting in V_{FB} can be associated with the compensation of fixed oxide positive charge (Q_f) by the negative charge employed during the annealing process [46]. Also, the shifting of C-V curves may be due to the interface trap charge and oxide charge [7].

In the observed C-V characteristics, a bulge (temporary increase) in the deep depletion side may be associated with dark current [47]. The C-V characteristics of MIS Ag/$BCZT_{0.9}$/Si/Ag structures instantly shift from the accumulation side to the deep depletion side when a voltage pulse triggers the gate, Fig. 7.2. If the gate potential is held constant, thermally produced minority carriers will subsequently enter the surface potential well, which may increase the Ag/$BCZT_{0.9}$/Si/Ag MIS capacitance with asymptotic inversion condition. The magnitude and rate both of the observed dark current can be determined from the storage time, which is usually a few milliseconds [47]. Ta_2O_5 and $SrTiO_3$ exhibit a similar nature in the deep depletion side [48,49].

After the flat- band capacitance (C_{FB}) is determined, from Eq. (7.3), the amount of the offset of the corresponding voltages, ΔV_{FB}, from the dual sweep C-V curves, Figs. 7.9, may be used as a quantitative measure of how big the hysteresis is. The density of interface states D_{it}, may be estimated at the flat- band voltage (flat- band condition), from the Lehovec's method [5], for evaluation of built- in charges from capacitance- voltage plots,

$$D_{it} = \left[\frac{(C_o - C_{FB})C_{FB}}{3(\delta C/\delta V)_{FB} qKTA} \right] - \left[\frac{C_o^2}{(C_o - C_{FB})Aq^2} \right], \qquad (7.11)$$

where A is area of the electrode.

In addition, it was found that the width of hysteresis voltage was not influenced by different sweep rates, showing that the observed C-V curves were in steady state; and also proposing that the current C-V hysteresis is triggered by other sources [50], such as interface trap density, etc. As mentioned earlier these curves show n- type carrier injection hysteresis (clockwise), as is showed by arrows, in the Fig. 7.9.

The density of states, N_{it}, recharges during each bias cycle, i.e., interface states that are occupied and released by injected and re-emitted charges during each bias cycle, is shown by [51],

$$N_{it} = C_o V_H / qA, \quad (7.12)$$

where V_H is amount of hysteresis.

The depletion capacitance C_d, being in series with the film capacitance; and maximum depletion width W_m, are calculated from Eq. (7.2) [51]. All the above parameters have been calculated from the measured C-V variations, for all the prepare samples, and have been given in Table 7.1. With increasing annealing temperature the flat band voltage was observed shifting towards 0 V, i.e., less negative, for the annealing temperatures ≤ 750 ^oC. For the films annealed at temperatures ≤ 750 ^oC, in the ambient atmosphere, it seems that due to the less escaping of alkaline earth metal ions and improved oxygen stoichiometry might have reduced n- type carriers. With increasing annealing temperature crystallinity of the films also improved than that for the samples deposited at RT and annealed at lower temperatures, Fig 7.1. The improved oxygen stoichiometry and crystallinity resulted in reduced magnitude of $V_{FB,}$ for the films annealed at temperatures ≤ 750 ^oC. Also, the escaping of volatile A-site constituents (barium, calcium ions) [51], might have triggered oxygen vacancies (charge compensation) with increasing processing temperature. Competition between the temperature dependent escaping of A- site and O- site constituents may be held responsible for the observed C-V characteristics and V_{FB} shifting of the prepared MIS structures.

The interface density of states D_{it}, which is related to the interfacial traps, for the structures (MIS) prepared under different conditions, was computed and presented in Table 7.1. The observations show that, among the prepared samples, interface density was measured minimum for the samples annealed at 500 ^oC. Values of D_{it} for $BCZT_{0.9}$, in the present results, are lower than that for other reported [20] materials; e.g., 5.95×10^{13} $eV^{-1}cm^{-2}$ for $NaNbO_3$, etc. Materials, with lower value of interface states, find applications in the field of insulating low ε dielectrics.

Hysteresis voltages have been found between 0.1 and 0.92 V, for all the prepared samples. Utilizing the hysteresis voltage, the density of states (N_{it}), which is being recharge at each cycle, has been calculated. On annealing, at and above 700 ^oC, films crystallize. N_{it} was found maximum for the films annealed at 700 ^oC. For the $BCZT_{0.9}$ samples, the depletion layer capacitance and depletion width values have been calculated.

The capacitance of depletion layer (C_d) was found 39.81 pF, for the films deposited at RT, and corresponding width (W_m) of the layer was measured 510 nm; for the samples annealed at 500

^{o}C, C_d was found 48.02 pF, and corresponding W_m was obtained 423 nm; for the films annealed at 600 ^{o}C, C_d was found 42.40 pF, and corresponding width of the layer was obtained 479 nm; for the films annealed at 650 ^{o}C, C_d was found 50.22 pF, and W_m was obtained 404 nm; for the films annealed at 700 ^{o}C, C_d was found 62.43 pF, and W_m was obtained 339 nm; for the films annealed at 750 ^{o}C, C_d was found 60.08 pF, and W_m 338 nm. Also, small capacitance (C_∞) value was found about 33.2 pF for the films deposited at RT. The measured C_∞ matches closely with that calculated from the given relation [20,50]

Table 7.1 Various parameters determined from the C-V variations of the prepared $BCZT_{0.9}$ thin film-assisted MIS structures.

Parameters	RT	500 ^{o}C	600 ^{o}C	650 ^{o}C	700 ^{o}C	750 ^{o}C
C_o (pF)	200	236	486	649	712	782
C_∞ (pF)	33.2	39.9	39.0	46.6	55.3	55.8
C_{FB} (pF)	117.01	138.65	184.27	227.64	263.72	273.63
V_{FB} (V)	-2.33	-0.95	-0.37	-0.35	-0.35	-0.32
V_H (V)	0.92	0.45	0.50	0.15	0.44	0.12
N_{it} ($x10^{11}$ cm^{-2})	5.86	3.38	7.73	3.09	9.97	2.99
D_{it} ($x10^{+13}$ $eV^{-1}cm^{-2}$)	0.646	0.197	0.208	0.283	0.284	0.286
DC	38.01	44.84	92.34	122.93	135.28	148.81
C_d (pF)	39.81	48.02	42.40	50.22	62.43	60.08
W_m (nm)	510	423	479	404	339	338
Q_i (x 10^{-10} $eV^{-1}cm^{-2}$)	4.66	2.24	1.79	2.26	2.49	2.51
C_s ($fF/\mu m^2$)	1.01	1.20	2.47	3.29	3.62	3.99
Q_c ($fC/\mu m^2$), at 8V	9.17	10.82	22.28	29.67	32.65	35.91

where C_o- capacitance of accumulation region, C_∞- capacitance of inversion region, C_{FB}- flat-band capacitance, V_{FB}- flat- band voltage, V_H - amount of hysteresis, N_{it} - density of states, D_{it} - density of interface states, DC- dielectric constant, C_d- maximum capacitance of depletion layer, W_m- maximum depletion width, Q_i - Effective trapped charge, C_s- charge storage capacity, Q_c- charge storage density.

$$C_o = \varepsilon_f A/ [d + (\varepsilon_f / \varepsilon_s)W_m] \quad (7.13)$$

The minimum capacitance calculated from relation (7.13) is found 33.2 pF and is identical as found from the C-V plots of the films deposited at RT. The dielectric constant (K) of the deposited films was measured from the C-V plots, using the capacitance at the charge accumulation [52]. For Ag/$BCZT_{0.9}$/Si capacitors, at 1 MHz, maximum capacitance (782 pF)

was observed for the films annealed at 750 ^{o}C, Fig. 7.9. The dielectric constant of the $BCZT_{0.9}$ films, deposited at RT and subsequently annealed at 500, 600, 650, 700 and 750 ^{o}C, was found 38, 45, 91, 123, 135 and 148, respectively, Fig. 7.10. The observed dielectric constant (K) of $BCZT_{0.9}$ films, annealed at 750 ^{o}C, at 1 MHz, was found higher than the reported low frequency results [53-55].

With the rise in annealing temperature, the enhanced density and grain size may be associated with the observed rise in the dielectric constant of the $BCZT_{0.9}$ films [56]. For annealing temperatures below 600 ^{o}C, the prepared $BCZT_{0.9}$ films exhibit poor dielectric features, probably due to their amorphous structure and weak boundary-dominated leakage currents [57]. Stoichiometry, strain, microstructure, and a 'dead layer' close to the interface between the film and the electrodes frequently have an influence on the dielectric characteristics of thin films [58]. The observed maximum dielectric constant for the prepared $BCZT_{0.9}$ films is 148.81 (at 1 MHz), which is lower than the value reported for bulk. Films were only deposited in an argon environment, so the lack of oxygen may have caused the decreased relative permittivity. The development of an interfacial SiO_2 layer on the silicon substrate prior to deposition could be the one reason for the observed minimum (effective) in relative permittivity, despite adequate cleaning. In addition, for non- volatile memory device applications, material may have a large charge storage capacity. Usually, this is achieved by decreasing the thickness of the insulating layer, which strictly influences the reliability of the capacitors. The charge storage capacity for a planar capacitor is shown by the relationship [20],

$$C_s = \varepsilon_o \varepsilon_r A / d, \qquad (7.14)$$

where ε_r is the dielectric constant of the film. From the C-V measurements, the charge storage density was computed using the relation [20];

$$Q_c = \varepsilon_o \varepsilon_r E, \qquad (7.15)$$

where E is the applied electric field. Charge storage capacity and density have been calculated for the RT deposited films, and the films annealed at 500, 600, 650, 700 and 750 ^{o}C. Maximum charge storage capacity (3.99 $fF/\mu m^2$) and density (35.91 $fC/\mu m^2$) were found for the films annealed at 750 ^{o}C. At higher annealing temperatures, the dielectric constant was found sufficiently increased as compared to its base composition $BaTiO_3$ [54]. Hence, at the MPT

region, the $BCZT_{0.9}$ system has a remarkable charge storing capacity for memory device applications. The leakage current density and charge storage density of the deposited films together may be suitable for use in DRAM applications.

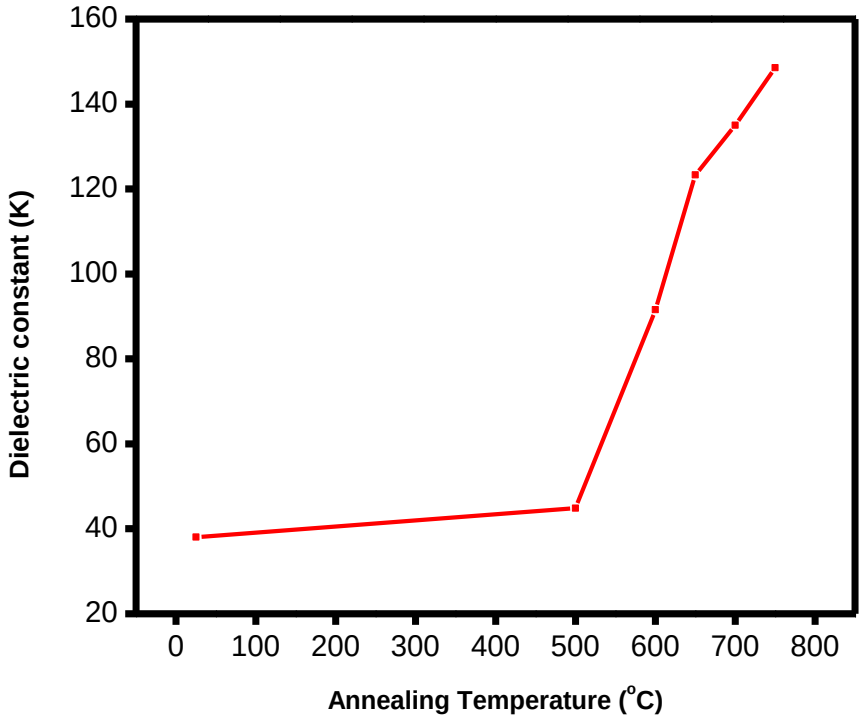

Fig. 7.10 Annealing temperature variation of K of $BCZT_{0.9}$ thin films.

7.4 Discussion

The dielectric constant was obtained maximum, 148 (at 1 MHz), and leakage current density minimum, 3.6×10^{-9} A/cm^2 (at 3.0×10^2 kV/cm electric field), for the films annealed at 750 ^oC. Electrical properties improved for the films annealed at 750 ^oC than other annealed films. The improved oxygen stoichiometry and increased density of the films may be the cause of the increased dielectric constant and decreased band gap with an increase in annealing temperature. Further studies on $BCZT_{0.9}$ thin film system, with varying deposition temperature, annealing temperature, composition (y), deposition rate, oxygen pressure, etc., and deposition in the presence of forming gases, like hydrogen or nitrogen, preparation in the atmosphere of the volatile constituents (Ba, Ca) to maintain the stoichiometry of the film, etc., may be helpful in further understanding of the characteristic features of the system for different technological applications.

References

[1] T. Ueda, A. Noma, D. Usda, GaAs MMIC Chip-sets for mobile communication systems with on-chip ferroelectric capacitors, Integrated Ferroelectrics. 7 (1995) 45-60. https://doi.org/10.1080/10584589508220220

[2] H. Takasu, The ferroelectric memory and its applications, Journal of Electroceramics. 4 (2000) 327-338. https://doi.org/10.1023/A:1009910525462

[3] N. Izyumskaya, Y.I. Alivov, S.J. Cho, H.H. Morkoç, H. Lee, Y.S. Kang, Processing, structure, properties, and applications of PZT thin films, Critical Reviews in Solid State and Materials Sciences. 32 (2007) 111-202. https://doi.org/10.1080/10408430701707347

[4] M. Dawber, K.M. Rabbe, J.F. Scott, Physics of thin-film ferroelectric oxides, Review of Modern Physics. 77 (2005) 1083-1130. https://doi.org/10.1103/RevModPhys.77.1083

[5] K. Lehovec, A. Slobodskoy, Field effect capacitance analysis of surface states on silicon, Physica Status Solidi (b). 3 (1963) 447-464. https://doi.org/10.1002/pssb.19630030309

[6] K. Corp, N.M. Albuquweque, R. Womack, An experimental 512-bit nonvolatile memory with ferroelectric storage cell, IEEE Journal of Solid-State Circuits. 23 (1988) 1171-1175. https://doi.org/10.1109/4.5940

[7] E.H. Nicollian, J.R. Brews, MOS Physics and Technology, 1st ed., Wiley Publishing, Hoboken, 1982.

[8] M.J. Deen, F. Pascal, Journal of Material Science: Material in electronics, 17 (2006) 549-575. https://doi.org/10.1007/s10854-006-0001-8

[9] P.C. Joshi, Structural and electrical characteristics of $SrTiO_3$ thin films for dynamic random access memory applications, Journal of Applied Physics. 73 (1993) 7627. https://doi.org/10.1063/1.353960

[10] D.R. Frankl, Some effects of material parameters on the design of surface space-charge varactors, Solid- State Electronics. 2 (1961) 71-76. https://doi.org/10.1016/0038-1101(61)90058-2

[11] L.M. Terman, An investigation of surface states at a silicon/silicon oxide interface employing metal-oxide-silicon diodes, Solid-State Electronics. 5 (1962) 285-299. https://doi.org/10.1016/0038-1101(62)90111-9

[12] A.S. Grove, B.E. Deal, E.H. Snow, C.T. Sah, Investigation of thermally oxidized silicon surfaces using metal-oxide-semiconductor structures, Solid- State Electronics. 8 (1965) 145-163. https://doi.org/10.1016/0038-1101(65)90046-8

[13] B.E. Deal, E.H. Snow, C.A. Mead, Barrier energies in metal-silicon dioxide-silicon structures, Journal of Physics and Chemistry of Solids. 27 (1966) 1873-1879. https://doi.org/10.1016/0022-3697(66)90118-1

[14] K.H. Zaininger, F.P. Heiman, MOS and vertical junction device characteristics of epitaxial silicon on low aluminum-rich spinel, Solid-State Electronics. 13 (1970) 943-948. https://doi.org/10.1016/0038-1101(70)90092-4

[15] R. Castagne, Comptes Rendus, Academy of Sciences Paris. 267 (1968) 866.

[16] M. Kuhn, A quasi-static technique for MOS CV and surface state measurements, Solid- State Electronics. 13 (1970) 873-885. https://doi.org/10.1016/0038-1101(70)90073-0

[17] W. K. Kappallo, J.P. Walsh, A current voltage technique for obtaining low-frequency c-v characteristics of mos capacitors, Applied Physics Letters. 17 (1970) 384. https://doi.org/10.1063/1.1653446

[18] S.M. Sze, Physics of Semiconductor Devices, 2nd ed., Wiley Publishing, New York, 1981.

[19] D.K Schroder, Defects in microelectronic materials and devices: Electrical characterization of defects in gate dielectrics, 1st ed., CRC Press publishing, Boca Raton, 2009.
[20] V. lingwal, N.S. Panwar, Capacitance-voltage characteristics of $NaNbO_3$ thin films, Journal of Applied Physics. 94 (2003) 4571. https://doi.org/10.1063/1.1608470
[21] D.J. Fitzgerald, A.S. Grove, Surface recombination in semiconductors, Surface Science. 9 (1968) 347-369. https://doi.org/10.1016/0039-6028(68)90182-9
[22] A. Goetzberger, M. Schulz, Fundamentals of MOS Technology, Advances in solid state physics, 1st ed., Pergamon-Vieweg publishing, Braunschweig, 1973.
[23] D. Circuits, T.I Kamins, M. Chan, Device Electronic for Integrated Circuits, 3rd ed., John Wiley & Sons publishing, New York, 2002.
[24] B.G. Streetman, S.K. Banerjee, Solid State Electronic Devices, 6th ed., Prentice Hall publishing, New Jersey, 2005.
[25] R.F. Pierret, Semiconductor Device Fundamentals, 1st ed., Pearson Higher Education publishing, London, 2003.
[26] R.C. Jaklevic, J. Lambe, Experimental study of quantum size effects in thin metal films by electron tunneling, Physical Review B. 12 (1975) 4146. https://doi.org/10.1103/PhysRevB.12.4146
[27] P. Czoschke, H. Hong, L. Basile, T. Chiang, Quantum oscillations in the layer structure of thin metal films, Physical Review Letters. 91 (2003) 226801. https://doi.org/10.1103/PhysRevLett.91.226801
[28] B.E. Deal, E.L. MacKenna, P.L. Castro, Characteristics of Fast Surface States Associated with SiO_2-Si and Si_3N_4-SiO_2-Si Structures, Journal of the Electrochemical Society. 116 (1969) 997-1005. https://doi.org/10.1149/1.2412205
[29] Z. Chen, B.B. Jie, C.T. Sah, Effects of energy distribution of interface traps on recombination dc current-voltage line shape, Journal of applied physics. 100 (2006) 114511. https://doi.org/10.1063/1.2364621
[30] B.E. Deal, Standardized terminology for oxide charges associated with thermally oxidized silicon, IEEE Transactions on Electron Devices. 27 (1980) 606-608. https://doi.org/10.1109/T-ED.1980.19908
[31] A. Stesmans, V.V. Afanasev, Nature of the P_{b1} interface defect in (100) $SiSiO_2$ as evealed by electron spin resonance ^{29}Si hyperfine structure, Microelectronic Engineering. 48 (1999) 113-116. https://doi.org/10.1016/S0167-9317(99)00350-0
[32] W. Shockley, On the surface states associated with a periodic potential, Physical Review. 56 (1939) 317-323. https://doi.org/10.1103/PhysRev.56.317
[33] F.G. Allen, G.W. Gobeli, Work function, photoelectric threshold, and surface states of atomically clean silicon, Physical Review. 127 (1962) 150-158. https://doi.org/10.1103/PhysRev.127.150
[34] E.H. Snow, A.S. Grove, B.E. Deal, C.T. Sah, Ion transport phenomena in insulating films, Journal of Applied Physics. 36 (1965) 1664. https://doi.org/10.1063/1.1703105
[35] R. Swanepoel, Determination of the thickness and optical constants of amorphous silicon, Journal of Physics E: Scientific Instruments. 16 (1983) 1214. https://doi.org/10.1088/0022-3735/16/12/023
[36] M. Pulver, G. Dorda, Flat band voltage hysteresis of MNOS structures, Physica status solidi (a). 1 (1970) 65-70. https://doi.org/10.1002/pssa.19700010108

[37] P.J.M. Whorter, P.S. Winokur, Simple technique for separating the effects of interface traps and trapped oxide charge in metal-oxide-semiconductor transistors, Applied Physics Letters. 48 (1986)133. https://doi.org/10.1063/1.96974
[38] C.N. Berglund, Surface states at steam-grown silicon-silicon dioxide interfaces, IEEE Transactions on Electron Devices. 13 (1966) 701-705. https://doi.org/10.1109/T-ED.1966.15827
[39] S.B. Krupanidhi, G.M. Rao, Pulsed laser deposition of strontium titanate thin films for dynamic random access memory applications, Thin Solid Films. 249 (1994) 100-108. https://doi.org/10.1016/0040-6090(94)90093-0
[40] T. Sawada, H. Hasegawa, Interface state band between GaAs and its anodic native oxide, Thin Solid films. 56 (1979) 183-200. https://doi.org/10.1016/0040-6090(79)90063-4
[41] C. Chanaliere, S. Four, J.L. Autran, R.A.B. Devine, N.P. Sandler, Properties of amorphous and crystalline Ta_2O_5 thin films deposited on Si from a $Ta(OC_2H_5)_5$ precursor, Journal of Applied Physics. 83 (1998) 4823. https://doi.org/10.1063/1.367277
[42] A. Goetzberger, J.C. Irvin, Low-temperature hysteresis effects in metal-oxide-silicon capacitors caused by surface-state trapping, IEEE Transactions Electron Devices. 15 (1968) 1009-1014. https://doi.org/10.1109/T-ED.1968.16554
[43] G.R. Bai, H.L.M. Chang, D.J. Lam, Y. Gao, Preparation and structure of $PbZrO_3$ epitaxial films by metalorganic chemical vapor deposition, Applied Physics Letters. 62 (1993) 1754. https://doi.org/10.1063/1.109596
[44] G.M. Rao, S.B. Krupanidhi, Study of electrical properties of pulsed excimer laser deposited strontium titanate films, Journal of Applied Physics. 75 (1994) 2604. https://doi.org/10.1063/1.356235
[45] S.V.J. Chandra, S. Uthanna, G.M. Rao, Effect of substrate temperature on the structural, optical and electrical properties of dc magnetron sputtered tantalum oxide films, Applied Surface Science. 254 (2008) 1953-1960. https://doi.org/10.1016/j.apsusc.2007.08.005
[46] E. Atanassova, Thin RF sputtered and thermal Ta_2O_5 on Si for high density DRAM application, Microelectronics Reliability. 39 (1999) 1185-1217. https://doi.org/10.1016/S0026-2714(99)00038-4
[47] L. Bornstein, Numerical Data and Functional Relationships in Science and technology Group III, Crystal and Solid State Physics, Wiley publishing, Hoboken, US, 1982: pp. 326. https://doi.org/10.1002/crat.2170170310
[48] K. Iijimo, Y. Tomita, R. Takayama, I. Ueda, Preparation of c-axis oriented $PbTiO_3$ thin films and their crystallographic, dielectric, and pyroelectric properties, Journal of Applied Physics. 60 (1986) 361. https://doi.org/10.1063/1.337654
[49] K. Sreenivas, A. Mansingh, M. Sayer, Structural and electrical properties of rf sputtered amorphous barium titanate thin films, Journal of Applied Physics. 62 (1987) 4475. https://doi.org/10.1063/1.339037
[50] B. Panda, A. Dhar, G.D. Nigam, D. Bhattacharya, S.K. Ray, Relationship between plasma parameters and film microstructure in radio frequency magnetron sputter deposition of barium strontium titanate, Journal of Applied Physics. 83 (1998) 1114. https://doi.org/10.1063/1.366802
[51] M. Okuyama, Y. Matsui, H. Nakano, Y. Hamakawa, $PbTiO_3$ ferroelectric thin film gate fet for infrared detection, Ferroelectrics. 33 (1981) 235-241. https://doi.org/10.1080/00150198108008091

[52] V. Lingwal, N.S. Panwar, Morphotropic phase transitions in mixed sodium-potassium niobate system, Ferroelectrics. 300 (2004) 3-14. https://doi.org/10.1080/00150190490442146
[53] G.D. Wilk, R.M. Wallace, J.M. Anthony, High-K gate dielectrics: Current status and materials properties considerations, Journal of Applied Physics. 89 (2001) 5243-5275. https://doi.org/10.1063/1.1361065
[54] W.S. Choi, J. Yi, B. Hong, The effect of cerium doping in barium zirconate titanate thin films deposited by rf magnetron sputtering system, Materials Science and Engineering B. 109 (2004) 146-151. https://doi.org/10.1016/j.mseb.2003.10.081
[55] Z. Yu, J. Ramdani, J.A. Curless, C.D. Overgaard, J.M. Finder, R. Droopad, K.W. Eisenbeiser, J.A. Hallmark, W.J. Ooms, V.S. Kaushik, Epitaxial oxide thin films on Si (001), Journal of Vacuum Science & Technology B: Microelectronics and Nanometer Structures Processing, Measurement, and Phenomena. 18 (2000) 2139. https://doi.org/10.1116/1.1303737
[56] B.C. Luo, D.Y. Wang, M.M. Duan, S. Li, Growth and characterization of lead-free piezoelectric $BaZr_{0.2}Ti_{0.8}O_3$-$Ba_{0.7}Ca_{0.3}TiO_3$ thin films on Si substrates, Applied Surface Science. 270 (2013) 377-381. https://doi.org/10.1016/j.apsusc.2013.01.033
[57] K. Prabahar, R. Ranjith, A. Srinivas, S. V. Kamat, B. Mallesham, V. L. Niranjani, J. P. Praveen, D. Das, Effect of deposition temperature on the microstructure, ferroelectric and mechanical properties of lead free BCZT ceramic thin films, Ceramics International. 43 (2017) 5356-5361. https://doi.org/10.1016/j.ceramint.2017.01.032
[58] P. Bao, T.J. Jackson, X. Wang, M.J. Lancaster, Barium strontium titanate thin film varactors for room-temperature microwave device applications, Journal of Physics D: Applied Physics. 41 (2008) 063001. https://doi.org/10.1088/0022-3727/41/6/063001

CHAPTER-8

Conclusions and scope for future work

8.1 Conclusions

The solid-state reaction technique was used to prepare the ceramic pellets of $(Ba_{1-x}Ca_x)(Zr_{1-y}Ti_y)O_3$, (x = 0.140-0.160, y = 0.9), which were then subjected to double sintering. Its composition and auxiliary conditions significantly influence the characteristics of the material. Several factors, such as powder impurity, particle size, processing and sintering methods, etc., significantly impact the properties of samples. To achieve repeatable results, each of these parameters needs to be carefully managed. In this study, high purity (> 99.5 %) powders of barium carbonate ($BaCO_3$), calcium carbonate ($CaCO_3$), titanium oxide (TiO_2) and zirconium oxide (ZrO_2) were used as raw materials. The compositions of BCZT ceramics were prepared using a solid-state reaction route with double sintering. Using Cu$K_{\alpha 1}$ radiation with a wavelength of 1.5406 Å, XRD measurements of all the prepared compositions were performed at room temperature (RT). With the help of a scanning electron microscope, the surface morphology and grain size of the produced samples were investigated. For dielectric measurements, specimens were electroded, with conducting silver paste in a metal-insulator-metal (MIM) arrangement. The dielectric constant (ε), loss tangent (tan δ), and electric conductivity (σ) of the prepared composition samples were measured at 10, 100 and 1000 kHz, and in the temperature range from room temperature to 450 ^oC.

The prepared $(Ba_{1-x}Ca_x)(Zr_{0.1}Ti_{0.9})O_3$ ($0.140 \leq x \leq 0.160$) compositions exhibit polycrystalline behaviour as observed in the measured X-ray diffraction patterns. ICSD data were used for peak indexing. ICSD stands for Inorganic Crystal Structure Database. The lattice parameters were calculated from the observed XRD data and High Score Plus software [1]. The chosen space group for these refinements was orthorhombic (C) [2], and tetragonal (P4mm). The estimated lattice parameter values and the published values [2] were found to be equivalent.

For all the prepared samples, varied grain sizes and porosity were noted via SEM studies. The prepared compositions' average grain size varied between 1.03 and 1.7 µm, and the composition (x) variation in density of the prepared pellet samples was measured to be between 3.8 and 4.2 g/cc. The dielectric characteristics of the samples are significantly influenced by density and

porosity [3,4]. According to the observed EDX data, the content of calcium and barium has remarkably escaped from all of the processed samples, except for the composition x = 0.150.

The temperature and composition (x)-dependent dielectric properties [dielectric constant (ε), loss (tan δ), and electric conductivity *(σ)*] of the prepared compositions were measured over a broad range of frequencies as well as temperatures. With an increase in frequency, typically, ε and tan δ were found to decreasing, and σ increase, for the prepared compositions. With increasing the calcium content (x), ε, tan δ, and σ were observed, generally, increasing with x, except for the composition x = 0.150, at all the measured temperatures and frequencies. An irregular decrease was found in the dielectric properties, near MPB (morphotropic phase boundary), with anomalously lower values of ε, tan δ, and σ, at x = 0.150, among the prepared compositions [5]. Such an anomalous dielectric behaviour, near these compositions of $(Ba_{1-x}Ca_x)(Zr_{1-y}Ti_y)O_3$ system, (x = 0.140-0.160 and y = 0.9), was observed for all the measured temperatures (RT to 450 ^oC) and frequencies (10 kHz to 1 MHz). A break in the shifting of the XRD peaks was also found at these samples. From the composition-property diagram of solid solution systems, at MPB, the ferro- composition has two or more phases and has extremal electro- physical properties [6-8]. MPB exhibits sharp structural and electrical properties change in response to composition change in a solid solution [9,10]. The composition-property diagram of solid solutions includes a morphotropic zone, which is highly interesting. The sample (x = 0.150) and MPT calculated by changes in entropy and enthalpy followed by thermal and X-ray measurements are in agreement [11].

Tian et al. [12] and Fu et al. [13] presented a phase schematic of $(Ba_{1-x}Ca_x)(Zr_{1-y}Ti_y)O_3$ system, (x, y = 0 to 1), showing different crystalline structures. Temperature-dependent dielectric measurements exhibit two distinct phases with transitions near 100 ^oC, showing tetragonal symmetry from RT to about 100 ^oC; and above 100 ^oC, cubic symmetry was observed. The high-temperature X-ray diffraction (HT-XRD) measurements were made on the samples with x = 0.150 and 0.155, in the temperature range from RT to 450 ^oC. The dielectric properties (ε, tan δ, and σ) of the $(Ba_{1-x}Ca_x)(Zr_{1-y}Ti_y)O_3$, (x = 0.140-0.160, y = 0.9) ceramics were measured. At all the measured frequencies and temperatures, the observed dielectric constant, loss and electric conductivity exhibit minimum values for the compositions with x = 0.150, among the prepared compositions. The HT-XRD measurements show a distinct phase transition, from tetragonal to cubic phase, at around 100 ^oC, consistent with the dielectric measurements.

Like other oxides, with the increase in frequency, usually, ε and tan δ were found decreasing, and σ increasing, for the prepared compositions. The findings are consistent with the previously reported results [4,14,15]. Among the prepared compositions, a structural anomaly was observed; and the ε, tan δ and σ were observed minimum, at all the measured frequencies and temperatures, for the composition with x = 0.150, exhibiting morphotropic-like phase boundary at this composition. Among the prepared compositions, a significant escaping of alkali earth metal (Ba and Ca) ions was observed in the sintered pellets, with a minimum for the composition with x = 0.150. The composition-dependent structural anomaly and decreased A-site vacancies may be held responsible for the observed morphotropic-like behaviour, in these p-type perovskite compositions, at x = 0.150.

The observed dielectric constant peaks at certain temperatures (T_c) are attributed to the structural phase transitions in these ABO_3 kind perovskites. The Structural phase transition of the perovskites is associated with a significant temperature-dependent vibrational mode-the soft mode [16-18]. At the transition temperature, the soft-mode frequency tends to zero, and the lattice observes a displacement leading to the structural anomaly-the structural phase transition [16-18]. The soft mode substantially impacts the dielectric characteristics of ABO_3 type perovskites [16-18], which explains their anomalous behavior, near T_c. At the transition temperature (T_c), the soft mode frequency tends to zero, and the lattice observes a displacement leading to the structural anomaly- the structural phase transition.

At MPB, extremal electro-physical properties of the ceramics have been reportedly observed [19]. To explore the piezoelectric characteristics of the $(Ba_{1-x}Ca_x)(Zr_{0.1}Ti_{0.9})O_3$ ceramics, (x = 0.140-0.160, y = 0.9), near the morphotropic composition, sample variation of converse piezoelectric coefficient (d_{33}^*), coercive field, remnant polarization, and current polarization measurements were taken at RT. To carry out piezoelectric measurements, double-sintered compositions were used. The piezoelectric measurements such as piezoelectric coefficients and polarization were carried out using a piezo-meter (aixACCT Systems GmbH, aixPES) and ferroelectric (PE-loop tracer). The P-E (polarization *vs* electric field) hysteresis loops of the prepared $(Ba_{1-x}Ca_x)(Zr_{0.1}Ti_{0.9})O_3$ compositions were measured at room temperature, at 1 Hz frequency (triangular wave), with an applied peak electric field 8.28 kV/cm. The hysteresis loops exhibit a good ferroelectric nature of the prepared ceramics. For the prepared $(Ba_{1-x}Ca_x)(Zr_{1-y}Ti_y)O_3$ compositions, (x = 0.140-0.160, y = 0.9), with increasing the calcium content (x value),

the area of the polarization-electric field (PE) hysteresis loops was observed increasing, up to x = 0.150, which after that reduces with a rise in x. The maximum strain was found for the composition with x = 0.150, among the prepared BCZT samples. For the prepared BCZT compositions, the observed variation of coercive field (E_c) and remnant polarization (P_r) with Ca content (x) have been investigated. In the prepared composition range, the maximum value of remnant polarization (P_r) was found 20.82 $\mu C/cm^2$; and the maximum coercive field (E_c), 3.384 kV/cm, for the samples with x = 0.150. These observations may be attributed to the increased distortion in the lattice of the BCZT ceramics, near MPB, at x = 0.150 [20]. Decreasing the volume of switchable domains, the coercive field (E_c) may also increase due to the cell's more significant deformation [20]. The variation of polarization current with the applied electric field was studied. Among the prepared samples, the highest magnitude (3.48×10^{-5} A) was observed for the compositions with x = 0.150. According to previously reported findings and current observations, the preparation method, content, and structure significantly impact the piezoelectric characteristics of BCZT ceramics. The structural anomaly, and extremal values of converse piezoelectric constant (d_{33}*), strain (%), remnant polarization, and coercive field indicate a MPB- like composition, near x = 0.150, in the prepared BCZT ceramics.

8.1.1 Applications of ceramic capacitor

Extensive research on some ferroelectric materials belonging to the ABO_3 structural family has revealed that they are helpful for dielectric heating, tuning circuits, filters circuits, sensors and actuators, RF application, microwave applications etc. [21-24]. Physical properties such as tangent loss, dielectric constant, piezoelectricity and pyroelectricity, which depend on the type and class of materials and their synthesis/fabrication technique, determine the applicability of materials for devices. Because of their strong dielectric characteristics, titanate ceramic materials have been investigated as potential compounds [25-30]. The prepared pellet samples of the BCZT ceramics can be worked as a ceramic capacitor. Ceramic capacitors were extensively used due to their low cost and high breakdown voltage (chapter 4). They are reliable due to good frequency response characteristics. It is ideally suited for the application of AC signals due to its non-polarized nature.

8.1.2 LCR circuit operating condition

In the parallel LCR circuit, the prepared pellet samples may be used as a capacitor in the place of electrolyte capacitor. The ceramic capacitor has two electrodes separated by a dielectric medium. A potential difference of high frequency is applied across the electrodes. A sinusoidal signal is taken as an input for the parallel LCR circuit, Fig. 8.1. At a particular frequency, the capacitive and inductive reactance will be equal in the parallel LCR circuit. Thus they will cancel out each other at that frequency. This phenomenon is called resonance. The resistance, capacitance and inductance of the parallel LCR circuit are given by 10 kΩ, 0.10 nF and 0.5 mH, respectively. Again, a 10 kΩ series resistance was added to get high Q factor. The gain *vs* frequency variations were measured using a 5 V_{p-p} (peak to peak) sinusoidal signal with a variation in frequency from 1 kHz to 3 MHz. At around 700 kHz, the gain of the LCR circuit was found to increase. This phenomenon may be occurred due to the resonance effect. To carry out the gain-frequency characteristics of the prepared BCZT ceramics, a function generator (Keysight, 33500B series) was used. A DSO (digital storage oscilloscope, Keysight DSO-X 2024A) was used to measure the change in output voltage and frequency.

In conclusion, changing the frequency of the applied voltage in a LCR circuit can significantly impact the circuit's behaviour and altering the circuit's impedance. From the gain characteristics, it can work as a band-pass filter. Understanding how frequency affects an LCR circuit is crucial for various applications, including tuning circuits, filters, and oscillators. The resonant frequency is a key parameter that governs the circuit's behaviour.

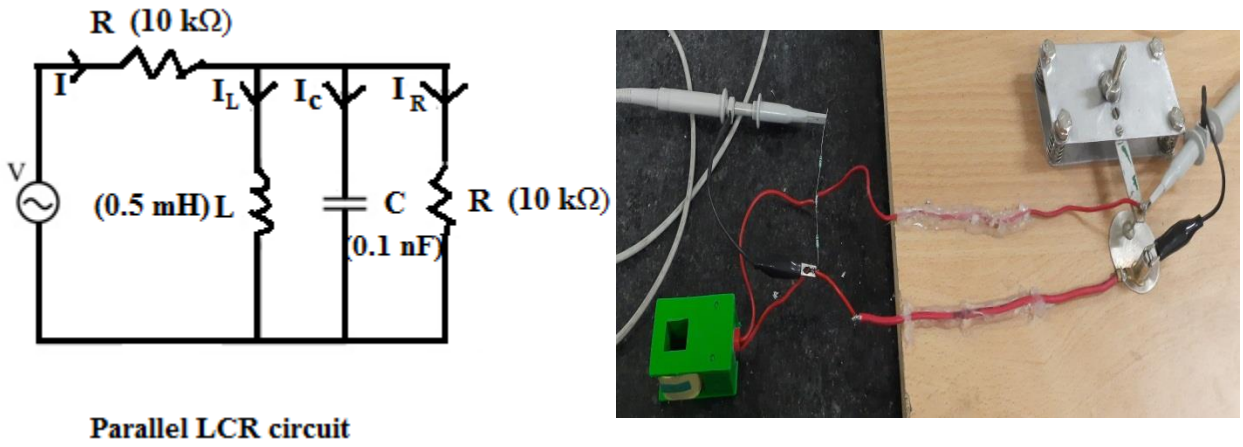

Fig. 8.1 Circuit diagram with an applied voltage.

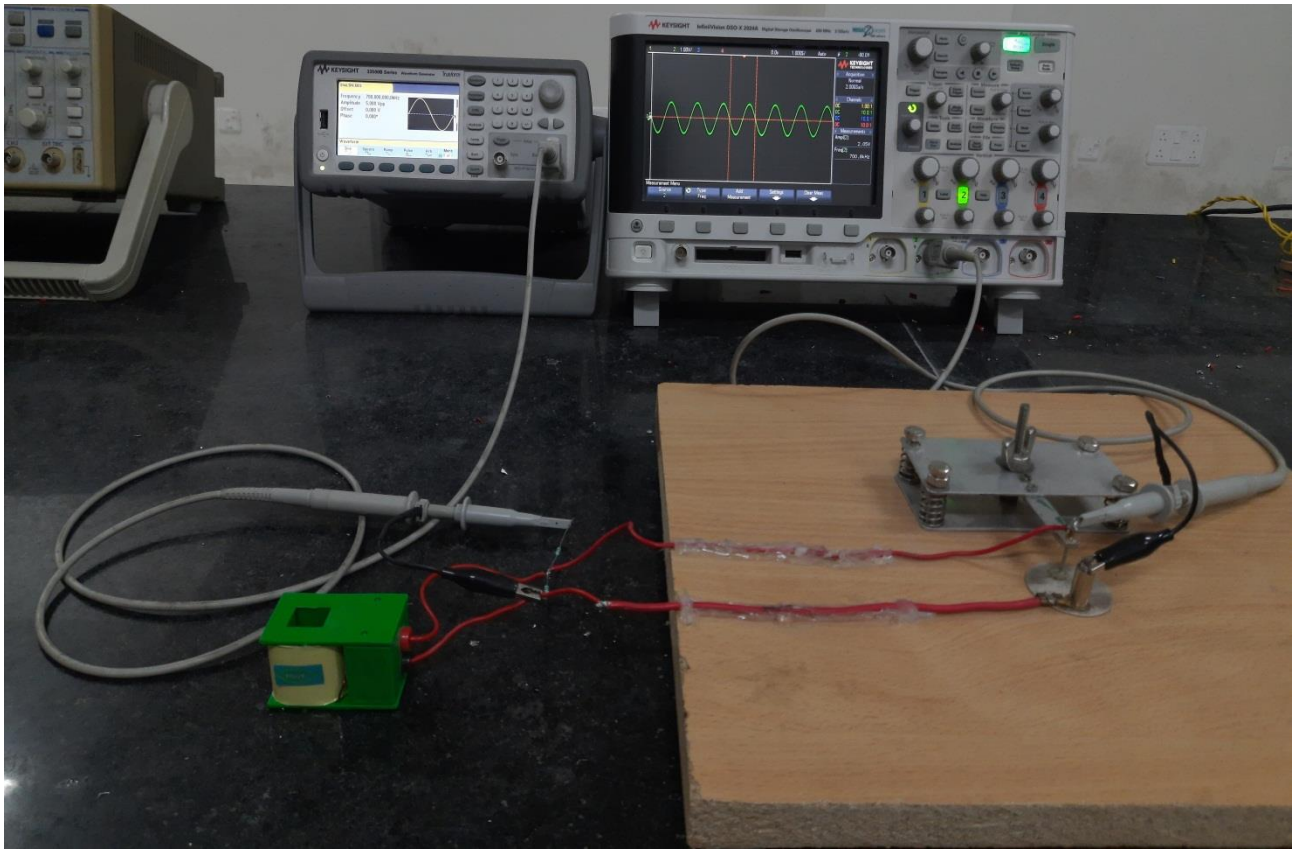

Fig. 8.2 Parallel LCR circuit with an applied sinusoidal voltage (frequency 700 kHz, 5 V_{p-p})

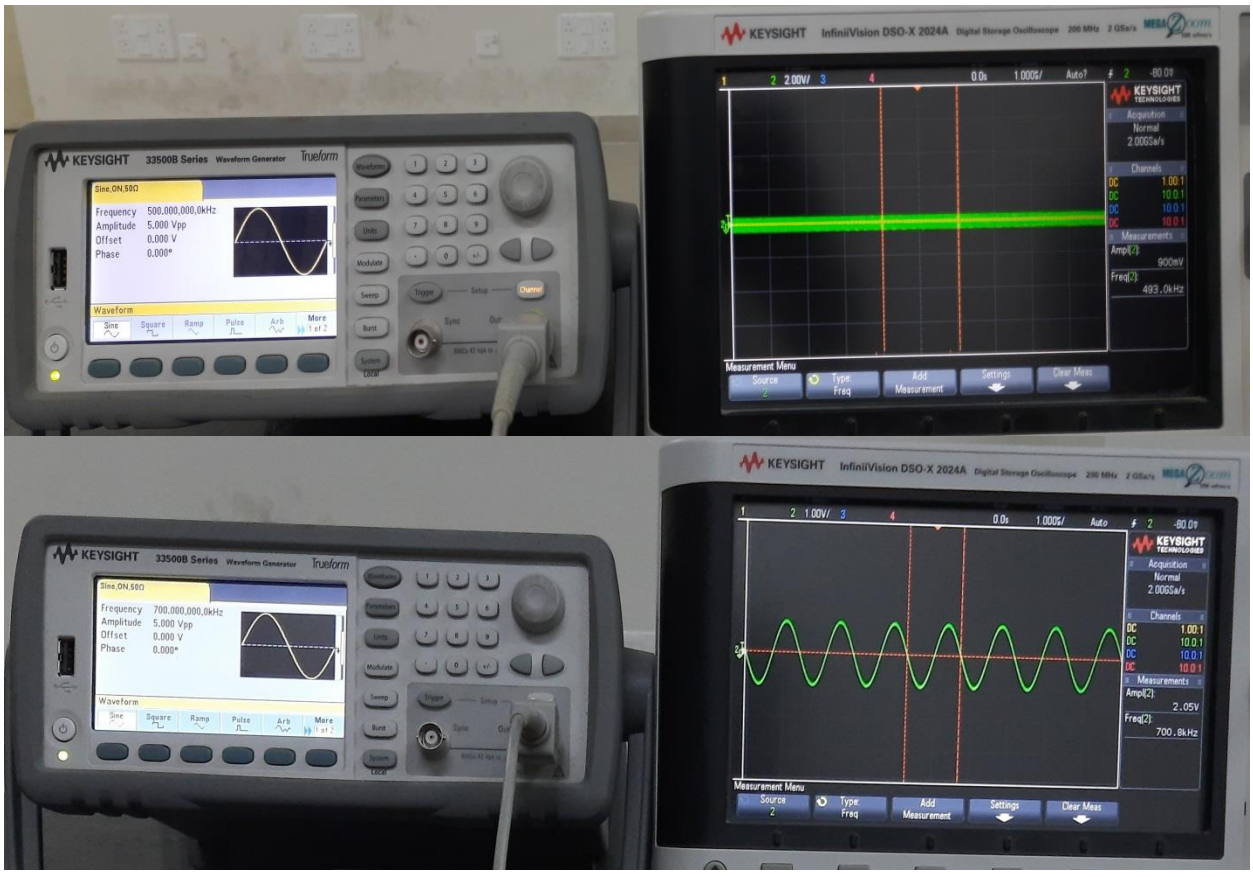

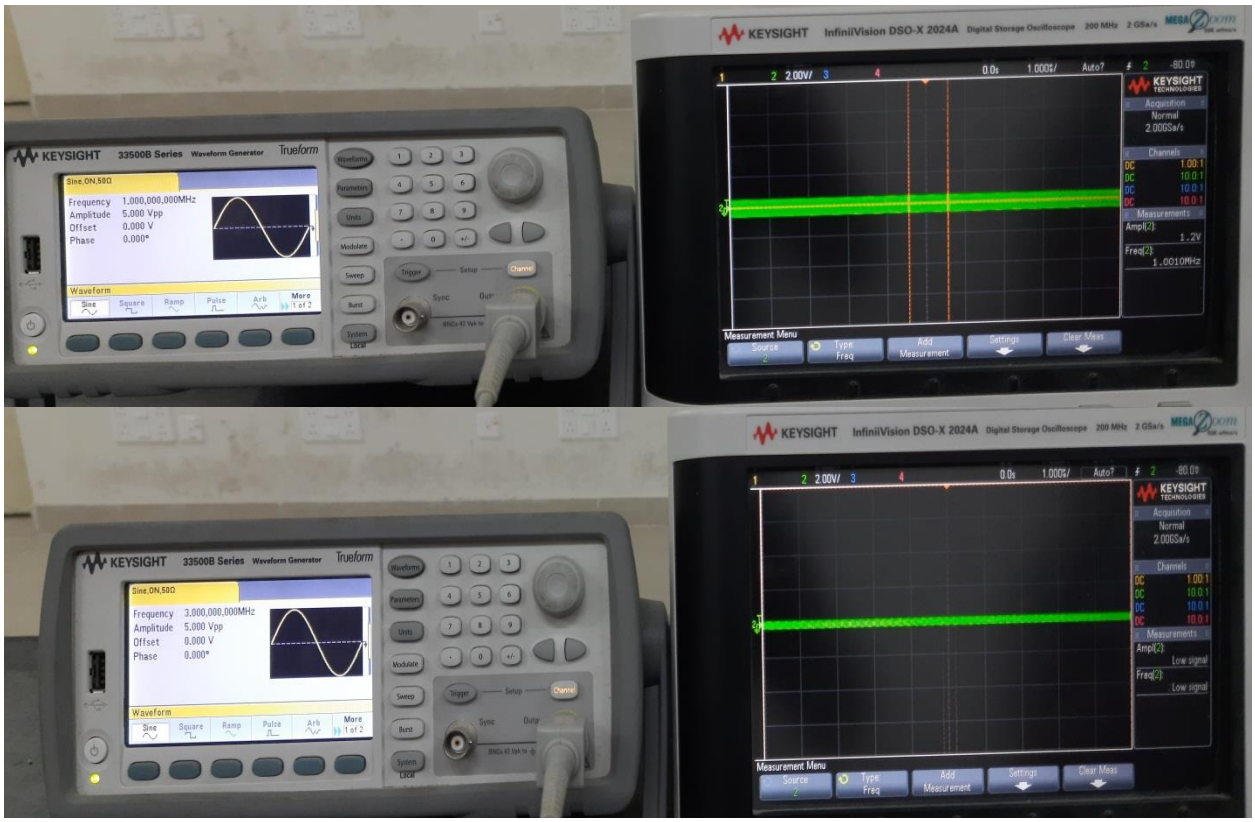

Fig. 8.3 (a) Input sinusoidal signal with a magnitude of 5 $V_{p\text{-}p}$ (left), (b) Frequency response characteristics of parallel LCR circuit with an applied sinusoidal voltage (right)

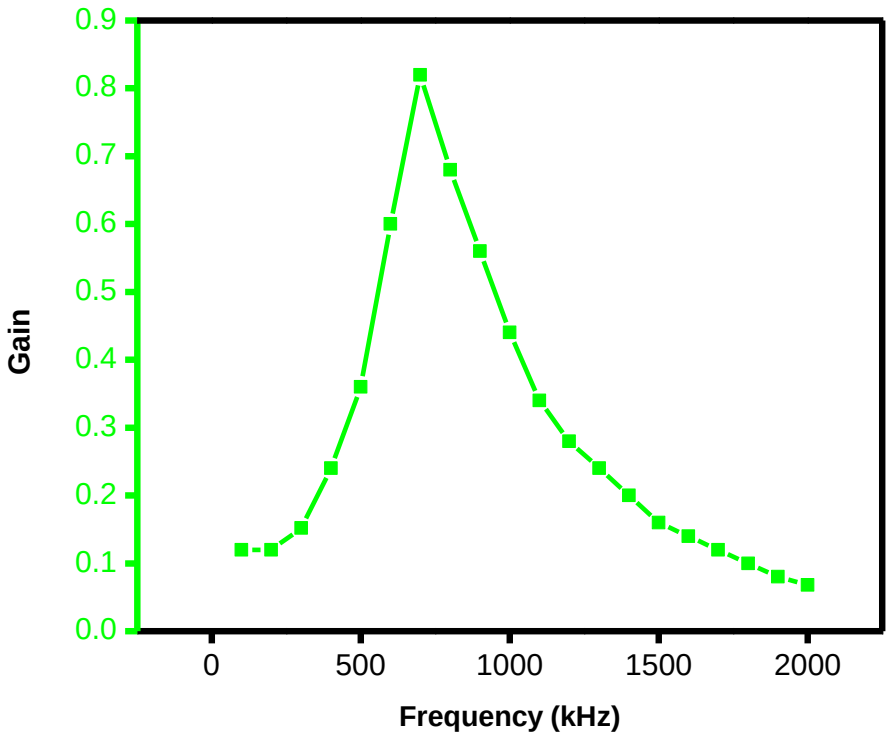

Fig. 8.4 Gain *vs* frequency response analysis of the parallel LCR circuit.

From the frequency response analysis graph of the parallel LCR circuit, the maximum gain was measured at around 700 kHz frequency. The Q-factor and bandwidth of the parallel LCR circuit are calculated at resonance frequencies around 4.57 and 0.153 MHz, respectively. Thus, the ceramic capacitor can be used in a tuned amplifier. The advantage is that the ceramic capacitors have a very minimum value (nF range) and can provide a resonance frequency near the MHz range.

The growing demand for miniaturization and ferroelectric thin films in memory devices, electromechanical devices, high-frequency sensor applications [31], etc., has extended the study further to the thin films of these materials. Thin films were deposited, on quartz and p-Si (100) substrates, by radio frequency (RF) sputtering of ceramic barium calcium zirconate titanate $[(Ba_{1-x}Ca_x)(Zr_{0.1}Ti_{0.9})O_3]$, (x = 0.155, y = 0.9), target. With varying deposition and annealing conditions, films were prepared. The film deposition conditions drastically influence the structure, crystallization, electron trap densities, presence of voids, defects, film-substrate interaction, stoichiometry and chemical composition etc. [32]. For electrical and optical measurements, thin films were deposited onto silicon and quartz substrates, respectively.

The as-deposited films were annealed for one hour at different temperatures, between 500 and 800 ^oC. However, films peeled out on annealing at 800 ^oC. From the observed XRD patterns, it was observed that the films annealed at and above higher temperatures (700 ^oC), show crystalline structure with a common orientation (020). The films were observed orientating towards (020) plane, when the films were annealed above 450 ^oC. It was observed that the transmittance of the films increased with a rise in annealing temperature up to 600 ^oC; and decreases with further rising annealing temperature. The transmittance was measured to decrease (~73-87%) with further increase in annealing temperature (between 650 and 750 ^oC), which may be associated with the multi-orientation of the crystallites on annealing, (XRD data, Fig. 2.1, Chapter-2), which may cause in the scattering of incident photons and hence reduced transmittance [33].

The optical transmittance plots were used to compute the film thickness (d), refractive index (n_o), and other optical properties of the prepared $BCZT_{0.9}$ films using the famous Swanepoel's envelope technique [34]. As photon energy increased, the films' refractive index (n_o), absorption coefficient (α), and extinction coefficient typically increased. The measured optical parameters were found to be consistent with the earlier reported results [35]. The film thickness was calculated from the transmittance data and was obtained as 330 ± 10 nm for the films deposited

at RT. It remained the same after annealing at various temperatures. To understand the related methods, the directly allowed energy band gap (led by photon-electron interaction, and following α^2 *vs* hν plot), indirect allowed energy band gap (led by photon-phonon interaction, and following $\alpha^{1/2}$ *vs* hν plot), direct forbidden band gap (led by photon-phonon assisted interaction, and following $\alpha^{2/3}$ *vs* hν plot); and indirect forbidden band gap (led by exciton interaction, and following $\alpha^{1/3}$ *vs* hν plot) have been computed for all the prepared samples. From such observations, a convincing illustration was found for the α^2 *vs* hν curve and recommends direct transition possibility, in the deposited $BCZT_{0.9}$ films, by photon-electron interaction. The band gap widens (red shifts) for the films annealed at higher temperatures, according to the measured variation of the optical band gap as a function of annealing temperature [36]. This observed band gap widening may be explained on the basis of the Burstein effect [37].

To understand the conduction mechanisms in the Ag/$BCZT_{0.9}$/Si/Ag MIS structure, insulating films were annealed at 500, 600, 650, 700 and 750 ^oC. After annealing in an oxygen atmosphere and different temperatures, silver electrodes were deposited to carry out electrical measurements. The observed current-voltage (I-V) behaviour suggests several conduction mechanisms in $BCZT_{0.9}$ assisted MIS structure. For the films annealed at 600, 650, 700 and 750 ^oC, the linear variation of leakage current shows the ohmic conduction for $E < 1.21 \times 10^2$ kV/cm. In contrast, the films deposited at RT and annealed at 500 ^oC, show ohmic conduction for $E \leq 1.05 \times 10^2$ kV/cm. The current-voltage variations of the prepared films exhibit different conduction mechanisms above a critical field, e.g., Schottky emission, Poole-Frenkel, and other conduction processes. The linearity of the plots obtained using different methods shows that ohmic conduction dominates in the smaller field region ($E \leq 1.05 \times 10^2$ kV/cm), Schottky emission in the applied field range (1.05×10^2 kV/cm $< E \leq 1.81 \times 10^2$ kV/cm), and space-charge-limited conduction in the higher fields ($E > 1.81 \times 10^2$ kV/cm), for RT deposited films and the films annealed at 500 ^oC. Similarly, for the films annealed from 600 to 750 ^oC, ohmic conduction in the lower fields ($E \leq 1.21 \times 10^2$ kV/cm) followed by space-charge-limited conduction in the higher fields ($E > 1.21 \times 10^2$ kV/cm), has been observed. The current study's deposited film thickness was relatively high (around 330 nm), so there are few chances of tunneling through the film volume. Tunneling can be significantly possible through extremely thin films (less than 50 nm). The films, annealed from 600 to 750 ^oC, indicated a probability of tunneling conduction at the higher fields ($E \geq 1.96 \times 10^2$ kV/cm). The probability of tunneling conduction decreases in

the films annealed from 600 to 750 ^{o}C as the annealing temperature rises due to an increased interfacial SiO_2 layer, which raises the field to find tunneling conduction in higher fields ($\geq 1.96 \times 10^2$ kV/cm). From these present observations, conduction mechanisms in Ag/$BCZT_{0.9}$/Si/Ag MIS structure comprises ohmic, Schottky emission, and space-charge-limited conduction mechanisms dominating different field regimes, for the as-deposited and the films annealed at 500, 600, 650, 700 and 750 ^{o}C films.

The conduction mechanisms were further confirmed by comparing the refractive indices obtained from I-V characteristics with that obtained optically. Joshi and Cole [38] have found that the dominating conduction mechanism may be determined by calculating the refractive index (n) obtained from I-V characteristics ($\varepsilon = n^2$), and comparing it with that obtained from the optical measurements (n_o). Where the values of the refractive indices obtained from the two approaches are comparable, that determines the dominating conduction mechanism. From the I-V measurements, the measured conduction mechanism in Ag/$BCZT_{0.9}$/Si/Ag MIS structure comprises ohmic, Schottky emission, and space-charge-limited conduction mechanisms dominating at different rising applied field regions.

The prepared Ag/$BCZT_{0.9}$/Si/Ag MIS structure's measured capacitance-voltage (C-V) characteristics show that the prepared samples' capacitance decreases with increasing frequency. The loss tangent (tan δ) was observed small in the films annealed at 750 ^{o}C, which can be attributed to the incorporation of oxygen in the stoichiometry of the films, and to the improved density as well. At lower annealing temperatures, the tan δ was found to increase, which can be due to less oxygen stoichiometry in the film lattice.

The prepared thin films had visible accumulation, depletion, and inversion phenomena. It was observed that the C-V plots of all prepared samples show clockwise hysteresis. In the capacitance-voltage plots, the clockwise and anti-clockwise hysteresis indicate electron and hole ejection into the film, respectively [39]. The clockwise hysteresis suggests positive Q_i, which shifts the C-V curve to a more negative side along the voltage axis. The anti-clockwise hysteresis suggests negative Q_i, shifting the C-V plot to a more positive side along the voltage axis [40,41]. Flat-band voltage, flat-band capacitance, interface density of states, the highest capacitance of depletion layer, and corresponding widths of the depletion layer, minimum capacitance, charge storage density, charge storage capacity, magnitude of hysteresis and density of interface states have been calculated, from the measured C-V variations, for all the prepared MIS structures.

From the C-V plots, the flat-band capacitance (C_{FB}) was found 117.01, 138.65, 184.27, 227.64, 263.72 and 273.63 pF, for the films deposited at RT, and annealed at 500, 600, 650, 700 and 750 ^{o}C, respectively. The flat-band voltage (V_{FB}) was observed -2.33, -0.95, -0.37, -0.35, -0.35 and -0.32 V, respectively. For all the prepared films, the flat-band voltage (V_{FB}) moved towards the left side concerning the ideal one.

With increasing annealing temperature, the flat-band voltage was shifted towards 0 V, i.e., it becomes less negative, up to 750 ^{o}C. This may be attributed to the following supposition. With increasing annealing temperature ($\geq$ 500 ^{o}C), it was observed that owing to the less escaping of alkali ions and improved oxygen stoichiometry might have reduced n-type carriers. Also, with the increase in annealing temperature, the crystallinity of the films enhanced than that for the samples deposited at RT and annealed at lower temperatures. The improved oxygen stoichiometry and crystallinity resulted in a reduced magnitude of $V_{FB,}$ for the films annealed from 500 to 750 ^{o}C temperature. Competition between the temperature-dependent escaping of A- and O-site constituents may be held accountable for the obtained C-V characteristics and V_{FB} shifting of the prepared $BCZT_{0.9}$ thin films.

The capacitance in the accumulation zone was used to compute the dielectric constant. The dielectric constant (ε) was found to be 38.01, 44.84, 92.34, 122.93, 135.28 and 148.81 for the films deposited at RT, annealed at 500, 600, 650, 700 and 750 ^{o}C, respectively, at 1 MHz, which are less than that measured results of the respective bulk pellets. The decrease in dielectric constant (ε) may be observed due to the deterioration in Ba and Ca stoichiometry and improvement in oxygen stoichiometry of the deposited films.

Charge storage capacity and density have been calculated for the as-deposited and the films annealed at 500, 600, 650, 700 and 750 ^{o}C. Charge storage capacity (3.99 fF/μm^2) and charge storage density (35.91 fC/μm^2) were found to be maximum for the films annealed at 750 ^{o}C. For the films that were annealed at 750 ^{o}C, the maximum relative permittivity (148) was obtained. At higher annealing temperatures, the dielectric constant was found sufficiently increased as compared to its base composition $BaTiO_3$ [42]. Hence, at the MPB region, this system $(Ba_{1-x}Ca_x)(Zr_{0.1}Ti_{0.9})O_3$ has reasonable charge storing capacity and charge storage density, for memory device applications. At lower annealing temperatures, due to low dielectric constant, low charge storing capacity, and low density of interface states, it may be useful in digital

circuits, ultrasonic delay lines, and insulating dielectrics to differentiate the conducting parts (transistors and wire interconnects) from one another, etc.

The significant composition-dependent variations in the dielectric properties and occurrence of morphotropic phase regions exhibit that $(Ba_{1-x}Ca_x)(Zr_{0.1}Ti_{0.9})O_3$ system has tremendous technological potential for developing tailor-made materials for industrial applications. Carrying out further careful and systematic studies, particularly for the improved stoichiometry of the thin film material, with varying composition (x) and processing conditions, may be helpful in further understanding the characteristic features of this lead-free system for different technological approaches.

8.2 Scope for future work

The ferroelectric perovskite lead-free materials exhibit good electrical properties, making them a potentially efficient alternative in the place of lead-based ferroelectrics. Electrical properties of lead-free $(Ba_{1-x}Ca_x)(Zr_{1-y}Ti_y)O_3$ (x, y = 0 to 1) ceramics were optimized in the current work using grain growth, chemical modification, and double sintering. The systematic investigations may show much information to understand the influences of grain growth, dopants and sintering on the dielectric and piezoelectric properties of BCZT ceramics. Also, the prepared $BCZT_{0.9}$ thin films show enhanced dielectric and minimum leakage current density. This work still has some limitations, so more research will need to be done.

- The electrical properties significantly depend on the sintering conditions. The sintering process may affect the prepared pellet samples' density, grain size, and other properties. Although, similar sintering conditions have been applied to the prepared pellet samples. One can vary the sintering temperature in accordance to the melting point of the composition. Therefore, more work needs to be done to get optimized sintering results.
- The present work systematically studied variation in A- site at MPB. However, variations in B- site may be performed to understand the change in the electrical properties.
- Piezoelectric materials may be a suitable choice to be used as a nanogenerator. Also, the enhanced output voltage will be necessary for nanogenerator applications. Therefore, more work needs to be done in this area.
- The study of compatible high K thin film materials can be helpful for memory devices, thin film capacitors, electromechanical devices, and high-frequency sensor applications.

The optical properties, leakage current density and dielectric constant were measured in the present study. More variations in deposition conditions and annealing temperature need to be done to get application-leading results.

- Variations in substrate temperature and biasing may result in enhanced dielectric constant and depreciation in the leakage current.
- Temperature variation of the electrical measurements may be performed to understand the thin film device properties.

References

[1] L.V. Azaroff, Elements of X-ray Crystallography, 1st ed., McGraw Hill Book Publishing, New York, 1968.

[2] S. Sen, R. Choudhay, Effect of doping Ca ions on structural and electrical properties of $Ba(Zr_{0.05}Ti_{0.95})O_3$ electroceramics, Journal of Materials Science: Materials in Electronics. 15 (2004) 671-675. https://doi.org/10.1023/B:JMSE.0000038922.74021.d6

[3] B. Malic, J. Koruza, J. Hrescak, J. Bernard, K. Wang, J. Fisher, A. Bencan, Sintering of lead-free piezoelectric sodium potassium niobate ceramics, Materials. 8 (2015) 8117-8146. https://doi.org/10.3390/ma8125449

[4] S. Singh, J. Negi, N.S. Panwar, Dielectric properties of $Na_{1-x}K_xNbO_3$, near x = 0.5 morphotropic phase region, Journal of Physics and Chemistry of Solids. 123 (2018) 311-327. https://doi.org/10.1016/j.jpcs.2018.08.018

[5] I.P. Raevskii, L.A. Reznichenko, O.I. Prokopalo, Phase-transition and electrical-properties of ferroelectric sodium niobate-based solid-solutions, Inorganic Materials. 15 (1979) 872-875.

[6] B. Jaffe, W.R.J. Cook, H. Jaffe, Piezoelectric ceramics, 1st ed., Academic Press publishing, London, 1971.

[7] K. Kakimoto, K. Akao, Y. Guo, H. Ohsato, Raman scattering study of piezoelectric $(Na_{0.5}K_{0.5})$ NbO3-LiNbO3 ceramics, Japanese Journal of Applied Physics. 44 (2005) 7064-7067. https://doi.org/10.1143/JJAP.44.7064

[8] Y. Ishibashia, M. Iwata, A theory of morphotropic phase boundary in solid-solution systems of perovskite-type oxide ferroelectrics, Japanese Journal of Applied Physics. 38 (1999) 800. https://doi.org/10.1143/JJAP.38.800

[9] Y. Saito, H. Takao, T. Tani, T. Nonoyama, K. Takatori, T. Homma, T. Nagaya, M. Nakamura, Lead-free piezoceramics, Nature. 432 (2004) 84-87. https://doi.org/10.1038/nature03028

[10] S.E. Park, T.R. Shrout, Ultrahigh strain and piezoelectric behavior in relaxor based ferroelectric single crystals, Journal of Applied Physics. 82 (1997) 1804. https://doi.org/10.1063/1.365983

[11] V.J. Tennery, K.W. Hang, Thermal and X-ray diffraction studies of the $NaNbO_3$-$KNbO_3$ System, Journal of Applied Physics. 39 (1968) 4749. https://doi.org/10.1063/1.1655833

[12] Y. Tian, L. Wei, X. Chao, Z. Liu, Z. Yang, Phase transition behavior and large piezoelectricity near the morphotropic phase boundary of lead-free $(Ba_{0.85}Ca_{0.15})(Zr_{0.1}Ti_{0.9})O_3$ ceramics. Journal of the American Ceramic Society. 96 (2013) 496-502. https://doi.org/10.1111/jace.12049

[13] D. Fu, Y. Kamai, N. Sakamoto, N. Wakiya, H. Suzuki, M. Itoh, Phase diagram and piezoelectric response of $(Ba_{1-x}Ca_x)(Zr_{0.1}Ti_{0.9})O_3$ solid solution, Journal of Physics: Condensed Matter. 25 (2013) 425901. https://doi.org/10.1088/0953-8984/25/42/425901

[14] J. Negi, S. Singh, N.S. Panwar, Structural and dielectric anomaly in $Na_{1-x}K_xNbO_3$, at x = 0.315, Phase Transitions, 92 (2019) 149-158. https://doi.org/10.1080/01411594.2018.1563789

[15] D. Biswas, P. Sharma, N.S. Panwar, Composition dependent electrical properties of $(Ba_{1-x}Ca_xZr_{0.1}Ti_{0.9})O_3$ ceramics, near morphotropic phase boundary ($0.140 \leq x \leq 0.160$), ECS Journal of Solid State Science and Technology. 10 (2021) 033002. https://doi.org/10.1149/2162-8777/abea61

[16] W. Cochran, Crystal stability and the theory of ferroelectricity, Advances in Physics. 9 (1960) 387-423. https://doi.org/10.1080/00018736000101229
[17] E. Pytte, Theory of perovskite ferroelectrics, Physical Review B. 5 (1972) 3758. https://doi.org/10.1103/PhysRevB.5.3758
[18] B.S. Semwal, N.S. Panwar, Dielectric properties of perovskite crystals, Bulletin of Materials Science. 15 (1992) 237-250. https://doi.org/10.1007/BF02927502
[19] R. Guo, L.E. Cross, S.E. Park, B. Noheda, D.E. Cox, G. Shirane, Origin of the High Piezoelectric Response in $PbZr_{1-x}Ti_xO_3$, Physical Review Letters. 84 (2000) 5423-5426. https://doi.org/10.1103/PhysRevLett.84.5423
[20] S. Mitra, A.R. Kulkarni, O. Prakash, Diffuse phase transition and electrical properties of lead-free piezoelectric $(Li_xNa_{1-x})NbO_3$ $(0.04 \leq x \leq 0.20)$ ceramics near morphotropic phase boundary, Journal of Applied Physics. 114 (2013) 064106. https://doi.org/10.1063/1.4817815
[21] S.O. Nelson, Dielectric properties of agricultural products-measurements and applications, IEEE transactions on Electrical Insulation. 26(1991) 845-869.https://doi.org/10.1109/14.99097
[22] C. Wenhua, Y. Lina, Design and simulation of high frequency tuned amplifier, Third International Conference on Measuring Technology and Mechatronics Automation, Shanghai, China, 2011, pp. 919-921. https://doi.org/10.1109/ICMTMA.2011.230
[23] A.K. Tagantsev, V.O. Sherman, K.F. Astafiev, J. Venkatesh, N. J.Setter, Ferroelectric Materials for Microwave Tunable Applications, Journal of Electroceramics. 11 (2003) 5-66. https://doi.org/10.1023/B:JECR.0000015661.81386.e6
[24] P.W. Smith, Pulsed, high power, RF generation from nonlinear dielectric ladder networks - Performance limits, IEEE Pulsed Power Conference, Chicago, USA, 2011, pp. 167-172, https://doi.org/10.1109/PPC.2011.6191408
[25] X. Wang, P. Liang, X. Chao, Z. Yang, Dielectric Properties and Impedance Spectroscopy of $MnCO_3$-Modified$(Ba_{0.85}Ca_{0.15})(Zr_{0.1}Ti_{0.9})O_3$ Lead-Free Ceramics, Journal of the American Ceramic Society. 98 (2015) 1506-1514. https://doi.org/10.1111/jace.13481
[26] M.H. Frey, Z. Xu, P. Han, D.A. Payne, The role of interfaces on an apparent grain size effect on the dielectric properties for ferroelectric barium titanate ceramics, Ferroelectrics. 206 (1998) 337-353. https://doi.org/10.1080/00150199808009168
[27] M. McQuarrie, F.W. Behnke, Structural and dielectric studies in the system (Ba, Ca)(Ti, Zr)O_3. Journal of the American Ceramic Society. 37 (1954)539-543.https://doi.org/10.1111/j.1151-2916.1954.tb13986.x
[28] W. Li, Z. Xu, R. Chu, P. Fu, G. Zang, Piezoelectric and Dielectric Properties of $(Ba_{1-x}Ca_x)(Ti_{0.95}Zr_{0.05})O_3$ Lead-Free Ceramics, Journal of the American Ceramic Society. 93 (2010) 2942-2944. https://doi.org/10.1111/j.1551-2916.2010.03907.x
[29] W. Li, Z. Xu, R. Chu, P. Fu, G. Zang, High piezoelectric d_{33} coefficient in $(Ba_{1-x}Ca_x)(Ti_{0.98}Zr_{0.02})O_3$ lead-free ceramics with relative high Curie temperature, Materials Letters. 64 (2010) 2325-2327. https://doi.org/10.1016/j.matlet.2010.07.042
[30] W. Chaisan, R. Yimnirun, S. Ananta, Two-stage sintering of barium titanate ceramic and resulting characteristics, Ferroelectrics, 346 (2007) 84-92. https://doi.org/10.1080/00150190601180380
[31] B.P. Zhu, W. Ke Guo, G.Z. Shen, Q. Zhou, K.K. Shung, Structure and electrical properties of (111)-oriented $Pb(Mg_{1/3}Nb_{2/3})O_3$-$PbZrO_3$-$PbTiO_3$ thin film for ultra high frequency transducer applications, IEEE Transactions on Ultrasonics, Ferroelectrics, and Frequency Control. 58 (2011) 1962-1967. https://doi.org/10.1109/TUFFC.2011.2038

[32] S.M. Sze, Physics of Semiconductor Devices, 2nd ed., Wiley Publishing, New York, 1981.
[33] R.A. Smith, Wave Mechanics of Crystalline Solids, 2nd ed., Chapman and Hall publishing, London, 1969.
[34] R. Swanepoel, Determination of the thickness and optical constants of amorphous silicon, Journal of Physics E: Scientific Instruments. 16 (1983) 1214. https://doi.org/10.1088/0022-3735/16/12/023
[35] S.P.P. Sadhu, M. Rath, S. Posam, S. Muthukumar V., M.S.R. Rao, K.B.R. Varma, Large nonlinear refraction in pulsed laser deposited BCZT thin films on quartz substrates, Journal of the Optical Society of America B. 35 (2018) 2625-2632. https://doi.org/10.1364/JOSAB.35.002625
[36] D.Y. Jiang, D.Z. Shen, K.W. Liu, C.X. Shan, Y.M. Zhao, T. Yang, B. Yao, Y.M. Lu, J.Y. Zhang, Effect of post annealing on the band gap of $Mg_xZn_{1-x}O$ thin films, Semiconductor Science and Technology. 23 (2008) 035002. https://doi.org/10.1088/0268-1242/23/3/035002
[37] E. Burstein, Anomalous optical absorption limit in InSb, Physical Review. 93 (1954) 632. https://doi.org/10.1103/PhysRev.93.632
[38] P.C. Joshi, M.W. Cole, Influence of postdeposition annealing on the enhanced structural and electrical properties of amorphous and crystalline Ta_2O_5 thin films for dynamic random access memory applications, Journal of Applied Physics. 86 (1999) 871. https://doi.org/10.1063/1.370817
[39] V. lingwal, N.S. Panwar, Capacitance-voltage characteristics of $NaNbO_3$ thin films, Journal of Applied Physics. 94 (2003) 4571. https://doi.org/10.1063/1.1608470
[40] E.H. Nicollian, J.R. Brews, MOS Physics and Technology, 1st ed., Wiley Publishing, New York, 1982.
[41] E.H. Snow, A.S. Grove, B.E. Deal, C.T. Sah, Ion transport phenomena in insulating films, Journal of Applied Physics. 36 (1965) 1664. https://doi.org/10.1063/1.1703105
[42] W.S. Choi, J. Yi, B. Hong, The effect of cerium doping in barium zirconate titanate thin films deposited by rf magnetron sputtering system, Materials Science and Engineering B. 109 (2004) 146-151. https://doi.org/10.1016/j.mseb.2003.10.081

Don R. Sarma
09. 06. 23